

ADVANCED MATERIALS FOR LITHIUM BATTERIES

by

Rochelle Weber

Submitted in partial fulfilment of the requirements
for the degree of Doctor of Philosophy

at

Dalhousie University
Halifax, Nova Scotia
April 2020

© Copyright by Rochelle Weber, 2020

TABLE OF CONTENTS

LIST OF TABLES	vi
LIST OF FIGURES	vii
ABSTRACT	xiii
LIST OF ABBREVIATIONS AND SYMBOLS USED	xiv
ACKNOWLEDGEMENTS	xvi
CHAPTER 1 INTRODUCTION.....	1
1.1 Motivation	1
1.2 Lithium-Ion Cells	5
1.2.1 Positive Electrode	7
1.2.2 Negative Electrode.....	8
1.3 Electrolyte	9
1.3.1 The Solid Electrolyte Interphase (SEI).....	11
1.4 Anode-Free Lithium-Metal Cells.....	13
1.4.1 Performance Challenges	16
CHAPTER 2 EXPERIMENTAL METHODS.....	23
2.1 Pouch Cells.....	23
2.2 Electrolyte	25
2.3 Cycling.....	25
2.4 Electrochemical Impedance Spectroscopy (EIS).....	26
2.4.1 Cycling with Automatic EIS.....	30

2.4.2	Symmetric Cells.....	30
2.5	Scanning Electron Microscopy (SEM)	31
2.6	Surface Area (Argon BET)	32
2.7	X-ray Photoelectron Spectroscopy (XPS).....	40
2.8	X-ray Diffraction (XRD).....	41
2.8.1	<i>Operando</i> XRD - Material Cycling	44
2.8.2	<i>In-situ</i> XRD - Material Synthesis	45
2.9	TGA-DSC-MS	50
CHAPTER 3 ELECTROLYTE ANALYSIS		52
3.1	Nuclear Magnetic Resonance Spectroscopy (NMR)	52
3.2	Method 1 – Composition.....	57
3.3	Method 2 – Amount	58
3.4	Electrolyte Analysis	59
3.5	Summary	64
CHAPTER 4 ANODE-FREE POUCH CELL DEGRADATION MECHANISMS		65
4.1	Cell Performance.....	65
4.2	Lithium Morphology	67
4.3	Lithium Surface Area	73
4.4	Electrolyte Consumption.....	77
4.5	Electrode Surface Studies.....	82

4.6	Gas Generation.....	86
4.7	Conclusions	88
CHAPTER 5 FURTHER STUDIES IN ANODE-FREE CELLS.....		90
5.1	New Electrolyte Blends.....	90
5.2	Hot Formation	94
5.3	Conclusions	100
CHAPTER 6 RESISTANCE GROWTH IN LITHIUM-ION POUCH CELLS WITH LiNi _{0.80} Co _{0.15} Al _{0.05} O ₂ POSITIVE ELECTRODES.....		101
6.1	Resistance Growth During Cycling	101
6.2	Resistance as a Function of Voltage	111
6.3	Conclusions	117
CHAPTER 7 X-RAY DIFFRACTION STUDY OF SINGLE-CRYSTAL LiNi _{0.5} Mn _{0.3} Co _{0.2} O ₂		118
7.1	Single-Crystal Material	120
7.2	Volume Change.....	125
7.3	Conclusions	130
CHAPTER 8 X-RAY DIFFRACTION STUDIES OF HIGH NICKEL CATHODE MATERIALS DURING SYNTHESIS.....		133
8.1	Synthesis of LiNiO ₂	134
8.2	Synthesis of Mg and Al doped LiNiO ₂	137
8.3	Powder Synthesis using a Preheating Step.....	142
8.4	Powder Synthesis without Precursor Additions	144
8.5	Conclusions	144

CHAPTER 9	CONCLUSIONS.....	147
9.1	Summary	147
9.2	Future Work	148
9.2.1	Anode-Free Salts.....	148
9.2.2	Anode-Free Pore Volume Measurements.....	149
9.2.3	Anode-Free Formation, Rate, and Geometry.....	150
9.2.4	Anode-Free EIS	151
9.2.5	Symmetric Cell Cycling.....	151
9.2.6	Comparison to Solid-State Electrolyte.....	151
9.2.7	<i>In-situ</i> XRD Heating Method Development.....	152
9.2.8	Single-Crystal LNMO.....	153
9.2.9	Anode-Free High-Nickel Cobalt-Free Cell.....	154
REFERENCES	155
APPENDIX A	168

LIST OF TABLES

Table 1-1. Energy density and specific energy of an anode-free cell compared to a lithium-ion cell.....	14
Table 1-2. Stack energy density for theoretical anode-free cells with different positive electrode materials.	16
Table 3-1. List of NMR experiments for analyzing electrolyte with the components used in anode-free cells.	60
Table 3-2. Proton NMR chemical shifts for electrolyte components in d-DMSO.	62
Table 3-3. Fluorine NMR chemical shifts for electrolyte components in d-DMSO.....	63
Table 3-4. Boron NMR chemical shifts for electrolyte components in d-DMSO.	63
Table 3-5. Calculated electrolyte compositions compared to the composition measured by NMR.	64
Table 7-1. X-ray diffraction refinement parameters for polycrystalline and single-crystal NMC532 electrodes.	124
Table 9-1. Two potential large-anion fluorinated salts that could be tested in anode-free cells.	148

LIST OF FIGURES

Figure 1-1. Lithium-ion pouch cell and schematics.	5
Figure 1-2. Voltage profiles for example cathode and anode.	6
Figure 1-3. Crystal structure of a positive electrode material.	7
Figure 1-4. Chemical structure of some lithium salts used in electrolytes.	10
Figure 1-5. Chemical structure of some carbonate solvents used in electrolytes.	11
Figure 1-6. Chemical structure of two cyclic carbonates commonly used as electrolyte additives.	12
Figure 1-7. Anode-free pouch cell pictures and schematics.	13
Figure 1-8. Diagram of lithium metal plating, dendrite growth, and degradation modes by SEI formation or isolated metallic lithium formation.	17
Figure 1-9. Copper foil current collector used in this work.	21
Figure 1-10. SEM images of lithium nuclei deposited at different current densities	22
Figure 2-1. Plastic and metal pouch cell testing fixtures used to apply various levels of stack pressure.	24
Figure 2-2. Example circuits and impedance responses shown as Nyquist plots.	27
Figure 2-3. Equivalent circuit for impedance at electrode particle.	28
Figure 2-4. Example of a Nyquist plot from an EIS measurement of a lithium-ion cell. ...	29
Figure 2-5. Work-flow for building symmetric coins cells from a pouch cell.	30
Figure 2-6. (a) Negative electrode with plated lithium metal after charging in an anode-free lithium-metal pouch cell.	34
Figure 2-7. (a) Nitrogen BET isotherm from surface area measurement of two samples of lithium foil.	36
Figure 2-8. Repeated nitrogen BET runs on the same piece of lithium foil.	38
Figure 2-9. Argon and Nitrogen BET measurement of lithium metal electrode from a pouch cell after 1 charge cycle.	39
Figure 2-10. Comparison of BET measured on a graphite sample using either argon or nitrogen.	40
Figure 2-11. Schematic of X-rays interacting with atoms in a crystal lattice.	42
Figure 2-12. Example of an X-ray diffraction pattern for NMC532.	43

Figure 2-13. <i>In-situ</i> XRD heating apparatus at the Canadian Light Source.	46
Figure 2-14. <i>In-situ</i> XRD heating fixture mounted on the beamline.	47
Figure 2-15. <i>In-situ</i> XRD heating profile during <i>in-situ</i> XRD run.	48
Figure 2-16. An example of part of a CCD image.	49
Figure 2-17. Example of mask used to integrate CCD images without the aberrations in the horizontal direction.	50
Figure 3-1. An illustration of the energy difference between nuclei with spin-up (+1/2) and spin-down (-1/2) magnetic moments in an external applied magnetic field.	53
Figure 3-2. The series of steps in an NMR measurement.	55
Figure 3-3. Example of proton NMR spectrum for DEC.	56
Figure 3-4. Detailed view of peaks in NMR spectrum.	56
Figure 3-5. Pouch cells and NMR samples for electrolyte analysis.	57
Figure 3-6. Measuring total electrolyte amount with NMR.	59
Figure 3-7. Example of NMR spectra (¹ H) for electrolyte analysis by NMR.	61
Figure 3-8. Example of NMR spectra (¹⁹ F) for electrolyte analysis by NMR.	62
Figure 4-1. Capacity retention versus cycle number for anode-free pouch cells using electrolytes with different lithium salts.	65
Figure 4-2. Capacity retention versus cycle number as a function of upper cut-off voltage for anode free pouch cells with two electrolytes with different salts: 1.2 M LiDFOB versus 0.6 M LiDFOB + 0.6 M LiBF ₄	67
Figure 4-3. SEM characterization of lithium morphology from anode-free pouch cells after cycling with different electrolytes.	68
Figure 4-4. Cycling data and SEM images for anode-free pouch cells with either 1.2M LiDFOB or dual-salt LiDFOB/LiBF ₄ electrolyte cells cycled under pressure.	70
Figure 4-5. SEM images of plated lithium in the dual-salt 0.6M LiDFOB + 0.6M LiBF ₄ electrolyte under 1200 kPa after 50 cycles at the top of charge and after ~80% of the lithium is stripped away.	71
Figure 4-6. SEM images showing the evolution of lithium morphology in pouch cells from cycle 1 to cycle 100.	72
Figure 4-7. SEM images of the lithium metal from two different locations on the same anode after 1 cycle, 5 cycles, 10 cycles, or 20 cycles.	73

Figure 4-8. Cycling data and surface area measurements for anode-free lithium metal cells cycled with 1M LiPF ₆ in FEC:DEC (1:2 vol) electrolyte.	74
Figure 4-9. Cycling data and surface area measurements for anode-free lithium metal cells cycled with 1M LiDFOB 0.2 M LiBF ₄ in FEC:DEC (1:2 vol) electrolyte.	76
Figure 4-10. Average amount of electrolyte versus cycle number for anode-free cells with either 0.9m LiPF ₆ electrolyte or 0.9m LiDFOB electrolyte.	77
Figure 4-11. Electrolyte composition during cycling for anode-free pouch cells that started with 0.9m LiPF ₆ electrolyte, 0.9m LiDFOB electrolyte, or 0.5m LiDFOB + 0.5m LiBF ₄ electrolyte.	78
Figure 4-12. Fluorine NMR spectra for cells that started with 1M LiDFOB electrolyte showing the formation of LiBF ₄ during cycling.	80
Figure 4-13. Salt concentration vs cycle number for cells that started with 1.1 m (1.2 M) LiDFOB electrolyte charged to either 4.2 V or 4.5 V at 40°C.	81
Figure 4-14. Boron and phosphorous XPS data from anodes and cathodes harvested from anode-free cells formed with different electrolytes: 1M LiPF ₆ , 1M LiDFOB, or 0.6M LiDFOB 0.6M LiBF ₄	83
Figure 4-15. XPS spectra for lithium electrodes harvested from anode-free cells formed with different electrolytes: 1M LiPF ₆ , 1M LiDFOB, or 0.6M LiDFOB 0.6M LiBF ₄	84
Figure 4-16. XPS spectra for cathodes harvested from anode-free cells formed with different electrolytes: 1M LiPF ₆ , 1M LiDFOB, or 0.6M LiDFOB 0.6M LiBF ₄	85
Figure 4-17. Images and <i>in-situ</i> volume data for anode-free pouch cells with 1.2M LiDFOB or dual salt (0.6M LiDFOB 0.6M LiBF ₄) electrolyte charged between 3.6-4.3 V or 3.6-4.5 V.	87
Figure 5-1. Normalized discharge capacity vs cycle for cells with increased LiDFOB content either by increasing electrolyte volume or salt concentration.	90
Figure 5-2. Normalized discharge capacity vs cycle number for cells with other salt combinations.	91
Figure 5-3. Electrolyte composition vs cycle number for anode-free cells cycled with one of two electrolytes (1) 0.5m LiDFOB 0.5m LiPF ₆ or (2) 0.5m LiDFOB 0.5m LiPF ₆ 0.5m LiBF ₄ both with FEC:DEC (1:2 vol) solvent.	92
Figure 5-4. Normalized discharge capacity vs cycle for anode-free cells with 0.6M LiDFOB 0.6M LiBF ₄ FEC:DEC (1:2 vol) electrolyte tested at different temperatures	94
Figure 5-5. SEM images of initial lithium morphology in cells with 0.6M LiDFOB 0.6M LiBF ₄ FEC:DEC (1:2 vol) electrolyte tested at 20°C or 40°C.	95

Figure 5-6. Normalized discharge capacity vs cycle for anode-free cells with 0.6M LiDFOB 0.6M LiBF ₄ FEC:DEC (1:2 vol) electrolyte tested at different temperatures and pressures.....	96
Figure 5-7. Normalized discharge capacity vs cycle for anode-free cells with 0.6M LiDFOB 0.6M LiBF ₄ FEC:DEC (1:2 vol) electrolyte tested at 20°C and different pressures, with or without hot (40°C) formation.	97
Figure 5-8. SEM images of lithium morphology after 20 cycles in cells with 0.6M LiDFOB 0.6M LiBF ₄ FEC:DEC (1:2 vol) electrolyte tested with or without hot (40°C) formation.....	98
Figure 5-9. Normalized discharge capacity vs cycle for anode-free cells with 1.8M LiDFOB 0.4M LiBF ₄ FEC:DEC (1:2 vol) electrolyte tested at 20°C after hot (40°C) formation.....	99
Figure 5-10. Normalized discharge capacity vs cycle for anode-free cells tested with either C/2 or C/5 discharge.	99
Figure 6-1. Normalized discharge capacity and delta V for three types of lithium-ion pouch cells with NCA positive electrodes measured over 200 cycles.....	102
Figure 6-2. The electrode and full cell impedance for NCA/graphite-SiC pouch cells at 10°C, before and after cycling.	104
Figure 6-3. Nyquist and Bode plots of impedance for an NCA positive electrode, measured using symmetric cells at 10°C, before and after cell formation.	105
Figure 6-4. Cracks observed after use for NCA and NMC particles with images of pristine material for comparison.	107
Figure 6-5. Cross-sectional TEM images of NCA particles and corresponding SAED patterns before and after 350 cycles at 1C and 60°C from 2.5 V – 4.2 V.	108
Figure 6-6. (a) Normalized discharge capacity and delta V growth for NCA/graphite cells cycled in different voltage ranges at 40°C and C/3.	110
Figure 6-7. Resistance as a function of voltage and cycle number for NCA/graphite cells cycled at 40°C and C/3 in different voltage ranges.	111
Figure 6-8. EIS spectra for three types of lithium-ion pouch cells with NCA positive electrodes at three different voltages (3.1 V, 3.8 V, 4.2 V) all measured at 40°C before and after 200 cycles.	112
Figure 6-9. The resistance for three types of lithium-ion pouch cells with NCA positive electrodes as a function of voltage and cycle number measured at 40°C.	114
Figure 6-10. Positive and negative electrode impedance at different voltages at 40°C (measured using symmetric cells after pouch cell formation), and full-cell resistance values plotted as a function of cathode lithium content.....	115

Figure 6-11. Equivalent circuit and schematic to represent the impedance of lithium traveling through the SEI (surface-film + rock-salt layer) and bulk NCA.	117
Figure 7-1. Fractional capacity and normalized delta V versus cycle number for single crystal NMC532/graphite cells tested between 3.0 and 4.3 V.	118
Figure 7-2. The normalized capacity of pouch cells with single-crystal NMC532 cathode or polycrystalline NMC532 cathode tested at 40°C, C/2 CCCV from 3.0 to 4.4 V.	119
Figure 7-3. SEM images of electrodes made from polycrystalline or single-crystal NMC532.	120
Figure 7-4. X-ray diffraction of electrodes made from polycrystalline and single-crystal NMC532.	123
Figure 7-5. X-ray diffraction patterns and refinements for polycrystalline and single-crystal NMC532 electrodes.	124
Figure 7-6. Cell potential vs. specific capacity and dQ/dV vs potential for polycrystalline and single-crystal NMC532.	125
Figure 7-7. <i>Operando</i> X-ray diffraction data for polycrystalline and single-crystal NMC532.	126
Figure 7-8. Detailed view of the (10 $\bar{8}$) and (110) peaks for polycrystalline and single-crystal NMC532 at the bottom of the first discharge and at the bottom of the second discharge.	127
Figure 7-9. Lattice parameters and unit cell volume for polycrystalline and single-crystal NMC532 as a function of specific capacity.	128
Figure 7-10. Lattice parameters and unit cell volume for polycrystalline and single-crystal NMC532 as a function of average cell potential during each XRD scan.	129
Figure 7-11. Cross sectional SEM of a single crystal NMC532 positive electrode taken from a cell tested at 1C:1C 20°C with 97% capacity retention after 5300 cycles.	131
Figure 7-12. Cross sectional SEM of retrieved positive electrode from cycled SC811 pouch cell at 4.3 V.	132
Figure 8-1. XRD patterns recorded from 100°C to 800°C during heating for the LNO samples prepared with LiOH•H ₂ O.	135
Figure 8-2. Detailed view of (003) and (10 $\bar{8}$)/(110) Bragg peaks during heating for LNO prepared with LiOH•H ₂ O or Li ₂ CO ₃ and Delta 2θ vs temperature for the (10 $\bar{8}$)/(110) combined peak.	136
Figure 8-3. Detailed view of (003) and (10 $\bar{8}$)/(110) Bragg peaks during heating for LNO, LNMO, and LNAO all prepared with LiOH•H ₂ O.	137

Figure 8-4. FWHM of the (003) Bragg peak vs temperature, and delta 2θ for the (10 $\bar{8}$)/(110) combined peak vs. temperature during heating for LNO, LNMO, and LNAO all prepared with LiOH•H ₂ O.....	138
Figure 8-5. Combined TGA-DSC-MS data for LNO, LNMO, and LNAO all prepared with LiOH•H ₂ O.....	140
Figure 8-6. Detailed view of the (003) and (10 $\bar{8}$)/(110) Bragg peaks during heating for LNO, LNMO and LNAO all prepared with Li ₂ CO ₃	141
Figure 8-7. Delta 2θ for the (10 $\bar{8}$)/(110) combined peak vs. temperature during heating for LNO, LNMO, and LNAO all prepared with Li ₂ CO ₃	142
Figure 8-8. Detailed view of the (003) and (10 $\bar{8}$)/(110) XRD peaks during heating for LNAO and LNAO with 480°C preheat, and the FWHM of the (003) peak vs. temperature.	143
Figure 8-9. Detailed view of the (003) and (10 $\bar{8}$)/(110) Bragg peaks during heating for LNAO and LNAO without precursor and delta 2θ for the (10 $\bar{8}$)/(110) combined peak vs. temperature.	145

ABSTRACT

Advanced lithium battery materials promise some combination of higher energy density, lower cost, longer lifetime, and faster charging rates compared to traditional lithium-ion batteries. This work studies lithium-metal anodes in “anode-free cells” which aim to increase cell energy density, and cutting edge cathode materials that can extend cell lifetime or reduce cost.

Lithium-metal anodes are yet to be used in commercial products at a large scale since they lose capacity at a much faster rate than traditional lithium-ion batteries. Here a method is developed to quantify the surface area of lithium-metal electrodes by argon gas adsorption. Methods are also developed to analyze electrolyte from lithium-metal cells in order to understand the extent and type of reactions occurring with the lithium-metal electrode. These studies are used to develop an optimized electrolyte that extends cell lifetime.

Advanced cathode materials are then studied. Resistance growth is monitored in pouch cells with $\text{LiNi}_{0.80}\text{Co}_{0.15}\text{Al}_{0.5}\text{O}_2$ cathode, a material that is used in commercial cells today. The crystal structure is studied versus lithium content, x , for single-crystal $\text{Li}_x\text{Ni}_{0.5}\text{Mn}_{0.3}\text{Co}_{0.2}\text{O}_2$, a recently developed cathode material that extends cell lifetime and has very little resistance growth. Lastly, synthesis is studied using *in-situ* high temperature diffraction for new lithium-transition metal-oxide cathode materials that are the focus of electrochemical studies by others in our laboratory.

LIST OF ABBREVIATIONS AND SYMBOLS USED

(+1/2)	Spin up magnetic moment
(-1/2)	Spin down magnetic moment
ΔV	Delta V
I_0	Intensity scale factor
u_z	Magnetic dipole moment
BET	Brunauer–Emmett–Teller
B_0	Applied magnetic field
C	Capacitor
CE	Coulombic Efficiency
d-DMSO	Deuterated dimethyl sulfoxide
DEC	Diethyl carbonate
DMC	Dimethyl carbonate
DMSO	Dimethyl sulfoxide
e-	Electron
EC	Ethylene carbonate
EIS	Electrochemical impedance spectroscopy
EMC	Ethyl methyl carbonate
EV	Electric vehicle
FEC	Fluoroethylene carbonate
FID	Free induction decay
GCMS	Gas chromatography mass spectroscopy
\hbar	Planks constant
ICP	Inverse coupled plasma spectroscopy
Im(Z)	Imaginary component of impedance
j	Imaginary number
LCO	Lithium cobalt oxide
Li+	Lithium-ion
NCA	Lithium nickel cobalt aluminum oxide
NMC	Lithium nickel manganese cobalt oxide
NMR	Nuclear magnetic resonance spectroscopy
O1P	Center point of NMR scan in ppm
PFA	Perfluoroalkoxy
p_0	Ambient pressure
PVDF	Polyvinylidene difluoride
R	Resistor
R_{ct}	Charge-transfer resistance
Re(Z)	Real component of impedance
RF	Radio frequency
SAED	Selected area electron diffraction
SEI	Solid electrolyte interphase
SEM	Scanning electron microscopy
SW	Sweep-width NMR scan in ppm
TEM	Transmission electron microscopy
ω	Frequency

V_{anode}	Anode potential
VC	Vinylene carbonate
V_{cathode}	Cathode potential
V_{cell}	Cell potential
wt%	Weight percent
XPS	X-ray photoelectron spectroscopy
XRD	X-ray diffraction
Z	Impedance
Φ	Work function
$DW(2\theta)$	Debye-Waller thermal factor
$F(hkl)$	Geometric structure factor
$L(\theta)$	Lorentz factor
$M(hkl)$	Multiplicity factor
$P(\theta)$	Polarization factor
d	Spacing between atomic planes
m	Magnetic moment
γ	Gyromagnetic ratio of nuclei
θ	Angle of incident X-ray beam
λ	X-ray wavelength

ACKNOWLEDGEMENTS

I appreciate all the help I received from Professors and Staff at Dalhousie University.

Thank you to Kevin Plucknett for supervision in the Engineering Department and for many useful discussions. Thank you to my other committee members Ian Hill and Lukas Swan. Thank you to my supervisor Jeff Dahn for his guidance and enthusiasm throughout the duration of this research.

Great acknowledgement goes to the other lab members who worked with me on these projects. Thank you to Matthew Genovese and Alex Louli for starting the anode-free work with me, and to Sam Hames and Cameron Martin for their extensive help while here as co-op students. Thank you to Hongyang Li for his cathode materials expertise and his partnership on the synchrotron studies. Many thanks to the Canadian Light Source beamline scientists, Chang-Yong Kim and Weifeng Chen, and to Toby Bond for his help as well. I acknowledge the receipt of support from the CLSI Graduate and Post-Doctoral Student Travel Support Program.

Thank you to FGS, and to George C. Reid and Lucille M. Reid for scholarship support. Lastly, thank you to Tesla-Canada R&D for financial support of this work and thank you in particular to Sunny Hy, Remi Petibon, and William Germscheid for their help and friendship.

CHAPTER 1 INTRODUCTION

1.1 Motivation

The current applications of lithium-ion batteries include but are not limited to electric vehicles, energy storage products, and portable electronics. Each of these technologies has different requirements but in general longer lifetime, higher energy density, and lower cost batteries are desired.

For applications like flight (drones) and electric vehicles, high energy density batteries can increase flying time and extend driving range. One of the most promising ways to achieve higher energy density compared to current lithium-ion batteries is to replace the traditional graphite anode with lithium-metal. Lithium-metal has an extremely high theoretical capacity at 3680 mAh/g, compared to 372 mAh/g for graphite. The anode potential of lithium-metal is also lower than graphite, which gives an additional boost in energy by increasing the average cell voltage. Cells with lithium-metal anodes are in particular compelling if they can be built in the “anode-free” configuration with liquid electrolyte. An “anode-free” lithium-metal cell forms the lithium metal electrode on the first charge when the lithium-ions originating from the cathode plate on the negative electrode current collector.¹⁻³ Manufacturing is simplified since all solid cell components are stable in air and existing lithium-ion manufacturing equipment could be used, including electrolyte filling machines.

Unfortunately anode-free cells have poor lifetimes. Lithium-metal is prone to react with electrolyte and form dendritic structures that can pierce the separator and short the cell, or can break away from the main electrode and lead to rapid capacity loss in the form of

isolated metallic lithium.⁴⁻⁶ These problems prevent mass commercialization of anode-free cells at the moment and they cannot currently be used in cars where battery warranties range from 5 – 8 years (>1000 charge/discharge cycles). The lifetime required for use in drones is somewhat more achievable, since the batteries can be easily replaced after 100 or so cycles.

For other battery applications like energy storage, the semi-permanent installations demand long-lifetime on the order of 10-20 years. Traditional lithium-ion cells are more appropriate for this application than anode-free cells. Even for cells with a graphite anode, any reactions that consume capacity must be minimized in order to achieve such long lifetime. One avenue to achieve long-lifetime is through the selection of an appropriate cathode. Advanced cathode materials aim to improve cell lifetime while maintaining high energy density and low cost. For example, recently developed single-crystal materials dramatically extend cell lifetime,^{7,8} and cobalt-free materials are being explored to reduce cost.⁹

Chapter 2 describes experimental methods used in this work: cell making, electrochemical testing, structural characterization by scanning electron microscopy (SEM), surface area measurements by argon adsorption, surface characterization by X-ray photoelectron spectroscopy (XPS), and materials characterization by X-ray diffraction (XRD).

The first half of this thesis focuses on anode-free lithium-metal cells. Chapter 3 develops a method for electrolyte analysis by Nuclear Magnetic Resonance Spectroscopy (NMR). Chapter 4 uses this and other methods to study degradation in anode-free lithium-metal

pouch cells. Chapter 5 uses the learnings from Chapter 4 to develop new electrolyte and formation procedures that improve capacity retention.

The second half of this thesis focuses on advanced cathode materials which are targeted for use in the highest energy density anode-free cells. Chapter 6 studies resistance growth in pouch cells with $\text{LiNi}_x\text{Co}_y\text{Al}_z\text{O}_2$ (NCA) positive electrodes, a material used in state-of-the-art commercial lithium-ion cells today. Chapter 7 uses XRD to study single-crystal $\text{LiNi}_x\text{Mn}_y\text{Co}_z\text{O}_2$ (NMC), an advanced cathode material with minimal resistance growth and long lifetime. Chapter 8 uses XRD to study synthesis of new cathode materials.

Lastly, Chapter 9 discusses conclusions and future work.

Many of the results presented here were previously published in the following manuscripts:

- **R. Weber**, J.-H. Cheng, A. J. Louli, M. Coon, S. Hy, and J. R. Dahn, Surface Area of Lithium-Metal Electrodes Measured by Argon Adsorption. *J. Electrochem. Soc.* **166**, A3250–A3253 (2019).

Contributions: Performed all pouch cell testing, ran all lithium-metal electrode BET measurements, and wrote the manuscript.

- **R. Weber**, M. Genovese, A. J. Louli, S. Hames, C. Martin, I. G. Hill, and J. R. Dahn, Long Cycle Life And Dendrite-Free Lithium Morphology In Anode-Free Lithium Pouch Cells Enabled By A Dual-Salt Liquid Electrolyte. *Nature Energy* **4**, 683–689 (2019).

Contributions: Prepared electrolyte and cycled pouch cells for two electrolyte types. Performed all sample prep, measurements, and data analysis for all XPS and NMR. Wrote the manuscript (with significant help from M. Genovese).

- M. Genovese, A. J. Louli, **R. Weber**, C. Martin, T. Taskovic, and J. R. Dahn, Hot Formation for Improved Low Temperature Cycling of Anode-Free Lithium Metal Batteries. *J. Electrochem. Soc.* **166**, A3342–A3347 (2019).

Contributions: Helped conceive the idea and plan experiments, some pouch cell testing.

- **R. Weber**, A. J. Louli, K. P. Plucknett, and J. R. Dahn, Resistance Growth in Lithium-Ion Pouch Cells with $\text{LiNi}_{0.80}\text{Co}_{0.15}\text{Al}_{0.05}\text{O}_2$ Positive Electrodes and Proposed Mechanism for Voltage Dependent Charge-Transfer Resistance. *J. Electrochem. Soc.* **166**, A1779–A1784 (2019).

Contributions: Performed all pouch cell cycling and EIS, analyzed all data with help from A.J. Louli for dVdQ, and wrote the manuscript.

- R. Weber, C. R. Fell, J. R. Dahn, and S. Hy, *Operando* X-ray Diffraction Study of Polycrystalline and Single-Crystal $\text{Li}_x\text{Ni}_{0.5}\text{Mn}_{0.3}\text{Co}_{0.2}\text{O}_2$. *J. Electrochem. Soc.* **164**, A2992–A2999 (2017).

Contributions from R. Weber: Performed all electrochemical measurements, performed all XRD, analyzed all data with help from Sunny Hy for refinements, and wrote the manuscript.

Appendix A includes license agreements to reproduce work previously published where required.

1.2 Lithium-Ion Cells

A typical lithium-ion cell is composed of a lithium-transition-metal-oxide cathode, a graphite anode, and an organic electrolyte. Figure 1-1a shows a lithium-ion pouch cell with only the external electrical connections visible, labelled as the positive tab and negative tab. Figure 1-1b shows the electrode jelly roll inside the pouch cell, made of a wound layer of anode (negative electrode), separator, and cathode (positive electrode). The electrodes are made from a mix of mostly active material (>90 wt% graphite or

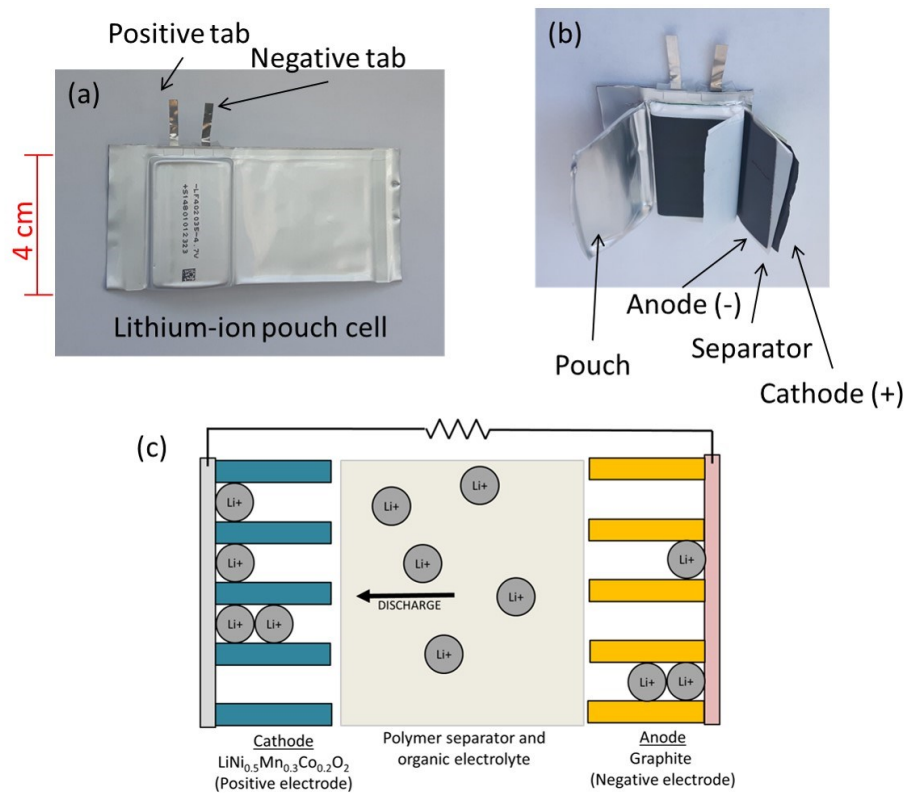


Figure 1-1. Lithium-ion pouch cell. (a) Pouch cell used in this work showing size and electrical connections (b) Inside of the pouch cell showing the components of the jelly roll: anode, separator, and cathode. (c) Schematic of the electrode stack during discharge.

lithium-transition-metal oxide), conductive carbon additive like carbon black, and a polymeric binder like polyvinylidene difluoride (PVDF). The anode is coated on a copper current collector and the cathode is coated on an aluminum current collector. During operation lithium-ions are shuttled through the separator between the cathode and the anode via a liquid electrolyte. The liquid electrolyte is made of an ion conducting lithium salt dissolved in an organic liquid. The graphite anode serves to store energy by intercalating lithium-ions during charge, and de-intercalating lithium-ions during discharge. A schematic of discharge is shown in Figure 1-1c with lithium-ions moving from the anode to the cathode.

Figure 1-2 shows example electrode potentials vs capacity. Figure 1-2a shows the electrode potential for a $\text{LiNi}_{0.5}\text{Mn}_{0.3}\text{Co}_{0.2}\text{O}_2$ (NMC532) cathode. Figure 1-2b shows the electrode potential for a graphite anode. Electrode potential is typically reported vs the potential of $\text{Li}^+ + e^- \leftrightarrow \text{Li}(s)$.¹⁰ The full cell potential is the difference in cathode and anode potential: $V_{\text{cell}} = V_{\text{cathode}} - V_{\text{anode}}$. For an anode-free lithium metal cell the anode

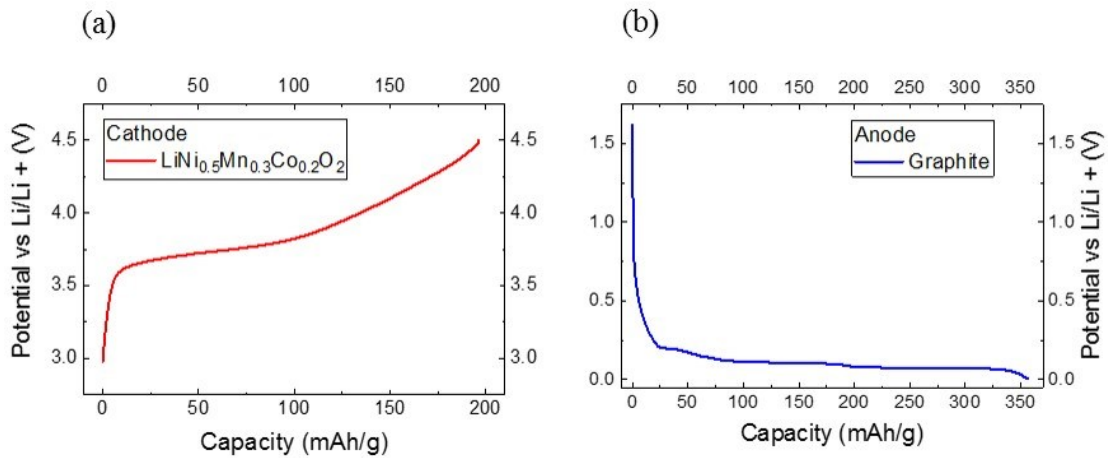


Figure 1-2. Voltage profiles for (a) $\text{LiNi}_{0.5}\text{Mn}_{0.3}\text{Co}_{0.2}\text{O}_2$ cathode and (b) graphite anode.

potential is $V_{\text{anode}} = 0$ vs Li/Li^+ , so the full cell potential is exactly that of the cathode.

Cells in this work use NMC532 with the voltage profile shown in Figure 1-2a.

1.2.1 Positive Electrode

Positive electrode materials are commonly layered transition metal oxides such as $\text{LiNi}_x\text{Mn}_y\text{Co}_z\text{O}_2$ (NMC), $\text{LiNi}_x\text{Co}_y\text{Al}_z\text{O}_2$ (NCA), and LiCoO_2 (LCO), but can also be olivine LiFePO_4 (LFP) or spinel LiMnO_2 (LMO).¹⁰ Figure 1-3 shows the crystal structure of a layered positive electrode material (NCA, NMC, LCO).

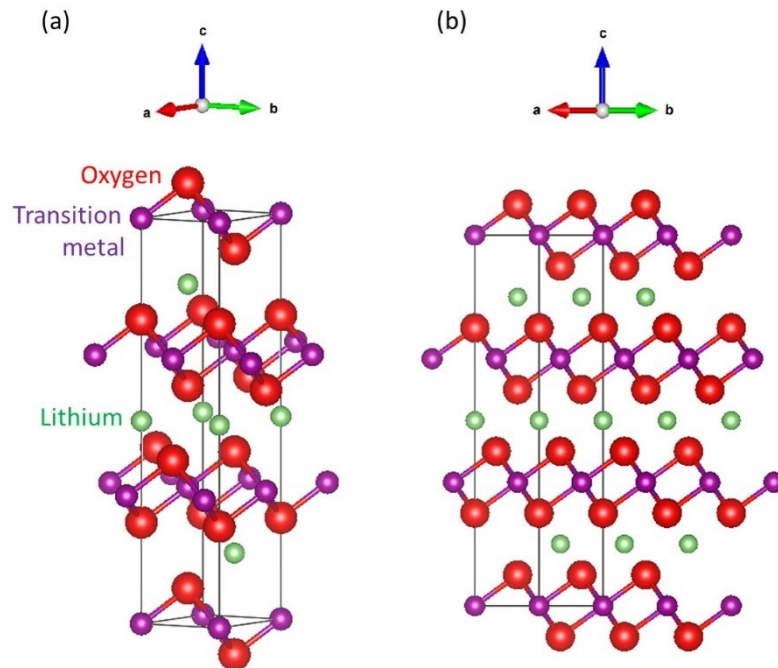


Figure 1-3. Crystal structure of a layered transition metal oxide positive electrode material. (a) One unit cell shown in an offset view and (b) three unit cells shown in a 110 projection. Space group is R-3m #166.

The space group for this structure is R-3m. Lithium-atoms are stored between the transition-metal/oxygen layers. During cell charging lithium atoms are extracted as ions

and electrons and the spacing between the layers changes, but the overall structure is maintained. In the NMC and NCA families several different transition metal compositions are used. $\text{LiNi}_{1/3}\text{Mn}_{1/3}\text{Co}_{1/3}\text{O}_2$ (NMC111), $\text{LiNi}_{0.5}\text{Mn}_{0.3}\text{Co}_{0.2}\text{O}_2$ (NMC532), $\text{LiNi}_{0.6}\text{Mn}_{0.2}\text{Co}_{0.2}\text{O}_2$ (NMC622), $\text{LiNi}_{0.8}\text{Mn}_{0.1}\text{Co}_{0.1}\text{O}_2$ (NMC811). Higher nickel content is usually preferred for increased specific capacity and lower cobalt content is preferred to limit cost. For similar reasons high nickel NCA materials like $\text{LiNi}_{0.8}\text{Co}_{0.15}\text{Al}_{0.05}\text{O}_2$ are preferred. However, for both NMC and NCA, higher nickel materials demonstrate worse lifetime and lower thermal stability.^{9,11-13} The choice of cathode materials is based on the trade-off between specific capacity, structural and thermal stability, and cost.

Recent development work for cathode materials focuses on maintaining the high energy density of high nickel NMC and NCA, while overcoming the lifetime and stability problems through coating, doping, micro-structuring, or electrolyte choice.^{7,14-18} Efforts have also been undertaken to reduce the cost of cathode materials by finding alternative dopants that can eliminate the need for cobalt.⁹

1.2.2 Negative Electrode

Commercial lithium-ion batteries typically use a graphite negative electrode. Graphite is made up of stacked layers of graphene held together by Van der Waals forces. During cell charging lithium atoms intercalate between the graphene layers as per the following reaction: $x\text{Li}^+ + xe^- + y\text{C}_6 \leftrightarrow y\text{Li}_x\text{C}_6$ where maximum theoretical storage capacity is 372 mAh/g for the phase LiC_6 .¹⁰

Negative electrode materials other than graphite are of interest to increase cell energy density. For example, silicon as an anode has a theoretical energy density of 3600

mAh/g.¹⁹ Since lithium-ions are stored through an alloy reaction, instead of intercalation like graphite, the anode undergoes a massive volume change during lithiation. The subsequent obliteration of silicon particles can lead to rapid capacity loss. Other alloy negative electrodes like tin, magnesium, silver, and zinc are possible anodes but these all suffer from the same mechanical capacity loss mechanism as silicon.¹⁹

Another pathway for higher energy density is using pure lithium metal as the negative electrode which has a theoretical capacity of 3860 mAh/g.⁶ Like silicon, lithium metal electrodes experience large volume changes which can lead to rapid capacity loss. In addition, lithium metal has the lowest potential of possible anodes which makes it the most prone to consume capacity through reduction of electrolyte components. Lithium-metal anodes are the primary topic of the first part of this thesis.

1.3 Electrolyte

The electrolyte in a lithium-ion cell is made from one or multiple lithium salts dissolved in an organic solvent blend, typically composed of two or more carbonates. Figure 1-4 shows the chemical structure of some lithium salts that can be used in the electrolyte. Each structure is shown with the chemical name and abbreviation used to refer to it. A lithium salt is selected for high solubility, high ionic conductivity, thermal stability, stability against reaction with all cell components, and price. The most common choice for lithium salt is lithium hexafluorophosphate (LiPF₆) which balances these attributes.²⁰ Other lithium salts have some major disadvantages that prevent widespread commercial adoption over LiPF₆. LiClO₄ is unstable at high temperature and high current density.^{20,21} Although LiAsF₆ is minimally toxic, the reduction products formed in a cell can be

highly toxic.^{20,22} LiBF_4 , LiBOB , and LiDFOB all have worse conductivity compared to electrolytes with LiPF_6 .²³⁻²⁵ The cathode current collector in cells with only LiFSI or LiTFSI will corrode since these salts do not passivate aluminum.^{20,22,26,27} LiPF_6 is not without its demerits though. Reactions with any residual moisture in the cell form HF , and this salt tends to thermally decompose.²⁸⁻³⁰ As mentioned LiPF_6 is popular not because it wins in all categories, but because it provides an acceptable balance of all the desirable attributes for a lithium salt. Figure 1-5 shows the chemical structure of some

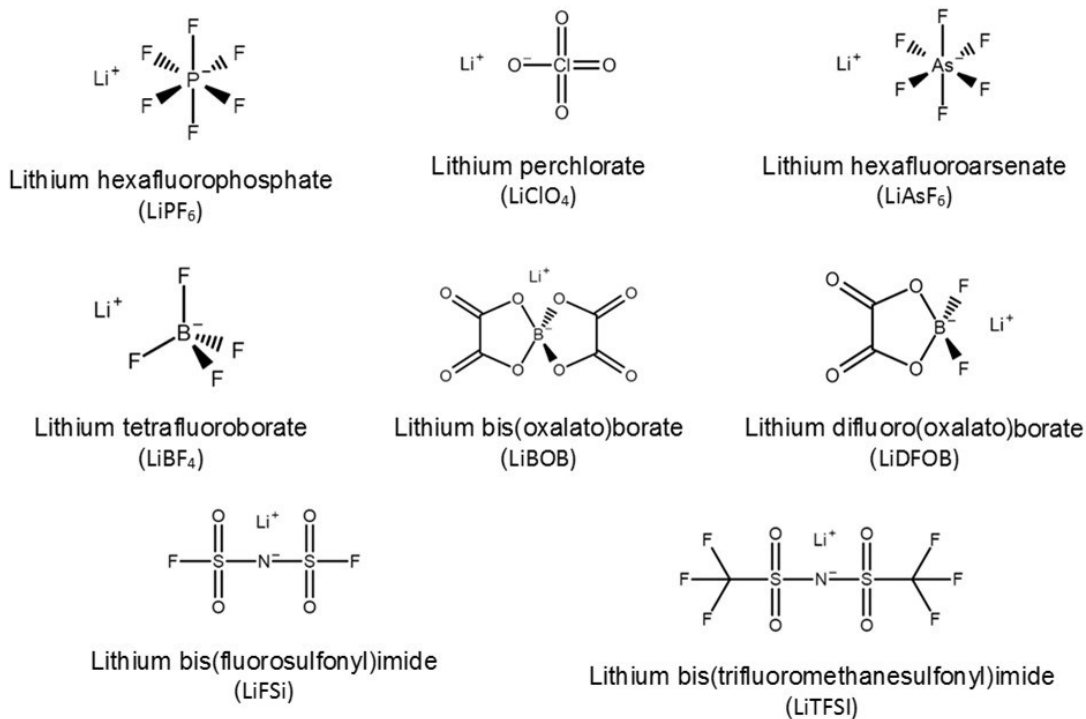


Figure 1-4. Chemical structure of some lithium salts used in electrolytes.

common solvents used in electrolyte. Each structure is shown with the common name and abbreviation used to refer to it. The electrolyte solvent system is selected for its ability to dissolve the salt, fluidity, stability against cell components, ability to remain a liquid in a wide temperature range, safety, toxicity, and cost. Commercial electrolytes have been

found to commonly use ethylene carbonate (EC) paired with linear carbonates (DMC, DEC, EMC) as a solvent system.^{10,20} EC has low viscosity and a high dielectric constant which allows it to dissolve salt to a high concentration.^{20,31,32} However, the melting point of EC is relatively high at 36.4°C but can be reduced by mixing it with a linear carbonate.^{20,31}

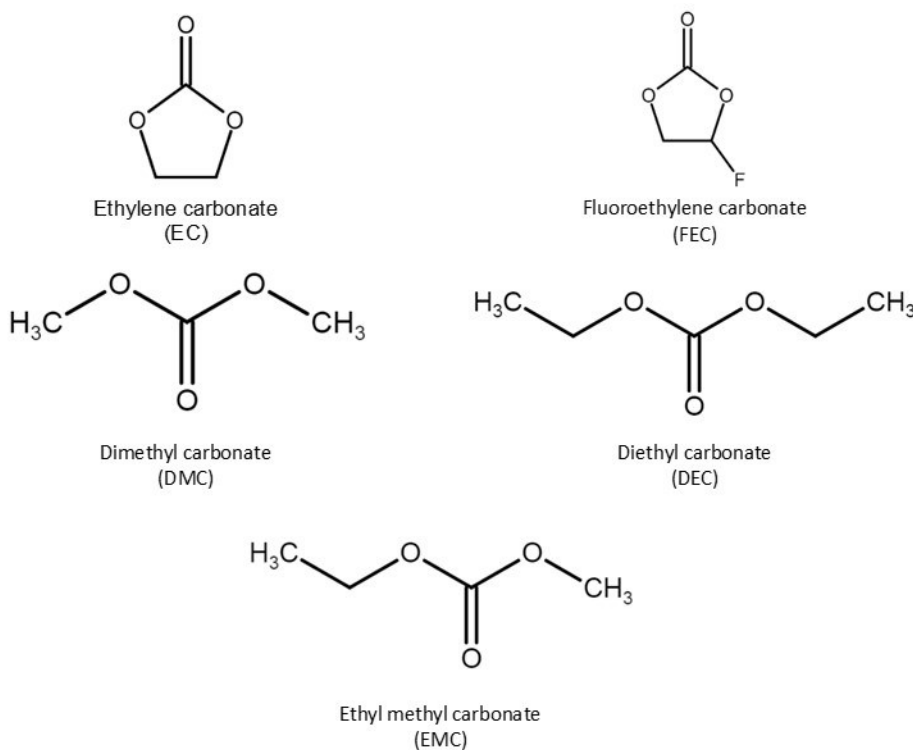


Figure 1-5. Chemical structure of some carbonate solvents used in electrolytes.

1.3.1 The Solid Electrolyte Interphase (SEI)

The electrolyte used in a lithium-ion cell must form a stable passivation layer on the electrodes in order to prevent long-term capacity loss driven by reactions between the electrolyte and electrodes. The passivation layer at the negative electrode, dubbed the solid electrolyte interphase (SEI), is formed upon reduction of electrolyte components

when the cell is first charged. The SEI is ionically conductive but electronically insulating. Lithium-ions can still pass through but further reduction of the electrolyte is slowed by limited electron transport.³³ For a typical EC-based electrolyte the SEI will be composed of reduction products of ethylene carbonate.^{34,35} However, the addition of other components with reduction potentials above EC can change the composition of the SEI and improve its properties (lower resistivity, better stability). Figure 1-6 shows two cyclic carbonates, fluoroethylene carbonate and vinylene carbonate, which are commonly used in electrolytes for traditional lithium-ion cells as additives that each make up < 5 weight% of the electrolyte.^{36,37} These additives function to form the SEI since they are reduced before EC. In this work fluoroethylene carbonate is also used as a solvent at concentrations > 5 wt%. Conversely, the initial oxidation of electrolyte components at the positive electrode forms a passivation layer that is sometimes referred to as the cathode electrolyte interphase (CEI). Similar to the SEI, this passivation layer influences stability and resistivity of the positive electrode.

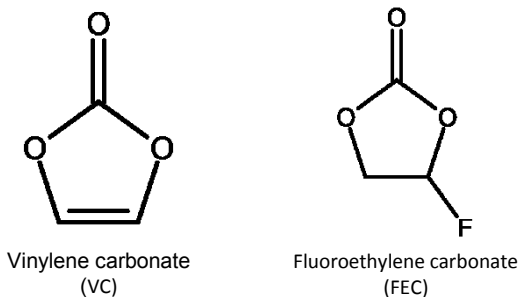


Figure 1-6. Chemical structure of two cyclic carbonates commonly used as electrolyte additives.

An immense number of electrolyte additives have been used to influence properties of the electrode interfaces,^{20,32,36,38-54} including some of the lithium salts from Figure 1-4 used as additives in conjunction with LiPF_6 as the primary salt.⁵⁵⁻⁵⁸

1.4 Anode-Free Lithium-Metal Cells

An anode-free lithium-metal cell can be built using the same components as a traditional lithium-ion cell minus the graphite anode. An anode-free cell operates by plating lithium metal directly on the anode current collector during charge and stripping lithium metal from the current collector during discharge. Removing the graphite anode reduces manufacturing and material costs as well as improves cell energy density by reducing weight and volume. Figure 1-7a shows an anode-free pouch cell next to a traditional lithium-ion pouch cell. Both use the same positive electrode, current collectors, separator,

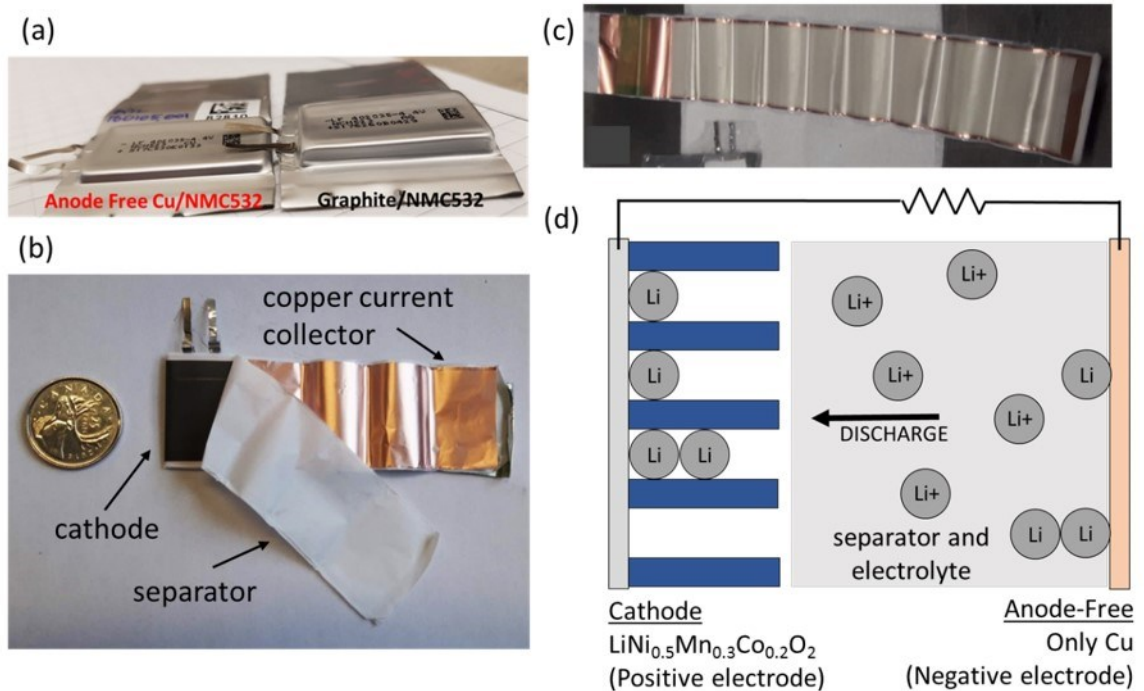


Figure 1-7. Anode-free cell. (a) Anode-free pouch cell compared to a traditional lithium-ion pouch cell (b) Electrode stack partially unrolled with a quarter for size comparison (c) Copper current collector with plated lithium metal (d) Schematic of anode-free cell during discharge.

and cell components, but volume is significantly reduced for the anode-free cell since it does not have a graphite anode. Figure 1-7b shows the electrode stack partially unrolled with a quarter for size comparison. Figure 1-7c shows the copper current collector with plated lithium metal. Figure 1-7d shows a schematic of an anode-free cell during discharge. Table 1-1 compares the energy of an anode-free cell and a traditional lithium-ion cell. Stack energy density is calculated from the volume of the electrode stack only, which excludes the volume of the pouch cell casing, tabs, excess separator and excess current collector foil. Aluminum and copper foil thicknesses are 10 μm , separator thickness is 20 μm , positive electrode specific capacity is 190 mAh/g , and positive electrode density is 3.5 g/cm^3 . Stack energy density is calculated for the anode-free cell in the charged state which has about 14 μm of lithium-metal plated. The energy density (Wh/L) that is shown in Table 1-1 is calculated for an assumed well-built commercial cell at 75% of the stack energy density (Wh/L). The first row in Table 1-1 shows the energy density and specific energy for a traditional NMC532/graphite pouch cell.⁵⁹ The second row of Table 1-1 shows the same information for the anode-free pouch cells used in this work. Not only does the anode-free-cell have lower volume and lower mass, the average voltage is also increased.

Table 1-1. Energy density and specific energy of an anode-free cell compared to a lithium-ion cell.

Cell	Positive Loading (mg/cm^2)	Average Voltage	Capacity (mAh)	Stack Energy Density (Wh/L)	Energy Density (Wh/L)	Mass (g)	Specific Energy (Wh/kg)
NMC532/graphite	21	3.75	240	795	596	4.5	200
NMC532/anode-free	16	3.9	260	1300	984	3.4	298

Consequently stack energy density for anode-free is higher than that of the traditional cell. Energy density and specific energy are also increased by using the anode-free configuration. The high energy density of anode-free cells makes them highly desirable for applications like electric vehicles, consumer electronics, and drones. In each case using anode-free cells can increase driving range of EVs, enable thinner phones or laptops, and increase the flying time of drones. With the growing markets for each of these technologies, anode-free cells continue to be more and more compelling.

Many positive electrode materials could be used in anode-free cells. These include but are not limited to: LiNiMnCoO_2 (NMC), LiNiCoAlO_2 (NCA), LiCoO_2 (LCO), LiFeO_2 (LFP), LiMnO_2 (LMO). Each of these transition metal oxides can plate lithium metal on the first charge cycle. Each has different specific capacity and voltage profiles, so the overall energy density of the cell depends on the choice of positive electrode material. Table 1-2 summarizes energy density for anode-free cells built with different positive electrode materials. In these calculations the cathode is 94% active material with a loading of 16 mg/cm^2 , so areal capacity is determined by the specific capacity of each material. Aluminum and copper foil thicknesses are 10 μm , separator thickness is 20 μm . Separator density is approximated as polyethylene (0.95 g/cm^3) with 40% porosity = 0.57 g/cm^3 . The cathode material influences both energy density and electrolyte choice. The electrolyte must be compatible with both lithium metal and the positive electrode. For example, for high-voltage cathodes like NMC532 and LCO high-voltage compatible electrolytes should be used.^{39-42,60-70}

Table 1-2. Stack energy density for theoretical anode-free cells with different positive electrode materials.

material	max voltage	reversible specific capacity (mAh/g)	areal capacity (mAh/cm ²)	average voltage	stack energy density (Wh/kg)	reference
NMC532	4.5	195	2.93	3.9	498	8
NMC811	4.3	195	2.93	3.8	485	⁷¹
NCA	4.2	199	2.99	3.7	482	⁷²
LCO	4.4	148	2.23	3.8	368	⁷²
LFP	3.6	165	2.48	3.4	367	⁷²

In this thesis anode-free cells with single-crystal $\text{LiNi}_{0.5}\text{Mn}_{0.3}\text{Co}_{0.2}\text{O}_2$ (NMC532) are studied since this positive electrode material is well characterized, it is known to have long lifetime, and many compatible electrolytes have been tested.^{7,8,43,59}

1.4.1 Performance Challenges

Anode-free cells have limited use in commercial products today since cell lifetimes are very short. Figure 1-8 (reproduced from reference)⁷³ shows how lithium metal is damaged during the repeated plating and stripping process. Figure 1-8a shows that if lithium metal plates in a porous, dendritic structure, isolated metallic lithium forms during stripping. Figure 1-8b shows less dendritic lithium, which loses less capacity to isolated metallic lithium. Figure 1-8c is the ideal scenario where lithium strips and plates in columns, and no lithium is isolated. In all three cases capacity is also lost in the reaction to form the SEI. For dendritic, high surface area lithium a lot of lithium can be consumed to form the SEI. Both SEI formation and isolated metallic lithium create “dead lithium” that can no longer be used to store energy in the cell. These mechanisms are minimized for columnar shaped lithium depicted in Figure 1-8c.⁷³

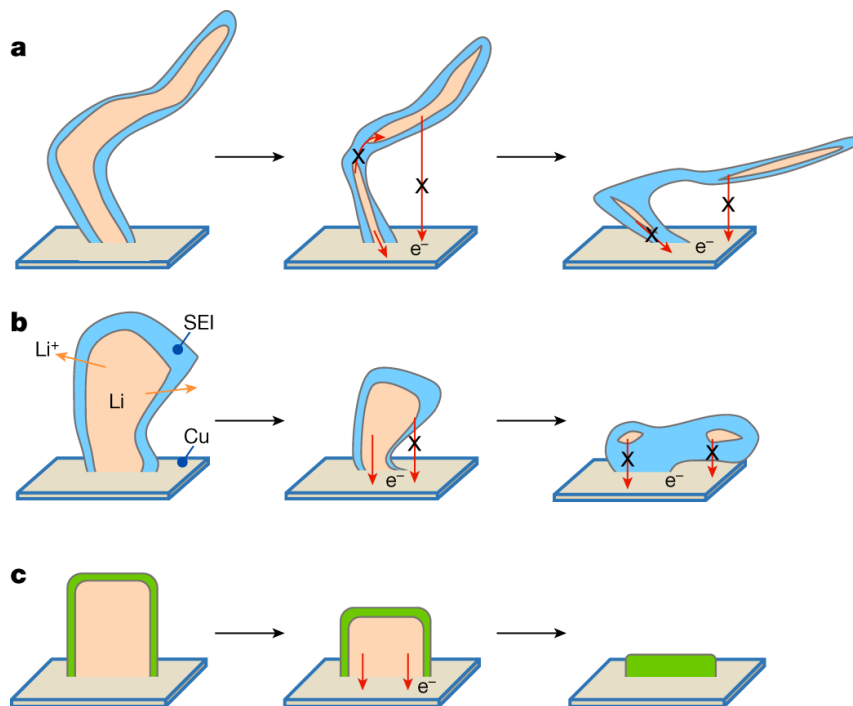


Figure 1-8. (a) Li deposits with whisker morphology and high tortuosity are more likely to lose electronic connection and maintain poor structural connection, leaving large amounts of unreacted metallic trapped in SEI. (b) Li deposits with large granular size and less tortuosity tend to maintain a good structural electronic connection, in which only small amounts of metallic are stuck in tortuous SEI edges. (c) An ideal Li deposit should have a columnar microstructure with a large granular size, minimum tortuosity and homogeneous distribution of SEI components, facilitating a complete dissolution of metallic lithium. Figure and caption reproduced from reference with permission (see Appendix A).⁷³

Lithium-metal batteries can also be built with a lithium metal foil on the copper current collector instead of in the anode-free configuration. Building cells with lithium foil is advantageous because it provides a reservoir of lithium that can extend lifetime. However energy density is decreased since the lithium foil adds mass and volume to the cell. Lithium foil reacts with water so manufacturing must be done in a dry room. The anode-free configuration is preferred to excess lithium metal since energy density is higher and manufacturing is simpler and less expensive.

Historically most work on lithium-metal batteries used excess lithium-metal, starting in the 1970s with the development of lithium metal cells at Exxon and the commercialization of a lithium-metal cell at Moli Energy in the 1980s.^{74,75} Papers specifically focused on anode-free cells are much more recent, with “Anode-Free Rechargeable Lithium Metal Batteries” in 2016 and “Anode-Free Sodium Battery through in Situ Plating of Sodium Metal” in 2017.^{1,2} Some papers published before 2016 test anode-free type cells by cycling against a bare copper current collector, but the focus of the papers is not to design an anode-free cell but rather to understand lithium metal cells.⁷⁶ Focus is shifting to anode-free cells since this configuration has the highest energy density and simplest manufacturing. For anode-free cells to be commercially viable, capacity loss mechanisms must be understood and mitigated. There is no excess reservoir of lithium to extend lifetime.

The simplest way to build an anode-free cell is with the same components as a traditional lithium-ion cell minus the graphite anode. However, liquid electrolytes that work in traditional lithium-ion cells do not necessarily work well in anode-free cells. For example an anode-free cell with a typical NMC111 positive electrode and typical 1.2M LiPF₆ in EC:EMC (3:7) electrolyte only had 23% capacity remaining after just the first cycle.⁷⁶ It is generally believed that an elastic, robust, or easily self-healing SEI is required for cells with lithium metal to accommodate the large volume changes during lithium-metal plating and stripping.⁷⁷⁻⁷⁹ Otherwise the SEI will constantly break and reform. Such an SEI is not needed for a graphite anode which has a relatively small volume change of ~10%. For lithium metal cells the SEI should also be homogeneous in order to minimize dendrite growth by preventing uneven plating and stripping. Since the SEI is determined

by the electrolyte composition, choosing the right electrolyte is crucial to making an anode-free cell with good capacity retention.

To improve the efficiency of lithium metal cycling, researchers have tried high salt concentration electrolytes, electrolytes that use ether solvents instead of carbonate solvents, many electrolyte additives including HF and H₂O, and electrolytes with fluorinated salts and additives.^{6,80-85} Each method is reported to lead to less dendritic lithium metal growth and in turn better capacity retention. Several mechanisms are thought to be at play here.

High-salt concentration electrolytes are supposed to prevent lithium-ion deficient regions in the electrolyte at the surface of the anode, which could lead to uneven, dendritic plating.^{2,6,86,87} The work in that space was done using LiFSI or LiTFSI based electrolytes, which in high concentration are expensive, highly reactive, and will corrode the aluminum current collector at the cathode.

Ether-based electrolytes are believed to form more robust, long-chain polymer SEIs. However ethers are unfavorable because they are not stable above 4 V.^{6,20,77,88} Most modern cathode materials operate up to 4.1 – 4.5 V, so cell energy will be significantly reduced if the electrolyte is limited to 4 V.^{17,74}

HF and H₂O were tried as electrolyte additives in particular because the formation of a LiF rich SEI led to more densely deposited lithium.^{6,82,89} Similarly, fluorinated salts and solvents are believed to promote the formation of LiF, and in the case of FEC the SEI formed on the lithium metal is supposed to have many desirable attributes: thin, conductive, flexible, and homogenous.^{6,83,90} LiDFOB was among the best fluorinated salt

tested for lithium metal cells, showing higher cycling efficiency than LiPF_6 and LiBF_4 especially when paired with FEC as a solvent.^{34,90}

Another approach to improve capacity retention in anode-free cells is use of a solid ceramic or solid polymer electrolyte where the rigid structure can resist dendrite growth. Ionic conductivity of ceramic electrolytes can be competitive with typical liquid electrolytes,^{91,92} but they still have problems with high interfacial resistance⁹³ and poor stability.⁹⁴ In addition, lithium dendrites were observed to grow through the grain boundaries of $\text{Li}_7\text{La}_3\text{Zr}_2\text{O}_{12}$ (LLZO) ceramic electrolytes.^{95,96} Compared to ceramics, polymer electrolytes have lower interfacial resistance but worse conductivity and less dendrite stopping power due to lower elastic modulus.⁹⁷⁻⁹⁹ Lastly, cell manufacturing is more complicated for solid electrolytes. Liquid electrolytes are preferred for their simpler manufacturing and easy introduction into existing lithium-ion manufacturing facilities.

Different current collector materials and treatments have been tested to improve efficiency of lithium metal cycling. Copper foil surface treatments have been explored including Cu_3P ,¹⁰⁰ thin layers of metals that alloy with lithium^{101,102}, and thin carbon coatings¹⁰¹. Extensive studies have been done on micro structured copper current collectors to improve capacity retention.¹⁰³⁻¹⁰⁸ However each of these current collector modifications complicate manufacturing, increase manufacturing cost, and often add weight or volume to the cell.

Figure 1-9 shows the surface of the copper foil from anode-free pouch cells used in this work. This foil has no special surface coatings or microstructure. Commercialization of anode-free cells will be accelerated if they can be made with already available mass

production current collectors. Since this work focuses on improving capacity retention through the choice of electrolyte, commercially available 10 μm thick copper foil is used as the negative current collector.

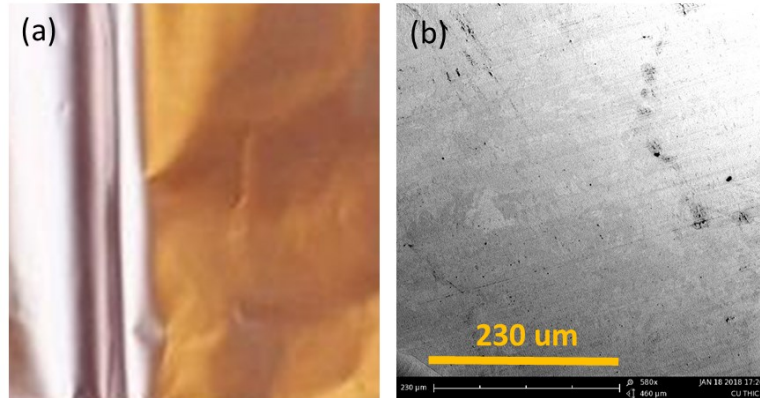


Figure 1-9. Copper foil current collector used in this work. (a) Optical image of the surface (b) SEM image of the surface.

External influences like temperature, pressure, and current density also affect the performance of lithium-metal. Increased temperature improves the pliability of lithium,^{109,109–111} which reduces surface area and dendrite formation but also accelerates reactions with the electrolyte. Applying pressure to the electrode stack is another proven strategy to suppress lithium dendrite growth and form lower surface area, less reactive lithium metal.^{112–115} Figure 1-10 (reproduced from reference)¹¹⁶ shows SEM images of lithium metal plated at different current densities, increasing from (a) to (j).¹¹⁶ At lower current density fewer lithium domains are nucleated and they grow larger with lower surface area.^{116,117}

The current density influences performance by changing the lithium morphology. For example, charging a Cu/LFP cell at 0.2 mA/cm^2 compared to 2 mA/cm^2 increased the coulombic efficiency to 99.8% from 98.8%.²

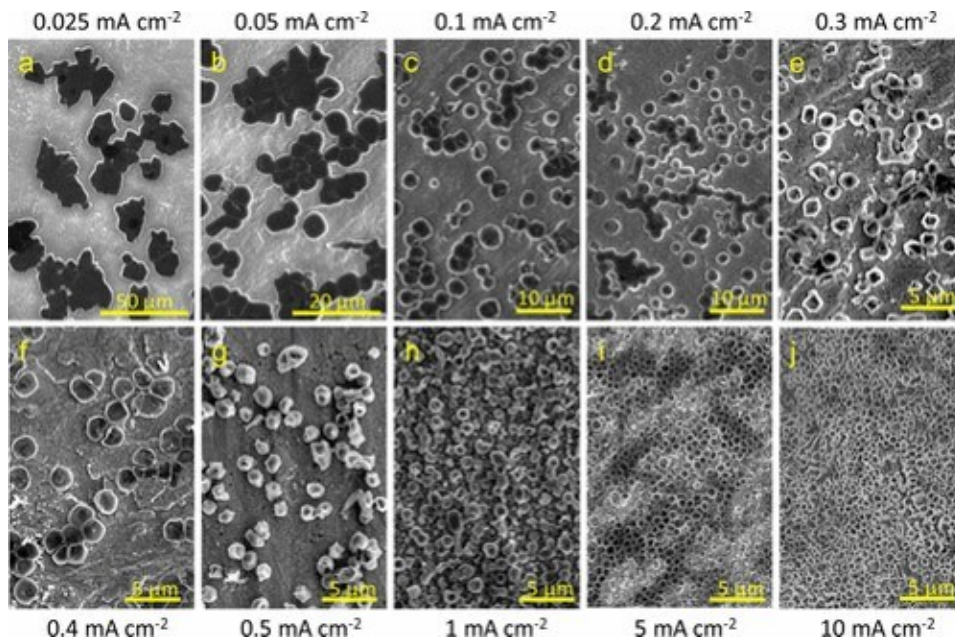


Figure 1-10. Lithium deposited at different current densities. (a–j) Ex situ SEM images of Li nuclei deposited on Cu at current densities of 0.025, 0.05, 0.1, 0.2, 0.3, 0.4, 0.5, 1, 5, and 10 mA cm^{-2} , respectively, for a total areal capacity of 0.1 mA h cm^{-2} . At lower current densities, the Cu substrate is visible underneath the sparsely distributed Li. Figure and caption adapted from reference with permission (see Appendix A).¹¹⁶

This work focuses on the development of high-voltage liquid electrolytes for anode-free cells. Ethers, high salt concentration, and solid/polymer electrolytes are avoided. No excess lithium-metal is used in the cells. In order to compare electrolytes other factors that influence the lithium cycling efficiency are kept constant: the current collector, charge/discharge rate, voltage, and temperature (with some exceptions).

CHAPTER 2 EXPERIMENTAL METHODS

2.1 Pouch Cells

Figure 1-1 and Figure 1-7 show pouch cells used in this work. The anode-free pouch cells are about 30 mm x 18 mm x 2.5 mm, the positive electrode is single-crystal particles of $\text{LiNi}_{0.5}\text{Mn}_{0.3}\text{Co}_{0.2}\text{O}_2$ (94% active, 16mg/cm², 3.5g/cm³, 10 μm thick Al), the negative electrode is a 10 μm thick bare copper current collector, and the separator is 14 μm thick polyethylene.⁷ Cells were manufactured by Li-Fun Technology (Xinma Industry Zone, Golden Dragon Road, Tianyuan District, Zhuzhou City, Hunan Province, PRC, 412000). Three graphite-based pouch cell chemistries were used for positive electrode studies (Chapter 6). NCA/Graphite (170 mAh balanced to 4.4 V) and NCA/Graphite-SiC (165 mAh balanced to 4.4 V) pouch cells were provided by Umicore (Chonan, South Korea). Machine made cylindrical NCA/graphite-SiO pouch cells (370 mAh balanced to 4.2 V) were provided by an undisclosed supplier.

All pouch cells were vacuum sealed in a dry room before shipping to Dalhousie University, where they were reopened in an argon-filled glovebox then dried in an antechamber under vacuum at 100°C for 14 hours. Cells were then filled in the glovebox with electrolyte, vacuum wetted for 1 minute, and finally vacuum sealed at -90kPa (MSK-115 A Vacuum Sealer). Anode-free pouch cells were filled with 0.5 mL of electrolyte. NCA/Graphite and NCA/Graphite -SiC cells were filled with 0.8 mL of electrolyte. NCA/Graphite-SiO cells were filled with 1 mL of electrolyte. To ensure complete wetting of the electrodes with electrolyte, cells sat at 1.5 V for 24 hours before

beginning testing. Anode-free cells went directly from wetting to testing without a formation step, unless otherwise noted.

NCA based pouch cells were all formed on a Maccor 4000 series cycler with the following procedure: (i) 40°C constant current charge at C/2 rate for 1 hour to reach 50% state of charge, (ii) 60°C storage at open circuit voltage for 22 hours, (iii) cells opened then vacuum sealed again inside the glovebox to remove gas, (iv) 40°C constant current charge at C/2 to 4.2 V, (v) constant voltage charge at 4.2 V for 1 hour, and then (v) constant current discharge at C/10 rate to 3.8 V.

Figure 2-1 shows fixtures that are used to apply pressure to the pouch cells during testing. The applied pressure keeps gas out of the electrode stack for all pouch cell types, and for

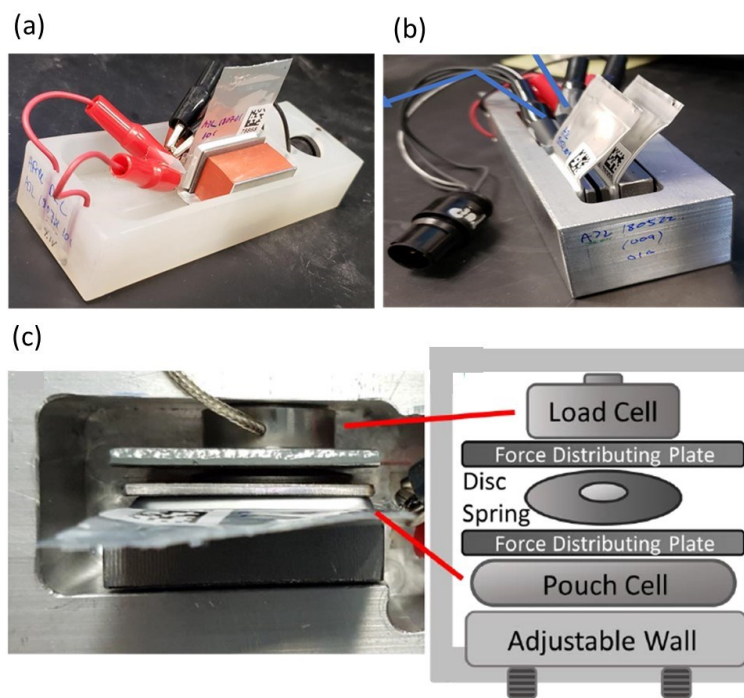


Figure 2-1. Pouch cell testing fixtures. (a) Plastic fixture with rubber blocks for ~75 kPa (b) Metal fixture with metal plates for >75 kPa (c) Diagram of metal plates and spring used to apply pressure in the metal fixture. Pressure plate diagram by Alex Louili.

anode-free cells the pressure maintains a controlled environment for lithium-metal plating and stripping. Figure 2-1a shows plastic fixtures for pouch cell testing where rubber blocks are used to provide ~ 75 kPa pressure to the electrode stack, estimated from a similar set-up with a load cell. Figure 2-1b shows metal fixtures for pouch cell testing where metal plates are used to apply >75 kPa pressure to the electrode stack. Figure 2-1c shows the arrangement of metal plates and springs which are screwed tight against the pouch cell to apply pressure. In this fixture a load cell can be used to monitor the pressure during testing.

2.2 Electrolyte

Electrolytes were mixed from individual chemicals in an argon glovebox using a precision balance and pipette. After mixing, electrolytes were transferred to the pouch sealing glovebox without exposing to air. Chemicals used in this work include: ethylene carbonate (EC, BASF purity $>99\%$), ethyl methyl carbonate (EMC, BASF purity $>99\%$), dimethyl carbonate (DMC, BASF purity $>99\%$), diethyl carbonate (DEC, BASF, purity $>99\%$), fluoroethylene carbonate (FEC, BASF, purity 99.4%), vinylene carbonate VC (BASF, purity $>99.8\%$), lithium hexafluorophosphate (LiPF_6 , BASF, purity 99.9%), lithium difluoro(oxalato)borate (LiDFOB, Capchem), and lithium tetrafluoroborate (LiBF_4 , BASF).

2.3 Cycling

Capacity retention of pouch cells was evaluated by repeated galvanostatic cycling. During each cycle, cells were charged at a constant current to an upper cutoff voltage, then discharged at a constant current to a lower cutoff voltage. Capacity (Ah) is recorded automatically by the testing equipment as the product of current (Amps) and time (hours).

Rate is designated as xC where 1/x is the number of hours to reach full capacity. For example 1C = 1 hr to fully charge the cell, and 0.5C = 2 hrs. During testing pouch cells were housed in boxes which control the temperature to within ± 0.1 °C. Cells were cycled on a Maccor series 4000 battery test system or Neware cyler (Shenzhen, China).

2.4 Electrochemical Impedance Spectroscopy (EIS)

Electrochemical impedance spectroscopy (EIS) is used to probe the resistance to current flow inside a battery from processes occurring on different time scales. For example, resistance of fast processes like ion flow through the electrolyte is separated from a slow processes like solid-state diffusion of lithium-ions in the electrode particles.

For potentiostatic EIS, the current response is recorded during the application of a sinusoidal voltage to the cell. The process is repeated in a range of frequencies. The impedance (Z) is calculated from voltage (V) and current (I) by the following equation:^{10,118}

$$Z(\omega t) = \frac{V(\omega t)}{I(\omega t)} = \frac{|V| \sin(\omega t)}{|I| \sin(\omega t - \varphi)}$$

where ω is the frequency and φ is the phase difference between the applied sinusoidal potential and measured sinusoidal current. The impedance can also be expressed using complex numbers:^{10,118}

$$Z(\omega) = |Z|e^{j\varphi} = Z_{real} \cos \varphi + jZ_{imaginary} \sin \varphi$$

Impedance data is often shown as a Nyquist plot, where Z_{real} is plotted on the x-axis and $Z_{imaginary}$ is plotted on the y-axis.

Figure 2-2 shows the impedance of two example circuits. The impedance of a resistor is entirely real and can be expressed as $Z = R$. The impedance of a capacitor has an imaginary component and can be expressed as $Z = \frac{-j}{\omega C}$. For circuit components in series the impedance adds directly: $Z_{total} = Z_1 + Z_2$, while for circuit components in parallel the impedance adds inversely: $\frac{1}{Z_{total}} = \frac{1}{Z_1} + \frac{1}{Z_2}$. The calculated impedance for each of the circuits is shown on a Nyquist plot in the frequency range 10 mHz to 100 kHz.

Figure 2-2a shows a resistor and capacitor in series. The impedance response is a vertical line on the Nyquist plot at $\text{Re}(Z) = 1 \text{ Ohm}$, which is determined by the resistor.

Figure 2-2b shows a resistor in series with a parallel resistor-capacitor (RC) circuit. As in

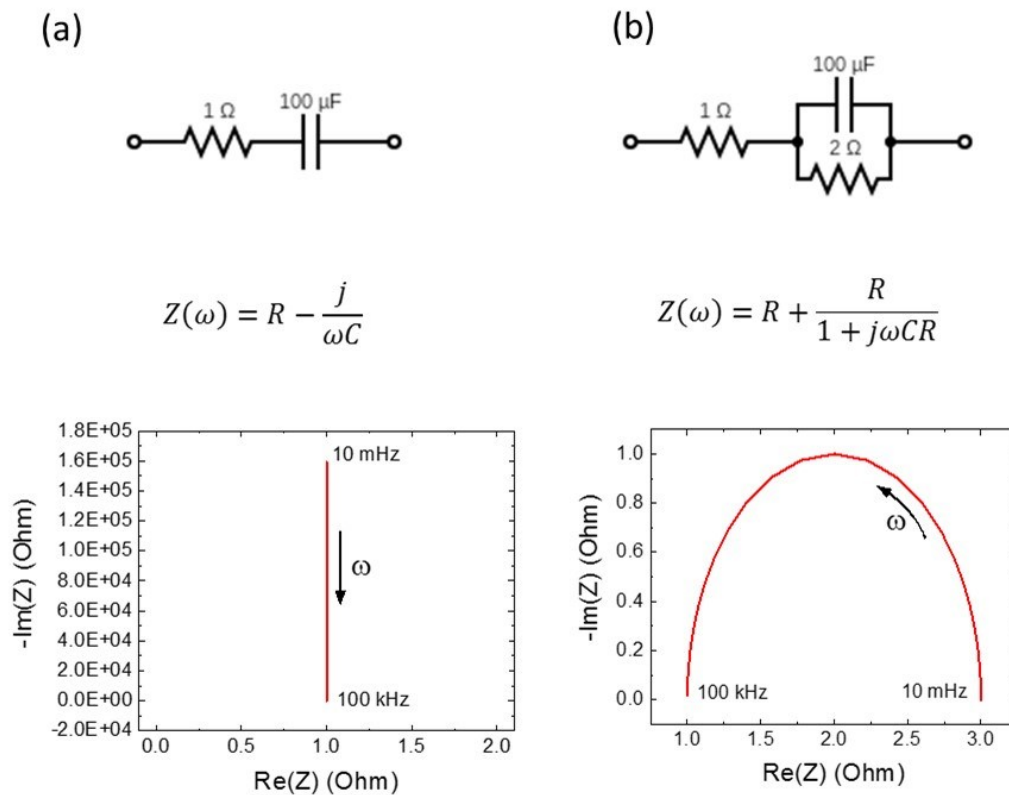
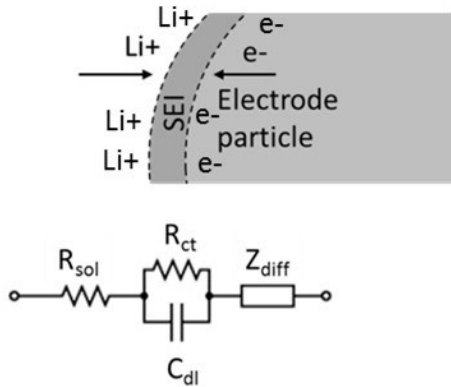


Figure 2-2. Example circuits and their impedance responses shown as Nyquist plots.

Figure 2-2a, the value of the series resistor determines the first intercept on $\text{Re}(Z) = 1$ Ohm. The RC circuit gives rise to the semicircular shape. The diameter of the semicircle is determined by the parallel resistor = 2 Ohms.

Figure 2-3a shows a circuit that models the processes at a battery electrode particle. Figure 2-3b shows the simulated Nyquist plot from this circuit where a Warburg element is used to model Z_{diff} . A resistor and capacitor in parallel model the charge transfer resistance at the SEI and the charging of the double-layer at the surface of the electrode, which gives rise to the semi-circular shape in the Nyquist plot. The first intercept with

(a)



R_{sol} = Electrolyte resistance

R_{ct} = Charge transfer resistance

C_{dl} = Double layer capacitance

Z_{diff} = Solid state diffusion

(b)

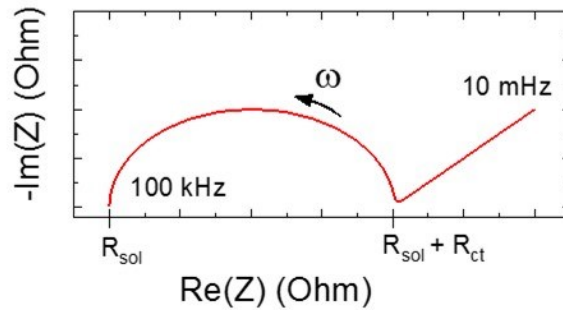


Figure 2-3. Equivalent circuit for impedance at electrode particle.

$\text{Im}(Z) = Z$ is at $\text{Re}(Z) = R_{\text{sol}}$ and the diameter of the semicircle is R_{ct} . Figure 2-4 shows a Nyquist plot of impedance data from a lithium-ion pouch cell of the type used in this thesis. Labels are shown for the approximate regions where each cell process contributes to the impedance. Resistance to ion flow through the electrolyte occurs at high frequency, electrode contact impedance at lower frequency, followed by charge transfer impedance, and then solid-state diffusion at the lowest frequency.^{10,119–123} The changes in these cell components can be tracked by measuring EIS throughout cell testing.

In this work EIS was measured with a Gamry (Warminster, PA, USA) frequency response analyzer card (FRA) or with a Biologic VMP3 electrochemical test station under conditions where temperature was controlled to $\pm 0.2^\circ\text{C}$. EIS was performed at ten points per decade between 100 kHz and 40 mHz or 10 mHz. A small 10 mV excitation was used to ensure that the current response was linearly proportional to the applied potential.

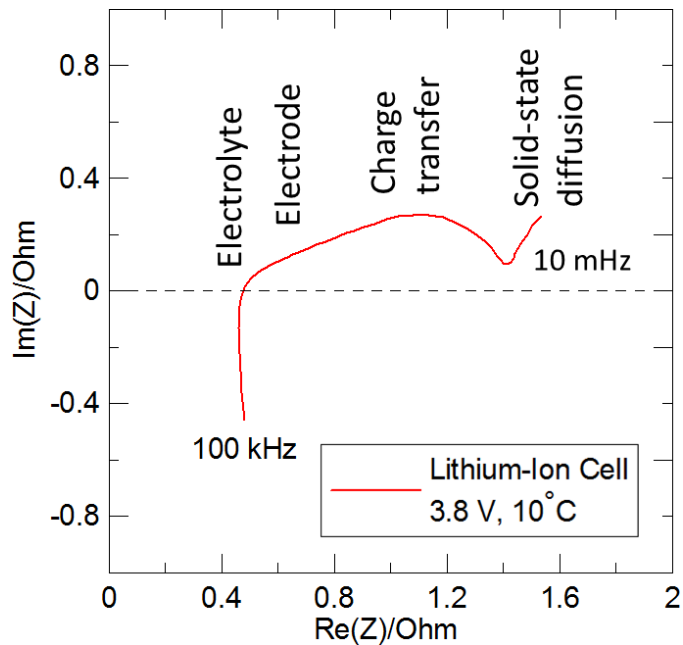


Figure 2-4. An example of a Nyquist plot from an EIS measurement of a lithium-ion cell.

2.4.1 Cycling with Automatic EIS

For positive electrode studies (Chapter 6), pouch cells were housed in $40 \pm 0.1^\circ\text{C}$ temperature controlled boxes connected to a Neware cycler (Shenzhen, China) and a computer with a Gamry (Warminster, PA, USA) frequency response analyzer card (FRA) for EIS. Cell connections were automatically switched between the cycling and EIS systems as described in previous work.¹²⁴ During testing, cells were charged and discharged between 3.0 V and 4.2 V at a rate of C/3 for 10 cycles, then charged and discharged in the same voltage range at a rate of C/20 for one cycle, with a pause every 0.1 V to measure EIS. EIS was performed with a 10 mV excitation and measured between 100 kHz and 40 mHz. The sequence of C/3 and C/20 cycles with EIS measurements was repeated for the duration of the test.

2.4.2 Symmetric Cells

Figure 2-5 shows the process of building symmetric coin cells from a dissected pouch cell. For positive electrode studies (Chapter 6), symmetric coin cells were used to measure the impedance contribution from each electrode.¹²⁵ For each symmetric cell, two 11 mm diameter (0.95 cm^2) punches were taken from one pouch cell electrode. The

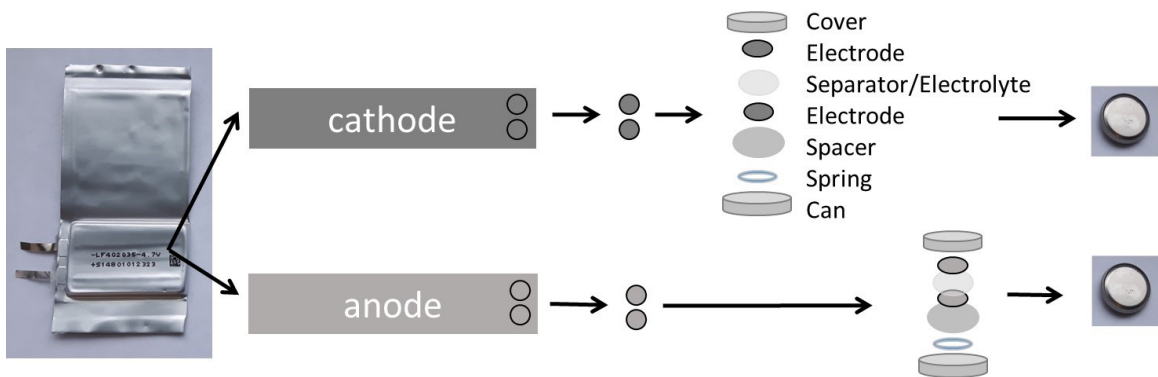


Figure 2-5. Work-flow for building symmetric coins cells from a pouch cell.

electrode active material is coated on both sides of the current collector, which was shown by Petibon *et al.* not to influence the measurements compared to a single-sided coating.¹²⁶ Electrode punches were reassembled in a coin cell with a polypropylene blown microfiber separator of 0.275 mm thickness and 3.2 mg/cm² areal loading (3M Co., Minneapolis, MN, USA), wetted with electrolyte of the same composition used in the pouch cell. All pouch cell disassembly and symmetric cell preparation was done inside a moisture controlled argon glovebox. For each symmetric cell, EIS was measured at 10 ± 0.1°C or 40°C (as indicated), with a 10 mV excitation from 100 kHz to 10 mHz. The experimental set-up used to measure EIS for many symmetric cells in sequence is described by previous researchers.¹²⁶

2.5 Scanning Electron Microscopy (SEM)

Scanning electron microscopy (SEM) is used to image the surface of battery electrode samples, including lithium-metal electrodes where the morphology can be correlated to the cell performance. In SEM a high energy electron beam is scanned over the surface of the sample. The image is formed from detection of secondary electrons (SE) or back-scattered electrons (BSE). SE are emitted by elements at the surface of the sample through ionization during inelastic scattering of incident electrons. BSE are incident electrons that were scattered elastically by elements in the sample. SE provide better resolution of the surface, but BSE provide contrast based on the average atomic mass of regions in the sample.¹²⁷

SEM images in this work were captured with a Phenom G2 Pro desktop scanning electron microscope (BSE detector, 5 kV accelerating voltage, 25 nm resolution) or with

a Hitachi S-4700 scanning electron microscope (3 kV accelerating voltage and 2.5 nm resolution).

To prepare lithium-metal electrode samples for SEM, cells were dissected in an argon atmosphere glovebox and electrode pieces were rinsed with DMC to remove residual salt. Dried samples were mounted on SEM stubs with conductive carbon tape. Samples were transferred from the glovebox to the SEM in an argon filled bag, and were briefly exposed to air for <30 seconds when loading in the SEM.

2.6 Surface Area (Argon BET)

SEM images were used to assess the quality of lithium metal, however in this work and in the literature SEM images typically cover only a small portion of the total electrode and usually only provide a top-down view of the lithium.^{2,82,87,102} “Good” lithium metal appears flat and compact, while “bad” lithium metal looks more dendritic and porous. In order to more quantitatively evaluate the quality of lithium-metal electrodes, a method was developed to use Brunauer–Emmett–Teller (BET) gas adsorption to measure the specific surface area of entire electrodes harvested from lithium-metal pouch cells.

BET surface area measurements operate on the principle of gas adsorption onto the surface of a material.^{128–130} Typically samples are cooled to liquid nitrogen temperatures in an evacuated glass tube. Then, a measured amount of nitrogen gas is pumped into the sample tube until it reaches a certain partial pressure. The pressure in the tube is a function of the free space in the tube as well as the amount of nitrogen gas that adsorbs onto the surface of the sample. Pressure and free-space are measured, so the

amount of adsorbed gas can be calculated. The amount of adsorbed gas is then translated to sample surface area by BET gas adsorption theory.^{128,130} Typically measurements are performed with nitrogen gas since it is lower cost compared to other inert gasses like argon or helium. However, nitrogen gas reacts with lithium-metal to form lithium nitride, so it cannot be used to measure the specific surface area of lithium-metal electrodes. Nitrogen will react with the electrode in addition to adsorbing so the surface area cannot be accurately evaluated. Instead the surface area of lithium-metal electrodes can be measured by argon BET, where argon is used in place of nitrogen. Just as an argon glovebox provides an inert atmosphere for lithium metal, argon BET provides an inert gas-adsorption measurement of electrode surface area.

Figure 2-6a shows a lithium-metal electrode harvested from a charged pouch cell. Figure 2-6b shows the blank BET tube (left) and the BET tube with the electrode sample (right) loaded onto the instrument. To prepare samples for surface area measurements, charged pouch cells were opened in an argon-filled glovebox and lithium metal electrodes were collected. Electrodes were rinsed with DMC to remove any residual lithium salt, and then were dried overnight in the glovebox before weighing and loading into a glass tube for BET surface area measurement. The BET tube was sealed with a rubber stopper to transfer the sample from the glovebox to the BET instrument where it was briefly open to air while attaching to the instrument (about 1 minute). Once the sample was attached, the measurement was started and the tube immediately went under vacuum. No evidence of reaction with moisture in the air was seen on the lithium metal electrode.



Figure 2-6. (a) Negative electrode with plated lithium metal after charging in an anode-free lithium-metal pouch cell. The electrode is ~40 cm long. (b) Electrode cut into four pieces and loaded into BET tube for surface area measurement.

Surface area measurements were performed with a Micromeritics Gemini VI Surface Area and Pore Size Analyzer. This instrument typically operates by immersing the sample in a liquid nitrogen bath and then injecting nitrogen gas into a glass tube with the sample of interest until a given partial pressure is reached, p/p^0 , where p^0 is atmospheric pressure outside of the BET tube. The volume of gas needed to reach a certain partial pressure depends on the amount that has been adsorbed onto the sample and the free space in the sample tube. More adsorption from a higher surface area sample requires more inlet gas to reach the same partial pressure. A blank tube (shown on the left in Figure 2-6b) is measured simultaneously to account for the gas adsorption that comes

from the surface of the tube. The difference in free space between the blank tube and the sample tube is accounted for by measuring it with helium gas. To avoid the reaction of nitrogen gas with lithium-metal, we use argon gas and liquid argon instead of nitrogen gas and liquid nitrogen. In this study, measurements were taken from 0.01 to 0.99 p/p⁰ on both adsorption and desorption. BET surface area was calculated using adsorption data points from 0.2 – 0.4 partial pressure. BET surface area was calculated in the MicroActive analysis software as follows: a least-squares linear regression was fit to relative pressure (p/p⁰) vs 1/(Q(p⁰/p-1) where Q is the quantity of gas adsorbed in mmol. From this fit BET surface area was calculated as follows:

$$SA_{BET} = \frac{CSA * 6.023 * 10^{23}}{(22414 \text{ cm}^3 \text{ STP}) * (10^{18} \frac{\text{nm}^2}{\text{m}^2}) * (S + Y_{int})}$$

where CSA is the molecular cross-sectional area in nm₂ for the adsorbent gas. For Nitrogen gas CSA = 0.162 nm² was used and for argon gas CSA = 0.142 nm² was used.¹²⁸ The volume of gas at standard temperature and pressure (STP) is 22414 cm³. S and Y_{int} are the slope and the Y intercept, respectively, from the fit from above. Specific surface area (m²/g) was then calculated by dividing surface area by the mass of lithium metal in the sample.

Note that an equilibration time of 5 seconds was used for all samples, meaning once a given partial pressure (p/p⁰) is achieved, gas is injected to maintain that partial pressure while some is adsorbed onto the surface of the sample. Injection continues until the volume adsorbed during 5 seconds is <1% of the total volume adsorbed. The

measurement will stop if equilibrium is not reached after 1 hour at a given partial pressure.

Figure 2-7 shows isotherms of gas quantity adsorbed (mmol/g) vs relative pressure in the BET sample tube. Figure 2-7a shows isotherms for nitrogen surface area measurements of small pieces of lithium foil (cut from a roll of 120 μm thick lithium foil purchased

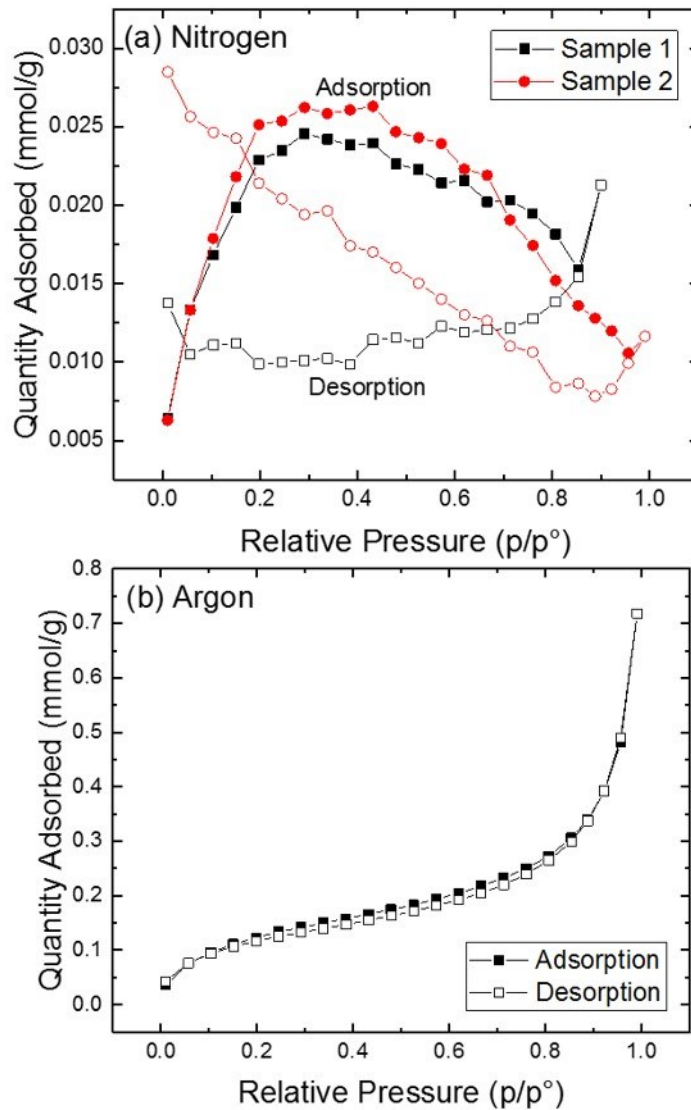


Figure 2-7. (a) Nitrogen BET isotherm from surface area measurement of two samples of lithium foil. (b) Argon BET isotherm from surface area measurement of a lithium metal electrode from a pouch cell.

from Rockwood Lithium). The adsorption isotherms do not match the desorption isotherms. A reaction between the lithium metal and nitrogen gas is occurring even while the sample is cooled to liquid nitrogen temperature, 77 K. Since nitrogen gas chemically reacts with lithium, the amount adsorbed is artificially high, and the chemically reacted nitrogen is unable to desorb. During adsorption the adsorption amount surprisingly decreases with increasing partial pressure. It is possible that the surface area of the sample decreases as lithium and nitrogen react to form lithium nitride: $6\text{Li} + \text{N}_2 \rightarrow 2\text{Li}_3\text{N}$. It is also possible that the lithium metal continues to react with some sort of contamination to form a higher volume of gas than was initially injected: $2\text{Li}_3\text{N} + 3\text{H}_2\text{O} \rightarrow 6\text{LiOH} + 2\text{NH}_3$. However, the second scenario is unlikely given that the same phenomena is not seen for the sample measured using argon gas. No moisture contaminants should be in the system. In contrast, the isotherm measured with argon gas (Figure 2-7b) is nearly identical for adsorption and desorption. Since argon is chemically inert to lithium, all of the gas that is adsorbed is recovered on desorption. Figure 2-8 shows repeated nitrogen BET runs on the same piece of ~0.04 g lithium foil. Each run takes 2.5 hours and the lithium reacts with the nitrogen throughout all four runs as indicated by the difference between adsorption (closed symbols) and desorption (open symbols). The amount adsorbed at the highest partial pressure increases for each subsequent run, indication that reacting rate is increasing. For the adsorption isotherm, quantity adsorbed may decrease for increasing partial pressure if the surface area of the sample decreases during the reaction with Nitrogen gas, or if the reaction also involves some moisture impurity that makes a higher volume of gas than what was injected: $6\text{Li} + \text{N}_2 \rightarrow 2\text{Li}_3\text{N}$, $2\text{Li}_3\text{N} + 3\text{H}_2\text{O} \rightarrow 6\text{LiOH} + 2\text{NH}_3$.

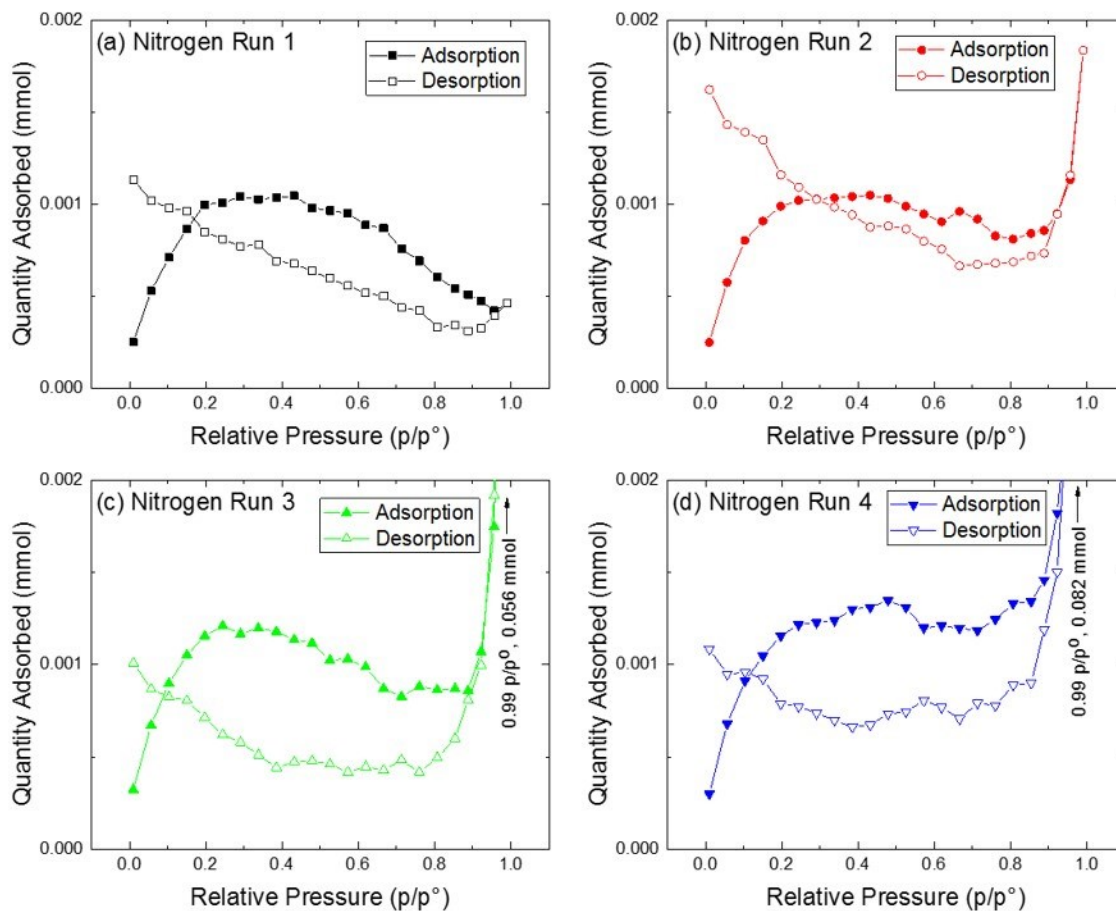


Figure 2-8. Repeated nitrogen BET runs on the same piece of ~0.04 g lithium foil.

Figure 2-9 shows an argon BET measurement of lithium metal electrode from a pouch cell after 1 charge cycle (a) and a nitrogen BET measurement on the same electrode immediately after argon BET was run. The gas quantity adsorbed was much higher for nitrogen BET due to the reaction of nitrogen gas with lithium metal, and at the highest partial pressure equilibrium was not reached in one hour (<1% adsorption over 5 seconds), so the measurement was aborted and desorption was not measured. Figure 2-10 shows a comparison of BET surface area measured on a graphite sample using both argon (red triangles) and nitrogen (black circles). Surface area is within 5% for the two methods which confirms the accuracy of measuring surface area with argon.

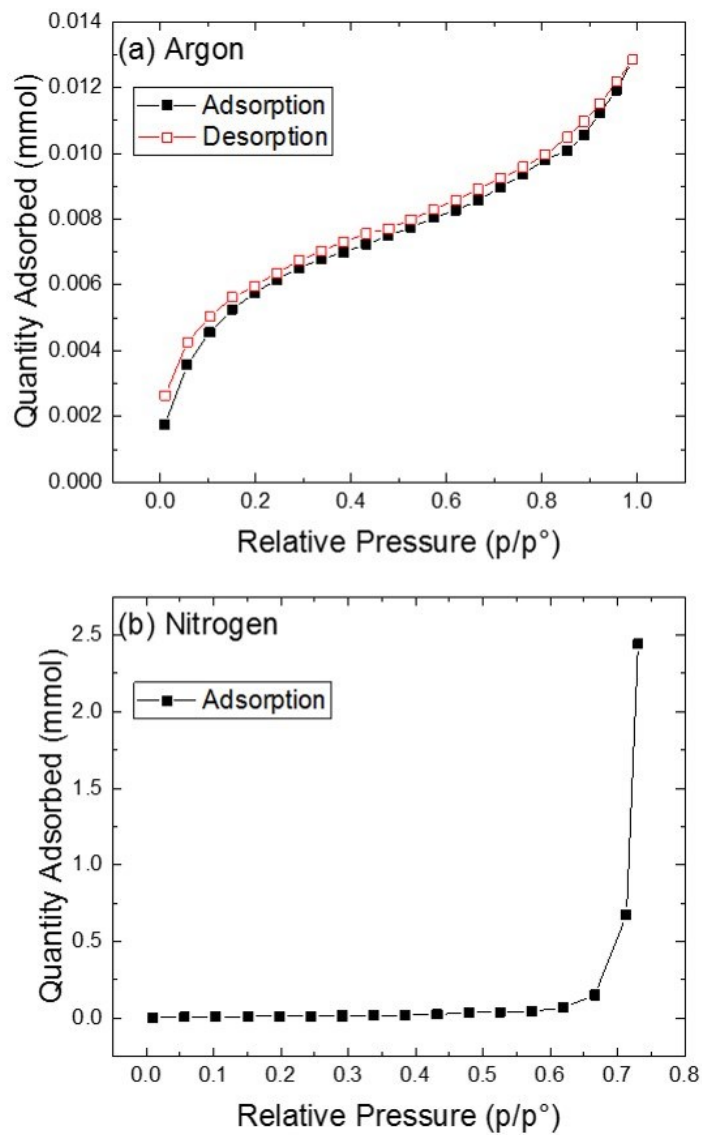


Figure 2-9. (a) Argon BET measurement of lithium metal electrode from a pouch cell after 1 charge cycle. (b) Nitrogen BET measured immediately after argon BET.

In Chapter 4 surface area measurements by argon adsorption are used to track the quality of lithium metal electrodes during cycling of anode-free cells.

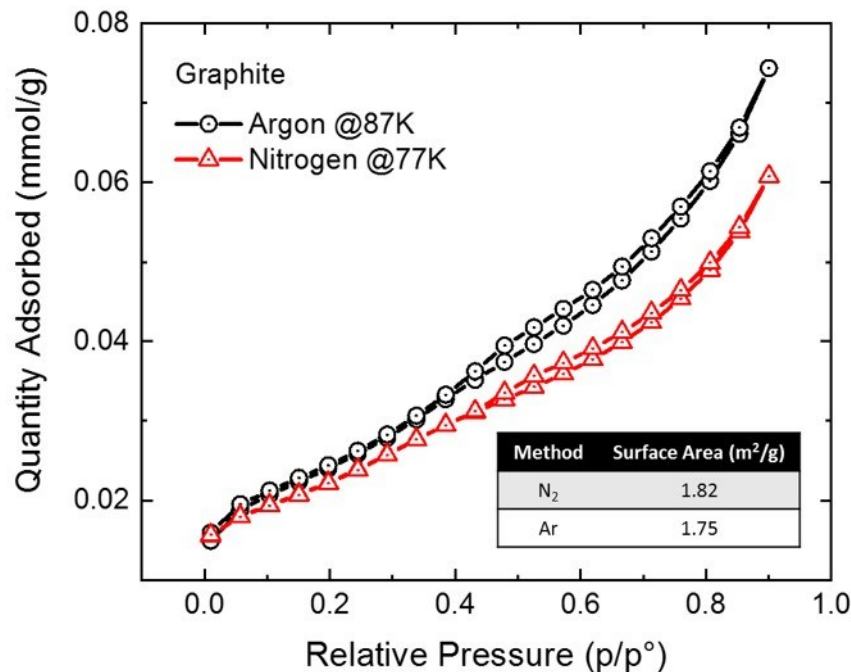


Figure 2-10. Comparison of BET measured on a graphite sample using argon (red triangles) or nitrogen (black circles).

2.7 X-ray Photoelectron Spectroscopy (XPS)

X-ray photoelectron spectroscopy (XPS) is a surface sensitive technique that can be used to characterize the composition of battery electrode SEIs.

XPS operates on the principle that X-ray irradiation of a sample excites photoelectrons from the core energy levels of elements that are present. The kinetic energy is measured for excited photoelectrons that escape from the surface of the sample. Electron binding energy is then determined from the kinetic energy (KE), incident photon energy ($h\nu$), and the instrument work function (Φ) through the relationship: $BE = h\nu - KE - \Phi$. Different elements are identified by the binding energies characteristic of their core electrons. For example, the 1s core electrons of oxygen are at a binding energy of about 530 eV.

Similarly for other common SEI components, carbon 1s is around 285 eV and fluorine 1s

is around 685 eV. The binding energy is also influenced by bonding states of each element so XPS can be used to both identify elements and to characterize their chemical bonding states. XPS sampling depth is limited by the ability of photoelectrons to escape the sample without inelastic scattering. Sampling depth is typically on the order of a few nanometers.¹³¹

To prepare electrodes for analysis by XPS, cells were formed at 40°C by holding at 1.5 V for 24 hours, charging at C/5 to 4.5 V, then discharging at C/2 to 3.8 V. After formation, cells were fully discharged to ~0.2 V before dissecting in an argon glovebox to harvest electrode samples. Each electrode piece was rinsed with EMC to remove any residual lithium salt. After drying, electrodes were mounted on rigid sample holders using ultra-high vacuum compatible copper tape (3M). Electrodes were moved from the glovebox to the XPS without exposing to air by using a custom transfer suitcase. A SPECS spectrometer with a Phoibos 150 hemispherical analyzer was used for XPS analysis with Mg K alpha radiation ($h\nu = 1253.6$ eV) under ultra-high vacuum conditions ($<2 \times 10^{-9}$ mbar).⁴⁶ Data was analyzed with CasaXPS software (version 2.3.18).

2.8 X-ray Diffraction (XRD)

X-ray diffraction can be used to characterize crystalline battery electrode materials, like NMC and NCA. Figure 2-11 shows a schematic of incident X-rays diffracting from atoms in a crystal lattice. For the two diffracted X-rays shown the difference in path length is $CA + AD = 2d \sin \theta$. A peak is seen in the diffraction pattern due to constructive interference if the diffracted X-rays are in phase. The angles at which this occurs depends on the spacing between the atom planes in the crystal and the X-ray wavelength. The relationship is described by Braggs law:¹³²

$$n\lambda = 2d \sin \theta$$

Where n is an integer, λ is the X-ray wavelength, d is the spacing between atomic planes, and θ is the angle of the incident X-ray beam. Figure 2-12 shows an example of an X-ray diffraction pattern measured for $\text{LiNi}_{0.5}\text{Mn}_{0.3}\text{Co}_{0.2}\text{O}_2$ using $\text{Cu-K}\alpha$ radiation ($\lambda = 1.5418 \text{ \AA}$). Intensity is plotted vs the scattering angle, two theta (degrees). Black circles show the measured data and the red line shows a fit to the experimental data, calculated by Rietveld refinement.

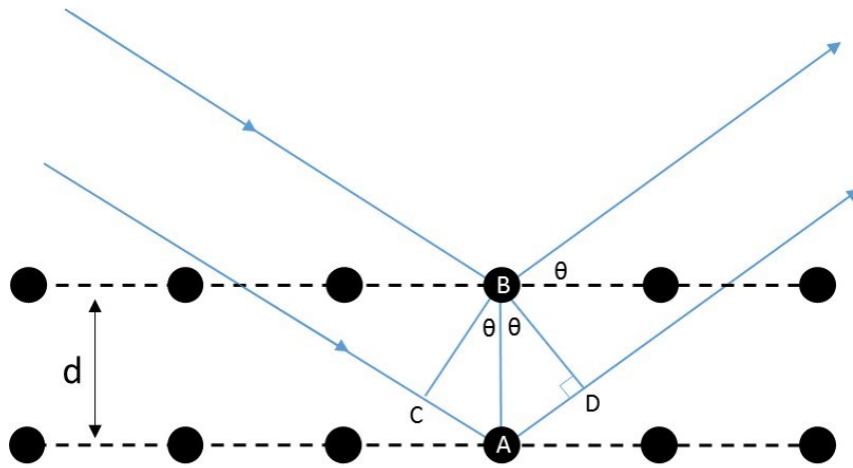


Figure 2-11. Schematic of X-rays interacting with atoms in a crystal lattice. Adapted from figure 3-2 in reference.¹³²

In this method an equation modeling the peak location, intensity, and shape is fit to the data by a linear least squares method.^{133,134} During refinement the sum of the squares of the difference between observed and calculated intensity is minimized:

$$M = \sum_i W_i (I_{obs} - I_{calc})^2$$

where the difference is weighted by the function $W_i = 1/I_{\text{obs}}$. The calculated profile is refined from an initial guess of atom positions, unit cell dimensions, peak shape, etc. The equation below describes intensity based on these parameters:

$$I(2\theta) = I_0 P(\theta) L(\theta) [F(hkl)]^2 M(hkl) DW(2\theta)$$

where I_0 is a scale factor, $P(\theta)$ is the polarization factor, $L(\theta)$ is the Lorentz factor, $F(hkl)$ is the geometric structure factor, $M(hkl)$ is the multiplicity factor, and $DW(2\theta)$ is the Debye-Waller thermal factor.¹³²

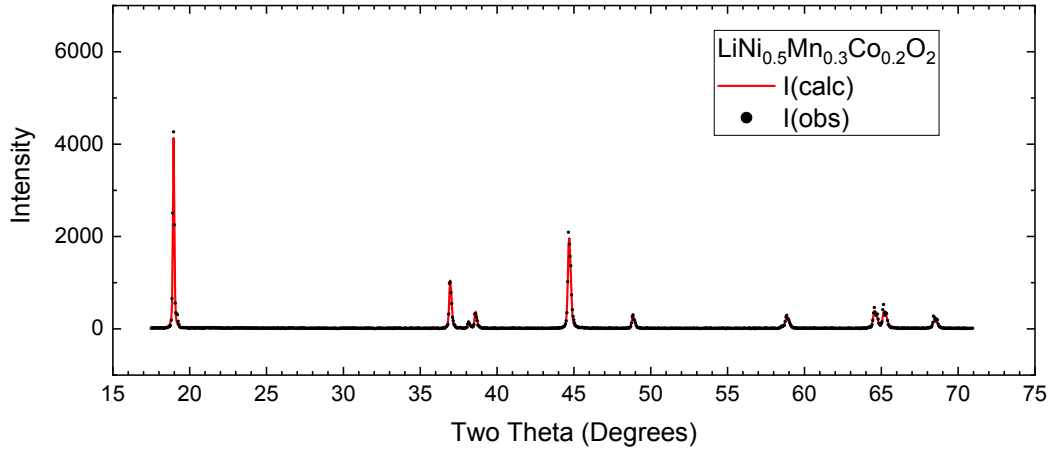


Figure 2-12. Example of an X-ray diffraction pattern for NMC532.

In this work GSAS and EXPGUI were used to fit XRD data.^{135,136} Initial atom positions, unit cell dimensions, and crystallographic space group are input to calculate $F(hkl)$ and $M(hkl)$. $P(\theta)$ is input based on the instrument used. I_0 is allowed to vary freely to best match the measured data. $DW(2\theta)$ is calculated from initial guesses for atom thermal vibrations. Parameters are then refined to match the measured data.

X-ray diffraction was performed on bare electrodes (Figure 7-4) with a Bruker D8-Discover diffractometer equipped with a diffracted beam monochromator and a Cu target X-ray source. Bare electrode diffraction patterns were taken in the range of scattering angles $2\theta = 15^\circ$ - 70° at steps of 0.01° with a dwell time of 4 seconds per step. Both scans used a 0.6 mm divergence slit, a 0.6 mm antiscattering slit, and a 0.1 mm receiving slit.

X-ray diffraction patterns for refinements (Figure 7-5) were measured on bare electrodes with a Siemens D500 diffractometer equipped with a diffracted beam monochromator and a Cu target X-ray source. Measurements were made in the range of scattering angles $2\theta = 15^\circ$ - 70° with a step size of 0.05° and an 8 second dwell time per step. Both scans used a 0.3° divergence slit, a 0.3° antiscattering slit, and a 0.15° receiving slit.

2.8.1 *Operando* XRD - Material Cycling

Coin cells were used for the *operando* XRD study (Chapter 7). Electrodes used in the coin cells were dried under vacuum at 110°C for 14 hours before transferring directly to an argon filled glovebox for coin cell assembly. Each standard 2325 size coin cell was assembled with one 13 mm diameter circular dried NMC532 electrode (single-sided coating on aluminum foil), two layers of 19 mm diameter Celgard 2320 separator, a lithium metal counter-electrode, and an excess of electrolyte consisting of 1M LiPF_6 in EC:DEC (1:2 wt:wt). The large can of the coin cells had an inset beryllium disc to allow for X-ray penetration. Before coin cell assembly, Roscobond pressure adhesive was used to seal a 0.010" thick x 0.850" diameter PF-60 Beryllium disc (Materion Electrofusion, 44036 South Grimmer Blvd, Fremont CA) into a 15 mm diameter hole cut into a typical 2325 size coin cell steel can. After coin cell assembly, the joint between the beryllium

disc and steel can was sealed with Loctite® EA 1C™ adhesive to ensure the seal would not leak during testing.

X-ray diffraction during the *operando* experiment was measured with a Siemens D5000 diffractometer equipped with a diffracted beam monochromator and a Cu target X-ray source. Measurements were made with a step size of 0.05° and a 20 second dwell time per step in the following limited ranges in order to minimize scan time: $2\theta = 17.8^\circ - 19.5^\circ$, $36^\circ - 39.5^\circ$, $43^\circ - 50^\circ$, $57^\circ - 60^\circ$, $63^\circ - 67^\circ$. All scans used a 0.5° divergence slit, a 0.5° antiscattering slit, and a 0.2 mm receiving slit. GSAS (General Structure Analysis System)¹³⁵ and EXPGUI (GSAS graphical user interface)¹³⁶ were used to refine the initial XRD scan for each coin cell, then the seqgas function was used to automatically refine all other XRD scans.

Coin cell cycling during the *operando* X-ray diffraction experiment was performed using E-One Moli Energy (Canada) battery cycling equipment. Electrodes were charged and discharged between 3 V – 4.5 V vs Li/Li⁺ at a rate of approximately C/50.

2.8.2 *In-situ* XRD - Material Synthesis

In-situ XRD was used to study LiNiO₂ (LNO), LiNi_{0.975}Mg_{0.025}O₂ (LNMO), and LiNi_{0.95}Al_{0.05}O₂ (LNAO) cathode materials during synthesis. Samples were prepared by Hongyang Li at Dalhousie University and XRD was measured during heating at Canadian Light Source (CLS, Saskatoon, Saskatchewan) with help from beamline scientists Chang-Yong Kim and Weifeng Chen. The sample preparation, experimental set-up, and data analysis are described below.

Dynamic XRD was measured during heating at the CLS Hard X-ray MicroAnalysis (HXMA) beamline using an apparatus built by the beamline scientists. Figure 2-13a shows a schematic of the apparatus used to heat the various samples. The powder (precursor + lithium source) was loaded into the middle of a small alumina tube (99.8%

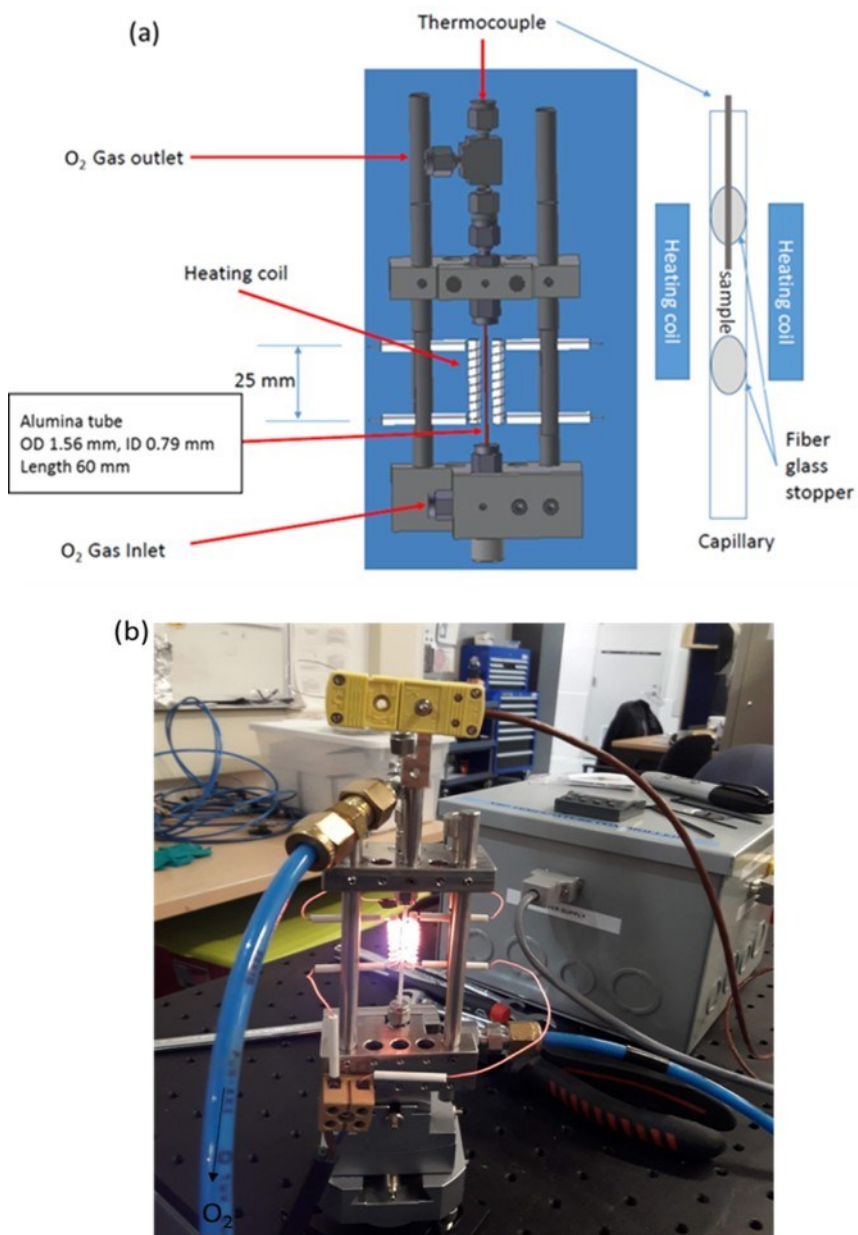


Figure 2-13. *In-situ* heating set-up at Canadian Light Source. (a) Schematic representation of the sample holder (provided by CLS) (b) Picture of the sample holder set-up with heating coils turned on.

alumina, 60mm long, 1.56 mm outer diameter, 0.79 mm inner diameter, Ceramic Solutions, Conroe, TX, USA). Alumina wool was packed at either end to hold the sample in place. The alumina tube was mounted in the metal fixture with Swagelok® fittings and graphite ferrules. Oxygen gas (99.993% purity) continuously flowed (~60 sccm) through the sample during heating, as shown. A thermocouple was inserted through the top Swagelok fitting, where it sat just above the sample in the alumina tube. Heating coils were positioned ~ 1 mm to either side of the alumina tube and were controlled by a DC power supply. Figure 2-13b shows a picture of the sample heating fixture, with blue oxygen tubes attached, a thermocouple inserted from the top, and the heating coils turned on. Figure 2-14 shows the sample heating fixture mounted in alignment with the X-ray beam. The X-ray energy was 17.998 keV and the corresponding wavelength was 0.6889 Å. The X-ray was centered on the sample tube with a spot size of about 0.3 mm. Data

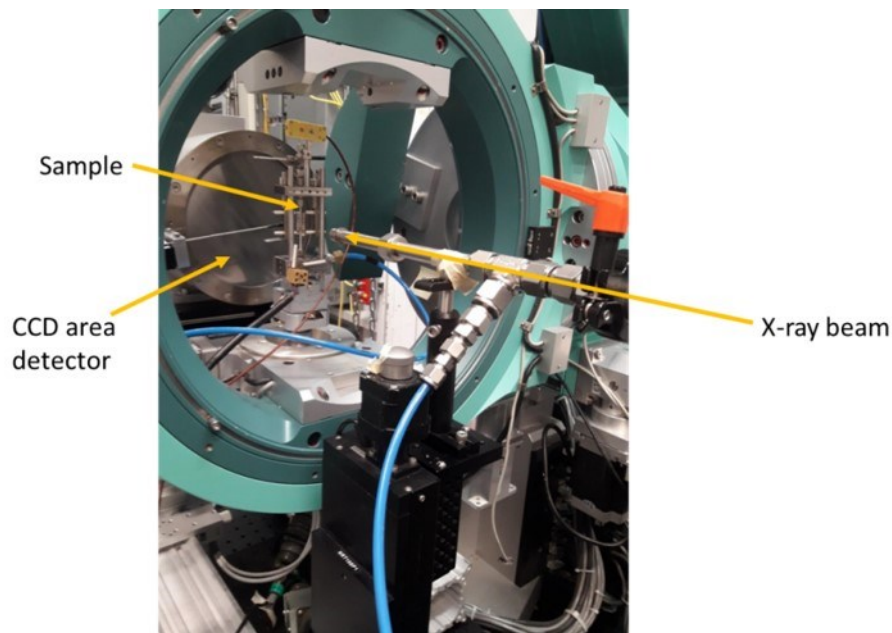


Figure 2-14. The sample heating fixture mounted on the beamline.

was collected with a charge coupled device (CCD) area detector mounted behind the sample. Diffraction patterns were acquired at each 1°C with a 1 second exposure time.

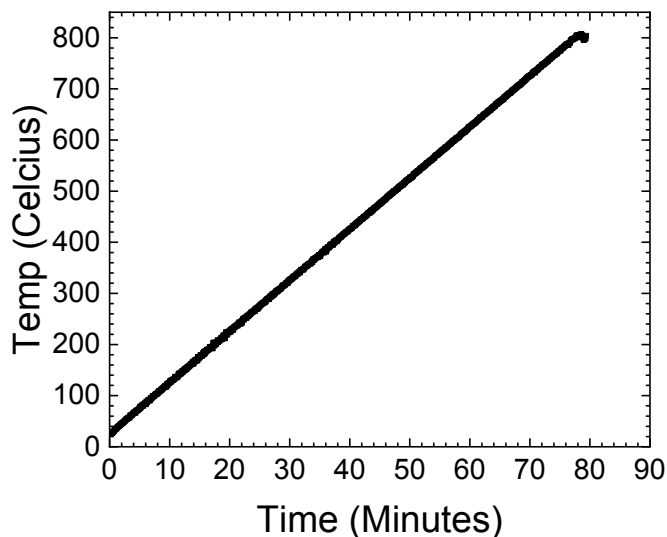


Figure 2-15. An example heating profile measured during an *in-situ* XRD run.

Figure 2-15 shows a representative heating profile measured during an *in-situ* XRD run. Heating was conducted with a 10°C/minute ramp rate, to a 800°C maximum temperature, with flowing oxygen throughout the duration of the test. The maximum achievable temperature with this set-up was 800°C.

Acquired CCD images were calibrated and integrated using Dioptas.¹³⁷ The CCD detector was calibrated from a lanthanum hexaboride (LaB₆) crystal pattern measured inside the alumina tube, with the exact sample set up as depicted in Figure 2-14.

Figure 2-16 shows an example of part of a CCD image captured during an *in-situ* XRD experiment. The smooth Debye-Scherrer rings are reflections from the sample, which have small crystallites ~100 nm in diameter. The coarse rings are reflections from the

alumina tube, which has larger crystallites and does not provide effective powder averaging. The image is cropped to the center to show how the rings in the vertical direction were sharp single rings, but the rings in the horizontal direction were broad and

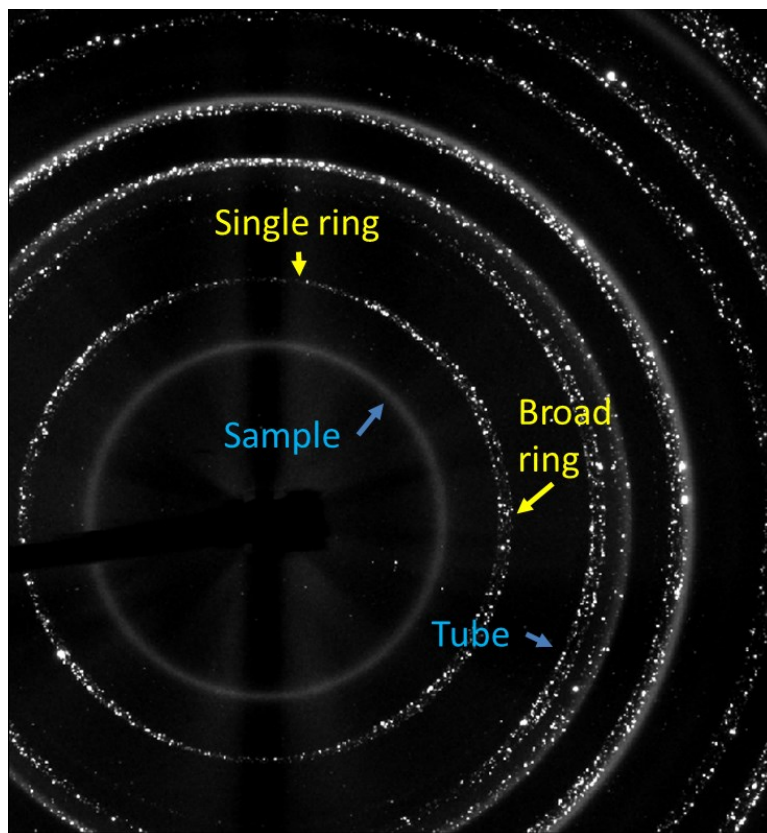


Figure 2-16. An example of part of a CCD image.

dispersed. The source of the aberration in the horizontal direction is unknown.

Figure 2-17a shows an example of a CCD pattern with a mask (shown in red) which was used to integrate only a slice of the data in the vertical direction; in this instance the mask covered the broad rings in the horizontal direction. Figure 2-17b shows examples of the integrated XRD patterns. The XRD pattern shown in purple was integrated without a mask, and has broad, unclear peaks. Conversely, the XRD pattern shown in white was

integrated with the mask, and has crisp clear peaks. All CCD images were subsequently integrated using the mask shown in Figure 2-17a.

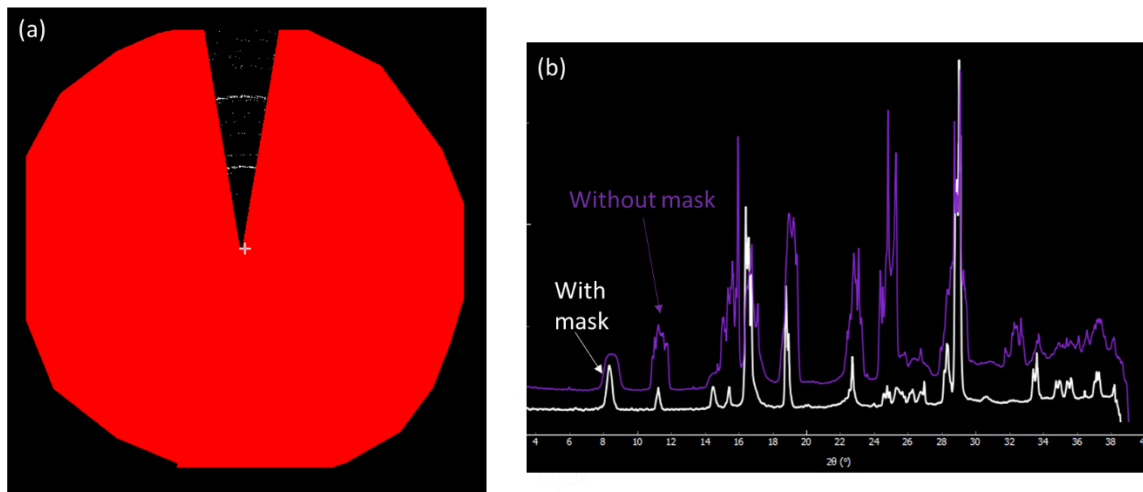


Figure 2-17. (a) Example of mask used in Dioptas to integrate CCD images without the aberrations in the horizontal direction. (b) Comparison of the XRD patterns integrated with and without the use of the mask shown in (a).

2.9 TGA-DSC-MS

Thermogravimetric analysis (TGA) differential scanning calorimetry (DSC) and mass spectrometry (MS) were used as complimentary measurements to the *in-situ* heating XRD data. TGA-DSC-MS was done on ~25 mg samples with a TA Instruments SDT Q600 coupled to a TA Discovery residual gas analyzer, which simultaneously measures mass loss and heat flow from the solid sample as well as mass spectra of the evolved gases. Samples were heated to 1000°C at a rate of 10°C/min, while O₂ was flowing; these conditions were set to largely mimic those used for the *in-situ* XRD heating experiments. Samples were dried at 100°C before TGA measurements. MS signals were tracked for mass numbers $m/e = 28$ (N₂), $m/e = 18$ (H₂O), and $m/e = 32$ (O₂). The oxygen

signal persisted throughout, a nitrogen signal was present in the beginning from air initially in the sample chamber, and the H₂O signal is shown with the TGA data.

CHAPTER 3 ELECTROLYTE ANALYSIS

Reaction of the lithium metal with electrolyte is a serious concern for capacity loss in anode-free cells so it is necessary to characterize the electrolyte, especially after cycling. Identifying which components react can help tailor the electrolyte to improve cycle life.

Methods to characterize electrolyte have been developed for use in traditional lithium-ion cells. For example, Petibon *et al.* used gas chromatography mass spectroscopy (GCMS) to identify and quantify solvents and additives.¹³⁸ GCMS was paired with inductively coupled plasma mass spectroscopy (ICPMS) to measure the salt concentration in the electrolyte. Together these methods completely characterize the electrolyte composition but require extensive sample preparation to separate the lithium salt from the rest of the electrolyte, since lithium salt is damaging to GC columns and cannot be put into the instrument. To study the electrolyte in anode-free cells we use nuclear magnetic resonance spectroscopy (NMR) which can analyze salt and solvent in one sample.

3.1 Nuclear Magnetic Resonance Spectroscopy (NMR)

Liquid NMR can be used to characterize electrolyte components since the technique is sensitive to any nucleus with a magnetic moment, which includes isotopes of hydrogen (^1H), carbon (^{13}C), fluorine (^{19}F), boron (^{11}B), phosphorous (^{31}P), and lithium (^7Li) where the superscript denotes the total number of protons and neutrons. Each of these isotopes has an odd number of protons or neutrons (or both) which gives the nucleus a net magnetic moment. Magnetic moment is quantized as spin-up (+) or spin-down (-) which for the nuclei listed is either +1/2 or -1/2. During an NMR measurement the sample is placed in a large applied magnetic field \mathbf{B}_0 which aligns the magnetic moments of the

nuclei. Figure 3-1 shows the energy difference between nuclei which are parallel (spin-up $m = +1/2$) and antiparallel (spin-down $m = -1/2$) to \mathbf{B}_0 . At $\mathbf{B}_0 = 0$ there is no difference in energy between the two spin-states. With increasing magnitude of applied magnetic field the energy difference increases. The energy of the dipole moment of each nucleus is equal to:

$$E = -u_z B_0$$

where u_z is the magnetic dipole moment and can be rewritten as:

$$E = -\gamma m \hbar B_0$$

where γ is the gyromagnetic ratio of the nucleus, m is the magnetic moment, and \hbar is Plank's constant. For a given magnetic field magnitude \mathbf{B}_0 , the energy difference between the two spin states is equal to:

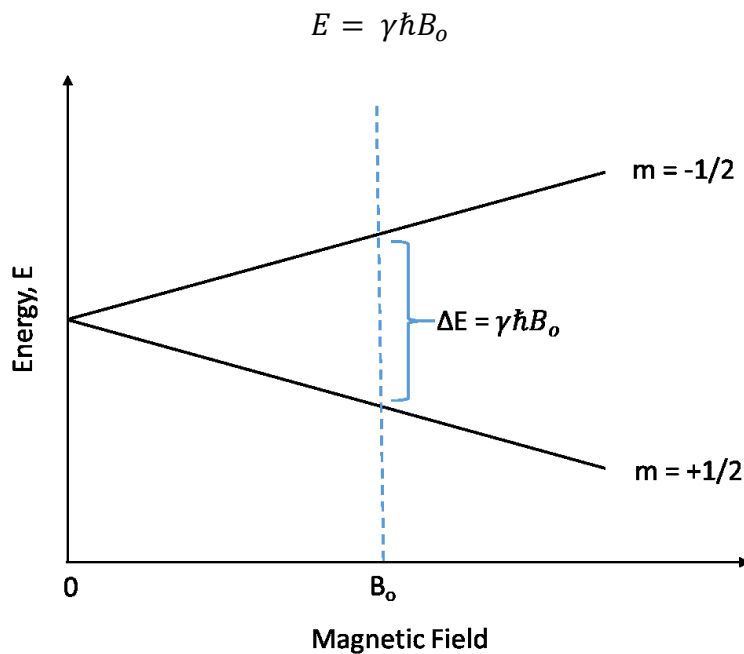


Figure 3-1. Illustration of the energy difference between nuclei with spin-up (+1/2) and spin-down (-1/2) magnetic moments in an external applied magnetic field.

With no external magnetic field a collection of nuclei will have equal populations of $+1/2$ and $-1/2$ spins since they have the same energy. In an applied magnetic field the lower energy for the spin-state $m = +1/2$ is preferred so there will be a larger population of $+1/2$ nuclei than $-1/2$ nuclei. In this case the net alignment of nuclei is parallel to \mathbf{B}_0 .

Figure 3-2a shows a vector \mathbf{v} to represent the net spin alignment parallel to \mathbf{B}_0 .

Figure 3-2b shows after applying a radio frequency (RF) pulse \mathbf{v} is not aligned to \mathbf{B}_0 . The RF pulse has a magnetic field perpendicular to \mathbf{B}_0 and frequency of oscillation close to the Larmor frequency of the target nuclei. The Larmor frequency is the frequency at which the spin state rotates around \mathbf{B}_0 and is equal to γB_0 . This nuclear magnetic resonance gives the technique its name. Figure 3-2c shows the precession of \mathbf{v} as it relaxes back into alignment with \mathbf{B}_0 . The oscillating magnetic field during this precession is measured as the free-induction decay (FID). Figure 3-2d shows after the measurement is complete and \mathbf{v} is fully back in alignment with \mathbf{B}_0 .

In modern NMR the applied RF pulse carries a range of frequencies able to excite many nuclei of interest at once, so the time based FID is converted to a frequency spectrum by Fourier transform.

Figure 3-3 shows an example of a proton NMR spectrum for DEC. NMR data is usually presented as intensity *vs* chemical shift in parts per million (ppm). The intensity can also be plotted *vs* resonance frequency as measured in Hertz (Hz) and is converted to ppm by dividing by the operating frequency of the spectrometer (500 MHz for the example shown). Although all the nuclei measured in Figure 3-3 are protons, the resonance frequency, and hence the chemical shift in ppm, is different due to the effect of chemical

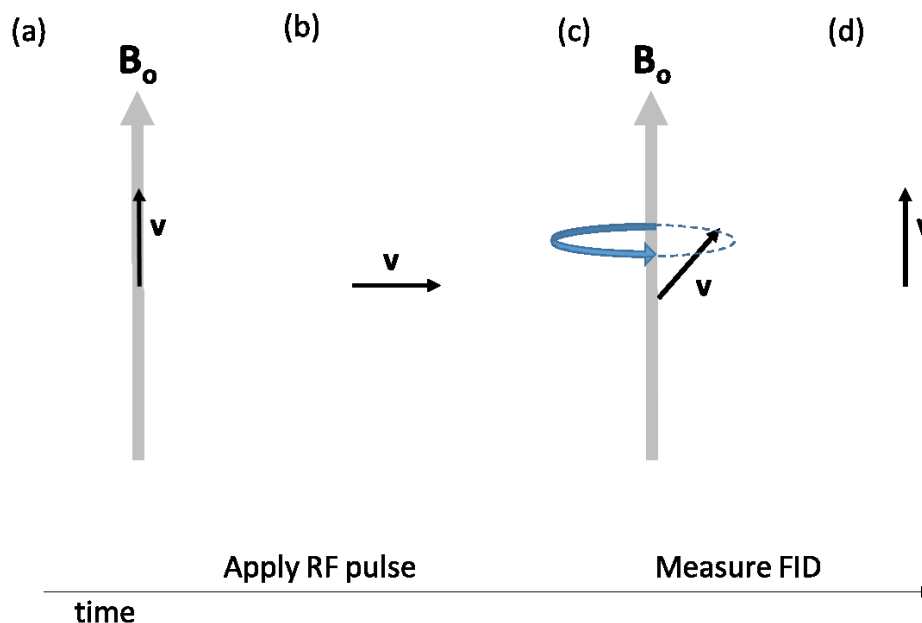


Figure 3-2. The series of steps in an NMR measurement (a) net nuclei magnetic moment, v , is aligned with external field, B_o (b) an RF pulse is applied and v is misaligned with B_o (c) during relaxation of v back to alignment with B_o the oscillating voltage signal during precession is measured (d) v returns to aligned state with B_o .

shielding. Nearby electron clouds shield nuclei from experiencing the full magnetic field B_o , which then reduces the resonance frequency for the nucleus. Protons in different chemical environments experience different levels of chemical shielding. For DEC shown in Figure 3-3 the four protons labelled (a) are near electronegative oxygen which acts to de-shield the nuclei. Consequently the resonance for (a) protons is at higher chemical shift than the (b) protons.

Figure 3-4 shows details of the peaks in Figure 3-3. Peaks from protons (a) are shown on the left and peaks from protons (b) are shown on the right. Each peak is split into multiple lines due to coupling with nearby protons. For protons at (a), there are three nearby

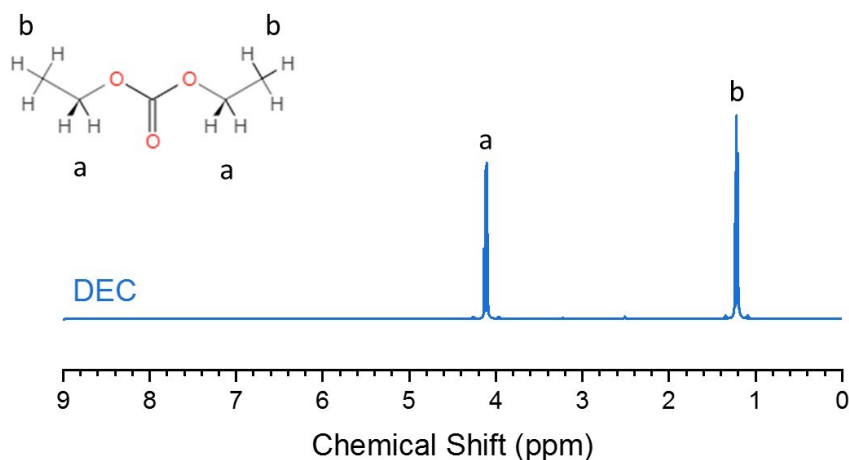


Figure 3-3. Example of proton NMR spectrum for DEC.

protons at (b) with $+1/2$ or $-1/2$ spin state. Depending on the spin state, the magnetic moment from protons at (b) shift the resonance of (a) slightly up or slightly down. Three protons at (b) split the (a) resonance into $n + 1 = 4$ lines. Conversely, two protons at (a) split the resonance for (b) into $n + 1 = 3$ lines. Figure 3-4 also shows the area under each peak normalized to the peak at 4.1 ppm. Peak area is proportional to nuclei concentration. The area of (b) is 1.5x the area of (a) since six protons contribute to the signal at (b) while only four contribute to the signal at (a).

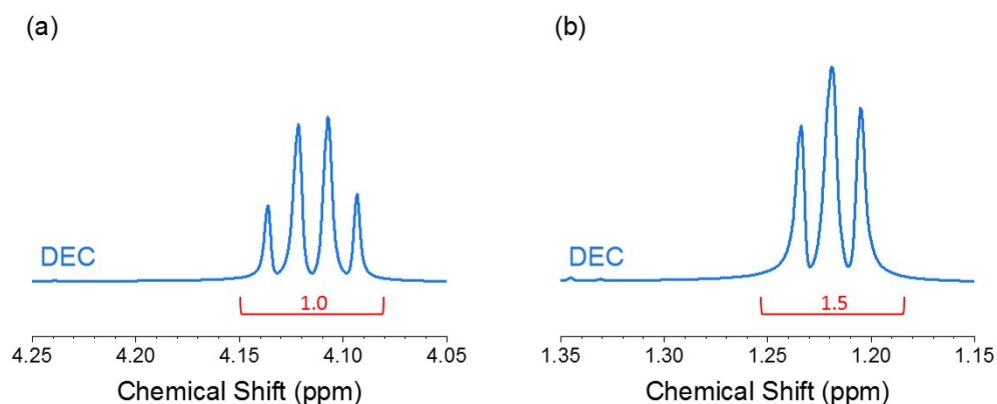


Figure 3-4. Detailed view of peaks in NMR spectrum from Figure 3-3.

The example shown for DEC can be replicated for other electrolyte components including FEC, DMC, and EMC. Fluorine NMR can be used to characterize fluorinated components including FEC, LiPF₆, LiDFOB, and LiBF₄. Electrolyte components are identified by the peak chemical shifts and the concentration of each component is calculated from the peak areas. The exact methods for sample preparation and electrolyte analysis are described in the next sections. Further information on the theory and application of NMR spectroscopy can be found in the references.^{139,140}

3.2 Method 1 – Composition

Two methods were used to analyze electrolyte. The first method gives the relative composition of electrolyte, which is reported as salt concentration (molal) and solvent

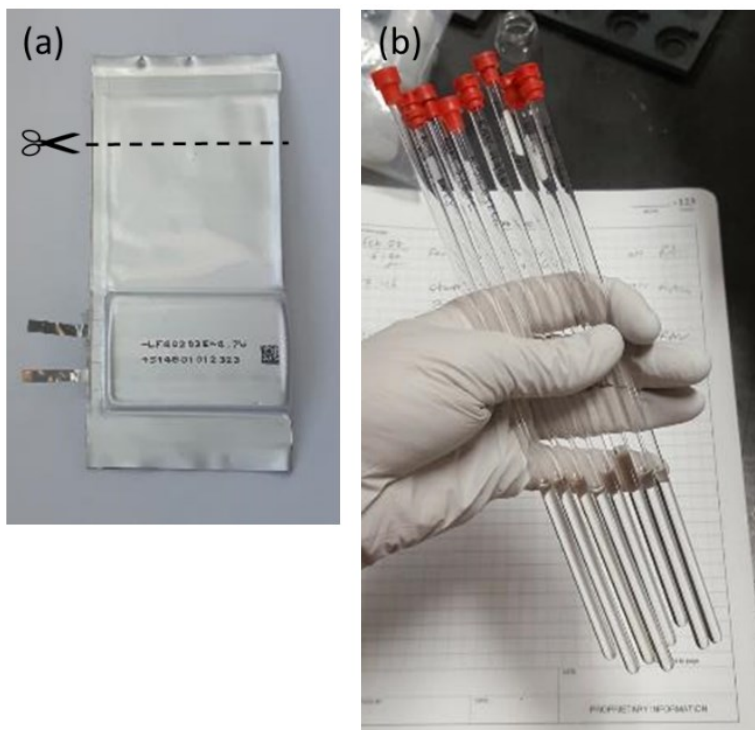


Figure 3-5. Measuring electrolyte composition with NMR (a) Pouch cell with dashed line where it is cut open to add NMR solvent (a) NMR tubes with prepared electrolyte samples.

fraction (wt%). Figure 3-5a shows a pouch cell to be analyzed by NMR and Figure 3-5b shows NMR samples prepared from eight pouch cells. To measure the salt concentration and relative amount of solvents in an electrolyte, NMR samples were prepared in the following way: the top of each pouch cell was cut open in a glovebox (Figure 3-5a) and filled with ~0.8 mL of NMR solvent. In this work anhydrous deuterated-dimethyl sulfoxide (DMSO, Sigma) was used. The NMR solvent was massaged into the jelly-roll, and then the electrolyte/d-DMSO mix was squeezed back out and collected in a small vial. Additional d-DMSO was added to the small vial as needed to reach 0.8 mL volume for the NMR sample. The liquid was then moved to an NMR tube through a syringe filter to remove any solid particle residue from the electrode. Prepared and filtered NMR samples are shown in Figure 3-5b. Most of the samples in this work were analyzed by this method.

3.3 Method 2 – Amount

The second method for electrolyte analysis gives relative composition as well as the total mass of each electrolyte component. Figure 3-6 shows a jelly roll (a) and perfluoroalkoxy (PFA) vial (b) used to measure the total amount of electrolyte in a pouch cell. In order to measure the total amount of electrolyte in a cell in addition to the composition, NMR samples were prepared in the following way: the top of each pouch cell was cut open outside of the glovebox and the jelly roll was moved to a PFA vial with 10 g of dimethyl carbonate (DMC, BASF) as shown in Figure 3-6b. Vials were sonicated for 10 minutes, mixed on a wrist-action shaker for 1 hour, sonicated for 10 minutes, mixed on a wrist-action shaker for 1 hour, sonicated for 10 minutes then mixed on a wrist action shaker overnight to ensure all of the electrolyte from the jelly roll dissolved into the DMC. After

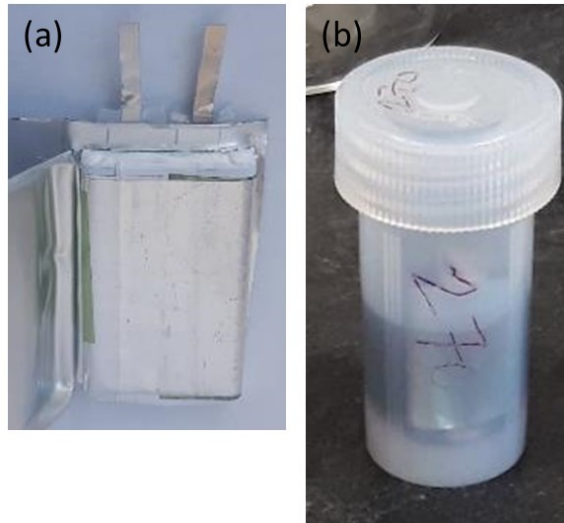


Figure 3-6. Measuring total electrolyte amount with NMR (a) Pouch cell cut open to show the jelly roll (b) Jelly roll and DMC inside of a PFA vial ready for extraction.

extraction 100 mg of the DMC/electrolyte mix was added to ~0.8 mL of anhydrous d-DMSO for NMR analysis. In order to remove solid particles the liquid was filtered through a syringe filter when putting it into the NMR tube.

As described, method (1) gives salt concentration and relative % of electrolyte components that were in the pouch cell. Method (2) is a total extraction method and gives salt concentration and total mass of each electrolyte component present in the pouch cell.

3.4 Electrolyte Analysis

Electrolyte samples were analyzed on a Bruker AV500 spectrometer at Dalhousie University. Table 3-1 shows the experiment parameters used to capture the electrolyte components in this work.

Table 3-1. List of NMR experiments for analyzing electrolyte with the components used in anode-free cells.

EXPERIMENT	n	O1P	SW	time
1d_1H	16	4.5	9	2:29
1d_11B	128	0	200	1:24
1d_19F_nobs	32	-100	200	1:08

In Table 3-1, n is number of scans, O1P is the center point of the scan in ppm, SW is the sweep-width of the scan in ppm, and time is in minutes for the complete experiment.

Fluorine NMR was run with no background subtraction (“nobs”).

Figure 3-7 shows an example of a proton spectrum for the electrolyte 1M LiPF₆ in FEC:DEC (1:2 vol) with spectrum for the individual components for comparison. Proton (¹H) spectra were collected over the range 0-9 ppm. Figure 3-8 shows an example of a fluorine spectrum for the electrolyte 1M LiPF₆ in FEC:DEC (1:2 vol) with spectrum for the individual components for comparison. Fluorine (¹⁹F) spectra were collected with no background suppression over the range -200-0 ppm. To assign each electrolyte component, individual chemicals were analyzed. Spectra for each component are shown. The chemical shifts for each component are summarized in Table 3-2 (proton NMR) Table 3-3 (fluorine NMR) and Table 3-4 (boron NMR). Boron NMR was sometimes run to confirm peak assignments from fluorine NMR but it was not used to calculate electrolyte compositions. Note that the boron spectrum will have a large hump from the NMR sample tube which is from the borosilicate glass. Peak areas from the ¹H spectrum were used to calculate relative FEC and DEC composition. The peak areas from the ¹⁹F spectrum were used to calculate salt amount relative to FEC, which was used with the

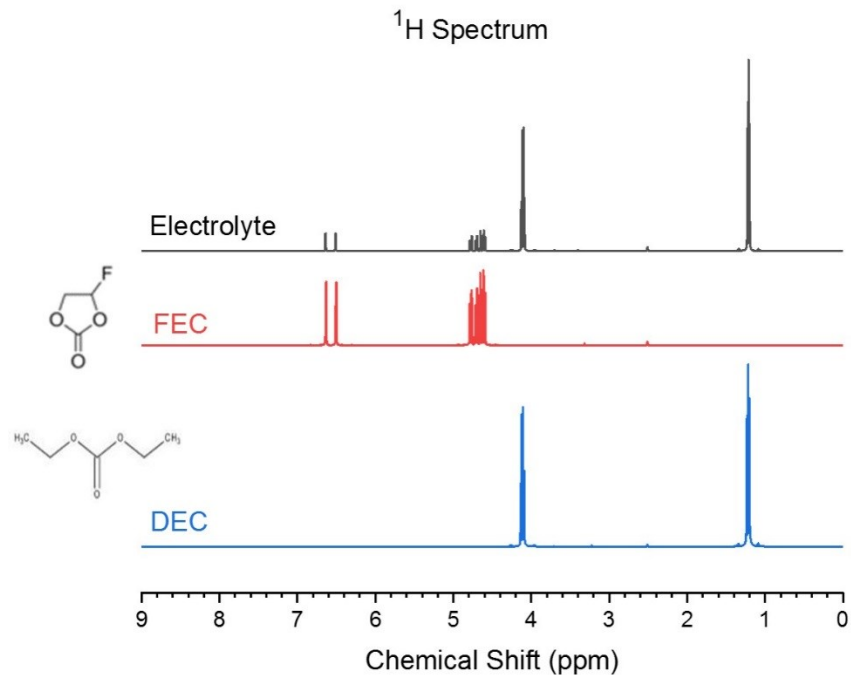


Figure 3-7. Example of electrolyte analysis by NMR. Proton (¹H) spectra for 1M LiPF₆ in FEC:DEC (1:2 vol) (black line), compared to individual components FEC (red line) and DEC (blue line).

information from the ¹H spectrum to calculate salt concentration. The electrolyte composition is then known.

For samples prepared by method 2 the compositions as well as the total amount of electrolyte were calculated. The mass of DMC present in the NMR sample was measured, so the DMC signal in the ¹H spectrum was used as a standard to calculate the mass of FEC and DEC extracted from the pouch cell. The peak areas from the ¹⁹F spectrum were used to calculate salt amount relative to FEC, which was used with the information from the ¹H spectrum to calculate salt concentration. The electrolyte composition as well as the total mass of each electrolyte present in the pouch cell is then known.

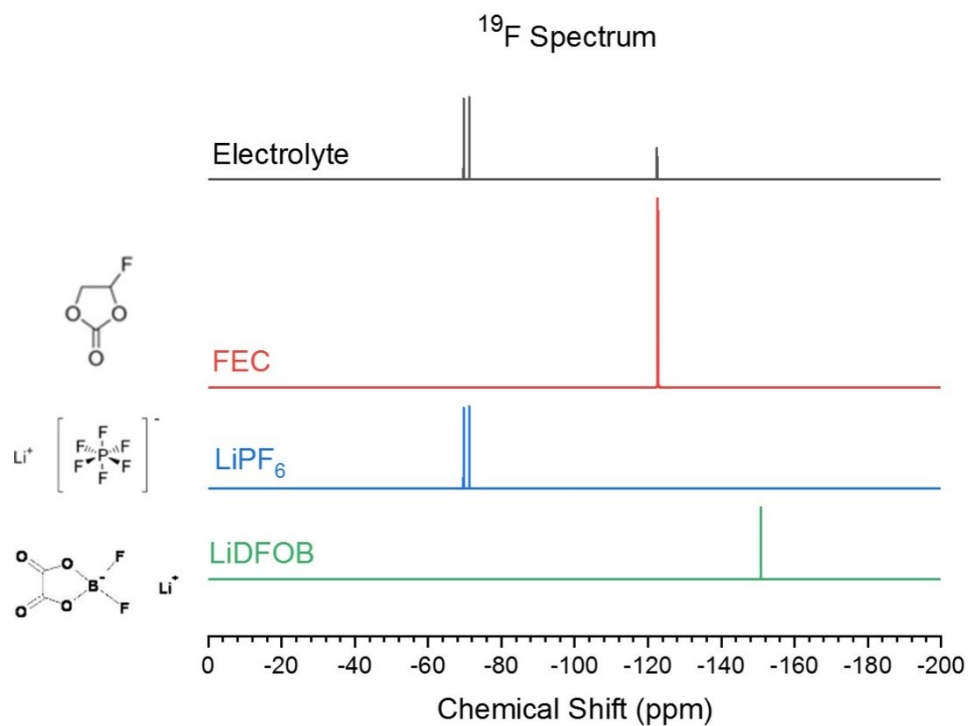


Figure 3-8. Example of electrolyte analysis by NMR. Fluorine (¹⁹F) spectra for 1M LiPF₆ in FEC:DEC (1:2 vol) (black line), compared to individual components FEC (red line), LiPF₆ (blue line), and LiDFOB (green line).

Table 3-2. Proton NMR chemical shifts for electrolyte components in d-DMSO.

Component	Molecular formula	¹ H Chemical Shift (ppm)
Methanol	CH ₃ OH	3.33
DMSO	(CH ₃) ₂ SO	~2.5
EC (ethylene carbonate)	C ₃ H ₄ O ₃	4.5
DMC (dimethyl carbonate)	C ₃ H ₆ O ₃	3.7
FEC (fluoroethylene carbonate)	C ₃ H ₃ FO ₃	6.7, 6.5, ~4.7
DEC (diethyl carbonate)	C ₅ H ₁₀ O ₃	4.2, 1.2

Table 3-3. Fluorine NMR chemical shifts for electrolyte components in d-DMSO.

Component	Molecular formula	¹⁹ F Chemical Shift (ppm)
FEC (fluoroethylene carbonate)	C ₃ H ₃ FO ₃	-122.4
LiPF ₆	LiPF ₆	-69.8, -71.4
LiBF ₄	LiBF ₄	-148
LiDFOB	LiBF ₂ (C ₂ O ₄)	-151
HF	HF	-190.8

Table 3-4. Boron NMR chemical shifts for electrolyte components in d-DMSO.

Component	Molecular formula	¹¹ B Chemical Shift (ppm)
LiBOB	LiB(C ₂ O ₄) ₂	7.4
LiBF ₄	LiBF ₄	-1.3
LiDFOB	LiBF ₂ (C ₂ O ₄)	3.05

Table 3-5 compares the composition as mixed calculated from the mass of each electrolyte component with the composition measured by NMR on cycle zero. The composition at cycle zero is measured by NMR from electrolyte extracted from a cell after filling and wetting. Clearly there is some error in the composition measured by NMR. It is possible that the composition changes during cell filling, wetting, or NMR sample preparation. Measurements taken for subsequent cycles use the same method as cycle 0 in order to accurately see trends in composition changes by having similar systematic error at all data points.

Table 3-5. Electrolyte compositions calculated from component masses added during electrolyte mixing (left column) compared to the composition calculated from NMR spectra measure on electrolyte extracted from pouch cells at “cycle 0” after wetting (right column).

Composition as mixed	Composition measured by NMR
0.90 m LiPF ₆ in FEC:DEC (44:56 wt%)	0.93 m LiPF ₆ in FEC:DEC (43:57 wt%)
0.90 m LiDFOB in FEC:DEC (44:56 wt%)	0.89 m LiDFOB in FEC:DEC (42:58 wt%)
0.5 m LiDFOB 0.5 m LiBF ₄ in FEC:DEC (44:56 wt%)	0.40 m LiDFOB 0.41 m LiBF ₄ in FEC:DEC (44:56 wt%)

3.5 Summary

NMR is an appropriate method to capture the large changes in electrolyte composition expected for anode-free cells during cycling. Electrolyte can be extracted from anode-free pouch cells, dissolved in d-DMSO, and analyzed by fluorine and proton NMR. This method is used in the next chapter to study degradation of anode-free pouch cells. For the solvents (FEC, DEC) and salts (LiPF₆, LiDFOB, LiBF₄) used in this work the complete electrolyte composition is known from the proton and fluorine NMR experiments.

CHAPTER 4 ANODE-FREE POUCH CELL DEGRADATION

MECHANISMS

4.1 Cell Performance

Anode-free pouch cells with different liquid electrolytes were tested by galvanostatic cycling. Cells were cycled on a Maccor series 4000 battery test system at 40°C, C/5 charge and C/2 discharge, between 3.6 V and 4.5 V. For these conditions the areal capacity was $\sim 2.4 \text{ mAh/cm}^2$ and total pouch cell capacity was $\sim 250 \text{ mAh}$. These cells are operating under a very lean electrolyte condition of approximately 2g/Ah. Cells were clamped during cycling with rubber blocks to achieve a low stack pressure of $\sim 75 \text{ kPa}$. Capacity retention data is summarized in Figure 4-1. Electrolytes were made incorporating various lithium-salts in a fluoroethylene carbonate (FEC):diethyl carbonate (DEC) (volume ratio 1:2) solvent blend. Cells with 1M LiPF₆ and 1M LiBF₄ single-salt electrolyte demonstrate the challenge of anode-free cycling as they fall below 80%

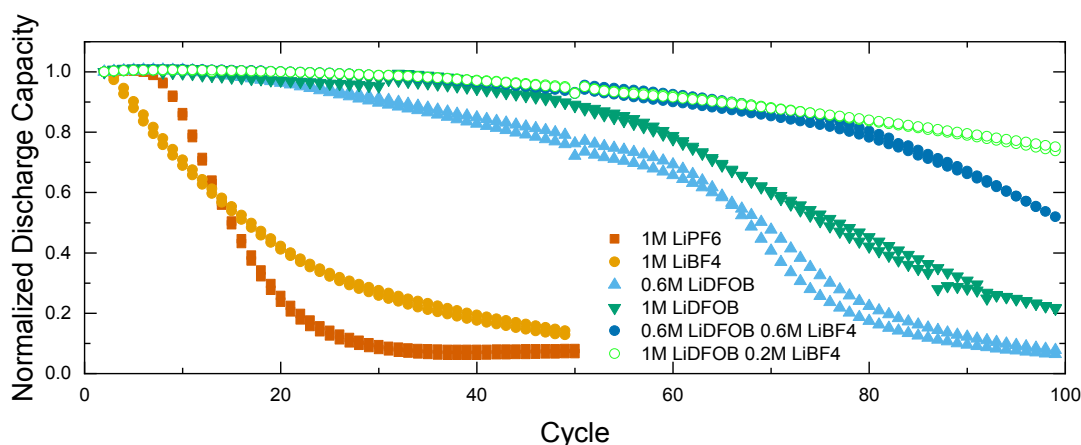


Figure 4-1. Capacity retention versus cycle number for anode-free pouch cells using electrolytes with different lithium salts. All electrolytes use an FEC:DEC (1:2 vol.) solvent mix. Pair cells for each electrolyte type are shown as matching symbols. Cycled at 40°C, 3.6 – 4.5V, C/5 charge, C/2 discharge, $\sim 75 \text{ kPa}$.

retention in less than 15 cycles. Cycling stability was dramatically improved with a 1M lithium difluoro(oxalate)borate (LiDFOB) single-salt electrolyte which reaches 60 cycles before falling below 80% capacity. Improved lithium metal cycling with LiDFOB has been reported by others especially in combination with FEC.^{34,90,141}

0.6M LiDFOB electrolyte with the addition of 0.6M LiBF₄ (dark blue circles), shows a substantial jump in initial capacity retention with the cell making it to 80 cycles with 80% capacity. Cells with a more optimized dual salt blend of 1M LiDFOB and 0.2M LiBF₄ made it to 90 cycles before dropping below 80% capacity, a significant achievement for an anode-free configuration under low applied pressure with limited excess electrolyte.

Figure 4-2 shows a comparison of LiDFOB and LiDFOB/LiBF₄ electrolytes charged to varying upper cutoff voltages at 40°C. Figure 4-2a shows the cycling performance of the 1.2M single salt LiDFOB electrolyte charged to 4.2, 4.3, or 4.5V. Surprisingly, the capacity retention of single salt LiDFOB cells improves with increasing upper cutoff voltage. Previous studies of LiDFOB electrolytes in lithium metal cells cycled below 4.3 V so this high voltage enhancement has not been reported before.^{90,142,143} Figure 4-2b shows the cycling performance of 0.6M LiDFOB 0.6M LiBF₄ dual salt electrolyte charged to 4.2, 4.3, or 4.5V. Capacity retention is similar for all upper-cutoff voltages. All cells have good capacity retention up to 80 cycles, and accelerating capacity loss after 80 cycles.

Under identical testing conditions the choice of electrolyte salt has a huge impact on the cell performance. To understand the degradation mechanisms the next sections study

electrolyte, SEI, and lithium morphology throughout cycling for cells with LiPF₆, LiDFOB, and LiBF₄ based electrolytes.

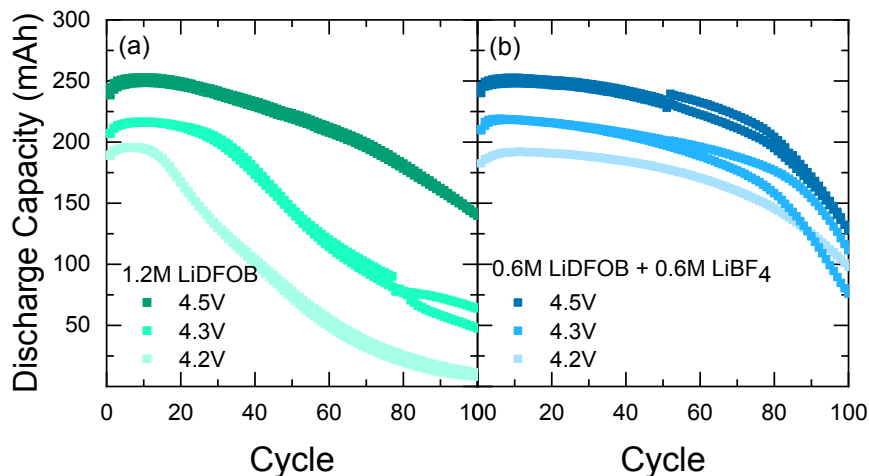


Figure 4-2. Capacity retention versus cycle number as a function of upper cut-off voltage for two electrolytes with different salts: 1.2 M LiDFOB (a) versus 0.6 M LiDFOB + 0.6 M LiBF₄ (b). All electrolytes use an FEC:DEC (1:2 vol.) solvent mix. Pair cells for each electrolyte type are shown as matching symbols. Cycled at 40°C, 3.6 V – 4.2, 4.3, or 4.5 V, C/5 charge, C/2 discharge, ~75 kPa.

4.2 Lithium Morphology

Figure 4-3a shows capacity retention vs cycle number for the single-salt 1M LiPF₆ (orange squares) and dual-salt 0.6M LiDFOB + 0.6M LiBF₄ (blue circles) electrolytes under varying applied pressure. Cells with 1M LiPF₆ constrained under low pressure (~75 kPa) have poor capacity retention (orange, closed squares). Previous reports have demonstrated the ability of increased stack pressure to improve lithium metal cycling efficiency,^{112–115} and here increasing the stack pressure of the LiPF₆ cell to 1200 kPa (orange, open squares) more than triples the number of cycles before the cells lose 60% of the initial capacity. Figure 4-3b and c show that lithium metal plated in the LiPF₆

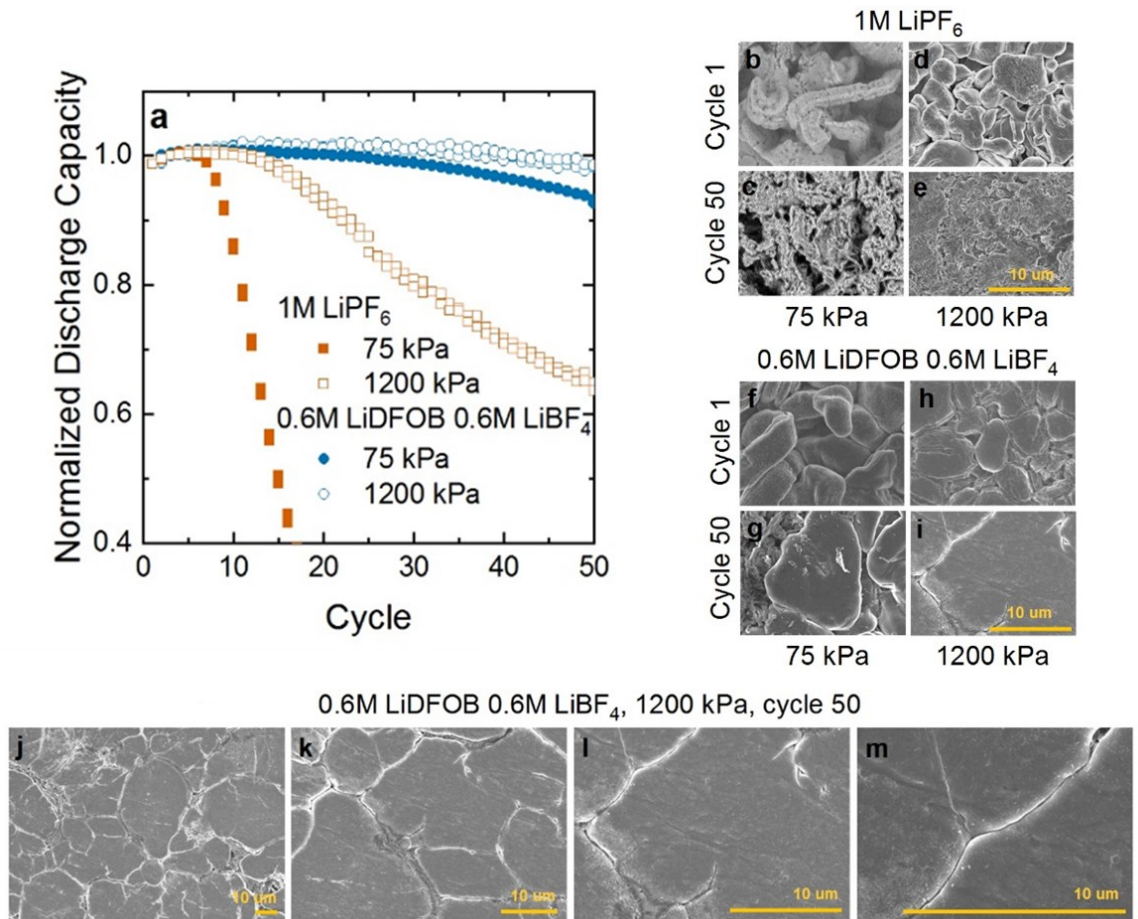


Figure 4-3. SEM characterization of lithium morphology. (a) Capacity retention versus cycle number for electrolytes with different lithium salts and two different stack pressures with pair cells shown as matching symbols. (b–i) SEM images of lithium morphology are shown for the two electrolyte and conditions. Images were captured on the first charge and after 50 cycles. (j–m) Additional SEM images of lithium morphology for cells with LiDFOB + LiBF₄ after 50 cycles at high pressure. Yellow scale bars on each image are 10 μm. SEM images from Alex Louli. Cycled at 40°C, 3.6 – 4.5V, C/5 charge, C/2 discharge, 75 or 1200 kPa.

electrolyte under low pressure is dendritic and has high surface area. Increasing stack pressure improves capacity retention by initially resulting in a more compact lithium surface after 1 charge (Figure 4-3d), and destroying the dendrite formation after 50 cycles (Figure 4-3e). Figure 4-3f shows that the dual-salt LiDFOB/LiBF₄ electrolyte results in a dendrite-free morphology even under low pressure, which is expected given the improved capacity retention shown in Figure 4-3a (blue, closed circles). Even after 50 cycles, the

morphology is mostly compact (Figure 4-3g). Higher stack pressure only slightly improves capacity retention for the dual-salt LiDFOB/LiBF₄ electrolyte; cells at 50 cycles with this electrolyte show ~95% capacity retention when cycled at 75kPa and ~97% capacity retention when cycled at ~1200 kPa (Figure 4-3a, blue circles).

The lithium in the dual-salt LiDFOB/LiBF₄ cells is densely packed and dendrite free for both low and high pressure cells after one charge (Figure 4-3f,h) and very flat after 50 cycles (Figure 4-3g, i-m). Figure 4-3j-m shows that this dual-salt electrolyte under 1200 kPa is made of smooth densely packed lithium domains up to 50 μm in diameter. For 1.2M LiDFOB cells cycled to lower voltage (4.3 V, 4.2 V in Figure 4-1c and d) or with lower salt concentration (1M LiDFOB in Figure 4-1b), it is expected that the poorer capacity retention would also result in worse lithium morphology.

Figure 4-4 shows a comparison of 1.2 M LiDFOB and dual-salt LiDFOB/LiBF₄ electrolyte cells cycled under pressure. Figure 4-4a shows normalized discharge capacity vs cycle shown for cells with dual salt electrolyte 0.6 M LiDFOB 0.6 M LiBF₄ (blue) and 1.2 M LiDFOB electrolyte (green) in FEC:DEC (1:2 vol). Closed symbols are for cells with low stack pressure (75 kPa) and open symbols are for cells with high stack pressure (1200 kPa). Pair cells are shown as matching symbols. The cells with 0.6M LiDFOB 0.6M LiBF₄ at high pressure (1200 kPa open blue symbols) ran for 90 cycles before reaching <80% of the original capacity. For the dual-salt electrolyte (blue), high pressure only increased capacity retention by about 3% at cycle 75. For comparison, switching to high pressure for 1.2M LiDFOB (green) greatly improved capacity retention for these cells to >90% at cycle 60 vs <85% at cycle 60 with low pressure. The dual-salt composition is less affected by pressure in the region before the cells “rollover”.

Figure 4-4b-e shows SEM images of plated lithium in 1.2M LiDFOB electrolyte after 1 cycle (b and d) and after 50 cycles (c and e) to 4.5V for low (b-c) and high (d-e) stack pressure. Similar smooth lithium morphology is seen on the first cycle for both electrolyte types, which makes sense given the similar capacity retention for 1.2M cells cycled to 4.5 V with these two electrolytes.

Figure 4-5 shows SEM images of plated lithium in the dual-salt 0.6M LiDFOB + 0.6M LiBF₄ electrolyte under 1200 kPa after 50 cycles at (a) the top of charge with the maximum amount of plated lithium and (b) at an intermediary state of charge with most (~80%) of the lithium stripped away. With most of the lithium stripped away, the morphology still consists of large, flat lithium domains, similar to the surface

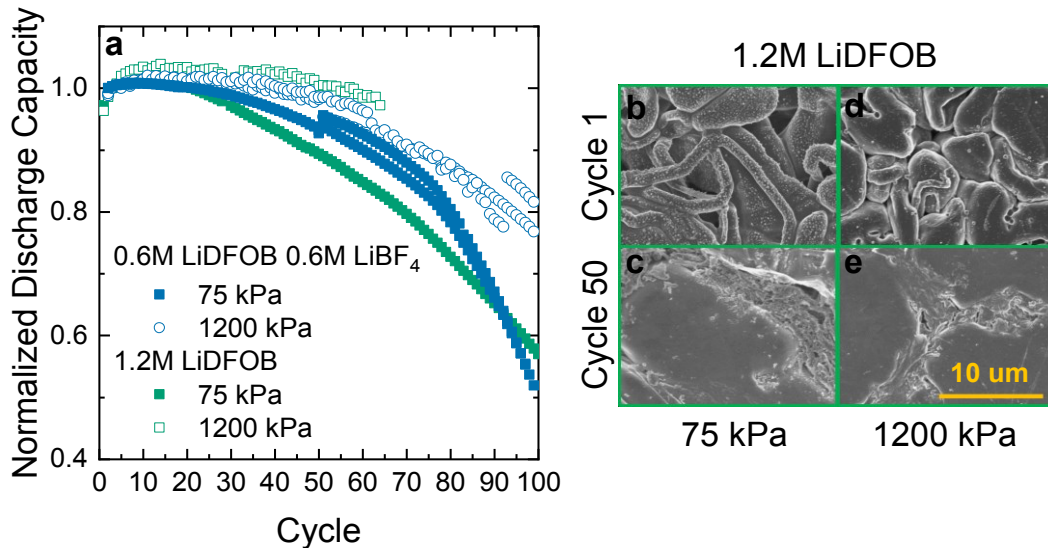


Figure 4-4. Comparison of 1.2M LiDFOB and dual-salt LiDFOB/LiBF₄ electrolyte cells cycled under pressure. (a) Normalized discharge capacity vs cycle shown for cells with dual salt electrolyte 0.6M LiDFOB 0.6M LiBF₄ (blue) and 1.2M LiDFOB electrolyte (green) in FEC:DEC (1:2 vol). (b-e) SEM images of plated lithium in 1.2M LiDFOB electrolyte after 1 cycle (b and d) and after 50 cycles (c and e) to 4.5V for low (b-c) and high (d-e) stack pressure. SEM images from Alex Louli. Cycled at 40°C, 3.6 – 4.5V, C/5 charge, C/2 discharge, 75 or 1200 kPa.

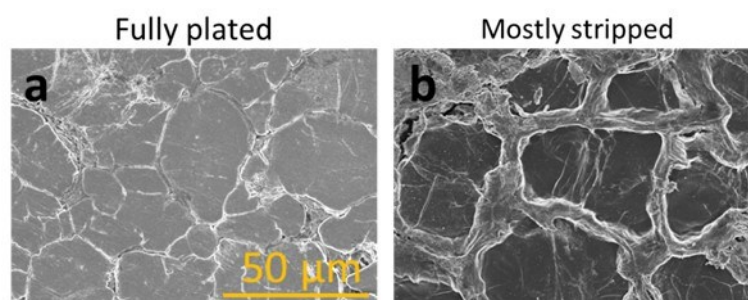


Figure 4-5. SEM images of plated lithium in the dual-salt 0.6M LiDFOB + 0.6M LiBF₄ electrolyte under 1200 kPa after 50 cycles at (a) the top of charge (b) after ~80% of the lithium is stripped away. SEM images from Alex Louli. Cycled at 40°C, 3.6 – 4.5V, C/5 charge, C/2 discharge, ~75 kPa.

morphology at the top of charge. Although cross-sections were not made, this suggests that the tightly packed domains achieved with LiDFOB/LiBF₄ electrolyte under 1200 kPa shown in Figure 4-3j-m are lithium columns.

Figure 4-6 shows SEM images of lithium morphology from cells stopped after 1 cycle (a), 20 cycles (b), 50 cycles (c), 80 cycles (d), or 100 cycles (e). Cells used 0.6M LiDFOB 0.6M LiBF₄ in FEC:DEC (1:2) electrolyte and were cycled at 40°C, 3.6 – 4.5V, C/5 charge, C/2 discharge, and ~75 kPa. SEM images at 50 cycles were previously shown in Figure 4-3 and Figure 4-4. The lithium domains are the largest at 50 cycles. At 80 cycles, the smooth dense structure of the lithium domains starts to get destroyed. What looks like dead porous lithium/SEI builds up in the grain boundaries. Large sections of this are evident after 100 cycles, and the lithium domains have shrunk. Recall from Figure 4-1 that capacity loss in cells with 0.6M LiDFOB 0.6M LiBF₄ electrolyte accelerates around cycle 60 and nearly 40% of overall capacity is lost between cycle 60 and cycle 80, at the same time as the lithium structure degrades.

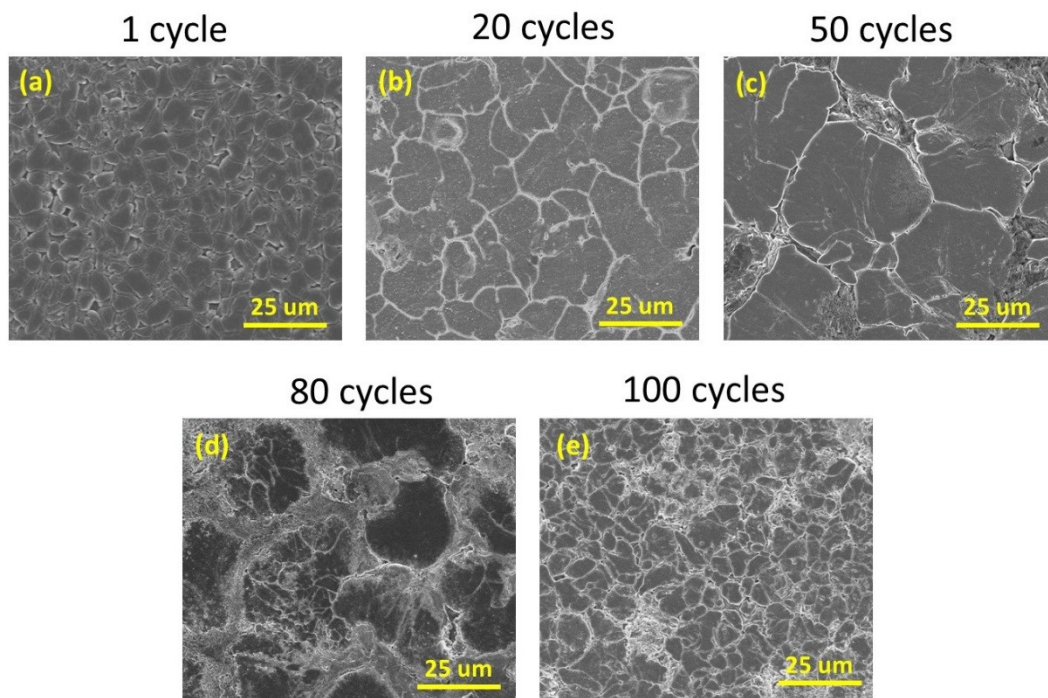


Figure 4-6. The evolution of lithium morphology from (a) cycle 1 to (e) cycle 100. Cells with 0.6M LiDFOB 0.6M LiBF₄ in FEC:DEC (1:2) cycled at 40°C, 3.6 – 4.5V, C/5 charge, C/2 discharge, ~75 kPa. SEM images from Alex Louli.

In this section SEM images were used to look at the local lithium morphology. Clearly the choice of electrolyte salt has a big impact on the lithium morphology, which in turn is related to cell capacity retention. Low surface area, less dendritic lithium consumes the least capacity through reactions with electrolyte and the formation of isolated metallic lithium. In the next section, surface area measurements are used to give a quantitative comparison of the bulk lithium electrode.

4.3 Lithium Surface Area

Figure 4-7 shows SEM images of the surface of the lithium-metal anode plated at 4.5 V after 1, 5, 10, or 20 charge-discharge cycles for cells with 1M LiPF₆ in FEC:DEC (1:2 vol) electrolyte cycled between 3.6 V – 4.5 V, at 40°C, with a C/5 charge and C/2 discharge, and ~75 kPa. SEM images are shown for two different locations on each

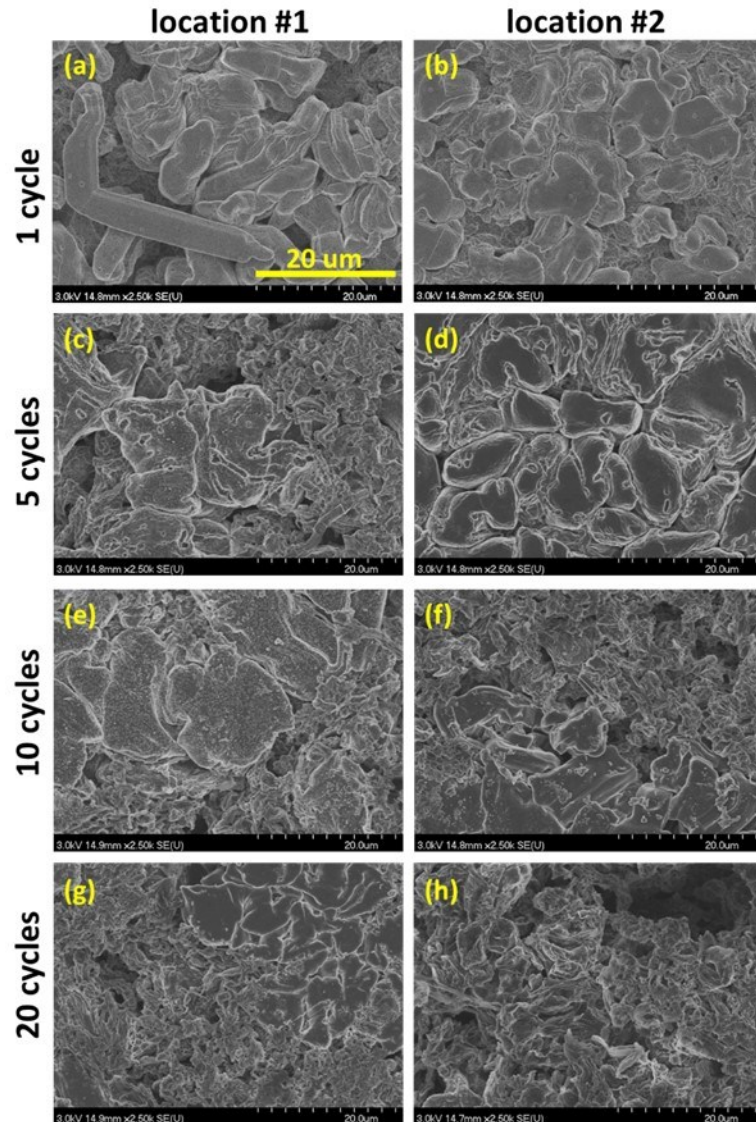


Figure 4-7. SEM images of the lithium metal from two different locations on the same anode after 1 cycle (a-b), 5 cycles (c-d), 10 cycles (e-f), or 20 cycles (g-h). SEM images from Alex Louli. Cells with 1M LiPF₆ in FEC:DEC (1:2) cycled at 40°C, 3.6 – 4.5V, C/5 charge, C/2 discharge, ~75 kPa.

electrode, labelled “location #1” and “location #2”. For example, Figure 4-7a-b show two images taken from an electrode harvested from one pouch cell. The lithium morphology looks more compact in area (b) compared to area (a), likely due to local differences in pressure. Surface area measurements by argon BET give a much better overall representation of the electrode surface area compared to selecting an SEM image that only shows one local region of the lithium electrode. In addition, it is very difficult to tell using SEM images how much the surface area of the electrodes increases with cycling number.

Figure 4-8a shows normalized discharge capacity vs cycle number for anode-free lithium metal cells with 1M LiPF₆ in FEC:DEC (1:2 vol) electrolyte cycled between 3.6 V – 4.5 V, at 40°C, with a C/5 charge and C/2 discharge, and ~75 kPa. Cells lose capacity rapidly, and only retain about 20% of the initial capacity after 20 cycles. Cells were stopped at 4.5 V (to have the maximum amount of plated lithium) after 1 cycle, 4 cycles,

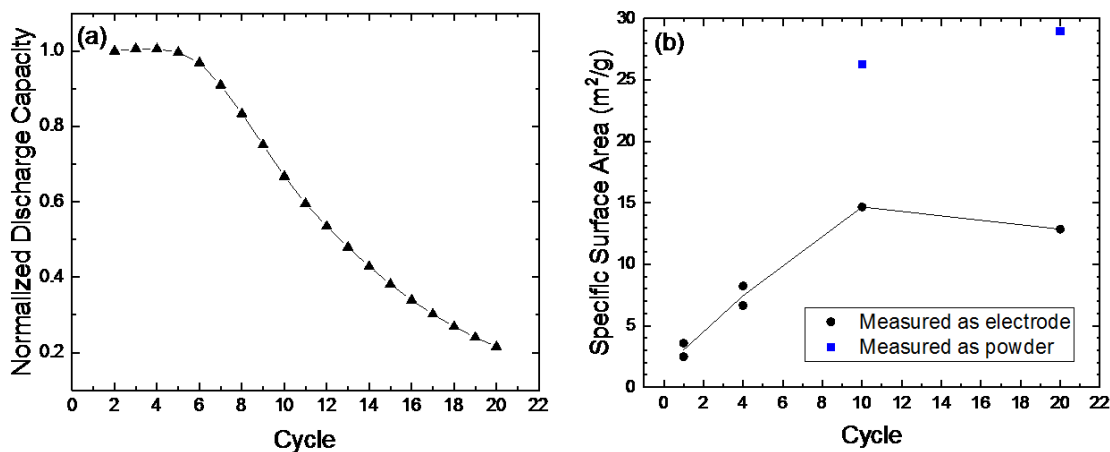


Figure 4-8. (a) Normalized discharge capacity vs cycle number for anode-free lithium metal cells cycled with 1M LiPF₆ in FEC:DEC (1:2 vol) electrolyte. (b) Surface area for lithium-metal collected from cells at different cycle counts. Black circles show data that was measured as an electrode and blue squares show data that was measured as lithium metal powder scraped off the electrode. The black line shows the average surface area for data that was measured as an electrode. Cycled at 40°C, 3.6 – 4.5V, C/5 charge, C/2 discharge, ~75 kPa.

10 cycles, and 20 cycles to harvest electrodes for surface area measurements and SEM. Similar cells were used for the SEM images in Figure 4-7. Figure 4-8b shows average surface area for electrodes from cells at different cycle counts. For cycle 10 and cycle 20, one pair cell was measured as lithium metal powder scraped off the electrode to compare to the surface area measurement from a full electrode. For surface area measurements of the full electrode, the surface area of the copper current collector was not subtracted since it is covered mostly in lithium.

The lithium specific surface area is less than $4 \text{ m}^2/\text{g}$ after 1 charge to 4.5 V, and increases rapidly during subsequent cycles. After only 4 cycles, the specific surface area doubled to about $8 \text{ m}^2/\text{g}$. With an increase in specific surface area, capacity loss is expected to accelerate due to an increased rate of reaction with the electrolyte and more dendritic or porous lithium (easier to become electrically isolated). When the cell starts to rapidly lose capacity around cycle 10, the specific surface area is massive at $\sim 20 \text{ m}^2/\text{g}$ of lithium. The specific surface area is similar for cycle 10 and cycle 20. The specific surface area measured as lithium powder is about two times larger than the specific surface area measured as an electrode. It is possible that crumbling the lithium metal off the current collector increases surface area by exposing the side adhered to the copper current collector and by opening up closed pores in the lithium metal.

The mass of the lithium plated over the entire 100 cm^2 electrode is $\sim 0.1 \text{ g}$, so after 10 cycles this corresponds to a total of $\sim 1.5 \text{ m}^2$ of surface area on the negative electrode distributed over $\sim 100 \text{ cm}^2$ of geometric area - a surface enhancement factor of 150. Not only will the increased surface area accelerate capacity loss, but the reactivity of lithium metal in the event of a cell puncture should be worse for higher surface area electrodes.

The safety of the cells will be the best if lithium metal surface area is minimized. Surface area should also be minimized since it may be difficult to maintain fully wet lithium-metal electrodes for very high surface area electrodes. Figure 4-9a shows the normalized discharge capacity vs cycle number for an example anode-free lithium metal cell cycled with 1M LiDFOB 0.2 M LiBF₄ in FEC:DEC (1:2 vol) electrolyte cycled between 3.6 V – 4.5 V, at 40°C, with a C/5 charge and C/2 discharge. Figure 4-9b shows surface area measured by argon BET for cells after 1, 25, or 50 cycles. Compared to the cells with 1M LiPF₆ electrolyte (Figure 4-8) the improved electrolyte here has ~1/4 of the surface area after 1 cycle and lower surface area in subsequent cycles. However, the surface area still increases dramatically during cycling. The surface area increases about 30 times after 50 cycles even though the cells have 90% capacity remaining. With this huge surface area the reaction rate with the electrolyte should be large but may not drastically impact

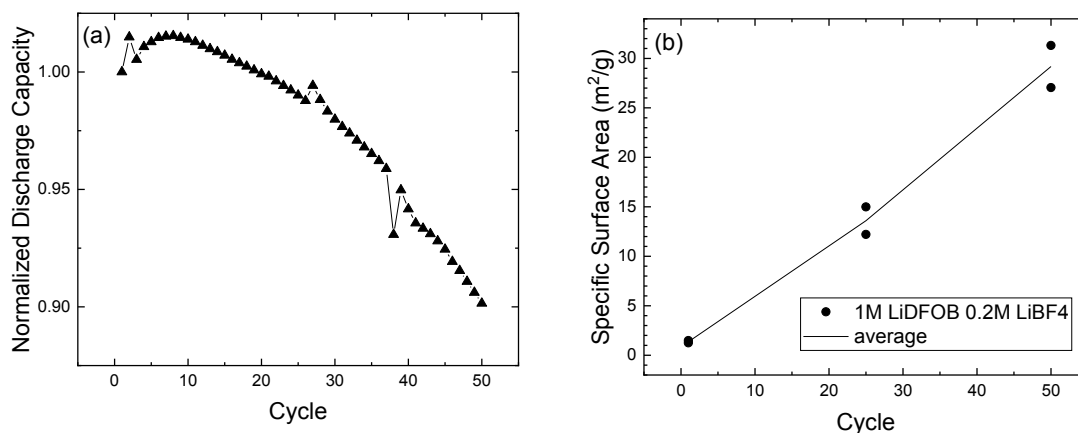


Figure 4-9. (a) Normalized discharge capacity vs cycle number for anode-free lithium metal cells cycled with 1M LiDFOB 0.2 M LiBF₄ in FEC:DEC (1:2 vol) electrolyte. (b) Surface area for lithium-metal collected from cells at different cycle counts. Two cells were measured at each cycle count and the black line shows the average. Cycled at 40°C, 3.6 – 4.5V, C/5 charge, C/2 discharge, ~75 kPa.

capacity loss until later than the 50 cycles tested here.

4.4 Electrolyte Consumption

Electrolyte samples prepared in d-DMSO were analyzed by liquid NMR on a Bruker AV500 spectrometer as described in the experimental section. Figure 4-10 shows the average amount of electrolyte versus cycle number for cells that start with either 0.9m (1M) LiPF_6 electrolyte (black) or 0.9m (1M) LiDFOB electrolyte (red). Error bars show the standard deviation of results from two cells. These cells underwent extraction based on method 2 described in the experimental section, which allows for the total amount of electrolyte to be calculated in addition to the relative composition. The total amount of electrolyte may change after formation (from cycle 0 to cycle 1) for the cells that start with 0.9m LiDFOB. Otherwise, the amount of electrolyte is the same within error from cycle-to-cycle. These results are important to show that the cells are not failing due to “dry out” during cycling. Electrolyte is not depleted.

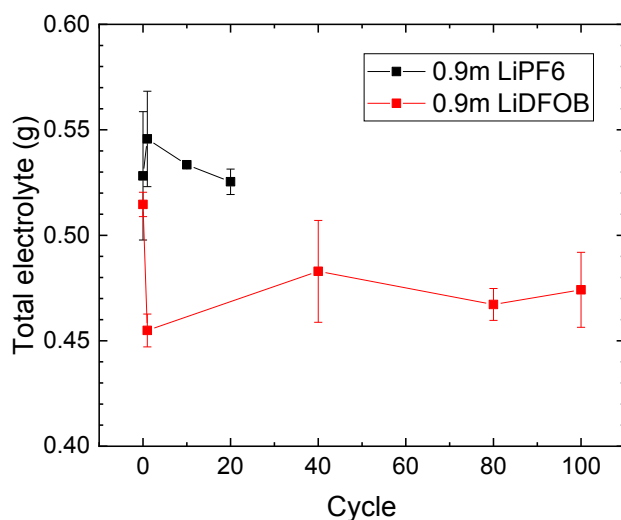


Figure 4-10. Average amount of electrolyte versus cycle number for cells shown in Figure 4a-d that start with either 0.9m LiPF_6 electrolyte (black) or 0.9m LiDFOB electrolyte (red). Cycled at 40°C, 3.6 – 4.5V, C/5 charge, C/2 discharge, ~75 kPa.

Figure 4-11 shows NMR measurements of electrolyte composition during cycling for anode-free cells that started with three different electrolytes: (a-b) 0.9m (1M) LiPF₆, (c-d) 0.9m (1M) LiDFOB, (e-f) 0.5m (0.6M) LiDFOB + 0.5m (0.6M) LiBF₄. All electrolytes used FEC:DEC (44:56 weight ratio = 1:2 volume ratio) solvent and cycling conditions were the same as cells in Figure 4-1: 40°C, C/5 charge, C/2 discharge between 3.6 V – 4.5 V at ~75 kPa.

For each electrolyte, Figure 4-11 shows the salt concentration measured on cycle 0 is higher than the salt concentration measured just after formation (cycle 1). Some salt may be consumed during the first charge cycle to form the initial SEI, which is also indicated by the presence of boron (for LiDFOB and LiBF₄ electrolytes) or phosphorous (for LiPF₆ electrolytes) on the electrode surface after formation (measured by XPS Figure 4-14).

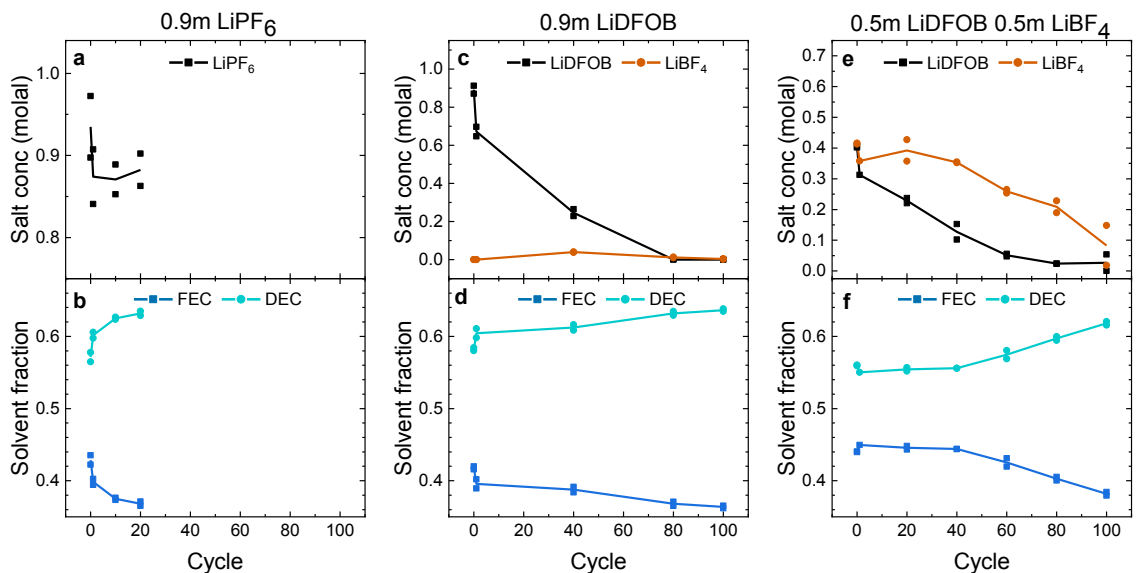


Figure 4-11. Electrolyte composition during cycling. a–e, Cells that started with 0.9 m LiPF₆ electrolyte (a,b), 0.9 m LiDFOB electrolyte (c,d) or 0.5 m LiDFOB + 0.5 m LiBF₄ electrolyte (e,f). All electrolytes used FEC:DEC (44 wt%:56 wt%) solvent. Pair cell measurements are shown as matching data points, with the average shown as a line. Cycled at 40°C, 3.6 – 4.5V, C/5 charge, C/2 discharge, ~75 kPa.

After formation, the cells with LiPF_6 (Figure 4-11a) maintain the same salt concentration during cycling, despite the fact that they have less than 20% capacity remaining at cycle 20. Not much salt is consumed in this system, and although the composition of the solvent shifts to slightly higher FEC ratio (Figure 4-11b) the amount of electrolyte measured at cycle 1 and cycle 20 is similar (Figure 4-10). The primary cause of capacity loss in this system is likely not from the consumption of lithium to form SEI, since this would also consume electrolyte. Instead these cells must lose most of their capacity from the formation of isolated metallic lithium, which is likely given the highly dendritic lithium morphology (Figure 4-3b-c). In contrast, both LiDFOB and LiBF_4 are consumed during cycling for cells that use single or dual-salt electrolytes (Figure 4-11c and 4e). Recall that in Figure 4-1b cells with single-salt LiDFOB electrolyte experienced “rollover” in capacity retention around cycle 60. From the electrolyte analysis results here, the rollover corresponds to when nearly all the salt is consumed. Although all of the salt is consumed, the total mass of electrolyte remains high (Figure 4-10) since the mass of salt is a small fraction of the total mass of electrolyte.

Figure 4-12 shows fluorine NMR spectra for cells that started with 1M LiDFOB electrolyte after 1 cycle (gray) and after 40 cycles (blue). 0.6M LiDFOB 0.6M LiBF_4 electrolyte is shown for comparison (purple) with component peaks labelled. For each spectrum chemical shift was normalized to the position of the LiDFOB peak. These spectra were selected from the experiments used to track electrolyte composition in Figure 4-11. The spectrum for 1M LiDFOB cells after 1 cycle show only LiDFOB is present in the electrolyte (gray). For cells after 40 cycles (blue) a small amount of LiBF_4 (< 0.1 molal) was detected by NMR. Figure 4-11c shows the amount of LiBF_4 measured

throughout cycling. More LiBF_4 may have been produced than was detected, since this salt was also shown to be consumed during cycling. Note that chemical shift for LiBF_4 changes with concentration, consistent with the results of Tulibaeva *et al.*¹⁴⁴

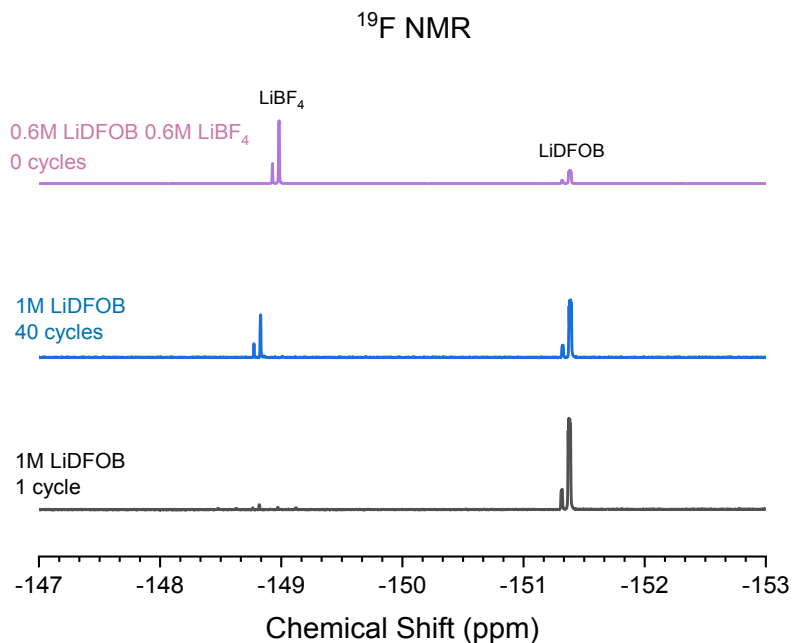


Figure 4-12. Fluorine NMR spectra for cells that started with 1M LiDFOB electrolyte. After 1 cycle (gray) and after 40 cycles (blue). 0.6M LiDFOB 0.6M LiBF_4 electrolyte is shown for comparison (purple) with component peaks labelled. Cycled at 40°C , 3.6 – 4.5V, C/5 charge, C/2 discharge, ~ 75 kPa.

Recall from Figure 4-1c that for cells with single-salt LiDFOB electrolyte, capacity retention vs cycle number improved with higher upper cutoff voltage. The best capacity retention was for the cells cycled up to 4.5 V. NMR measurements on cells that started with pure 1M LiDFOB electrolytes show that when LiDFOB is consumed a small amount of LiBF_4 is formed (Figure 4-11c and Figure 4-12). It is likely that higher voltage increases the amount of LiBF_4 formed, which then improves performance by turning the

electrolyte into a dual-salt LiDFOB + LiBF₄ composition. NMR measurements to test this theory are shown next.

Figure 4-13 shows salt concentration vs cycle number for cells that started with 1.1 m (1.2 M) LiDFOB electrolyte charged to either 4.2 V (black) or 4.5 V (red) at 40°C. The rate of LiDFOB consumption is higher at higher voltage, and higher voltage creates more LiBF₄. As previously speculated, capacity retention may be improved at higher voltage due to the increased amount of LiBF₄. If LiBF₄ is primarily generated from oxidation of LiDFOB at the cathode, more LiBF₄ will be seen at 4.5 V. Since the oxidation potential of LiDFOB is 4.3 V but LiBF₄ is still generated in the 4.2 V cell, LiDFOB must be converting to LiBF₄ at the negative electrode.⁵⁶ The increased amount of LiDFOB consumption and LiBF₄ generation in the 4.5 V cell can then be explained, in part, by the larger amount of lithium that is cycled compared to the 4.2 V cell.

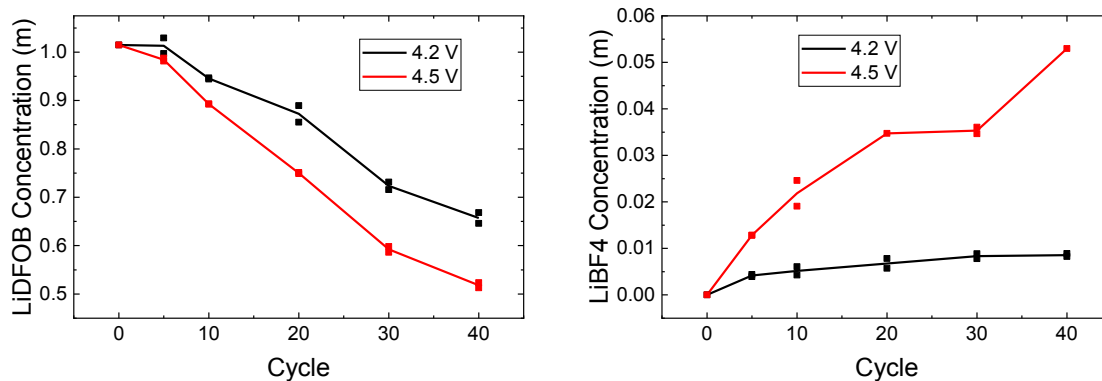


Figure 4-13. Salt concentration vs cycle number for cells that started with 1.1 m (1.2 M) LiDFOB electrolyte charged to either 4.2 V (black) or 4.5 V (red) at 40°C. All electrolytes use an FEC:DEC (1:2 vol.) solvent mix. Pair cell measurements are shown as matching data points, with the average shown as a line. Cycled at 40°C, 3.6 – 4.5V, C/5 charge, C/2 discharge, ~75 kPa.

The results of these electrolyte studies show that LiDFOB and LiBF₄ salts are consumed during cell cycling while LiPF₆ is not. When LiDFOB is consumed some LiBF₄ is generated, which can improve capacity retention for cells cycled at higher voltage. Although significant amounts of salt are consumed the total amount of electrolyte remains high during cell use since not much solvent is consumed. Lithium salt may be consumed on each cycle to reform the SEI which is damaged by the continuous volume change of the lithium metal electrode. LiPF₆ based electrolyte is either unable to reform the SEI, or the SEI that is formed is not robust enough to control the dendritic growth of the lithium. Next, SEI composition is studied.

4.5 Electrode Surface Studies

XPS measurements were taken on electrodes from anode-free cells after one C/5 charge C/2 discharge cycle (3.6 V – 4.5 V) at 40°C and ~75 kPa stack pressure.

Figure 4-14 shows boron and phosphorous XPS data for anodes (a-b) and cathodes (c-d) from anode-free cells formed with different electrolytes: 1M LiPF₆ (black), 1M LiDFOB (green), and 0.6M LiDFOB 0.6M LiBF₄ (blue). All electrolytes use FEC:DEC (1:2 vol) solvent. No background was subtracted. Spectra are offset vertically for clarity. The phosphorous region (a and c) shows that LiPF₆ reacts at the surface of both electrodes. As expected, no phosphorous is seen for cells without LiPF₆. The boron region (b and d) shows that LiDFOB/LiBF₄ react at the surface of both electrodes. Passivation of the Li_{1.2}Ni_{0.15}Mn_{0.55}Co_{0.1}O₂ cathode and graphite anode by LiDFOB was previously reported by Zhu *et al.*⁵⁶

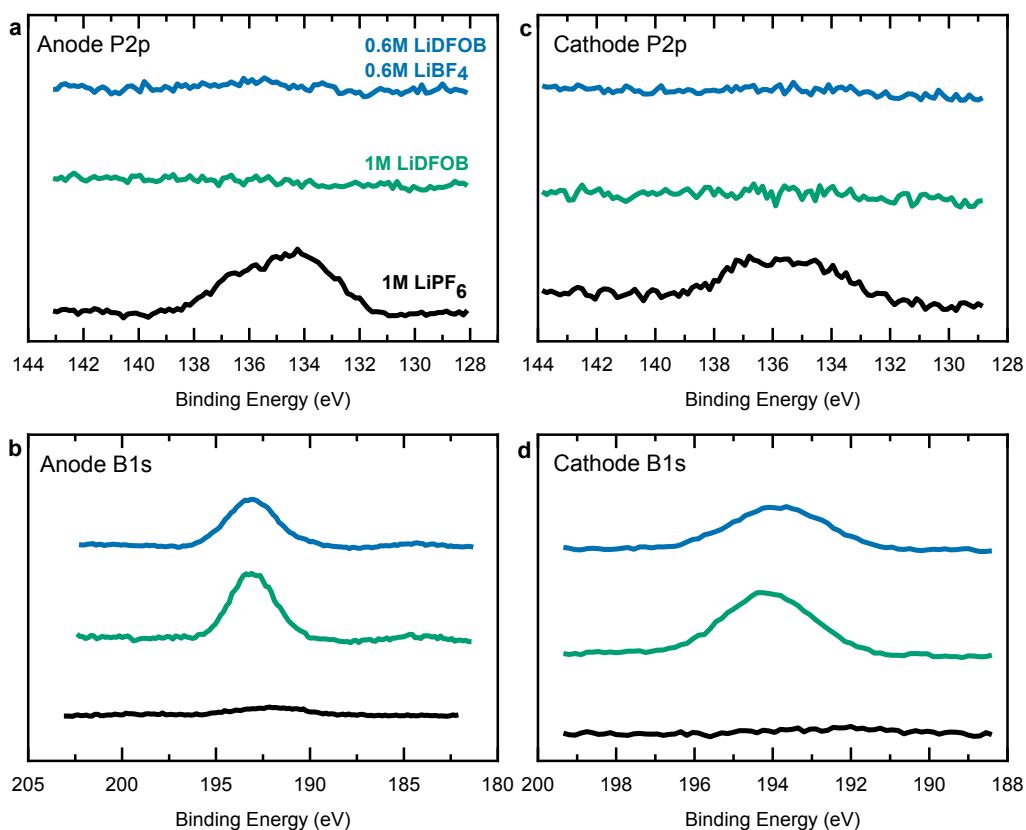


Figure 4-14. Boron and phosphorous XPS data. (a-b) Anode spectra and (c-d) cathode spectra for anode-free cells formed with different electrolytes: 1M LiPF₆ (black), 1M LiDFOB (green), and 0.6M LiDFOB 0.6M LiBF₄ (blue). Cells formed at 40°C, C/5 charge to 4.5V, C/10 discharge to 3.0 V, ~75 kPa

Figure 4-15 shows XPS spectra of the lithium electrode from anode-free pouch cells with three different electrolytes. Each spectrum corresponds to an electrode formed in a different electrolyte: 1M LiPF₆ (black), 1M LiDFOB (blue), and 0.6M LiDFOB + 0.6M LiBF₄ (green). All electrolytes use FEC:DEC (volume ratio 1:2) solvent mix. Sampling depth by this technique is 2–5 nm. In each region spectra are normalized to the highest intensity and a Shirley-type background was subtracted. Spectra are offset vertically for

clarity. Assignments of components by binding energy are from the NIST XPS database as well as other research papers.^{56,90,145}

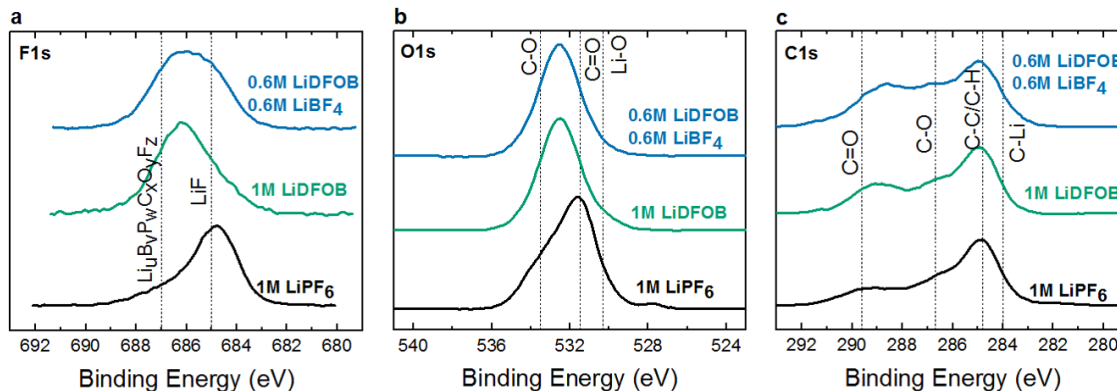


Figure 4-15. XPS spectra for lithium electrodes. (a) F 1s, (b) O 1s, and (c) C 1s. Lithium electrodes were from cells after formation with different lithium salts: 1 M LiPF₆ (black), 1 M LiDFOB (green) and 0.6 M LiDFOB + 0.6 M LiBF₄ (blue). All electrolytes use an FEC:DEC (1:2 vol.) solvent mix. Dashed lines show approximate binding energies of different SEI components. Cells formed at 40°C, C/5 charge to 4.5V, C/10 discharge to 3.0 V, ~75 kPa.

The fluorine 1s spectra in Figure 4-15a contain one component at 685 eV assigned to lithium fluoride (LiF) and a second component at higher binding energy that is broadly assigned to organic oxygen, carbon, boron, and fluorine-containing components which may be similar to the LiDFOB decomposition products proposed by Schedlbauer *et al.*¹⁴¹ The SEI formed with LiDFOB (green) has a higher ratio of organic fluorine components relative to LiF, whereas the SEI formed with LiPF₆ has more LiF relative to organic components. The increased organic component may contribute to the cycling efficiency in the single-salt LiDFOB cells. The SEI formed in the dual-salt LiDFOB + LiBF₄ electrolyte has a large contribution from both organic fluorine components and LiF. Other researchers speculated that large amounts of LiF in the SEI are favorable for good lithium plating.³⁴ Note that only information about relative composition of the SEI is known from this data, not the absolute amount of LiF present. It is possible there is less

total LiF for the LiPF₆ electrolyte since this salt was not seen to be consumed to the same extent as LiDFOB and LiBF₄. Here the cells with the best capacity retention have an SEI composed of both organic components and LiF. Oxygen 1s and carbon 1s spectra are shown in Figure 4-15b and Figure 4-15c, respectively, to further highlight the different organic SEI components formed in the three electrolytes.

Figure 4-16 shows cathode XPS spectra for anode-free cells formed with different electrolytes: 1M LiPF₆ (black), 1M LiDFOB (green), and 0.6M LiDFOB 0.6M LiBF₄ (blue). All electrolytes use FEC:DEC (1:2 vol) solvent. Components are indicated with dashed lines and assignments are made based on the NIST XPS database and various XPS resources from the literature.^{145–147} Spectra are offset vertically for clarity and a Shirley type background was subtracted from each one. In the fluorine region (Figure 4-16a), the positive electrode binder polyvinylidene fluoride (PVDF) is assigned to the component around 688 eV.¹⁴⁷ Each spectrum is normalized to the intensity of the PVDF component which should be the same for each cell. For cells with 1M LiDFOB

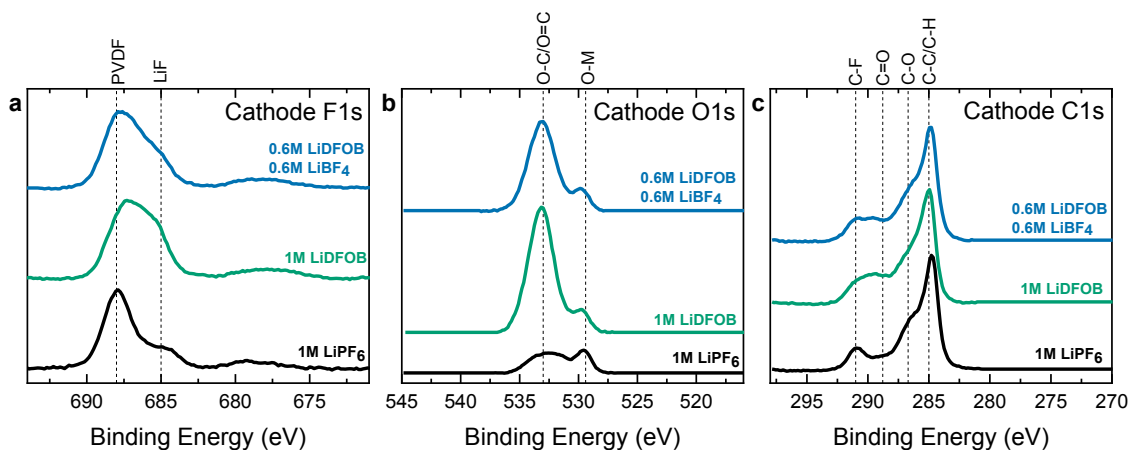


Figure 4-16. XPS spectra for cathodes. (a) F 1s, (b) O 1s, and (c) C 1s. Cathodes were from anode-free cells after formation with different lithium salts: 1M LiPF₆ (black), 1M LiDFOB (green), and 0.6M LiDFOB 0.6M LiBF₄ (blue). Cells formed at 40°C, C/5 charge to 4.5V, C/10 discharge to 3.0 V, ~75 kPa.

(green) or 0.6M LiDFOB 0.6M LiBF₄ (blue), the signal for LiF is stronger relative to PVDF than cells with 1M LiPF₆ (black). LiDFOB and LiBF₄ may be more prone to react at the cathode surface and form LiF, which matches the trend seen by NMR in Figure 4-11 that LiDFOB and LiBF₄ are consumed significantly during cycling but LiPF₆ is not. In the oxygen region (Figure 4-16b), the component “O-M” around 529 eV is assigned to metallic oxide in the lattice of the cathode material. Each spectrum is normalized to the height of this component which highlights the higher relative contribution from O-C/O=C components in cells formed with LiDFOB and LiBF₄. This trend also indicates that LiDFOB and LiBF₄ may be more prone to react at the cathode surface. Positive electrode passivation by LiDFOB was previously reported by Zhu *et al.*¹⁴⁸ The carbon region is shown (Figure 4-16c) with intensity normalized to the C-C/C-H component for each spectra. As seen in the F1s and O1s spectra, the components for cells with LiDFOB and LiBF₄ are different than for the cell with LiPF₆. The spectrum for the positive electrode formed with only 1M LiDFOB is similar to the spectrum for the positive electrode formed with 0.6M LiDFOB 0.6M LiBF₄.

4.6 Gas Generation

Figure 4-17 shows *in-situ* volume data for anode-free pouch cells. *In-situ* volume measurements were made using the apparatus developed by Aiken *et al.*¹⁴⁹ These measurements were performed in a temperature box at 40°C with minimal uniaxial pressure of (< 75 kPa) applied to the pouch cells with a constraining clip. The data in (a) show that adding LiBF₄ limits gas production and that the dual salt electrolyte operated to 4.3 V shows very little gassing.

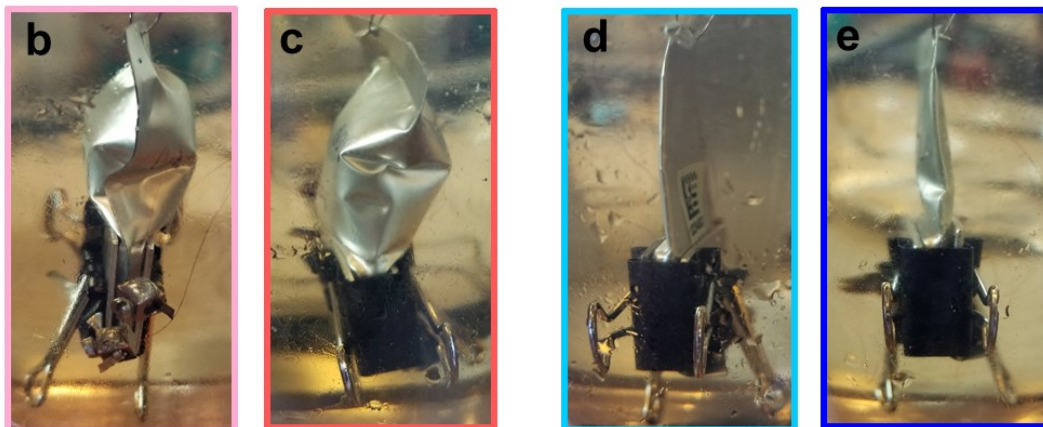
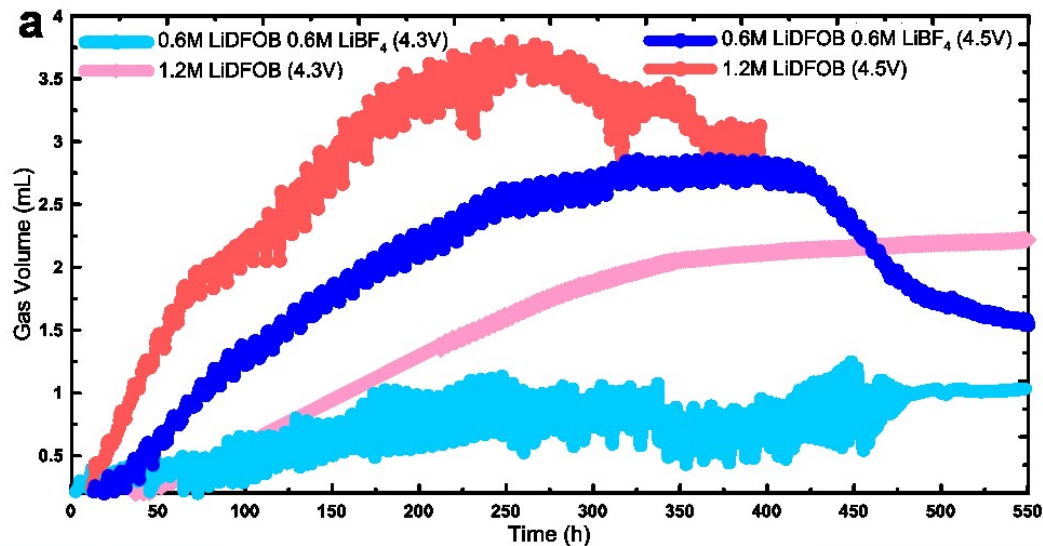


Figure 4-17. (a) *In-situ* volume data collected from Cu//NMC 532 anode-free pouch cells with single salt (1.2M LiDFOB) or dual salt (0.6M LiDFOB 0.6M LiBF₄) electrolytes charged between 3.6-4.3 V or 3.6-4.5 V. Images of pouch cells after 550 hours of cycling for 1.2M LiDFOB charged between (b) 3.6-4.3 V and (c) 3.6-4.5 V as well as 0.6M LiDFOB 0.6M LiBF₄ charged between (d) 3.6-4.3 V and (e) 3.6-4.5 V. Figure and gas measurements from Matt Genovese.

Cell that start with LiDFOB electrolyte were shown to have improved capacity retention at higher voltage (Figure 4-2). The problem with this performance improvement is that the poor oxidative stability of LiDFOB causes it to produce a lot of gas when cycled above 4.3 V (Figure 4-17).⁵⁶ It is also impractical to require a cell be consistently cycled to the top of charge to maintain good performance. Although the capacity retention for the dual salt LiDFOB/LiBF₄ blend is similar to 1.2M LiDFOB when cycled to 4.5V, the

dual salt LiDFOB/LiBF₄ blend has the added benefit that it maintains good cycling stability across varying upper cutoff voltage range (Figure 4-1d). The dual-salt blend also produces less gas, especially when charged only to 4.3 V (Figure 4-17). Since gassing is reduced for the LiDFOB/LiBF₄ blend, cells with 1M LiDFOB and 0.2M LiBF₄ were able to undergo 100 charge-discharge cycles. This was difficult for higher concentration cells with only LiDFOB due to the large amount of gas produced. Cells were almost rupturing and could not stay in the test fixture. Figure 4-17 shows that gas is generated in the beginning of cell life (< 300 hours), but is consumed later in cell life. The gas that is created from LiDFOB was identified to be CO₂,^{90,150,151} which is known to be consumed by lithium metal to form lithium carbonate.¹⁵²

4.7 Conclusions

Anode-free pouch cells with zero excess lithium were tested with FEC:DEC based liquid electrolytes using different lithium salts: LiPF₆, LiBF₄, and LiDFOB. Cells with a dual-salt LiDFOB+LiBF₄ electrolyte had the best performance of all the electrolytes tested—80% of the original capacity was retained for 90 cycles which is impressive cycle life for cells with no excess lithium. All previous reports of anode-free cells with liquid electrolytes fall below 80% capacity retention by 40 cycles or fewer.^{153–156} SEM images of the lithium show smooth lithium made up of large densely packed domains up to 50 μm in diameter, which are desirable to prevent the formation of isolated metallic lithium and to reduce the lithium reaction rate with electrolyte by minimizing surface area. This highly desirable lithium morphology in the dual-salt electrolyte may be influenced by the type of SEI formed compared to other electrolytes. XPS was used to show a dramatically different composition of the anode SEI formed in LiPF₆ and LiDFOB + LiBF₄ based

electrolytes. Cycle life in the dual-salt electrolyte is limited due to the continuous consumption of LiDFOB and LiBF₄ during cycling, which was observed by NMR analysis of the electrolyte. SEM images also show that with continuous cycling the good initial lithium morphology is destroyed.

In addition to SEI composition, other researchers have shown that properties like electrolyte diffusion can have a big effect on lithium morphology.¹⁵⁷ The transport properties of electrolytes used in this work have not yet been explored.

In the next chapter strategies to overcome this salt consumption are explored to achieve further gains in lifetime, such as increasing electrolyte content and molarity, and pairing salts that are consumed with those that are not. In addition, cycling temperature and formation procedures are changed to mitigate the capacity loss mechanisms seen here.

CHAPTER 5 FURTHER STUDIES IN ANODE-FREE CELLS

The results of Chapter 4 inspired electrolyte developments and new formation procedures for anode-free cells. These results include substantial contributions from Matt Genovese and Alex Louli and were published in the referenced paper.¹⁵⁰

5.1 New Electrolyte Blends

Cells were tested with increased salt content to delay the effects of salt loss in cells with LiDFOB/LiBF₄ based electrolytes. Figure 5-1 shows normalized discharge capacity vs cycle for cells with increased LiDFOB content either by increasing electrolyte volume (red) or salt concentration (pink). NMR results in Figure 4-11 show that cell failure by “rollover”—the rapid capacity loss beginning around cycle 70 for the cell with 0.5 mL of

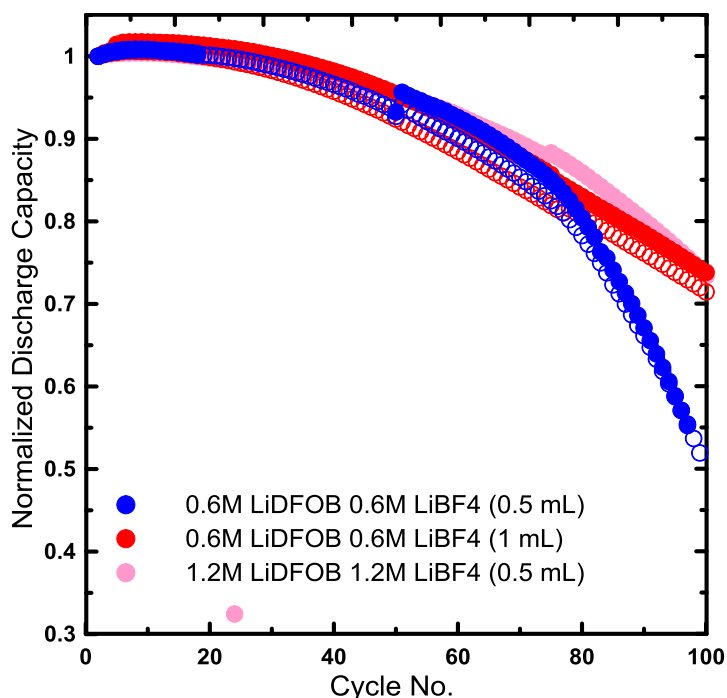


Figure 5-1. Normalized discharge capacity vs cycle for cells with increased LiDFOB content either by increasing electrolyte volume (red) or salt concentration (pink). Pair cells are shown as symbols of the same color. Cycled at 40°C, 3.6 – 4.5V, C/5 charge, C/2 discharge, ~75 kPa.

0.6M LiDFOB + 0.6M LiBF₄ electrolyte (blue) is caused by LiDFOB depletion. Rollover is delayed by increasing LiDFOB in cells, either by increasing the electrolyte concentration to 1.2M or increasing the total electrolyte volume to 1 mL. In both cases the LiDFOB content is doubled and the benefit to capacity retention is similar.

Figure 5-2 shows that adding LiPF₆ to LiDFOB electrolyte (pink) prevents rollover failure. The cells continue to cycle after all the LiDFOB is gone since LiPF₆ is not consumed and is still present in high concentration. It is also interesting to note that after all of the LiDFOB is consumed (expected around cycle 60 for 0.6M LiDFOB) the electrolyte composition should be 0.6M LiPF₆, but the cells retain capacity much better than those that started with only LiPF₆. Starting with LiDFOB in the beginning makes a

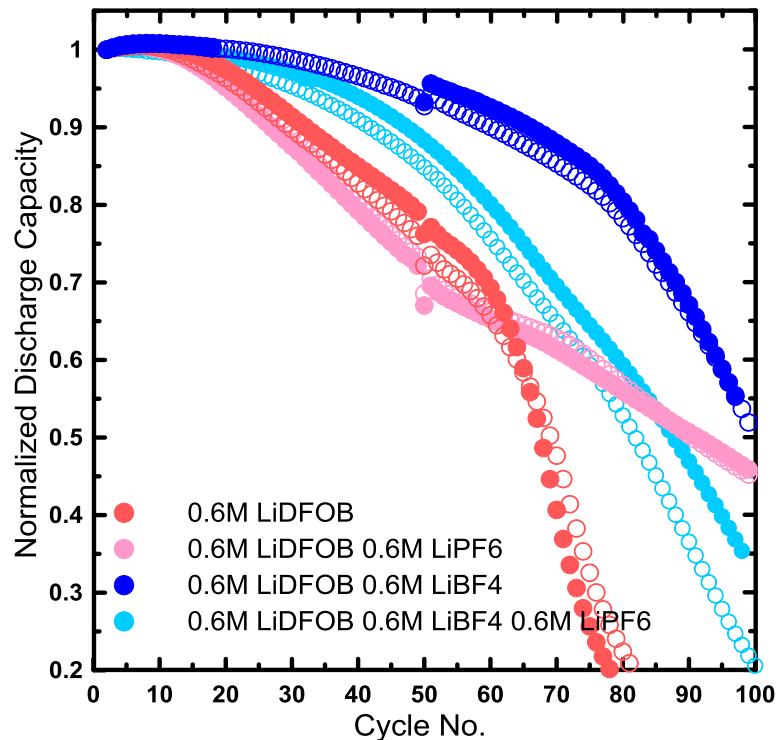


Figure 5-2. Normalized discharge capacity vs cycle for cells with other salt combinations. Pair cells are shown as symbols of the same color. Cycled at 40°C, 3.6 – 4.5V, C/5 charge, C/2 discharge, ~75 kPa.

huge difference even after all of it has been consumed, which may be due to better initial lithium morphology and a difference in SEI composition. Surprisingly, the tri-salt electrolyte with LiDFOB + LiBF₄ + LiPF₆ (light blue) did not perform better than the dual salt LiDFOB + LiBF₄ electrolyte (dark blue). Rollover is not prevented by the addition of LiPF₆, and the capacity retention before rollover is worse.

Figure 5-3 shows electrolyte composition vs cycle number for the two electrolytes shown in Figure 5-2: dual salt 0.5m (0.6M) LiDFOB 0.5m LiPF₆, and tri salt 0.5m LiDFOB 0.5m LiPF₆ 0.5m LiBF₄. Both electrolytes use FEC:DEC (1:2 wt) solvent. Figure 5-3a,c show salt concentration vs cycle number and Figure 5-3b,d show solvent fraction for the

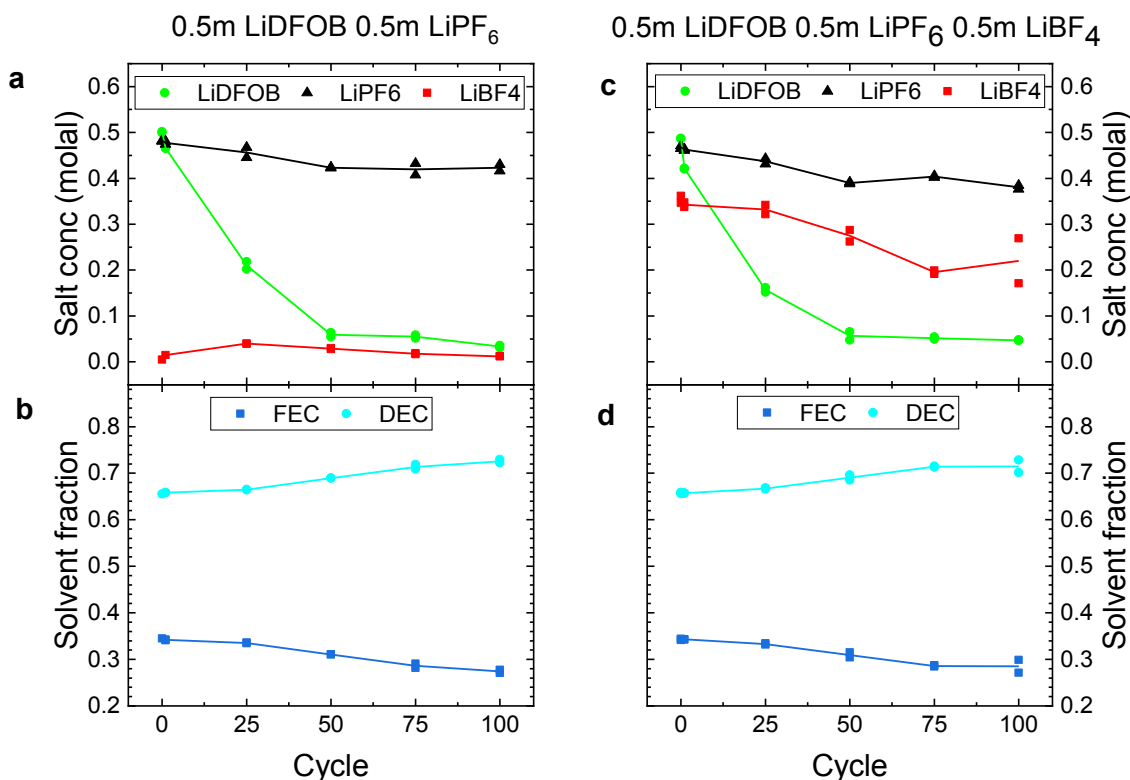


Figure 5-3. Electrolyte composition vs cycle number for two electrolytes (a,b) 0.5m LiDFOB 0.5m LiPF₆ and (c,d) 0.5m LiDFOB 0.5m LiPF₆ 0.5m LiBF₄. Both electrolytes use FEC:DEC (1:2 wt%) solvent. Data points are shown for each measurement with the average plotted as a line. Cycled at 40°C, 3.6 – 4.5V, C/5 charge, C/2 discharge, ~75 kPa.

same cells. In both electrolyte systems some FEC is consumed throughout cycling, as shown by the FEC solvent fraction which decreases from ~34% to ~28% after 100 cycles. In both electrolyte systems LiDFOB is consumed throughout cycling and is nearly gone after about 50 cycles. For both electrolytes only a small amount of LiPF₆ is consumed (if any) during cycling. For the dual salt 0.5m LiDFOB 0.5m LiPF₆ electrolyte a small amount of LiBF₄ is created while LiDFOB is consumed (Figure 5-3a). The creation of LiBF₄ was previously observed for electrolyte that started with LiDFOB only (Figure 4-11). Like other cells tested with LiDFOB these cells were observed to produce gas during cycling.

Previous data in Figure 4-1 and Figure 4-11 show that cells with single-salt LiDFOB electrolyte fail rapidly once all of the LiDFOB is gone, and Figure 5-2 shows that adding LiPF₆ to LiDFOB based electrolyte prevents the rapid “rollover” failure. Figure 5-3a shows that once all of the LiDFOB is consumed around cycle 50, cells continue to cycle well since LiPF₆ is not significantly consumed and the salt concentration remains high. However, for cells with LiDFOB, LiPF₆, and LiBF₄ in the electrolyte, capacity loss accelerates once all of the LiDFOB is gone despite the high salt concentration from the remaining LiPF₆ (Figure 5-3). Once LiDFOB is consumed LiBF₄ is consumed more rapidly, which may be why capacity retention gets worse. Cells with only LiBF₄ electrolyte previously showed terrible capacity retention (Figure 4-1) and LiBF₄ was shown to react during cycling. LiBF₄ may be reforming the SEI at the lithium metal electrode once the LiDFOB is gone. Although cells with only LiPF₆ electrolyte also had terrible capacity retention, LiPF₆ is not detrimental to performance when paired with

LiDFOB, as shown here. LiPF_6 is not consumed during cycling so it is not reforming the SEI at the lithium metal electrode once the LiDFOB is gone.

5.2 Hot Formation

The results of Chapter 4 show that rollover failure is driven by salt consumption, and since all of the previous testing was done at 40°C , it follows that lower temperature may slow salt consumption and extend lifetime. Figures in this section were provided by Matt Genovese and Alex Louli.

Figure 5-4 shows normalized discharge capacity vs cycle for anode-free cells with 0.6M LiDFOB 0.6M LiBF_4 FEC:DEC (1:2 vol) electrolyte tested at different temperatures.

Cells went directly on test at the temperature indicated without a formation step. Capacity retention clearly gets better with increasing temperature. After 50 cycles, cells tested at

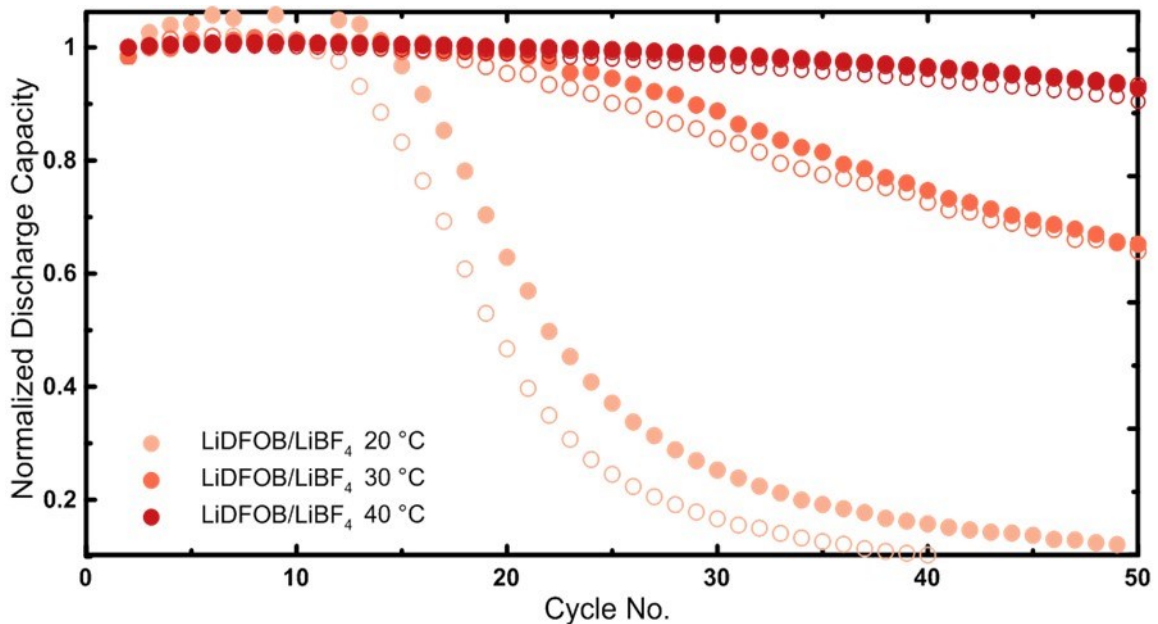


Figure 5-4. Normalized discharge capacity vs cycle for anode-free cells with 0.6M LiDFOB 0.6M LiBF_4 FEC:DEC (1:2 vol) electrolyte tested at different temperatures. Pair cells are shown as symbols of the same color. Cycled from 3.6 – 4.5V, C/5 charge, C/2 discharge, ~ 75 kPa.

40°C maintain >80% capacity, while cells at 30°C fall below 80% after about 30 cycles, and at 20°C cells drop below 80% and lose capacity quickly after about 15 cycles.

Although salt consumption may increase at higher temperature, compressive and tensile stress-strain measurements show that lithium metal is more malleable at higher temperature.^{2,3} The improved malleability leads to larger, less dendritic lithium domains which can improve capacity retention.⁴

Figure 5-5 shows SEM images of the lithium metal electrode at 4.5 V after two cycles at 20°C (a,b) or 40°C (c,d) for cells with 0.6M LiDFOB 0.6M LiBF₄ FEC:DEC (1:2 vol) electrolyte. As mentioned, the lithium domains are larger at higher temperature due to the

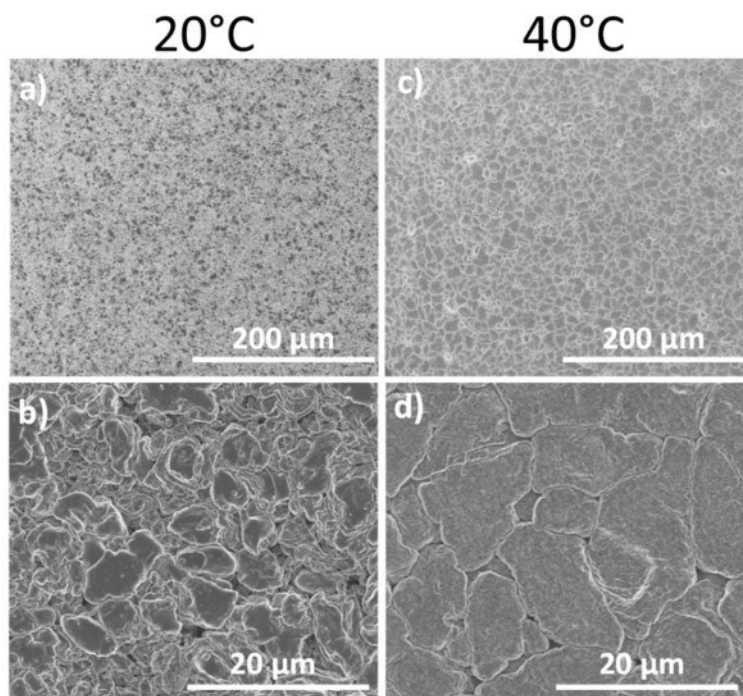


Figure 5-5. SEM images of initial lithium morphology in cells with 0.6M LiDFOB 0.6M LiBF₄ FEC:DEC (1:2 vol) electrolyte tested at 20°C (a,b) or 40°C (c,d). Cells were charged once at C/5 to 4.5V, ~75 kPa.

increased pliability of lithium metal. The robustness of the SEI may also be improved with the electrolyte reactions that occur at higher temperature.

Figure 5-6 shows capacity retention data for cells tested at 20°C or 40°C and high or low pressure. Cells went directly on test at the temperature indicated without a formation step. The performance of 20°C cells at high pressure (light blue) is almost on par with 40°C cells at low pressure (red). Higher pressure can be used to overcome the higher yield strength of lithium metal at lower temperature. In the case of the 40°C cells, capacity retention is improved with higher pressure (dark blue) but not as dramatically as it is at 20°C.

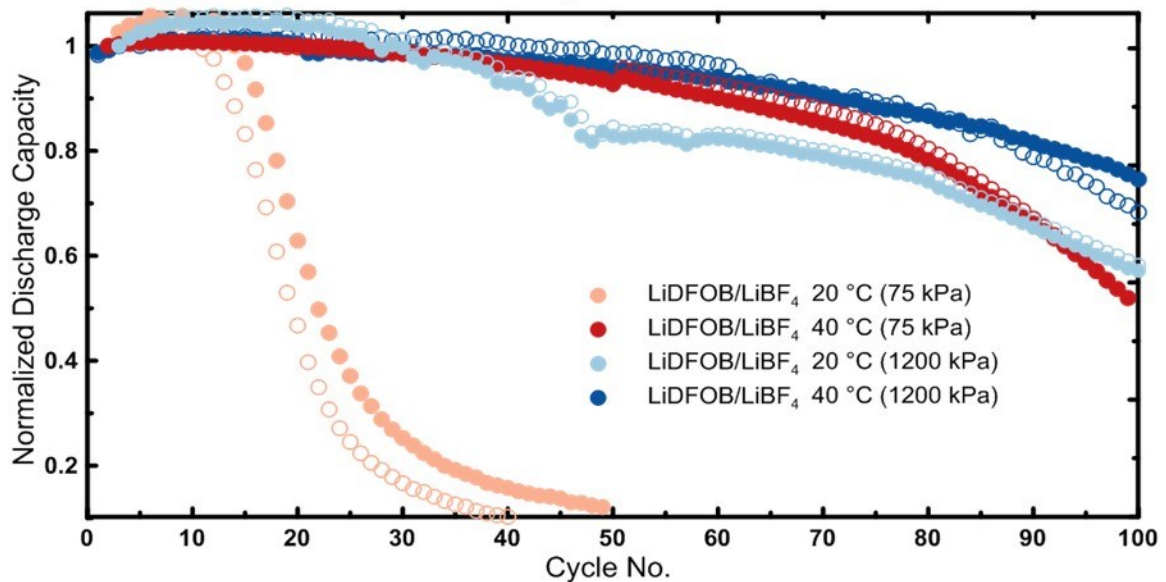


Figure 5-6. Normalized discharge capacity vs cycle for anode-free cells with 0.6M LiDFOB 0.6M LiBF₄ FEC:DEC (1:2 vol) electrolyte tested at different temperatures and pressures. Pair cells are shown as symbols of the same color. Cycled from 3.6 – 4.5V, C/5 charge, C/2 discharge.

Figure 5-7 shows cells tested at 20°C and different pressures, with or without hot (40°C) formation prior to cycle testing. Hot formation cells were charged at C/10 for 2 cycles (discharged at C/2) in a 40°C temperature box then transferred to a 20°C box for cycling.

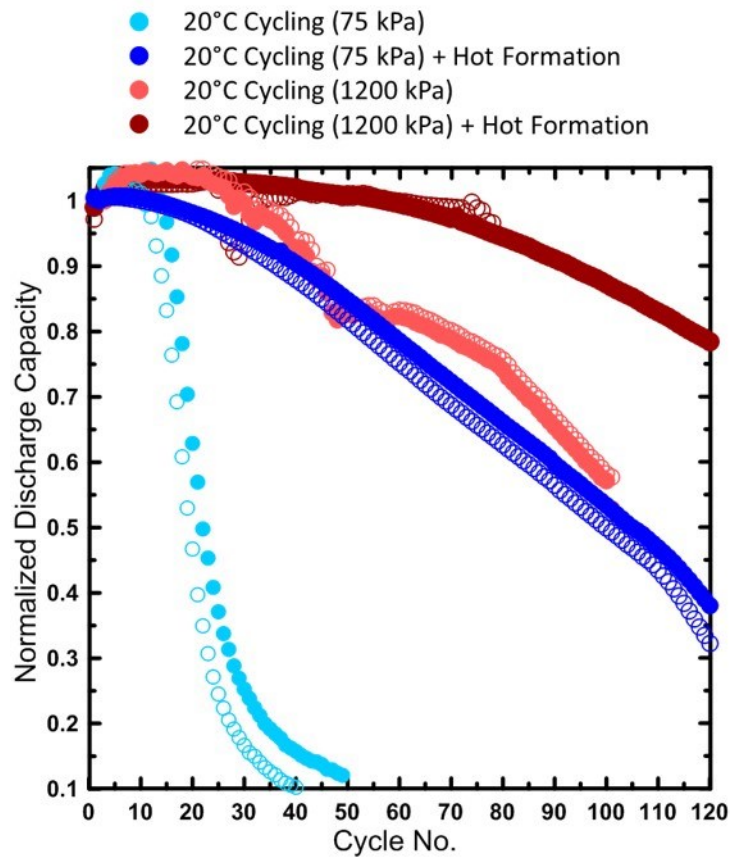


Figure 5-7. Normalized discharge capacity vs cycle for anode-free cells with 0.6M LiDFOB 0.6M LiBF₄ FEC:DEC (1:2 vol) electrolyte tested at 20°C and different pressures, with or without hot (40°C) formation. Cycled from 3.6 – 4.5V, C/5 charge, C/2 discharge.

The two cycles at higher temperature were designed to form better initial lithium morphology, which in turn improves capacity retention. Hot formation has a similar effect as high pressure (compare dark blue and orange data). The combination of hot formation with high pressure gives the best capacity retention overall (red). Figure 5-8. Shows SEM images of lithium morphology after 20 cycles in cells without (a,b) or with (c,d) hot (40°C) formation. Even after 20 cycles, the cells with hot formation maintain larger, less dendritic lithium.

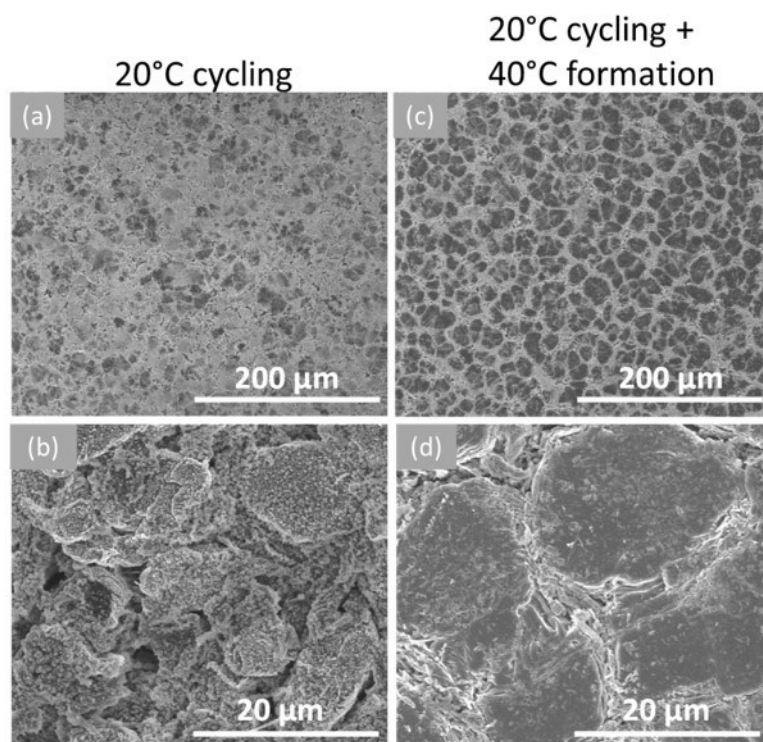


Figure 5-8. SEM images of lithium morphology after 20 cycles in cells with 0.6M LiDFOB 0.6M LiBF₄ FEC:DEC (1:2 vol) electrolyte tested without (a,b) or with (c,d) hot (40°C) formation. Cycled at 20°C from 3.6 – 4.5V, C/5 charge, C/2 discharge, ~75 kPa.

Figure 5-9 shows normalized discharge capacity vs cycle number for cells that were designed to have the best capacity retention possible. These cells (gray) have a high concentration dual salt LiDFOB/LiBF₄ electrolyte, hot formation, and low temperature cycling and make it to ~90 cycles with >80% capacity remaining. When high pressure is also used (blue) the cells are able to undergo 185 cycles with >80% capacity retention. It is important to note that C/5 charge, C/2 discharge are very favorable cycling conditions for lithium metal. Figure 5-10 shows normalized discharge capacity vs cycle for cells tested with either C/2 (black) or C/5 (red) discharge. Capacity retention is clearly worse for the cells with symmetric charge/discharge rates. Huge improvements must be made to develop electrolytes that give good performance under variable cycling conditions.

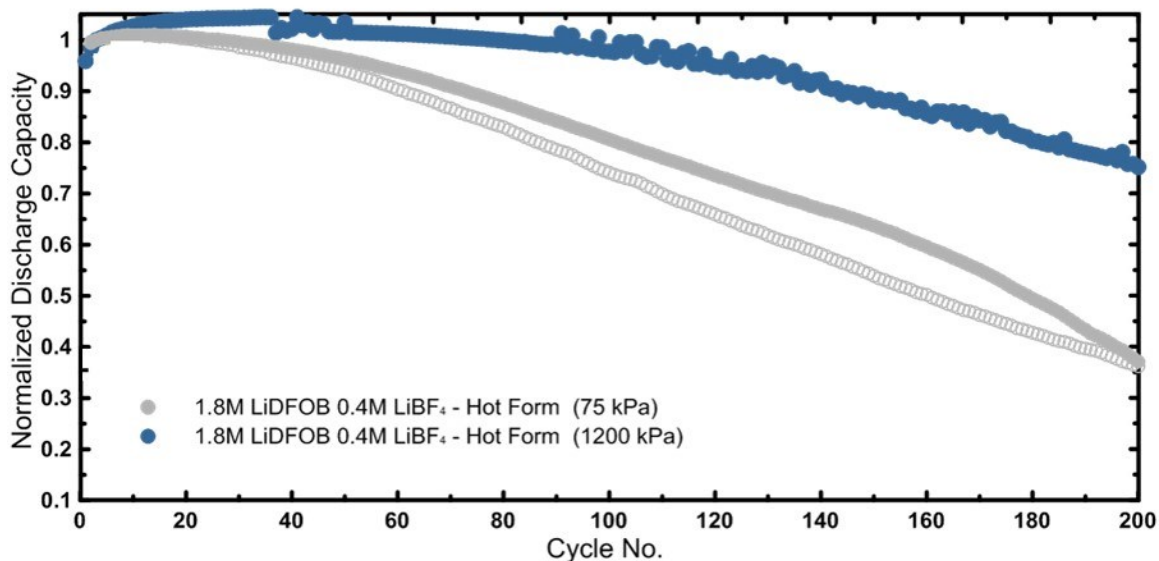


Figure 5-9. Normalized discharge capacity vs cycle for anode-free cells with 1.8M LiDFOB 0.4M LiBF₄ FEC:DEC (1:2 vol) electrolyte tested after hot (40°C) formation. Cycled at 20°C from 3.6 – 4.5V, C/5 charge, C/2 discharge.

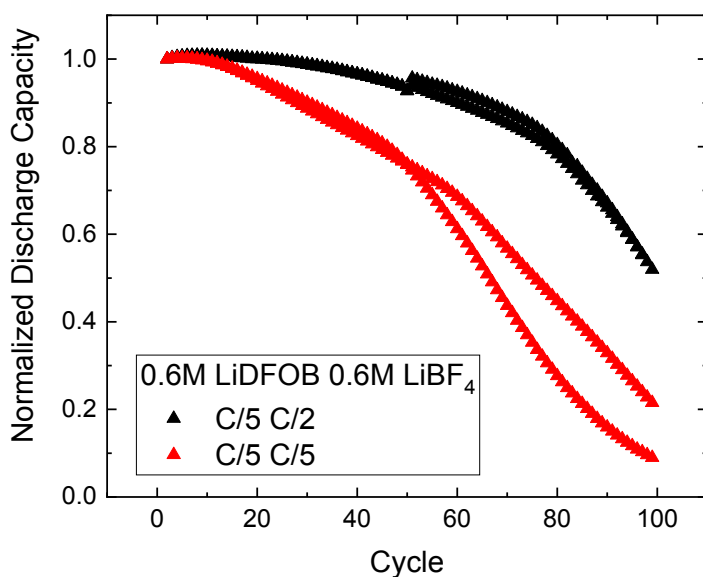


Figure 5-10. Normalized discharge capacity vs cycle for cells tested with either C/2 (black) or C/5 (red) discharge. Cells used 0.6M LiDFOB 0.6M LiBF₄ FEC:DEC (1:2) electrolyte and were cycled at 40°C from 3.6 – 4.5 V, 75 kPa, with C/5 charge. Data from pair cells are shown as matching symbols.

5.3 Conclusions

In the previous chapter, it was shown that LiDFOB and LiDFOB/LiBF₄ electrolyte had good capacity retention likely from the favorable SEI composition. However, cells ultimately failed due to the continuous consumption of both lithium salts. In contrast, fast capacity loss and very dendritic lithium was seen for cells with LiPF₆ and this salt was not consumed. Most of the capacity loss was not due to lithium metal reactions with electrolyte, but rather the formation of large amounts of isolated metallic lithium. In this chapter cell lifetime was improved by increasing electrolyte content and molarity, and pairing salts that are consumed with those that are not.

Although low temperature cycling may delay salt consumption, capacity retention was shown to be worse with decreasing temperature due to the lower malleability of lithium. Capacity retention was improved at low temperature by using a hot formation to create large lithium domains which persisted during low temperature cycling. Throughout this work, capacity retention was improved for anode-free cells from <10 cycles to 80% retention, to 185 cycles with 80% retention.

CHAPTER 6 RESISTANCE GROWTH IN LITHIUM-ION POUCH CELLS WITH $\text{LiNi}_{0.80}\text{Co}_{0.15}\text{Al}_{0.05}\text{O}_2$ POSITIVE ELECTRODES

The future of high energy density lithium batteries depends not only on the anode, but also the cathode. $\text{LiNi}_{1-x-y}\text{Mn}_x\text{Co}_y\text{O}_2$ (NMC) and $\text{LiNi}_{1-x-y}\text{Co}_x\text{Al}_y\text{O}_2$ (NCA) cathode materials are commonly used in commercial lithium-ion cells.¹⁵⁸ For both material types, higher nickel content increases specific capacity.^{13,37,159,160} Anode-free development work was done using a well characterized NMC532 cathode, but recall from Table 1-1 that other cathode materials can give equivalent or higher energy density. In particular, NCA could be used to build the highest energy density anode-free cells. In this chapter the degradation mechanism of $\text{Ni}_{0.80}\text{Co}_{0.15}\text{Al}_{0.05}\text{O}_2$ (NCA) are studied in traditional lithium-ion pouch cells.

6.1 Resistance Growth During Cycling

High nickel content positive electrode materials, like $\text{LiNi}_{0.80}\text{Co}_{0.15}\text{Al}_{0.05}\text{O}_2$ (NCA), have been observed to lose capacity due to impedance growth when cycled above 4.1 V vs. Li/Li^+ .¹⁶¹⁻¹⁶⁴ In this work pouch cells were tested with NCA positive electrodes and graphite, graphite-SiO, or graphite-SiC negative electrodes. SiO refers to Si in an SiO_2 matrix, and SiC refers to Si in a carbon matrix. In each case the pouch cells show high resistance at high voltage for every cycle, and resistance growth during cycling that is in part responsible for capacity loss.

Figure 6-1a shows the discharge capacity versus cycle number for each cell type, normalized to the first C/3 discharge cycles. Two cells of each type are shown as the

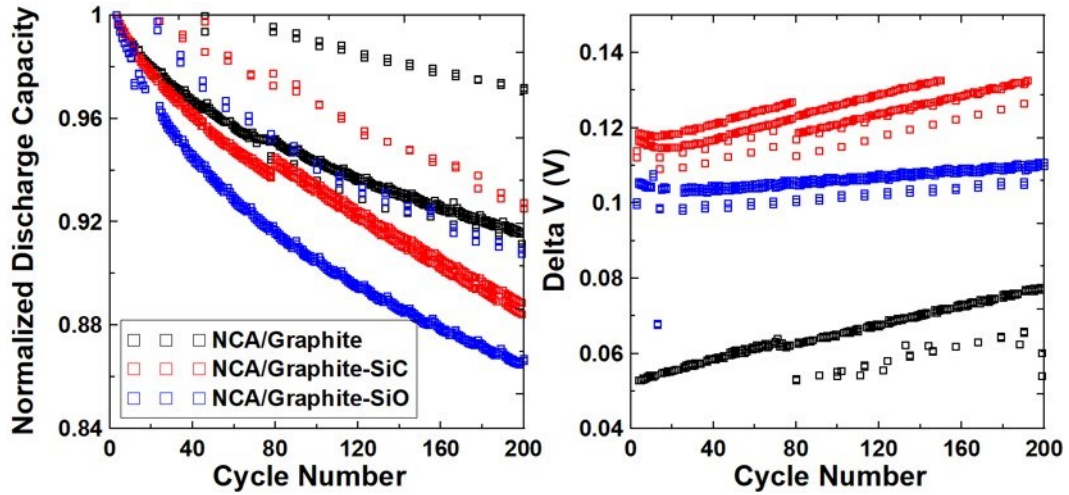


Figure 6-1. (a) Normalized discharge capacity and (b) ΔV between charge/discharge for each cell type, measured over 200 cycles. Two cells of each type are shown using the same symbols, with data overlapping. Cells were cycled at C/3 and 40°C from 3.0 – 4.2V with every 10th cycle at C/20 to measure EIS. The data points above the capacity trend and below the ΔV trend are from the C/20 cycles.

same symbols with the matching pair cell data overlapping. Cells were cycled at C/3 and 40°C from 3.0 – 4.2V with every 10th cycle at C/20 to measure EIS. During testing pouch cells were housed in 40 ± 0.1 °C temperature controlled boxes connected to a Neware cyclers (Shenzhen, China) and a computer with a Gamry (Warminster, PA, USA) frequency response analyzer card (FRA) for EIS measurements. Cell connections were automatically switched between the cycling and EIS system as described in previous work.¹²⁴ During testing, cells were charged and discharged from 3.0 V to 4.2 V at a rate of C/3 for 10 cycles, then charged and discharged in the same voltage range at a rate of C/20 for one cycle, with a pause every 0.1 V to measure EIS. EIS was performed with a 10 mV excitation and measured between 100 kHz and 40 mHz. The sequence of C/3 and C/20 cycles with EIS measurements was repeated for the duration of the test. The data points that fall above the capacity trend in Figure 6-1 are from the slower C/20 cycles used to measure EIS. The data shown in red circles has a break near 80 cycles where the

test was paused to repair the temperature controlled oven. EIS data is presented later in the chapter after experiments that are necessary to guide the interpretation of the EIS data.

Figure 6-1b shows ΔV for each cell type, which is the difference in average charge and average discharge voltages. The data points that fall below the ΔV trend are from the slower C/20 cycles used to measure EIS. Since ΔV increases during cycling for all three cell types, cell internal resistance growth is partly responsible for capacity loss.

NCA/graphite cells (black squares) show the highest ΔV growth but the lowest capacity loss. The two cell types with silicon-containing negative electrodes (red circles and blue triangles) may lose more capacity as a result of accelerated reaction with the electrolyte, since the electrolyte (1.2 M LiPF₆ in EC:EMC:DMC 25:5:70 volume ratio + 2% wt. VC) was not chosen to passivate the silicon well.^{19,165,166}

Figure 6-2 shows Bode plots of the electrode and full cell impedance of the NCA/Graphite-SiC pouch cells before and after the cycling shown in Figure 1. Electrode impedance was measured using symmetric cells, and full cell impedance was measured from reconstructed full cell coin cells. Electrodes for symmetric cells were harvested from full cells at 3.8 V. All spectra were measured at 10°C. The sum of the electrode impedances is shown as a dashed line, and it matches well with the reconstructed full cell impedance. (Note: As explained by Petibon *et al.*,¹²⁶ the individual electrode impedance is half the impedance of the corresponding symmetric cell, which contains two electrodes.) For the NCA/Graphite-SiC pouch cells, the impedance of the positive electrode increases in the 0.1 Hz to 10 Hz range after cycling, which corresponds to an

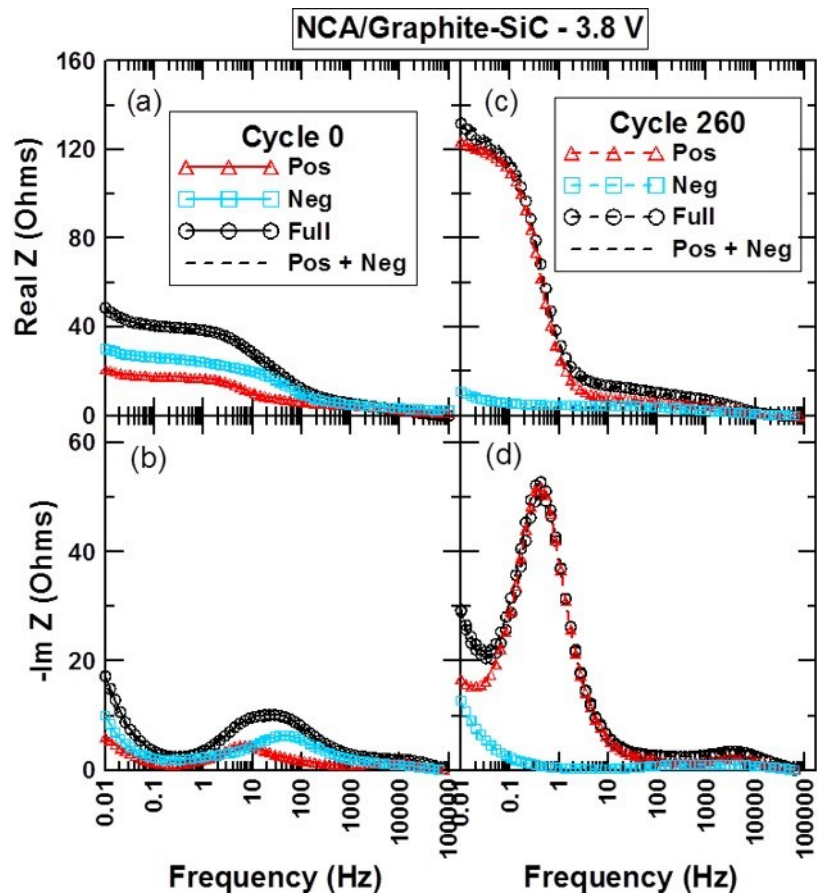


Figure 6-2. The electrode and full cell impedance for the NCA/graphite-SiC cells at 10°C, before and after cycling. For ease of comparison spectra are shifted to Real Z = 0 at the frequency where $-\text{Im } Z = 0$. Cells were cycled at C/3 and 40°C from 3.0 – 4.2V with every 10th cycle at C/20 to measure full cell EIS. Electrode impedance was measured with symmetric cells after 0 cycles (a,b) and 200 cycles (c,d).

increase in the charge transfer resistance.^{119–123,167} However, the region at higher frequency corresponding to positive electrode contact resistance does not increase during cycling.^{119–123,167} These assignments are supported by the referenced literature and by experiments shown later in this chapter. In the frequency range 0.1 Hz to 10 Hz the impedance of the negative electrode decreases after cycling likely because the surface

area of the silicon containing electrode increases during use. The positive electrode is clearly responsible for resistance growth in these cells.

Figure 6-3 shows the impedance spectra from NCA positive electrodes measured in symmetric cells, both before and after formation. The spectra support the assignment of the high frequency and middle frequency semicircles to the contact resistance and charge transfer resistance, respectively.^{119–123,167} Before formation, no contribution from an SEI is seen, and since the positive electrode is at 100% Li content, charge transfer associated with lithium intercalation is blocked. Consequently, the semicircle feature before formation is attributed to the contact resistance and capacitance of the electrode at the foil interface. To measure impedance after formation, a pouch cell was formed following the procedure in the experimental section and then was discharged to 3.0 V before disassembly. The positive electrode is no longer fully lithiated so charge transfer can occur. After formation, an additional semicircle appears at lower frequency which is

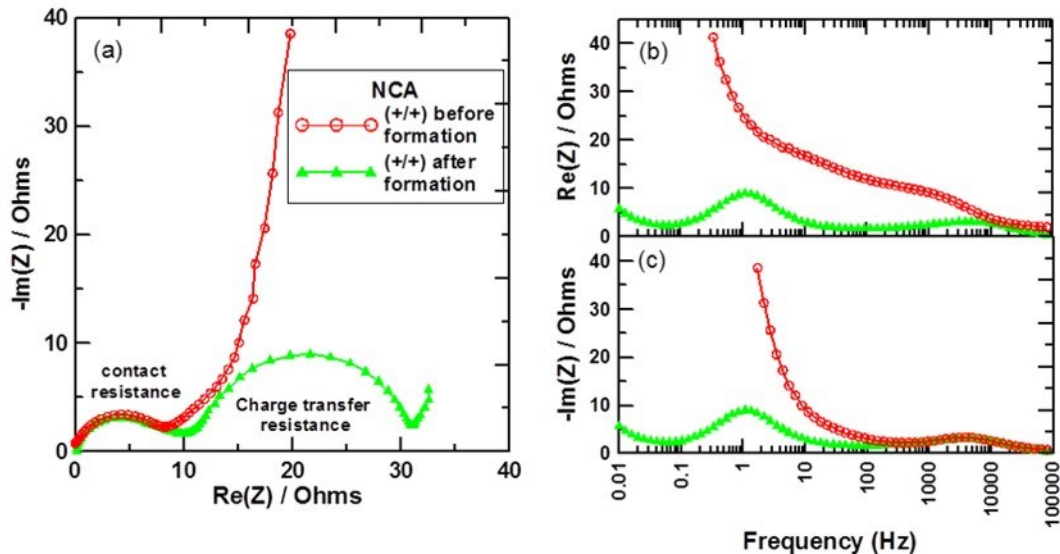


Figure 6-3. (a) Nyquist and (b-c) Bode plots of impedance for the NCA positive electrode, measured using symmetric cells at 10°C, before (electrodes are “blocking” electrodes) and after (electrodes can support lithium intercalation and associated charge transfer) cell formation. For ease of comparison spectra are shifted to Real Z = 0 at the frequency where $-\text{Im} Z = 0$.

assigned to the charge transfer resistance across the newly formed SEI. These results confirm that the increasing cell resistance shown in Figure 6-1 and Figure 6-2 comes from the positive electrode charge-transfer resistance.

Charge-transfer resistance includes the resistance associated with lithium-ion desolvation at the electrolyte/SEI interface, as well as the resistance from lithium-ion migration through the SEI.¹⁶⁸ Since the impedance of a cycled positive electrode is still high for symmetric cells built with fresh electrolyte (Figure 6-2c-d), we know that the charge transfer resistance is not increasing because of a change in the solvation process for the aged electrolyte. The resistance of ion migration through the SEI must consequently be increasing, which can happen in a few ways: (i) the active surface area of the electrode decreases, (ii) the composition of the SEI is changed, so that it is more resistant to ion migration, or (iii) the SEI thickens. It is unlikely that the active surface area decreased, since it has been observed that particle crack and surface area increases for high-nickel content positive electrode materials.^{17,109,162,163,169–172}

Figure 6-4 (adapted from references) shows SEM images of NCA and NMC particles in the pristine state, and then after testing under various high-voltage conditions.^{17,171,172}

Particles start as dense, compact spheres but show cracking between primary particles after cycling. Particles in (a) and (b) were charged once at C/3 to 4.5 V. Particles in (c) were cycled 100 times at C/10 from 2.7 V to 4.7 V. Particles in (d) were cycled 100 times at C/3 from 3.0 V to 4.3 V.

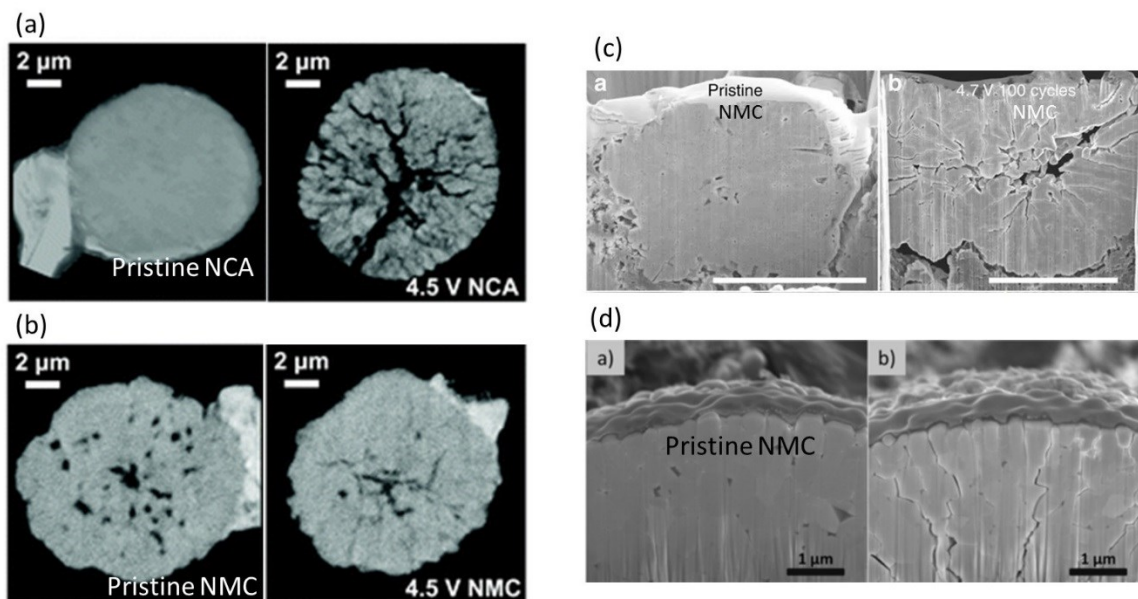


Figure 6-4. Cracks observed after use for (a) NCA¹⁷⁰ and (b-d) NMC^{17,170,171}, with images of pristine material for comparison. Particles in (a) and (b) were charged once at C/3 to 4.5 V. Particles in (c) were cycled 100 times at C/10 from 2.7 V to 4.7 V. Particles in (d) were cycled 100 times at C/3 from 3.0 V to 4.3 V. Figures adapted from references.^{17,170,171} (a-b) originally published by The Royal Society of Chemistry.

Figure 6-5 reproduced from Watanabe *et al.*¹⁶² shows TEM images of LiNi_{0.76}Co_{0.14}Al_{0.10}O₂ (NCA) cathode particles. Figure 6-5a shows an NCA particle before cycling made up of densely packed primary particles in a secondary particle agglomeration. Figure 6-5b shows an NCA particle after 350 cycles at 1C and 60°C from 2.5 V – 4.2 V where the primary particles have separated from each other, exposing new surfaces to the electrolyte. The selected area electron diffraction (SAED) patterns in Figure 6-5f (fresh NCA) and g (bulk NCA after cycling) show typical R-3m crystal structure expected for NCA material, while the SAED in Figure 6-5h (surface of NCA after cycling) shows Fm3m crystal structure from a NiO rock-salt layer that has formed. Many experiments have confirmed resistance increase caused by a thickening rock-salt layer on the surface of high nickel NCA and NMC cathode materials during cycling.^{173–177} As the particles

crack, new surfaces are exposed and more NiO is formed. Researchers have used several methods including positive electrode coatings and electrolyte additives to mitigate the growth of the rock salt layer and its associated resistance increase.^{124,178}

The cross-talk between the positive and negative electrode also influences the resistance growth. Rodrigues *et al.*¹²⁰ observed a huge difference in impedance growth when the same positive electrode was paired with two different negative electrodes (graphite or lithium-titanate), which led them to theorize that the cross-talk between the two electrodes plays an important role in preventing impedance growth.²⁸ Researchers have seen gas release from the positive electrode at high voltage,^{11,179} as well as gas consumption at the negative electrode.¹⁸⁰ Non-gaseous electrolyte oxidation products are

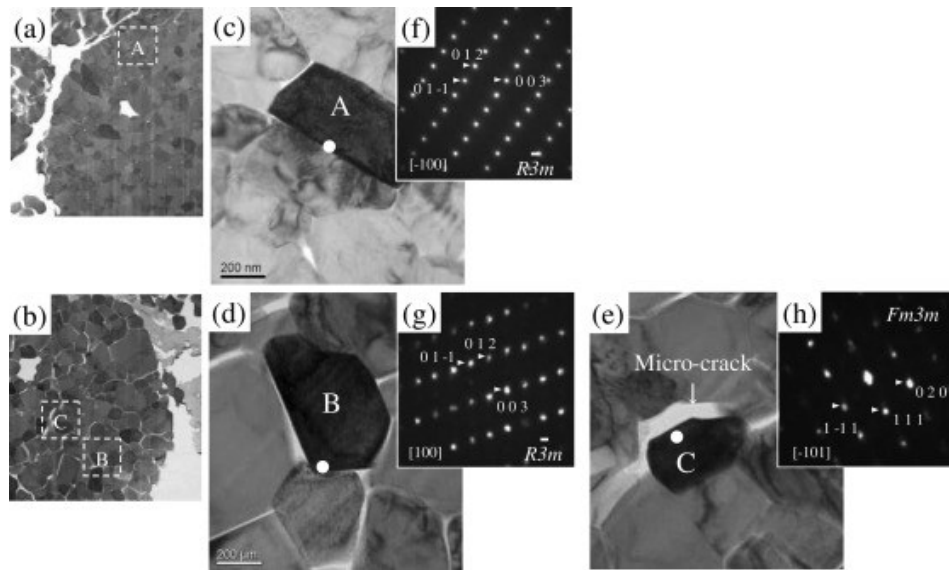


Figure 6-5. Cross-sectional TEM images of NCA particles (a, b), their magnifications (c–e) and corresponding SAED patterns (f–h) of NCA cathodes before (a, c, f) and after (b, d, e, g, h) after 350 cycles at 1C and 60°C from 2.5 V – 4.2 V. SAED patterns (f, g) were obtained from edge (A and B) of a primary particle faced on the neighbor particle, while SAED pattern (h) was obtained from that (C) faced on micro-crack. Figure and caption reproduced from reference with permission (see Appendix A).¹⁶¹

also known to migrate from the positive electrode and deposit onto the negative electrode.^{181,182} In positive electrode symmetric cells and positive electrode pouch bags, the impedance grows much more than for the same positive electrode material in a full cell,^{126,180} which indicates that the negative electrode can consume the gases and electrolyte oxidation products from the cathode that may normally increase charge transfer resistance through a reaction to form a rock-salt layer.¹⁷³⁻¹⁷⁷ Restricting cell cycling to the low voltage range can then suppresses impedance growth by avoiding the oxygen release and rock-salt formation which happens at high voltage. This is tested next. Figure 6-6 shows both the normalized discharge capacity and ΔV growth for NCA/Graphite cells cycled in different voltage ranges. Cells were cycled at C/3 and 40°C with every 10th cycle at C/20 to measure EIS. Limiting the charge voltage to 3.8 V hinders resistance growth in these cells. Figure 6-7 shows resistance vs voltage at various cycle numbers for the three voltage ranges tested in Figure 6-6. “Resistance” is the diameter of the semicircles in the Nyquist plot of impedance, which includes contact resistance and charge transfer resistance for both electrodes. Figure 6-8a indicates “resistance” on a Nyquist plot. The resistance at low voltage is reversible (Figure 6-7b), but when the cells are cycled in the high voltage region irreversible resistance growth happens across all voltages (Figure 6-7a,c). These results further suggest that the positive electrode gassing and electrolyte oxidation products formed at high voltages are related to increasing positive electrode charge transfer resistance, potentially by thickening or altering the rock-salt surface layer. Restricting cell cycling to the low voltage range < 3.8

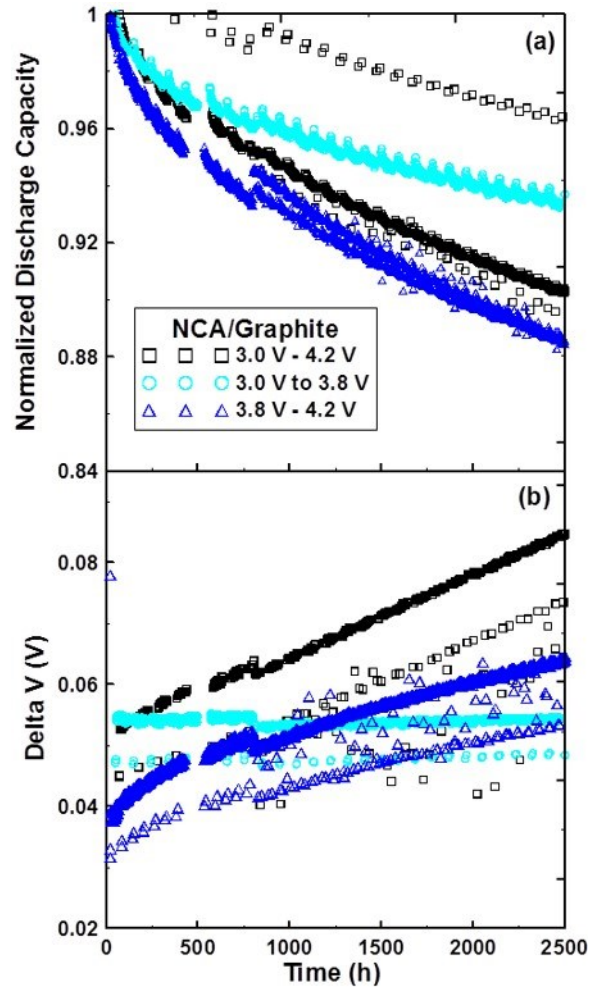


Figure 6-6. (a) Normalized discharge capacity and (b) ΔV growth for NCA/graphite cells cycled in different voltage ranges at 40°C and C/3.

V (Figure 6-6 and Figure 6-7) avoids these reactions and suppresses impedance growth. Restricting the voltage range also reduces the likelihood of particle cracking by limiting the material volume change. Restricted depth-of-discharge was used by other researchers as another strategy to limit resistance growth and capacity loss in high nickel positive electrode materials.^{162,163,169}

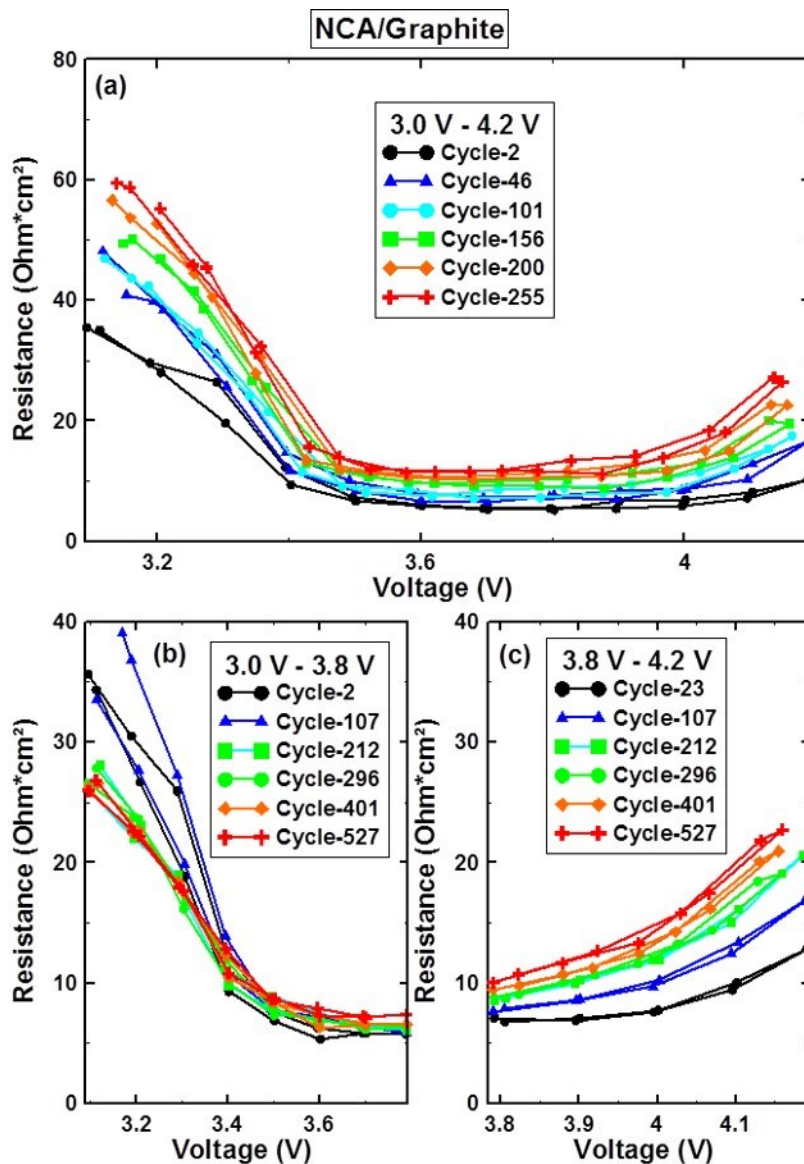


Figure 6-7. Resistance (the diameter of the semicircles in the Nyquist plot of impedance, which includes contact resistance and charge transfer resistance for both electrodes) as a function of voltage and cycle number is shown for NCA/graphite cells cycled at 40°C and C/3 in different voltage ranges (a) 3.0 V – 4.2 V, (b) 3.0 V – 3.8 V, (c) 3.8 V – 4.2 V.

6.2 Resistance as a Function of Voltage

This section further explores the voltage dependence of cell resistance, as previously shown in Figure 6-7. Figure 6-8 shows the evolution of the EIS spectra for each full cell

type during cycling from the same cells that were shown in Figure 6-1. Nyquist plots are shown for the data measured automatically during cycling from 100 kHz to 0.04 Hz, at 40°C. Spectra are shown at the beginning of life and after 200 cycles, for 3.1 V, 3.8 V, 4.2 V,

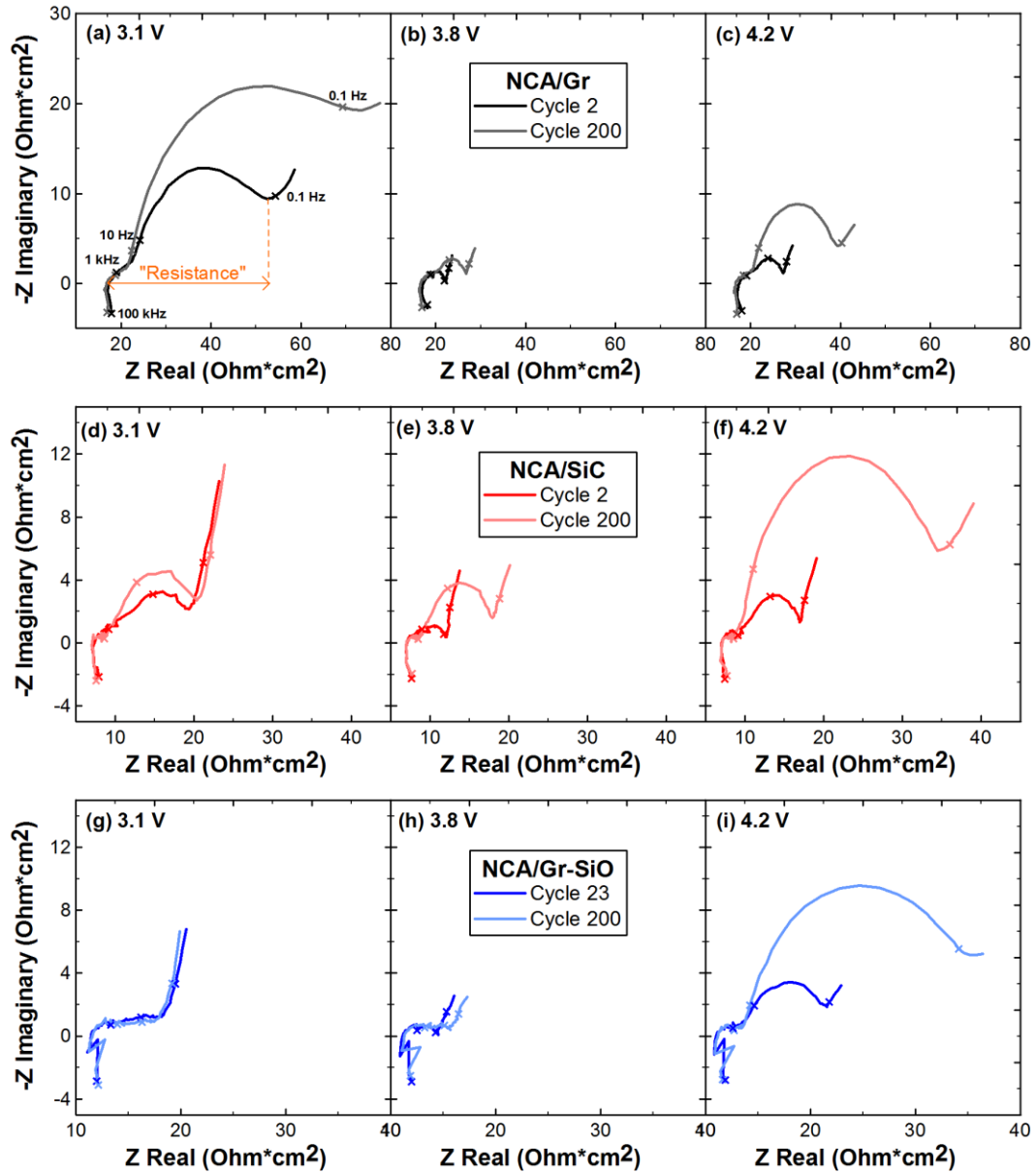


Figure 6-8. EIS spectra are shown for each full cell type at 3 different voltages: 3.1 V (a,d,g), 3.8 V (b,e,h) and 4.2 V (c,f,i), all measured at 40°C. The dark colored lines show spectra at the beginning of cycling and the light colored lines show spectra after 200 cycles, to highlight the change in the medium frequency feature from 1kHz to 0.01 Hz. As indicated in (a) data points are shown for the following frequencies: 100 kHz, 1kHz, 10Hz, and 0.1 Hz.

and 4.2 V. Spectra in Figure 6-8g-i start at cycle 23 because of an issue with temperature control during cycle 1 measurements. Each spectrum has one high frequency semicircle feature (from 100 kHz to 1 kHz) and one medium frequency semicircle feature (from 1 kHz to 0.01 Hz). The medium frequency semicircle grows with cycling while the high frequency semicircle does not change. As discussed in Figure 6-2, the medium frequency semicircle is attributed mostly to positive electrode charge-transfer resistance, which is seen here to have a different magnitude depending on the cell voltage.

Figure 6-9 shows the resistance of each cell plotted as a function of voltage. Solid symbols are for charge and open symbols are for discharge. For all cells the resistance grows during cycling in the high voltage region, and for cells with the graphite anode (Figure 5a) the resistance grows during cycling across all voltages. As illustrated in Figure 6-2, the resistance growth comes from the positive electrode charge-transfer resistance. Silicon-containing cells also show a difference in resistance between charge and discharge caused by the voltage hysteresis usually observed for silicon.¹⁸³ The hysteresis decreases during cycling likely as silicon degrades and its capacity decreases.

Figure 6-10a-c show EIS spectra measured at 40°C from pouch cells after formation and two weeks of storage at room temperature (black solid line), compared to the positive (gray dashed line), and negative (light blue solid line) impedance contributions measured at 40°C in symmetric coin cells constructed from the same pouch cells. The full cell voltages are listed above the corresponding spectrum: (a) 3.1 V, (b) 3.8 V, and (c) 4.2 V. Each spectrum is normalized by the electrode geometric area. The negative electrode impedance does not change significantly across the three voltages, but at 3.1 V and 4.2 V the positive electrode impedance is larger than it is at 3.8 V.

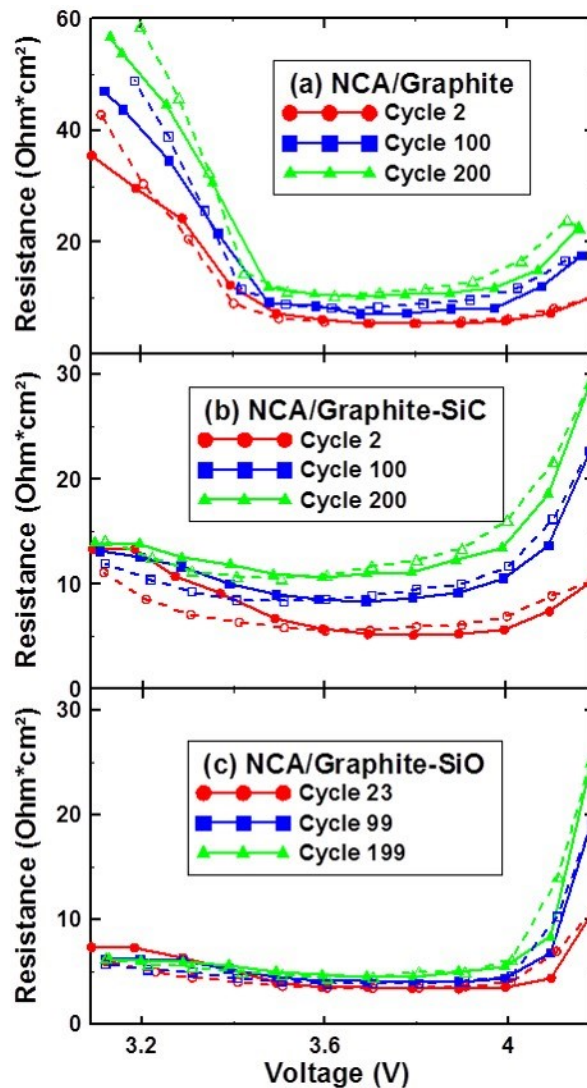


Figure 6-9. The resistance (the diameter of the semicircles in a Nyquist plot of EIS – see Figure 6-8) for each cell type as a function of voltage and cycle number measured at 40°C. EIS data is from the same cells shown in Figure 6-1 and cells were cycled at C/3 and 40°C from 3.0 – 4.2V with every 10th cycle at C/20 to measure EIS

Figure 6-10d shows the same resistance as Figure 6-9, but plotted as a function of the positive electrode lithiation state, i.e., the value of x in $\text{Li}_{1-x}\text{MO}_2$. The resistance trend seen in the pouch cells is related to the positive electrode state of charge at each pouch

cell voltage. The resistance is a minimum at approximately $x = 0.5$, and increases below $x = 0.25$ and above $x = 0.75$.

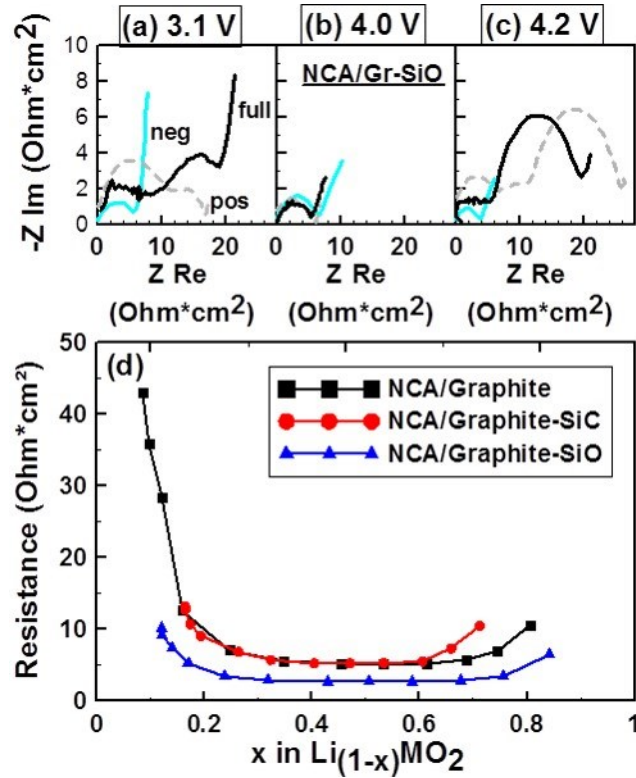


Figure 6-10. (a-c) Positive and negative electrode impedance at different voltages at 40°C (measured using symmetric cells after pouch cell formation). (d) The resistance values measured on cycle 2 (NCA/Graphite and NCA/Graphite-SiC) or 23 (NCA/Graphite-SiO) at 40°C previously shown in Figure 6-9 are presented as a function of cathode lithium content instead of full cell voltage.

Figure 6-11a shows an equivalent circuit with each element at the positive electrode active material particle that is expected to contribute to impedance. R_{film} and $R_{\text{rock-salt}}$ represent the resistance of ion migration through the surface-film and rock-salt layer, respectively. Each resistance is in parallel with a capacitance. Since each layer is expected to have different lithium-ion diffusion properties, a buildup of charge is

expected at the interfaces between: (i) the electrolyte and surface-film, (ii) the surface-film and rock-salt layer, and (iii) the rock-salt layer and NCA. The charge-transfer resistance of the interface is represented here as the two series RC circuits. Z_{NCA} represents the impedance of solid-state lithium diffusion in the bulk NCA.

The rock-salt layer must contain some lithium atoms since lithium-ions pass through this layer during cell operation. Since the rock-salt layer is an ionically conductive material, a change in lithium content would alter the lithium diffusivity and consequently change the charge-transfer resistance of the material. For example, the ionic conductivity is proportional to the carrier concentration multiplied by the carrier mobility. At low lithium contents in the rock-salt $Li_xTM_{1-x}O$ layer, one would expect slow lithium-ion diffusion. This could explain the large charge transfer resistance observed at high potentials where, like the bulk NCA material, the rock-salt layer may have a low lithiation state. In addition, lithium diffusion is expected to be low when lithium content is high, due to the small amount of lattice vacancies available for ion mobility.¹⁸⁴ In which case charge

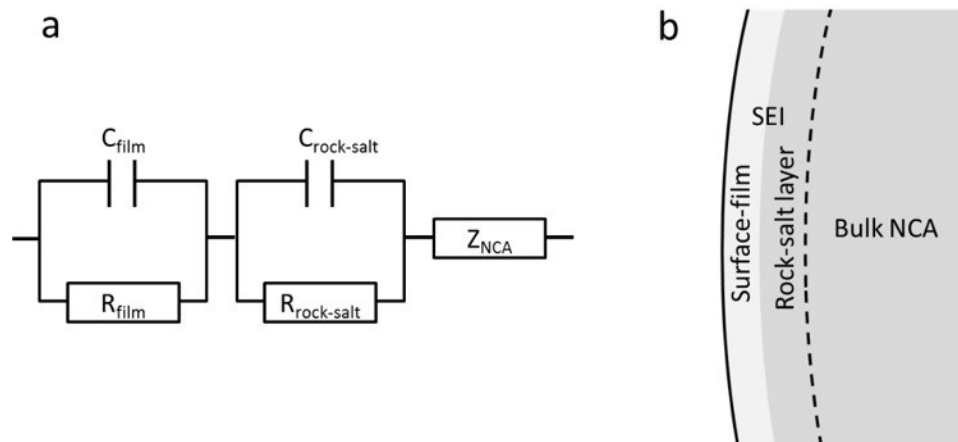


Figure 6-11. (a) Equivalent circuit to represent the impedance of lithium traveling through the SEI (surface-film + rock-salt layer) and bulk NCA (b) positive electrode layers from the equivalent circuit shown as a schematic. Adapted from Figure 2 of reference.¹²²

transfer resistance would also be high for low states-of charge, as is experimentally observed. Dees *et al.* modeled the impedance spectra of positive electrodes with different diffusion coefficient for the rock-salt layer, and showed that small diffusion coefficients give large charge transfer resistance.¹²²

Voltage-dependent charge transfer resistance has been presented in the literature,^{124,185–187} but a mechanism to explain the phenomenon has not been proposed until now. A *tour-de-force* experiment that can measure the lithium content in the rock salt layer as a function of potential will be required to prove or disprove this mechanism. Such experiments are beyond the scope of this work.

6.3 Conclusions

For the three cell types tested here, the positive electrode charge transfer resistance is large at low and high voltage, and grows in the high voltage region with cycling. This conclusion is based on the interpretation of the EIS spectra presented here, and is confirmed from work by other researchers.^{119–123,167} The associated literature shows that charge transfer resistance growth is due to the continued thickening of a rock-salt surface layer. Several strategies to suppress the formation of the rock-salt layer have been employed: coatings, electrolyte additives, and limiting the upper cutoff voltage of the cells. Continued cracking of the positive electrode material will expose new surfaces that will also form rock salt-layers. The next chapter studies single-crystal positive electrode materials which show very little or almost no resistance growth and virtually no micro cracking.

CHAPTER 7 X-RAY DIFFRACTION STUDY OF SINGLE-CRYSTAL

$\text{LiNi}_{0.5}\text{Mn}_{0.3}\text{Co}_{0.2}\text{O}_2$

Harlow *et al.* recently published results where pouch cells with single-crystal $\text{LiNi}_{0.5}\text{Mn}_{0.3}\text{Co}_{0.2}\text{O}_2$ (NMC532) cathode underwent thousands of cycles with little capacity loss and minimal resistance growth.⁵⁹ The data was presented as a benchmark for long-lasting lithium-ion cells.

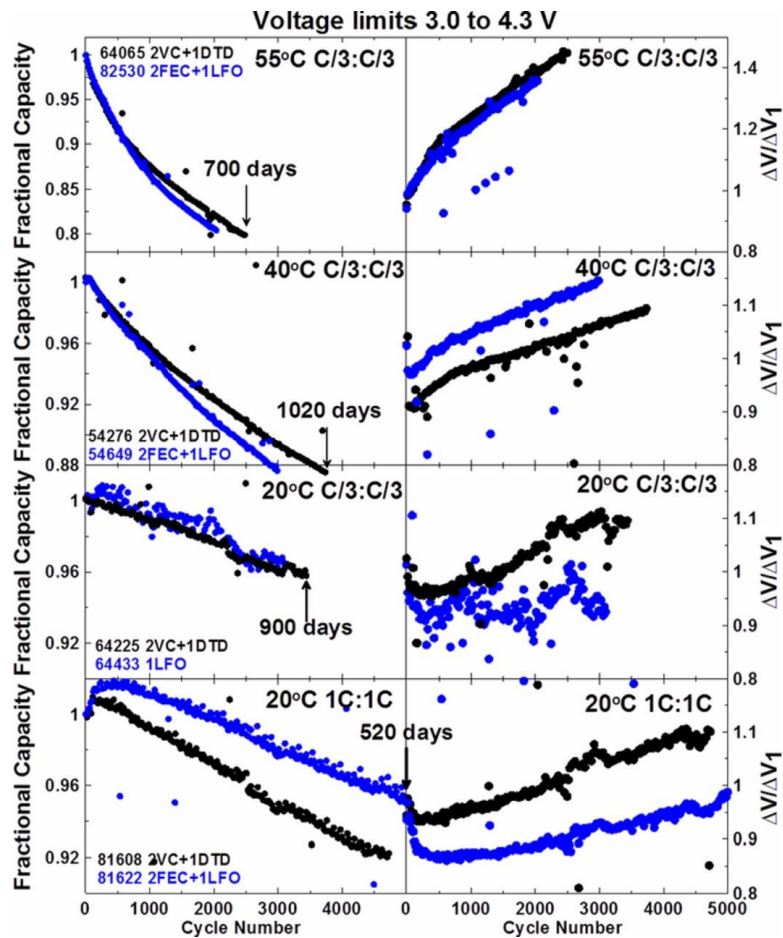


Figure 7-1. Fractional capacity and normalized ΔV plotted versus cycle number for single crystal NMC532/graphite cells tested between 3.0 and 4.3 V under the conditions shown in the legends. Figure and caption reproduced from reference under Creative Commons license.⁵⁹

Figure 7-1 shows fractional capacity vs cycle number from Harlow *et al.*⁵⁹ The cells tested at 1C and 20°C (bottom panel) amazingly retain >90% capacity after 5000 charge discharge cycles and show <10% resistance growth (ΔV). Even the cells tested at 40°C show impressive capacity retention compared to the NCA/graphite pouch cells from the previous chapter.

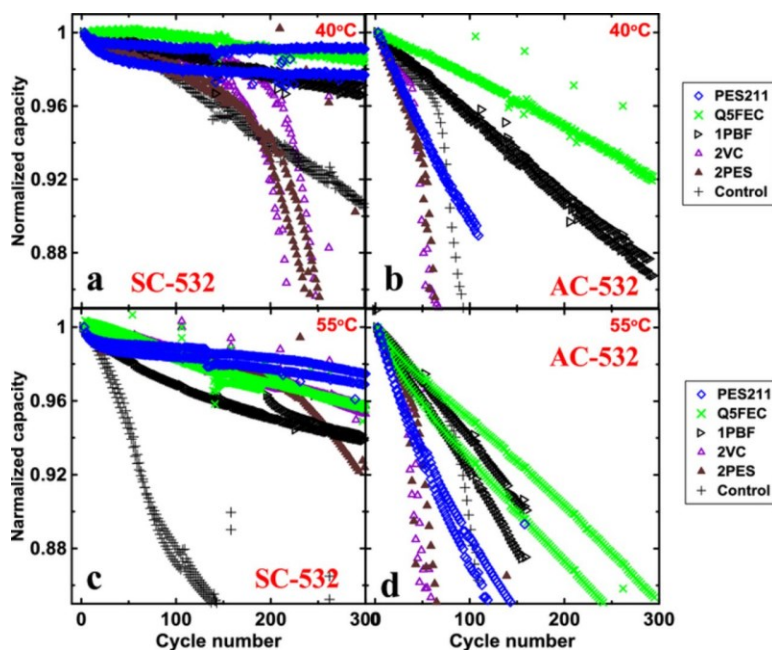


Figure 7-2. The normalized capacity of single-crystal NMC532: SC532 (a) and polycrystalline NMC532: AC-532 (b) cells, respectively, tested at 40°C (C/2 CCCV between 3.0 and 4.4 V) as a function of cycle number. Legend indicates electrolyte type. Figure and caption adapted from reference under Creative Commons license.¹⁸⁷

Figure 7-2 shows normalized capacity vs cycle number for pouch cells with single-crystal NMC532 (a,c) compared to pouch cells with polycrystalline NMC532 (b,d) tested under the same conditions by Li *et al.*¹⁸⁸ For the best performing electrolytes (green and blue) the single-crystal cells far outperform the polycrystalline cells.

7.1 Single-Crystal Material

Single-crystal NMC532 shares the same chemistry as traditional polycrystalline NMC532, but has entirely different particle morphology. Figure 7-3 shows SEM images of electrodes made from polycrystalline NMC532 (a) and single-crystal NMC532 (b). Electrodes were made of 96 wt% active material, 2 wt% carbon-black, and 2 wt% PVDF and were extracted from dry pouch cells provided by Li-Fun Technology (Xinma Industry Zone, Golden Dragon Road, Tianyuan District, Zhuzhou City, Hunan Province, PRC, 412000).

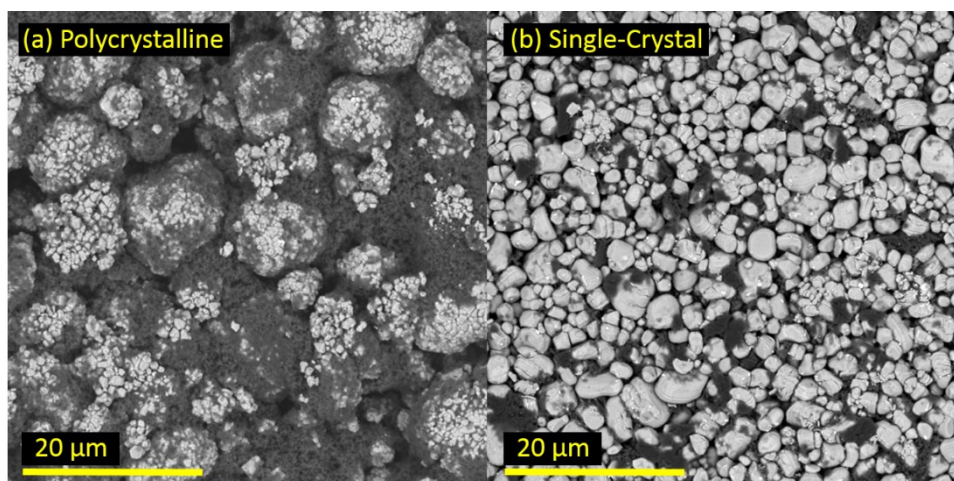


Figure 7-3. SEM images of electrodes made from (a) polycrystalline and (b) single-crystal $\text{Li}_x\text{Ni}_{0.5}\text{Mn}_{0.3}\text{Co}_{0.2}\text{O}_2$. The dark material in each electrode is conductive additive.

The polycrystalline material has $\sim 10 \mu\text{m}$ diameter secondary particles formed from agglomerates of smaller $\sim 300\text{-}500 \text{ nm}$ diameter primary particles. Each primary particle may be a single-crystal or contain grain boundaries. The material is referred to as “polycrystalline” because the secondary particles are polycrystalline regardless of the primary particle structure. NCA material with this agglomerate particle structure was seen by Watanabe *et al.* to crack apart during use (as discussed in the previous

chapter).¹⁶² In contrast, the electrode made from the single-crystal NMC532 has larger ~1-5 μm particles and there is no secondary particle structure. The material is referred to as “single-crystal” since most particles are single-crystals of NMC532. Li *et al.* used electron backscatter diffraction mapping to image the grains of the single-crystal material. The images showed that most of the particles are single-crystals of NMC532, free of grain boundaries.¹⁸⁸ The dark gray material in each image is conductive additive. The single-crystal material is known to have a titanium oxide coating as reported by Ma *et al.*¹⁷⁸ The coating functions to extend cell lifetime by suppressing reactions with the electrolyte, reducing impedance, and reducing gassing at high voltage.¹⁷⁸ The coating alone is likely not responsible for the long-lifetime since aluminum oxide coated polycrystalline materials did not perform as well as this single-crystal material.^{7,61} In addition, Ma *et al.* show that for some choices of electrolyte additives, excellent lifetime and minimal impedance growth can be obtained for uncoated single crystal NMC532, which virtually matches that for coated single crystal NMC532.¹⁷⁸

Within a polycrystalline material it is easy to imagine that crystal lattice expansion and contraction will push the primary particles apart. In this case new, uncoated, surface would be exposed to react with the electrolyte. But for the single-crystal material, individual particles expand and contract within the electrode binder/conductive additive matrix. No new uncoated surfaces are exposed by cracking, so no new opportunities arise for growth of a resistive surface layer. Parasitic reactions, gassing, and impedance growth would all be minimized which is extremely beneficial for long term capacity retention. The larger particle size for the single-crystal material could induce strain and limit volume change, but X-ray diffraction is used here to show the crystal structure and

volume change of polycrystalline and single-crystal NMC532 are identical. The materials expand and contract in the same manner, but the single-crystal material avoids cracking.

Figure 7-4 and Figure 7-5 show X-ray diffraction patterns measured from each dry electrode in air. Peaks indexed to the R-3m space group are labeled. Figure 7-5 includes refinements of the X-ray diffraction data where a single hexagonal layered phase (R-3m space group) was used. Refinement parameters are summarized in Table 7-1. The peak observed at 26.5° for the single-crystal material was ignored for the refinement since it is from the conductive carbon additive, like graphite (shown as an inset in Figure 7-4).

The intensities for the (003), (006), and (009) peaks are much larger for the single-crystal material than the polycrystalline material, which indicates that there is preferred orientation on the 00l axis for the single-crystal material in the calendared electrode (particles should tend to lie with the 00l planes parallel to the electrode surface).

Similarly, Rietveld refinement results of the electrodes indicate that the 00l axis shows considerable preferred orientation for the single-crystal electrode relative to the polycrystalline electrode. The single-crystal electrode March-Dollase (MD) preferential orientation fraction is 0.636 while the polycrystalline electrode MD preferential orientation factor is 0.972. An MD preferential orientation fraction less than 1 indicates preferential orientation and a smaller value indicates greater preferential orientation along the axis specified.

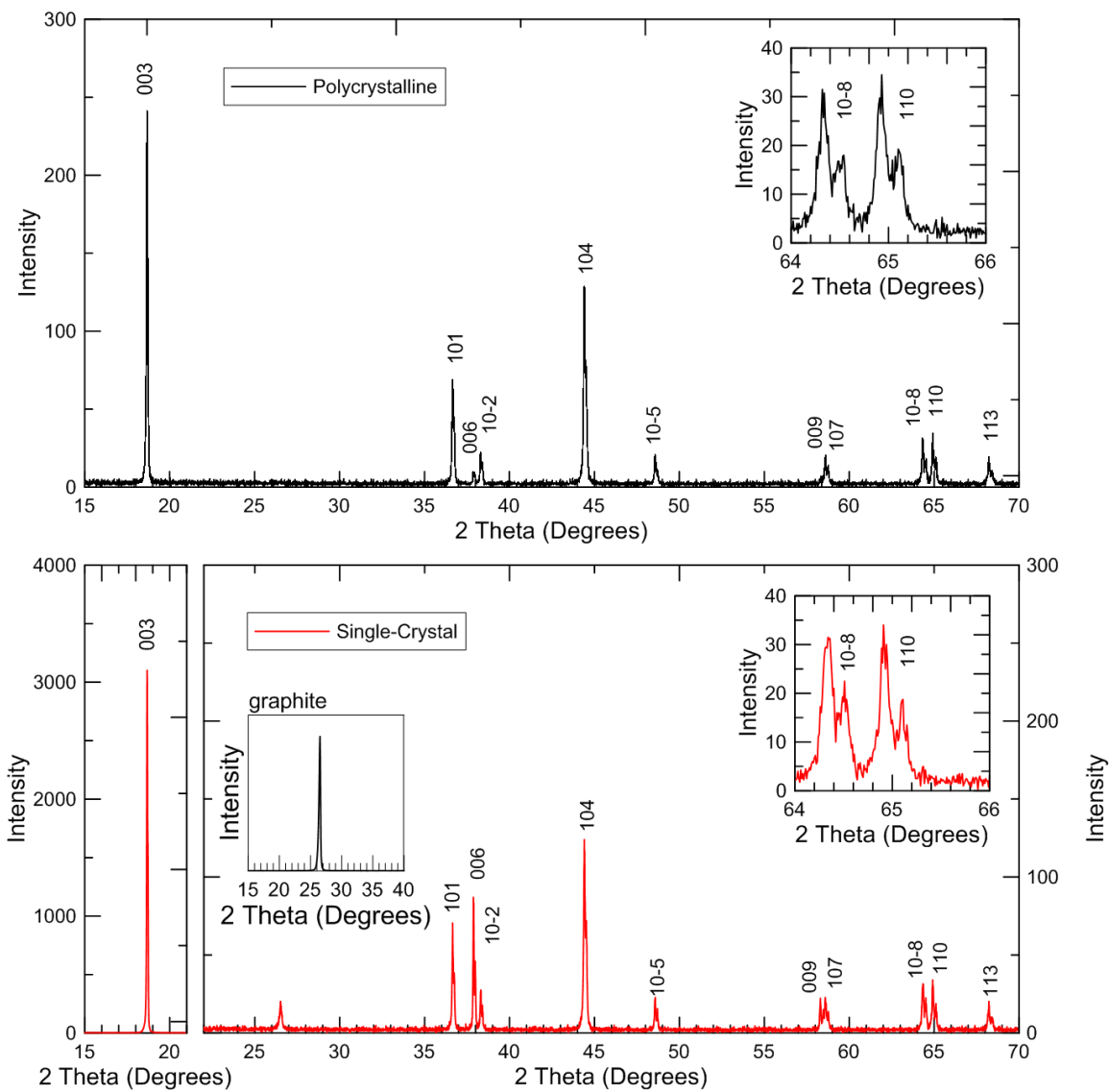


Figure 7-4. X-ray diffraction of electrodes made from polycrystalline (top/black) and single-crystal (bottom/red) $\text{Li}_x\text{Ni}_{0.5}\text{Mn}_{0.3}\text{Co}_{0.2}\text{O}_2$. Peaks indexed to the R-3m space group are labelled. The inset-zoom (for 64 to 66°) for both materials shows clear splitting between the peaks from K α 1 and K α 2 radiation. The second inset in the lower panel shows the graphite (002) peak (conducting additive) measured in a separate scan.

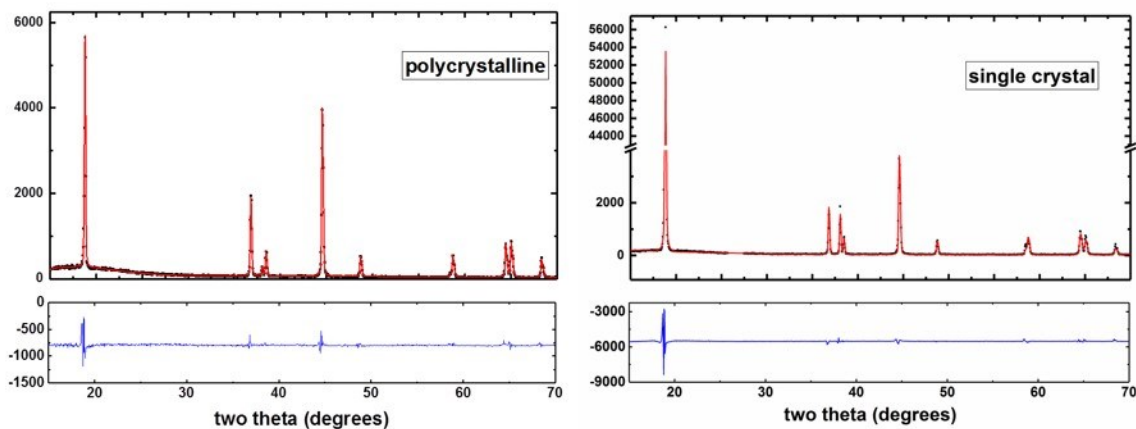


Figure 7-5. X-ray diffraction patterns (black dots) and refinements (red lines) are shown for polycrystalline and single-crystal electrodes. Parameters are summarized in Table 7-1.

Table 7-1. X-ray diffraction refinement parameters for polycrystalline and single-crystal NMC532 electrodes. Refinements are shown in Figure 7-5.

	a (\AA)	c (\AA)	c/a	Unit Cell Volume (\AA^3)	MD Preferential Orientation Fraction for 001 axis
Polycrystalline	2.86956(7)	14.2352(6)	4.9607	101.514(4)	0.972
Single-Crystal	2.87092(10)	14.23356(26)	4.958005	101.598(6)	0.636

Figure 7-6a shows the cell potential vs positive electrode specific capacity which is similar for the two materials, including ~ 25 mAh/g irreversible capacity loss during the first charge cycle. Figure 7-6b shows differential capacity (dQ/dV) vs potential (V) which is nearly identical for the polycrystalline and single-crystal cells.

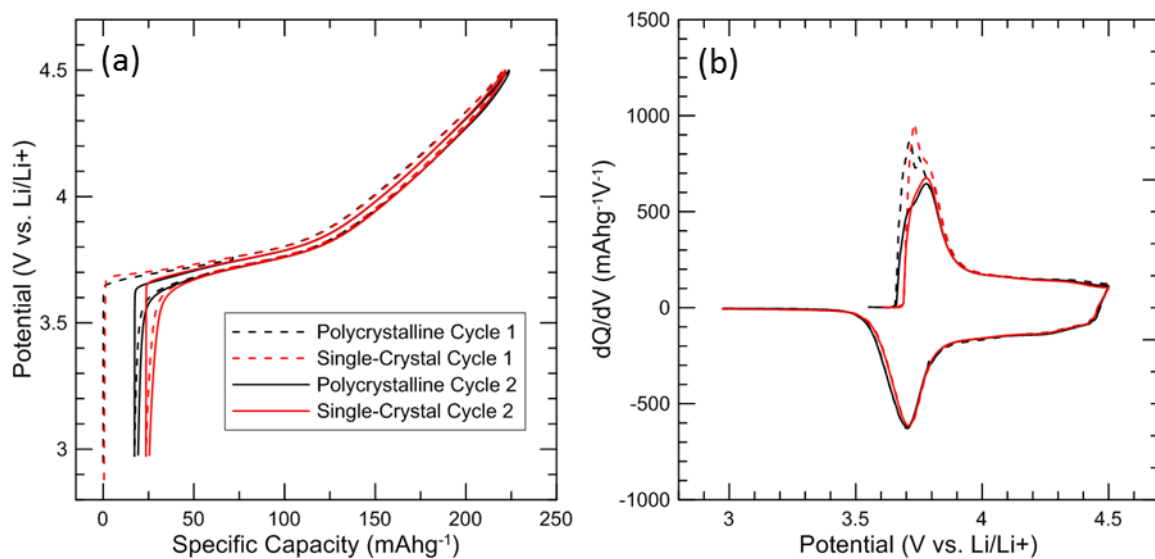


Figure 7-6. (a) Cell potential vs. specific capacity and (b) dQ/dV vs potential for both electrodes during the *operando* X-ray diffraction experiment at C/50.

7.2 Volume Change

Operando X-ray diffraction experiments were done to monitor the unit cell volume change for single-crystal and polycrystalline NMC532. Figure 7-7 shows data from the *operando* X-ray diffraction experiments. The right-hand panels show the cell voltage vs time. Each cell was charged and discharged at a rate of $\sim C/50$ between 3 V and 4.5 V vs Li/Li⁺ at room temperature ($\sim 22^\circ\text{C}$). Each X-ray diffraction scan ran for 2.2 hours, which corresponds to 10 mAh/g of charge passed ($\sim 4\%$ of the total capacity). The left-hand panels show the X-ray diffraction scans. For clarity, every other scan is plotted and the intensity of each scan is offset to match the cycling data. Some scans are missing from (a) and the charger current was C/350 for the first 100 hours of the test due to instrument issues. Each peak from the NMC532 material is labeled as indexed to the R-3m space group, and peaks from the lithium metal counter electrode and beryllium window are

indicated. As the crystal structure changes during cycling, the NMC peak positions shift with respect to scattering angle (2θ) but the Li and Be peaks remain fixed.

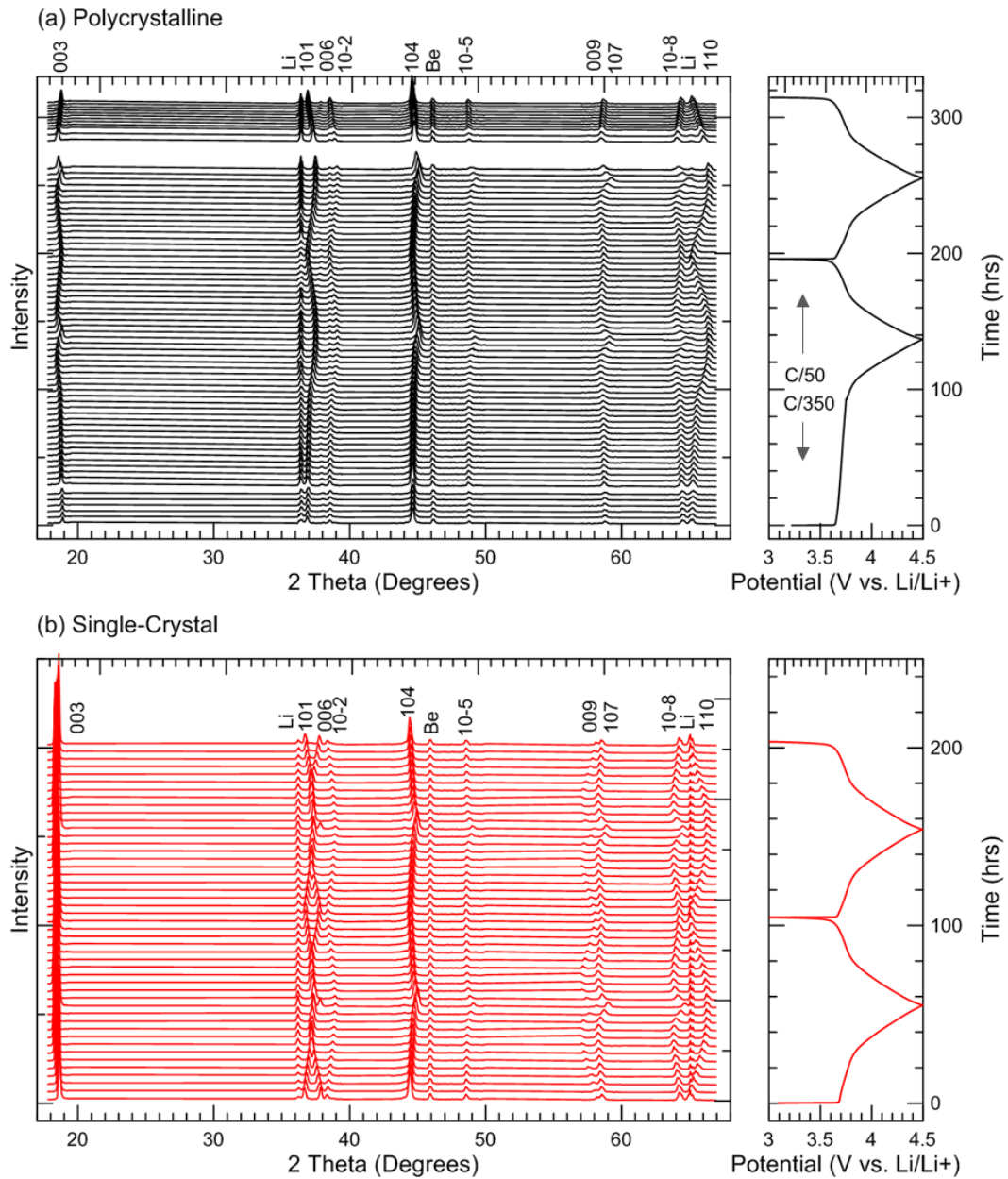


Figure 7-7. Operando X-ray diffraction data for NMC532 electrodes made from (a) polycrystalline material and (b) single-crystal material.

Figure 7-8 shows that at the bottom of the first and second discharges, X-ray diffraction peaks from the NMC532 return to the same position. This indicates that the changes in crystal structure observed during cycling are highly reversible. For the polycrystalline material, the lattice parameters at the bottom of the first discharge are: $a = 2.86 \text{ \AA}$, $c = 14.23 \text{ \AA}$ and at the bottom of the second discharge they return to $a = 2.86 \text{ \AA}$, $c = 14.24 \text{ \AA}$. For the single-crystal material, the lattice parameters at the bottom of the first discharge are: $a = 2.86 \text{ \AA}$, $c = 14.25 \text{ \AA}$ and at the bottom of the second discharge they return to $a = 2.86 \text{ \AA}$, $c = 14.26 \text{ \AA}$. Figure 7-8 also shows that the $K_{\alpha 1}$ and $K_{\alpha 2}$ splitting is sharper for the single-crystal material than it is for the polycrystalline material. Since peak broadening is inversely related to crystallite grain size according to the Scherrer formula,¹⁸⁹ the sharper peaks for the single-crystal material are indicative of the larger crystallite grain size.

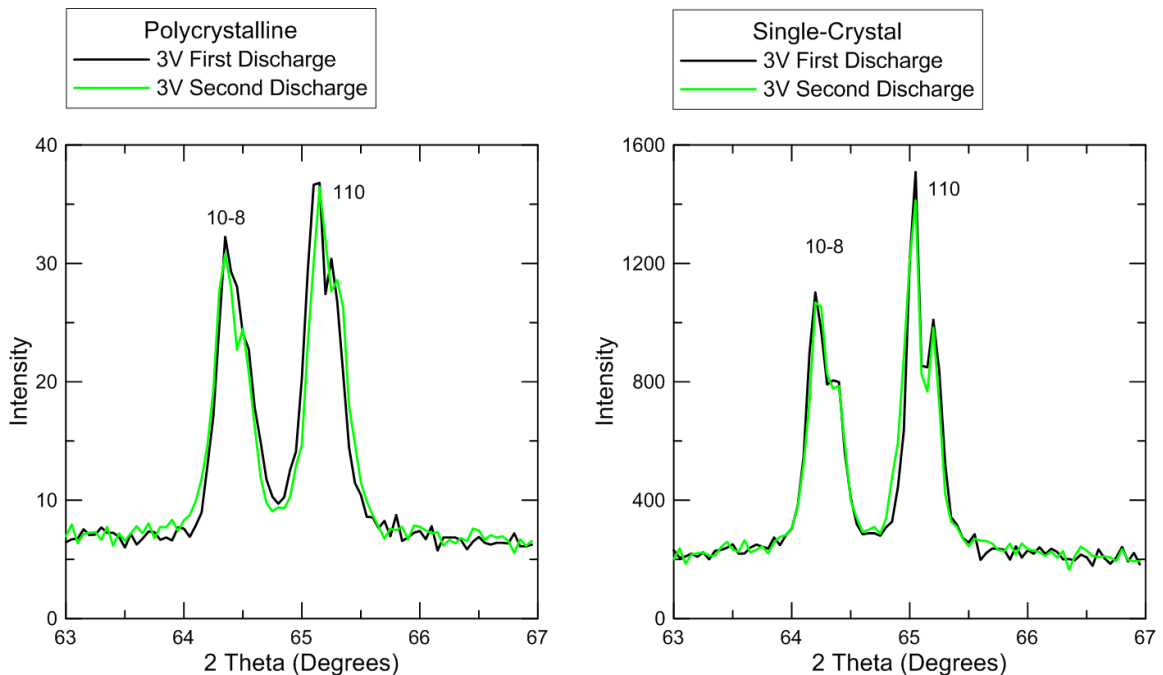


Figure 7-8. Detailed view of the $(10\bar{8})$ and (110) peaks for both materials at the bottom of the first discharge and at the bottom of the second discharge.

Figure 7-9 shows the a lattice parameter, the c lattice parameter, and the unit cell volume plotted as a function of positive electrode specific capacity. It is evident that the changes in crystal structure are reversible for both materials, especially the single-crystal material which returns to the exact a lattice and c lattice values during both cycles for charge and discharge. However, neither material returns to the initial lattice parameters observed in the range of the initial irreversible capacity loss. Note that the small “step” in the data for

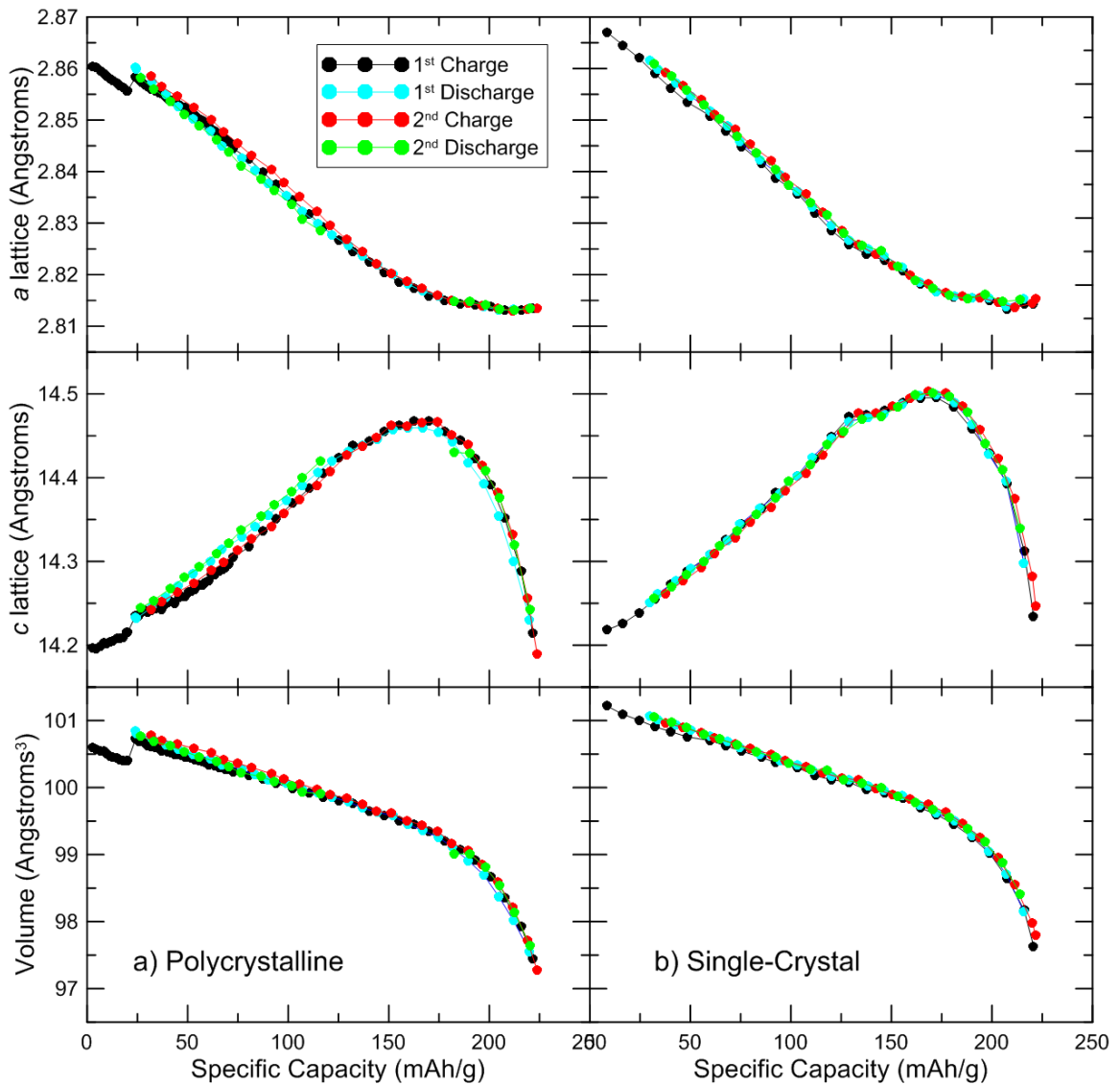


Figure 7-9. Lattice parameters and unit cell volume are shown as a function of specific capacity.

the polycrystalline material near 25 mAh/g coincides with the point a power failure interrupted the experiment briefly. It may be the case that the diffractometer angles were slightly shifted when the experiment resumed.

Figure 7-10 shows the lattice parameters and unit cell volume plotted as a function of electrode potential vs Li/Li^+ . Note that each data point is plotted vs average cell potential

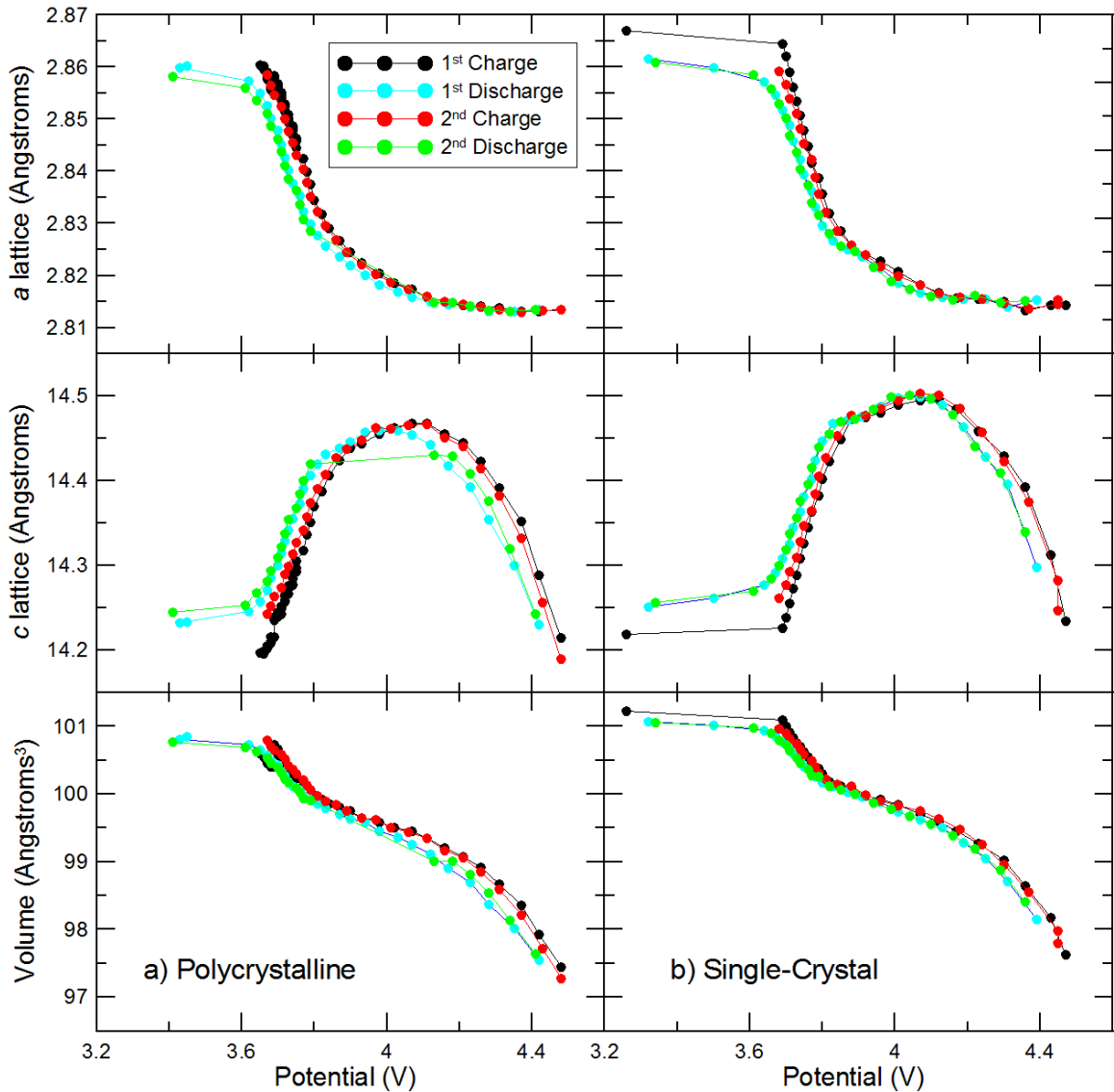


Figure 7-10. Lattice parameters and unit cell volume are shown as a function of average cell potential during each XRD scan.

during each 2.2 hour scan, so the results may be skewed for data near 3 V where the potential changes rapidly with time. Both polycrystalline and single-crystal materials follow the same trend in lattice parameters vs cell potential. The c lattice shifts from increasing to decreasing at 4.1 V, and the unit cell volume changes by 4% between 3 V and 4.5 V. As explained by Min *et al.*³⁷ the trends in lattice parameters during cycling are related to changes in the transition metal and Li layer spacing. Removing lithium from the crystal lattice initially reduces shielding between the oxygen layers, so the increased repulsion increases spacing between layers. Throughout delithiation, the volume of the transition metal layer decreases, as evidenced by the continual decrease of the a lattice parameter. The c lattice parameter initially increases because the change in lithium layer spacing is initially more pronounced. As the increasing repulsion across the lithium layer tapers off, the effect of the transition metal layer shrinking dominates and the c lattice begins to decrease. Near the end of delithiation, the decrease in c lattice with lithium content becomes quite steep.

7.3 Conclusions

An *operando* X-ray diffraction study of polycrystalline and single-crystal $\text{Li}_x\text{Ni}_{0.5}\text{Mn}_{0.3}\text{Co}_{0.2}\text{O}_2$ shows identical trends in lattice parameter evolution and unit cell volume change during cycling. Given the same volume change, polycrystalline materials are liable to lose capacity through particle cracking while single-crystal materials are not. This may help explain the outstanding performance of pouch cells built with single-crystal NMC532. Figure 7-11 (reproduced from reference) shows a cross-section SEM image of single-crystal NMC532 material after extensive cycling where the authors note “there are virtually no micro cracks in any of the electrode particles.” The electrode was

taken from a cell tested at 1C:1C 20°C which had 97% capacity retention after 5300 cycles. Some shearing is observed in particles for fresh and cycled electrodes, which may be due to electrode calendaring. Figure 7-12 (reproduced from reference)¹⁹⁰ shows a

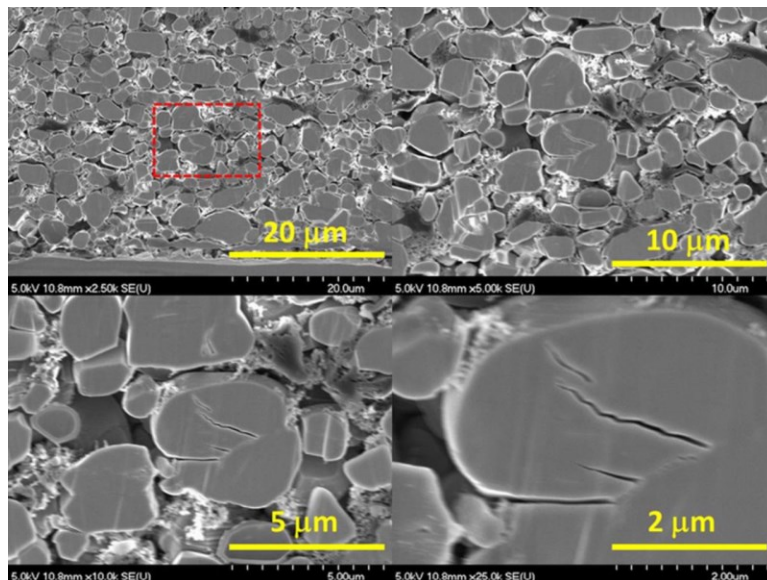


Figure 7-11. Cross sectional SEM of a single crystal NMC532 positive electrode taken from a cell tested at 1C:1C 20°C. The cell had 97% capacity retention after 5300 cycles. Notice that there are virtually no micro cracks in any of the electrode particles. This is why these cells show no loss of positive electrode active mass during cycling. Figure and caption from reference under Creative Commons license.⁵⁹

cross-section SEM image of single-crystal NMC811 material after extensive cycling where again there is no cracking. The electrode was taken from a cell after 1100 cycles at 20°C, 3-4.2V, 1C CCCV charge, 1C discharge. Just before the electrode was extracted for SEM the cell was charged to 4.3V (cathode at 4.38V vs Li/Li+) where NMC811 has a sharp ~5% unit cell volume change. Still there is no cracking. These results give hope that even high-nickel single crystal materials can avoid micro cracking.

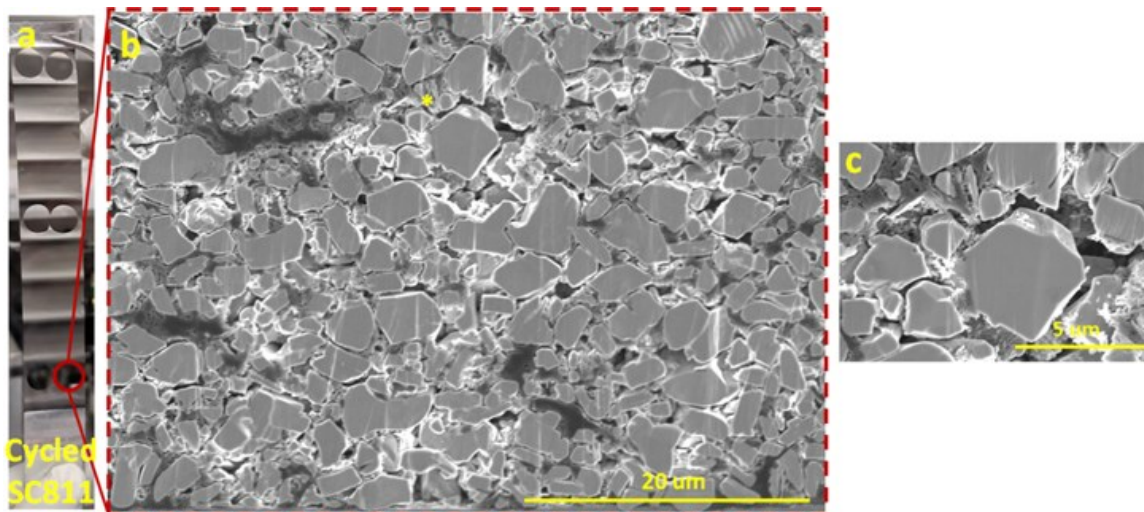


Figure 7-12. (a) Retrieved positive electrode from cycled SC811 pouch cell at 4.3 V. Two locations were punched for cross-section SEM. (b) Cross-section SEM image on electrode punched from the red-circled region of (a). (c) Zoomed-in image of region * in (b). Figure and caption from reference under Creative Commons license.¹⁸⁹

CHAPTER 8 X-RAY DIFFRACTION STUDIES OF HIGH NICKEL CATHODE MATERIALS DURING SYNTHESIS

Concurrent with the development of single-crystal materials,^{191–194} an effort was undertaken by Li *et al.* to eliminate cobalt from high-nickel positive electrode materials.⁹ Cobalt has traditionally been used in layered positive electrode materials (NMC and NCA) to provide thermal stability and longevity,^{18,195,196} but is expensive due to increasing demand and often associated with undesired mining practices.¹⁹⁷ There is consequently a desire to remove cobalt from these materials, and if necessary find an alternative dopant to achieve the same benefits. In commercial positive electrode materials like NMC and NCA, Co, Al, and Mn are typically used to partially substitute the nickel. Without these dopants, LiNiO₂ (LNO) undergoes phase transitions during cycling, which lead to rapid capacity loss during 100% DOD cycling.^{198,199} In a systematic study, Li *et al.* showed that when doped at a level of 5 at.%, Mg, Mn, and Al all suppress phase transitions in LNO, while Co alone does not.⁹ This suggests that Co may not actually be needed in these materials, as was historically believed.

In this work, cobalt-free layered positive electrode materials are studied during synthesis by *in-situ* X-ray diffraction (XRD). The samples chosen here are similar to those studied by Li *et al.*:⁹ LiNiO₂ (LNO), LiNi_{0.975}Mg_{0.025}O₂ (LNMO), and LiNi_{0.95}Al_{0.05}O₂ (LNAO) and can be made into single-crystal materials given appropriate synthesis methods. It is believed that the results reported here can be used to help identify optimal synthesis

procedures for each of these materials. Sample preparation and analysis are described in the experimental section. Processed data is presented in this chapter.

8.1 Synthesis of LiNiO₂

First, the synthesis of LiNiO₂ (LNO) was studied using either LiOH•H₂O or Li₂CO₃ as the lithium source. Figure 8-1 shows XRD patterns recorded at roughly every 25°C during heating for LNO prepared from a combination of Ni(OH)₂ and LiOH•H₂O. Unfortunately, many peaks from the alumina tube used in this experiment overlap with peaks from the sample. Labels are shown for sample peaks indexed to the R-3m group. Clear sample Bragg peaks having Miller indices (003), (101), (10 $\bar{5}$), (10 $\bar{8}$)/(110) are visible. The red boxes highlight the (003) and (10 $\bar{8}$)/(110) peaks, which are useful to follow specifically, in order to see the evolution of LiNiO₂ during heating. Below ~300°C the (003) peak is still present for the hydroxide precursor. Above ~600°C, the (003) and (10 $\bar{8}$)/(110) peaks appear for LiNiO₂. With increasing temperature the peak (2 θ) locations shift, and the peaks also become sharper. As shown in Chapter 7, the lattice parameters of layered cathode materials change during lithiation, which shifts the peak locations.^{199–201} This is most evident for the (10 $\bar{8}$)/(110) peaks. Peak sharpness changes during crystal growth, with narrower peaks for larger crystallite sizes, as described by the Scherrer formula.¹⁸⁹

Figure 8-2a and b show the (003) and (10 $\bar{8}$)/(110) Bragg peaks at roughly 25°C intervals during heating, for LNO prepared from Ni(OH)₂ and LiOH•H₂O (Figure 8a), compared to LNO prepared from Ni(OH)₂ and Li₂CO₃ (Figure 8b). Figure 8-2c shows the change in

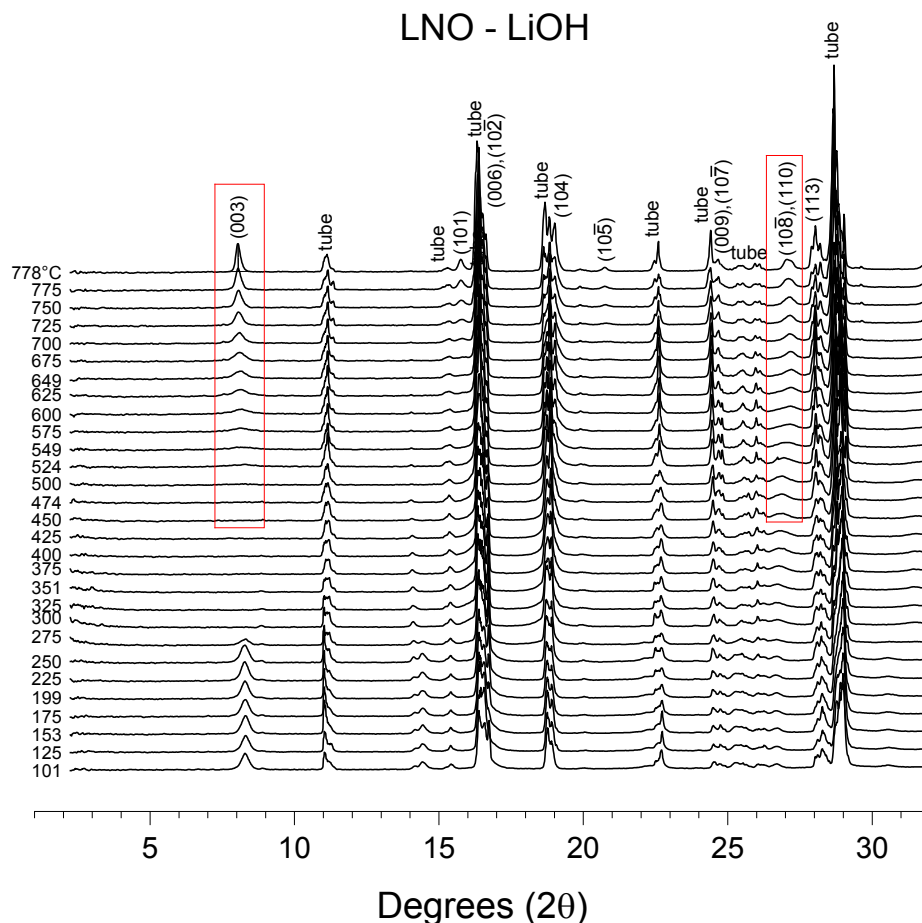


Figure 8-1. XRD patterns recorded at roughly every 25°C, from 100°C to 800°C, during heating for the LNO samples prepared with LiOH•H₂O. Sample peaks were indexed to the R-3m space group.

the $(10\bar{8})/(110)$ combined peak position vs. temperature. A single value of 2θ is used to indicate the position of the overlapping $(10\bar{8})/(110)$ peaks. Zeroshift is set as the measured scattering angle (2θ) at 400°C. The (003) peak appears at ~575°C for LiOH synthesis and ~775°C for Li₂CO₃ synthesis. The $(10\bar{8})/(110)$ peaks shift with respect to 2θ up to ~575°C for LiOH synthesis and ~775°C for Li₂CO₃ synthesis. Both phenomena show that when using Li₂CO₃ as the lithium source, instead of LiOH, a higher temperature is required to prepare fully lithiated, crystalline material. These results are

unsurprising considering LiOH melts at 471°C, while Li₂CO₃ does not melt until 723°C.²⁰² For this reason, higher temperatures are generally used for synthesis with Li₂CO₃.^{193,194}

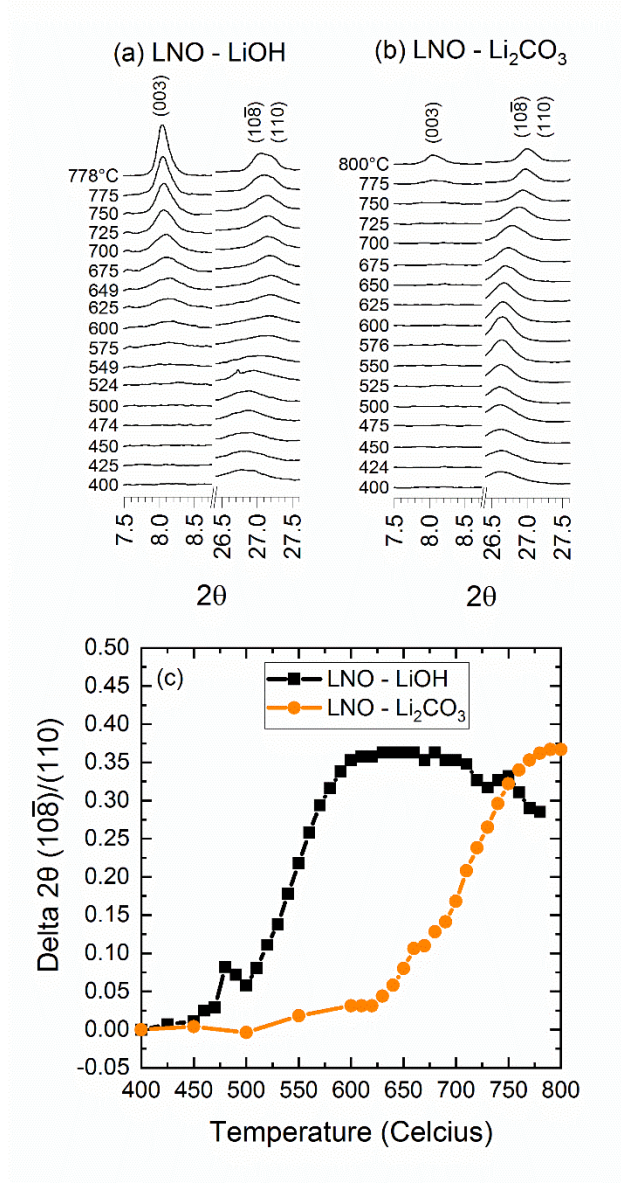


Figure 8-2. (a-b) Detailed view of (003) and (10̄8)/(110) Bragg peaks during heating for LNO prepared with (a) LiOH•H₂O or (b) Li₂CO₃. (c) Delta 2θ for the (10̄8)/(110) combined peak vs temperature during heating for LNO prepared with LiOH (black) or Li₂CO₃ (orange).

8.2 Synthesis of Mg and Al doped LiNiO₂

The synthesis of LiNi_{0.975}Mg_{0.025}O₂ (LNMO) and LiNi_{0.95}Al_{0.05}O₂ (LNAO) were studied using either LiOH•H₂O or Li₂CO₃ as the lithium source. Figure 8-3 shows (003) and (10 $\bar{8}$)/(110) Bragg peaks, recorded at roughly 25°C intervals, during heating from 400°C to 800°C for: (a) LNO, (b) LNMO and (c) LNAO, all prepared with LiOH•H₂O.

Compared to LNO, LNMO and LNAO have sharper (003) peaks at a lower temperature and the (10 $\bar{8}$)/(110) splitting is visible at 800°C. This indicates that both dopants reduce the temperature required to prepare a fully lithiated, crystalline material. Figure 8-4a shows the full-width half max (FWHM) of the (003) peak vs. temperature during heating for LNO (black), LNMO (red) and LNAO (green). All samples were prepared with

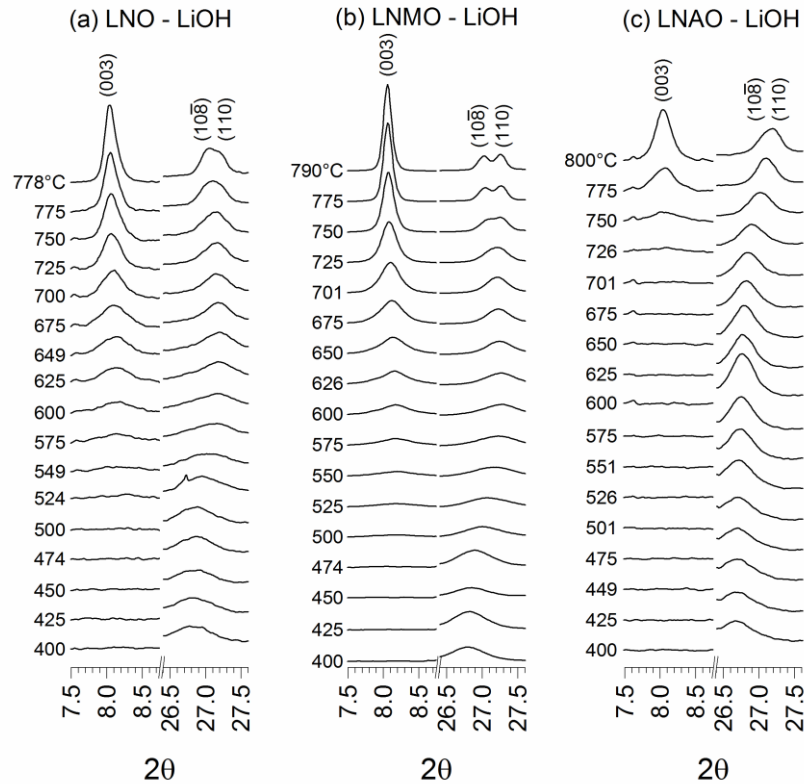


Figure 8-3. Detailed view of (003) and (10 $\bar{8}$)/(110) Bragg peaks during heating for: (a) LNO, (b) LNMO and (c) LNAO; all samples were prepared with LiOH•H₂O.

LiOH•H₂O. The FWHM was extracted from an (003) peak refinement done in GSAS.^{135,136} Figure 8-4b shows the change in the (10 $\bar{8}$)/(110) combined peak position vs. temperature. A single value of 2 θ is used to indicate the position of the overlapping (10 $\bar{8}$)/(110) peaks. Zero shift is set as the 2 θ value at 400°C, as before. For all samples, the FWHM decreases with increasing temperature, as both the crystal growth and lithiation progress. In the range 650-800°C, the FWHM is the smallest for the LNMO

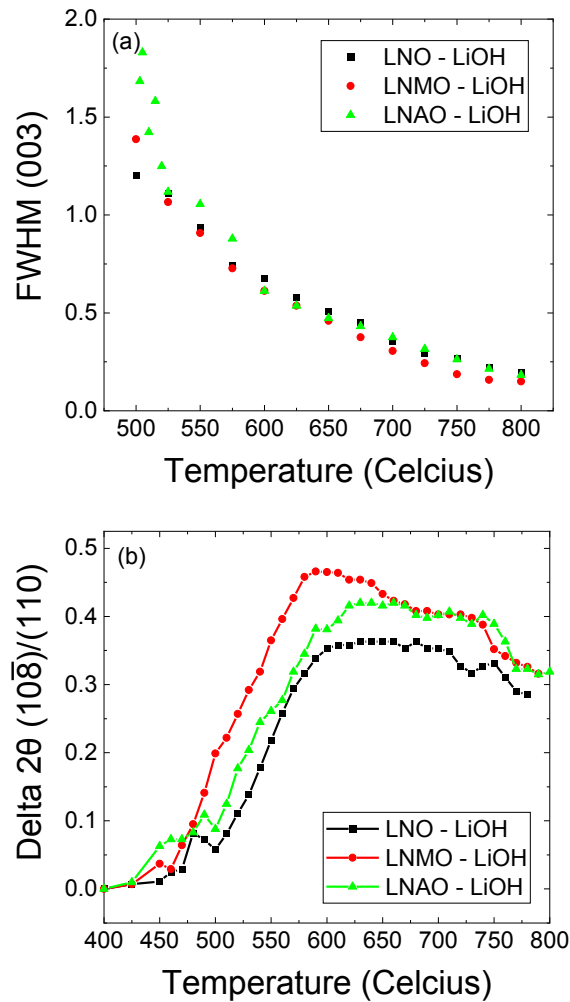


Figure 8-4. (a) FWHM of the (003) Bragg peak vs temperature, and (b) Delta 2 θ for the (10 $\bar{8}$)/(110) combined peak vs. temperature during heating for LNO (black) LNMO (red) and LNAO (green); all samples were prepared with LiOH•H₂O.

samples. The $(10\bar{8})/(110)$ peaks shift at the lowest temperature for LNMO. This data indicates that Mg doping may be beneficial to get a fully lithiated, crystalline material at a lower process temperature.

Figure 8-5 shows combined TGA-DSC-MS data for the same samples previously studied using the dynamic XRD approach. Figure 8-5a shows the normalized mass (wt.%) vs temperature curves, Figure 8-5b shows the ion current (nA) for mass number 18 (H_2O) vs temperature curves, and Figure 8-5c shows the associated heat flow vs temperature curves. At $\sim 260^\circ\text{C}$, as the hydroxide precursor converts to oxide, mass is lost and an associated peak in the heat flow curve is seen. At the same time a signal for water is detected by MS. In the corresponding XRD pattern for LNO (Figure 8-1) the hydroxide peak at $2\theta = 8.2^\circ$ disappears around 275°C . The onset of hydroxide to oxide conversion happens at $\sim 10^\circ\text{C}$ higher temperature for LNMO, which suggests that the Mg doping stabilizes the hydroxide. Sample lithiation should happen around the melting point of LiOH (471°C). Heat flow peaks are seen around 450°C as the samples lithiate and continues to lose mass. Some additional water is detected in this region originating from $\text{LiOH (l)} + \text{NiO (s)} + 1/4 \text{O}_2 \text{(g)} \rightarrow \text{LiNiO}_2 \text{(s)} + 1/2 \text{H}_2\text{O (g)}$, but less than during the hydroxide to oxide transition. In the corresponding XRD patterns the (003) Bragg peak appears above 500°C (Figure 8-3). Sample mass is stable from roughly 500°C to 800°C , which corresponds to the range in which crystal growth is seen from the peak sharpening in the XRD data (Figure 8-3). For full conversion of LiOH and Ni(OH)_2 to LiNiO_2 , $\sim 82\%$ of the original sample mass should be left. Note that the samples were preheated to 100°C so $\text{LiOH}\cdot\text{H}_2\text{O}$ was pre-dehydrated to LiOH. In the region labelled “crystal growth” the normalized weight percentage holds steady at about 82%. However, all three samples

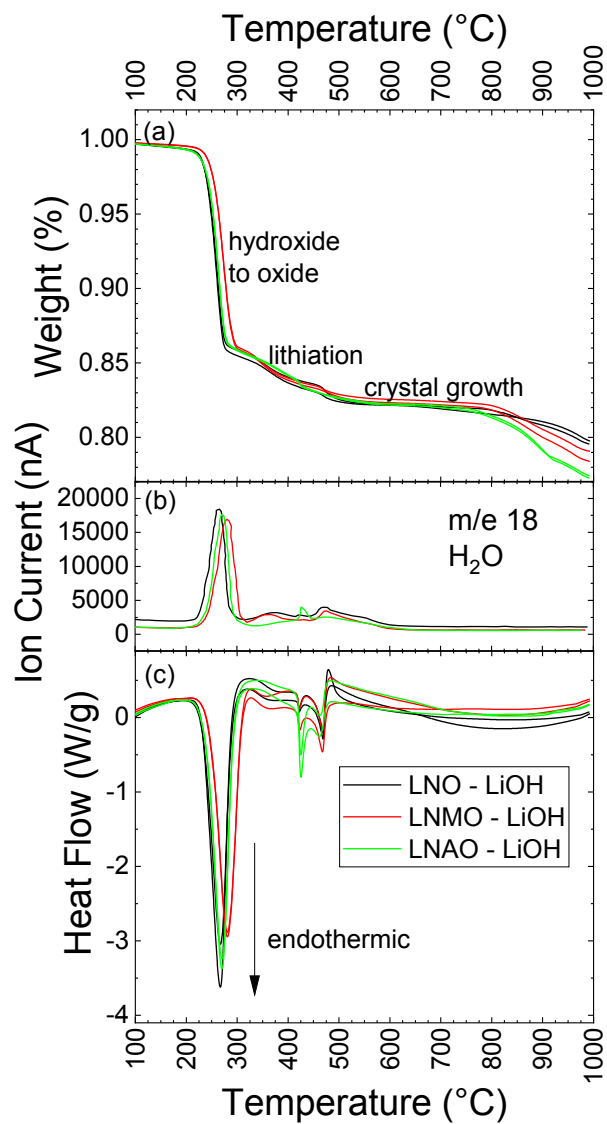


Figure 8-5. TGA-DSC-MS data for LNO, LNMO, and LNAO all prepared with LiOH. (a) Normalized sample mass (wt.%) vs. temperature. (b) Ion current for H₂O (mass 18) vs temperature. (c) Heat flow vs. temperature.

continue to lose mass above ~800°C, from lithium and oxygen loss. Compared to LNAO, LNMO loses less mass above 800°C.

Figure 8-6 shows the (003) and $(10\bar{8})/(110)$ Bragg peaks recorded at roughly 25°C intervals, between 400°C and 800°C, during heating for: (a) LNO, (b) LNMO and (c) LNAO, all prepared with Li_2CO_3 . Compared to LNO and LNAO, LNMO has sharper (003) Bragg peaks at a lower temperature and $(10\bar{8})/(110)$ peak splitting is visible at 800°C. This indicates that when using Li_2CO_3 , Mg doping is beneficial to reduce the temperature required to prepare fully lithiated, crystalline material.

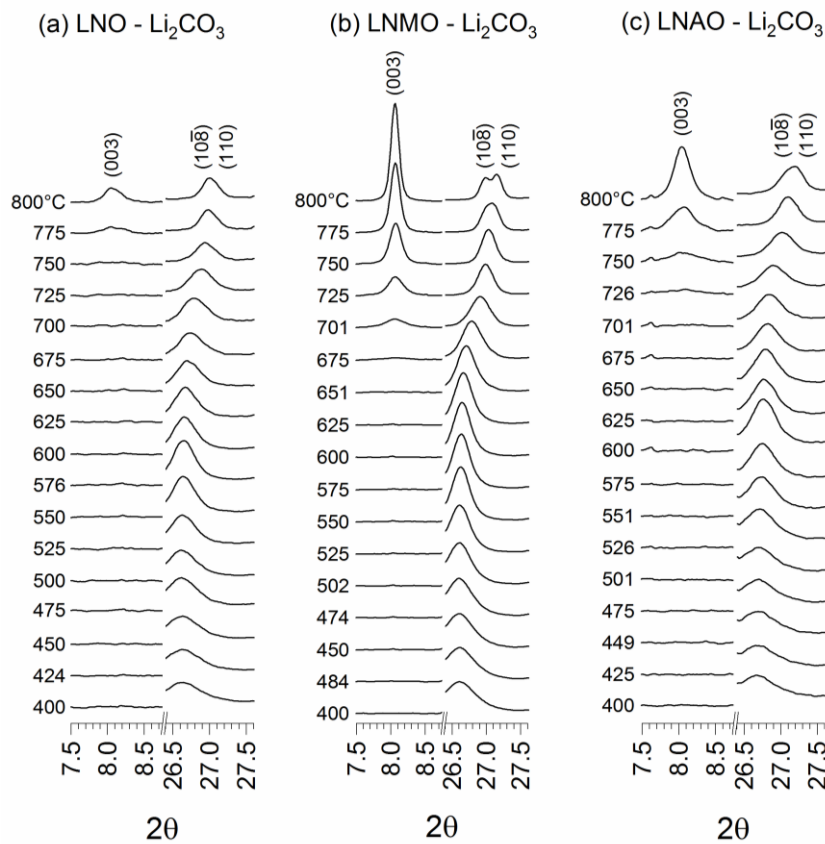


Figure 8-6. Detailed view of the (003) and $(10\bar{8})/(110)$ Bragg peaks during heating for: (a) LNO, (b) LNMO and (c) LNAO. All samples were prepared with Li_2CO_3 .

Figure 8-7 shows the change in the $(10\bar{8})/(110)$ combined peak position vs. temperature during heating for LNO (black), LNMO (red) and LNAO (green). All samples were prepared with Li_2CO_3 . A single value of 2θ is used to indicate the position of the

overlapping $(10\bar{8})/(110)$ peaks. Zero shift is set as the default 2θ value at 600°C in this instance. The $(10\bar{8})/(110)$ peaks shift at the lowest temperature for LNMO, which again indicates that Mg doping may be beneficial to get fully lithiated, crystalline material at a lower temperature.

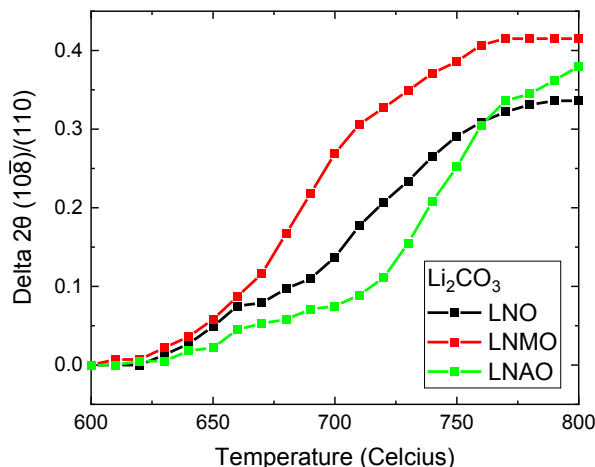


Figure 8-7. Delta 2θ for the $(10\bar{8})/(110)$ combined peak vs. temperature during heating for: LNO (black), LNMO (red) and LNAO (green); all samples were prepared with Li_2CO_3 .

8.3 Powder Synthesis using a Preheating Step

A two-step lithiation method, with a 480°C preheating stage, was recently developed by Li *et al.* to reduce impurities and “bricking” (powder sintered together in a hard brick) during synthesis of single-crystal NCA.¹⁹⁴ In this work the synthesis of LNAO samples, with and without a preheating step, were studied using the same *in-situ* XRD approach outlined earlier. Figure 8-8a and 13b show detailed views of the (003) and $(10\bar{8})/(110)$ XRD peaks during heating for: (a) LNAO and (b) LNAO with a 480°C preheat.

Figure 8-8c shows the FWHM of the (003) peak vs. temperature for both LNAO (green)

and LNAO with a 480°C preheat (blue). In each case, both samples were prepared with the addition of LiOH•H₂O. For the preheated sample, the (003) peak persists throughout the test and the (10 $\bar{8}$)/(110) combined peak does not move significantly during heating.

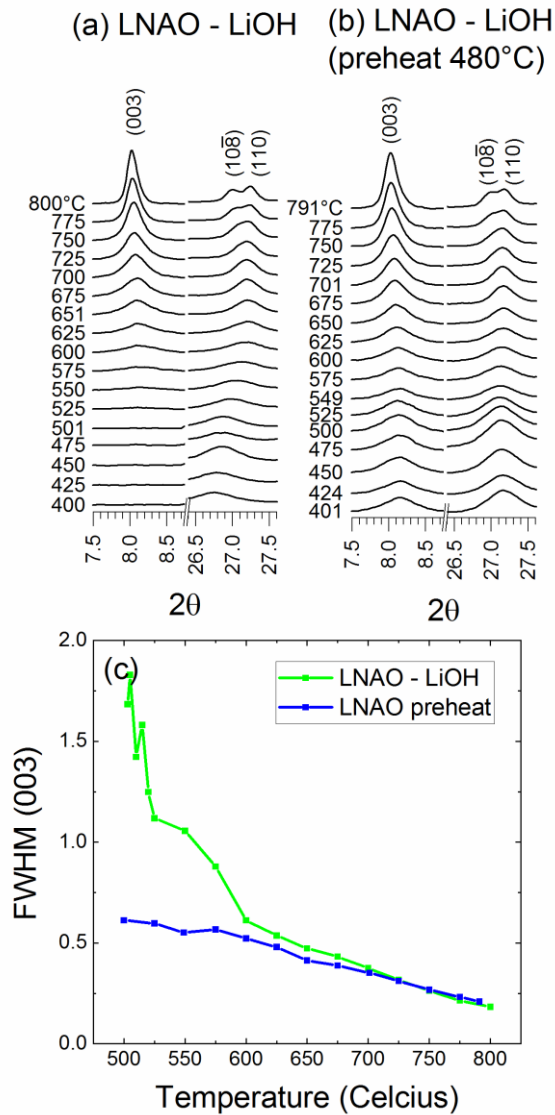


Figure 8-8. Detailed view of the (003) and (10 $\bar{8}$)/(110) XRD peaks during heating for: (a) LNAO and (b) LNAO with 480°C preheat. (c) The FWHM of the (003) peak vs temperature for LNAO (green) and LNAO with 480°C preheat (blue). Both samples were prepared with LiOH•H₂O.

The (003) peak FWHM vs. temperature curve is similar for both samples. These results suggest that the finished material is the same for synthesis both with and without a 480°C preheat step.

8.4 Powder Synthesis without Precursor Additions

Instead of the typical synthesis route using hydroxide precursors, samples can be prepared from the individual metal hydroxides. In this case, LNAO without any precursor was prepared from a combination of $\text{Ni}(\text{OH})_2$, $\text{Al}(\text{OH})_3$ and $\text{LiOH}\cdot\text{H}_2\text{O}$. Data is compared to LNAO prepared with precursor from $\text{LiNi}_{10.95}\text{Al}_{0.05}(\text{OH})_2$ and $\text{LiOH}\cdot\text{H}_2\text{O}$. Figure 8-9a and b show detailed views of the (003) and $(10\bar{8})/(110)$ Bragg peaks during heating for: (a) LNAO and (b) LNAO without precursor addition. Figure 8-9c shows $\Delta 2\theta$ for the $(10\bar{8})/(110)$ combined peaks vs. temperature, during heating for LNAO (green) and LNAO without precursor (red). In both cases the samples were produced with $\text{LiOH}\cdot\text{H}_2\text{O}$. The (003) peak grows at a similar rate for both samples, while the $(10\bar{8})/(110)$ combined peak shifts around the same temperature, if not slightly sooner, for the sample prepared without precursor. These results suggest that powder synthesis could be simplified by removing the usual step of making a precursor with the desired metal ratio before lithiation.

8.5 Conclusions

The synthesis of high nickel, cobalt-free positive electrode materials was studied by *in-situ* XRD. LiNiO_2 (LNO), $\text{Ni}_{0.975}\text{Mg}_{0.025}\text{O}_2$ (LNMO), and $\text{LiNi}_{10.95}\text{Al}_{0.05}\text{O}_2$ (LNAO) were prepared from hydroxide precursors with either $\text{LiOH}\cdot\text{H}_2\text{O}$ or Li_2CO_3 lithium sources and specific XRD peaks were measured during heating. The results show that samples

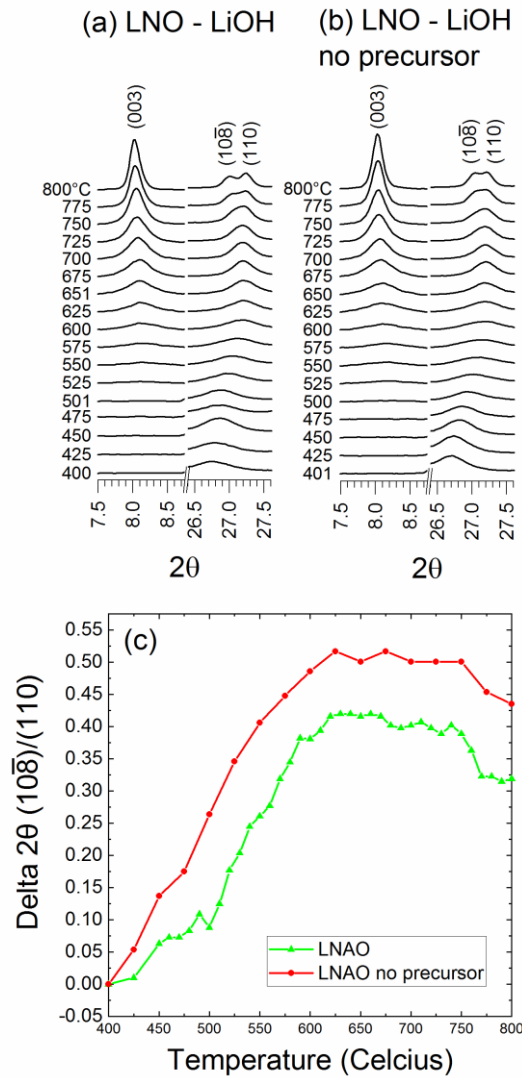


Figure 8-9. Detailed view of the (003) and (108)/(110) Bragg peaks during heating for: (a) LNAO and (b) LNAO without precursor. (c) Delta 2θ for the (108)/(110) combined peak vs. temperature during heating for LNAO (green) and LNAO without precursor (red). Both samples were prepared with LiOH•H₂O.

prepared using Li₂CO₃ require a higher synthesis temperature than LiOH, and that Mg doping may be beneficial with either lithium source to lower the temperature required to get fully lithiated, crystalline material. Additional experiments show that alternative

synthesis methods for LNAO using a 480°C preheat step or no precursor may give comparable final product as for LNAO prepared with one hydroxide precursor and one heating step. *Ex-situ* XRD and coin cell testing are required to verify the performance as positive electrode materials is the same.

CHAPTER 9 CONCLUSIONS

9.1 Summary

Lithium-metal anodes and high-nickel content layered positive electrode materials are highly desirable for their high specific capacity, but both are currently plagued by several problems that limit lifetime which were investigated in this thesis.

Anode-free lithium-metal cells lose capacity rapidly by either the formation of isolated metallic lithium or through irreversible reactions between electrolyte and lithium to form additional SEI. Huge volume changes and dendritic lithium morphology exacerbate these effects. High-nickel content positive electrode materials (NMC, NCA) have a myriad of their own problems, including the growth of a rock-salt surface layer which leads to high resistance during cycling (studied in this thesis), continued particle cracking during cycling, and a high cost due to the use of cobalt in the material.

There are some pathways to alleviate these failure mechanisms. For lithium-metal, the work in this thesis showed an appropriate choice of liquid electrolyte can suppress the formation of dendrites and extend cell lifetime. The literature showed that single-crystal positive electrode materials have minimal, if any, particle cracking during cycling, and when paired with surface coatings and electrolyte additives that suppress the formation of a rock-salt surface layer very long-lasting cells can be made.

The next logical step is to combine these advancements into a high-energy density anode-free lithium-metal cell made with a coated, single-crystal, cobalt-free cathode material. A cell of this chemistry has not yet been explored and would offer the highest energy

density and potentially longest lifetime of anode-free cells to date. The next sections discuss some specific projects in this direction.

9.2 Future Work

9.2.1 Anode-Free Salts

In this thesis only a small sampling of lithium salts were tested in anode-free cells, and these salts were not new, in the sense that they had previously been seen in the literature or are commonly used in lithium-ion cells. The results of Chapter 4 showed that LiDFOB gave good capacity retention (which reflects previous results from the literature), but was outperformed by the dual salt combination LiDFOB/LiBF₄. It was speculated that the organic/LiF hybrid SEI formed with LiDFOB/LiBF₄ was beneficial to capacity retention. Other new salts with large fluorinated anions should be tested.

Table 9-1. Three potential large-anion fluorinated salts that could be tested in anode-free cells. Short name, name, and molecular structure are shown.

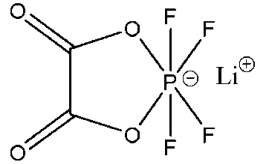
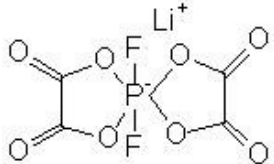
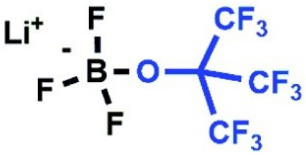
LiTFOP ²⁰³	Lithium tetrafluoro(oxalato)phosphate	
LiDFOB ²⁰³	Lithium difluoro bis-(oxalato) phosphate	
LiTFPFB ²⁰⁴	Lithium trifluoro(perfluoro-tert-butyloxy)borate	

Table 9-1 shows some potential candidates for salts in anode-free cells. These salts could be tested in combination with other known lithium salts to examine interactions. LiTFOP and LiDFOP are found in a patent,²⁰³ and LiTFPFB in the reference,²⁰⁴ but in-house synthesis may be required to develop new salts, like LiDFOP, which could boost the performance of anode-free cells even further.

Beyond testing new salts, additional mechanistic studies can be done. Chapter 4 primarily relied on SEI composition to probe the performance difference between salts, but there may be differences in electrolyte transport properties that influence capacity retention. For example, slow salt diffusion has been proposed to lead to dendritic lithium plating if lithium-ions are depleted at the anode surface and cannot be rapidly replenished.¹⁵⁷ Electrolyte transport properties should be investigated for anode-free electrolytes.

9.2.2 Anode-Free Pore Volume Measurements

In this thesis anode-free cells with LiPF₆ electrolyte grew dendritic and highly porous lithium anodes. For example see Figure 4-3 where cells lose capacity rapidly and SEM images show highly dendritic lithium morphology. When cells were dissected after cycling to harvest electrodes for SEM, no wetness from the electrolyte was visible. Although the electrodes appear “dry” NMR measurements showed that nearly all the original electrolyte is remaining (Figure 4-10). It is possible that the electrolyte is trapped in the pores of the electrodes and separator. With the ever increasing thickness and porosity of the lithium-metal anode there may be a point at which the pore volume exceeds the amount of electrolyte in the cell. In this event some areas of the anode or cathode would be “dry” and capacity loss would accelerate. Cells could be tested with a higher volume of electrolyte, but the same amount of salt in the cell, for example 1 mL of

0.6M LiPF₆ electrolyte instead of 0.5mL of 1M LiPF₆ electrolyte. Refilling cells with electrolyte part way through testing could also be tried to revive cells.

9.2.3 Anode-Free Formation, Rate, and Geometry

In Chapter 5 forming anode-free cells at 40°C and C/10 charge was shown to be immensely beneficial to capacity retention when cycled at 20°C. Lithium domains increase in size with increasing temperature and decreasing charge rate, so the effects should be even better with higher temp and slower rate. 55°C formation was tested with no added benefit, but slower rates were not yet explored. A systematic study could be done to see if there is a limit to lithium domain size with charge rate. Is there a charge rate at which the entire 100 cm² lithium-metal electrode is one continuous sheet, free of grain boundaries?

If anode-free cells were used in electric vehicles, the charge profile could be controlled but the discharge profile is entirely based on individual user. In this context it would be interesting to explore what charge conditions (rate, variable rate, temperature) gives the best performance under a variety of discharge conditions. Experiments like this have been done in the literature. Laman *et al* tested cycle life of lithium-metal coin cells with a molybdenum disulfide positive electrode and found that intermediate (~C/3) charge rates maximized lifetime.²⁰⁵ More recently Jiao *et al* tested cycle life of lithium metal coin cells with NMC positive electrode material, and found that lifetime was reduced by both plating higher areal capacity of lithium and by increasing the plating rate.²⁰⁶ Variable areal capacity and charge/discharge rates should be tested in anode-free NMC532 pouch cells.

Lastly, the anode-free cells tested in this work had soft pouch cell casings which required plastic and metal fixtures to apply external pressure. Cylindrical anode-free cells built in steel cans should be tested.

9.2.4 Anode-Free EIS

Degradation studies done in this thesis were destructive. Cells had to be cut open to measure NMR, and electrodes were removed for SEM and XPS. EIS should be used as a non-destructive method to track the degradation, and the results could be linked to the aforementioned degradation studies. An automatic EIS setup could be used, like that used in Chapter 6 to study lithium-ion pouch cells. Similar to Chapter 6, symmetric cells could also be used to study the individual cathode and anode impedance in anode-free cells.

9.2.5 Symmetric Cell Cycling

The results of Chapter 4 indicate that LiDFOB salt is primarily consumed at the negative electrode to reform the SEI, which breaks during lithium-metal expansion. Symmetric coin cells could be cycled to measure the amount of salt consumed at each individual electrode. One set of cells would be cycled with positive vs positive electrodes and one set of cells would be cycled with negative vs negative. Electrolyte composition after cycling could be measured by NMR. Such work has been done by Alex Louli and Jack deGooyer to be published soon.

9.2.6 Comparison to Solid-State Electrolyte

Capacity loss due to dendrite growth may fundamentally limit the lifetime of anode-free cells with liquid electrolytes, especially at low temperatures and high charge rates where dendrites have a high yield stress.¹⁰⁹ The SEI formed in liquid electrolytes may not

suppress dendrite growth under these conditions, but a high strength solid-electrolyte could. Solid electrolytes cannot be ignored as candidates for long-life anode-free cells and should be tested head-to-head with liquid electrolyte anode-free cells developed in this thesis.

As mentioned in the introduction, several solid-state electrolytes with high conductivity have been discovered, with the highest conductivity at 25 mS/cm for

$\text{Li}_{9.54}\text{Si}_{1.74}\text{P}_{1.44}\text{S}_{11.7}\text{Cl}_{0.3}$.^{91,92} One of these materials may be commercially viable if the interfacial and high voltage stability can be improved. For an initial comparison with liquid electrolyte, solid electrolytes could be tested in a cell with a low-voltage cathode (like LFP), similar to what has been done in the past for LLZO solid electrolyte which is unstable at high voltage. Two potential candidates are Li_3PS_4 , and $\text{Li}_7\text{P}_2\text{S}_8\text{I}$ which may give long-term stability against lithium-metal since the initial decomposition products (Li_2S , Li_3P , LiI , Li_2O) are electrically insulating.^{94,207} These materials have a low calculated oxidation potential (2.31 V vs Li/Li^+), but it has been suggested that appropriate cathode coatings may improve the long-term stability after initial oxidation.⁹⁴

9.2.7 *In-situ* XRD Heating Method Development

In Chapter 8 a special apparatus was used to measure XRD of cathode materials during synthesis. This apparatus was developed for the beamline at CLS and has some disadvantages when used to study cathode materials. The biggest problem was that the sample must be housed in an alumina tube, which contributed many extra diffraction peaks and made it impossible to do refinement on the full XRD patterns. For other, non-cathode materials, a fused silica tube can be used which gives broad humps and could more easily be differentiated from the sharp sample peaks. However, silica reacts with

the lithium sources used in cathode synthesis so this is not an option. In addition, the small amount of sample (< 100 mg) makes it difficult to do any other analysis (ICP, SEM, electrochemical testing). Using an alumina tube with a larger inner diameter and thinner walls would reduce the signal from the tube and increase the sample size. In this work, the alumina tubes were 1.56 mm OD and 0.79 ID. If tubes with thinner walls but the same OD are not available, the heating apparatus could be adapted to accommodate a larger OD tube.

These problems could be avoided by adding a sample heating stage to a lab-scale diffractometer. Samples could sit in open alumina boats with oxygen flowing over the surface. In this case XRD could be measured free from alumina peaks and a larger amount of sample could be heated at once. For example, Bruker makes a furnace sample stage compatible with the Bruker D8 Discover diffractometer in our lab. The sample stage heats up to 1100°C using an AlCr heater, and can operate in an oxidative atmosphere.

9.2.8 Single-Crystal LNMO

Chapter 8 showed that it may be possible to use a lower synthesis temperature with $\text{LiNi}_{0.975}\text{Mg}_{0.025}\text{O}_2$ (LNMO), compared to LiNiO_2 (LNO) and $\text{LiNi}_{0.95}\text{Al}_{0.05}\text{O}_2$ (LNAO). Lower synthesis temperatures of LNMO should be tested in typical lab scale experiments with SEM, *ex-situ* XRD, and electrochemical testing to see if quality material can be made at a lower temperature. Previously, LNMO was synthesized at 700°C with 20 hr dwell time and LiOH.^{9,208} Data in Figure 8-4 suggests that a temperature as low as 600°C should be tested with LiOH.

In addition, single-crystal LNMO should be tested as a potentially long-life cobalt-free material. However, it is known that even 2.5 atom% Mg doping reduces the materials specific capacity.²⁰⁸ Single-crystal LNO with a Mg based coating could be tested to get the lifetime benefits of Mg doping without the capacity penalty.

9.2.9 Anode-Free High-Nickel Cobalt-Free Cell

The anode-free and positive electrode developments in this work should be combined into a high energy density lithium battery. Even though high-nickel, cobalt-free cathode materials are still in early development, using them in an anode-free cell may not compromise lifetime at all given that the rapid capacity loss is driven by the lithium metal anode. If a cathode material were used with ~ 245 mAh/g (like LNO - most optimistic scenario) and 3.8 V average, an anode-free cell could potentially reach 500 Wh/kg. [This assumes 75% of stack energy density could be reached in a commercial cell, and stack energy density is calculated with 21 mg/cm² cathode loading, 3.5 g/cm³ cathode density, 94% active material, 10 μ m thick aluminum and copper foil, 14 μ m thick separator and separator density is approximated as polyethylene (0.95 g/cm³) with 40% porosity = 0.57 g/cm³.] A high-nickel cobalt-free anode-free battery would be the ultimate culmination of the work in this thesis.

REFERENCES

1. A. P. Cohn, N. Muralidharan, R. Carter, K. Share, and C. L. Pint, *Nano Lett.*, **17**, 1296–1301 (2017).
2. J. Qian, B. D. Adams, J. Zheng, W. Xu, W. A. Henderson, J. Wang, M. E. Bowden, S. Xu, J. Hu, and J.-G. Zhang, *Adv. Funct. Mater.*, **26**, 7094–7102 (2016).
3. B. J. Neudecker, N. J. Dudney, and J. B. Bates, *J. Electrochem. Soc.*, **147**, 517–523 (2000).
4. F. Ding, W. Xu, X. Chen, J. Zhang, M. H. Engelhard, Y. Zhang, B. R. Johnson, J. V. Crum, T. A. Blake, X. Liu, and J.-G. Zhang, *J. Electrochem. Soc.*, **160**, A1894–A1901 (2013).
5. D. Aurbach, E. Zinigrad, H. Teller, and P. Dan, *J. Electrochem. Soc.*, **147**, 1274–1279 (2000).
6. D. Lin, Y. Liu, and Y. Cui, *Nat. Nanotechnol.*, **12**, 194–206 (2017).
7. J. Li, A. R. Cameron, H. Li, S. Glazier, D. Xiong, M. Chatzidakis, J. Allen, G. A. Botton, and J. R. Dahn, *J. Electrochem. Soc.*, **164**, A1534–A1544 (2017).
8. R. Weber, C. R. Fell, J. R. Dahn, and S. Hy, *J. Electrochem. Soc.*, **164**, A2992–A2999 (2017).
9. H. Li, M. Cormier, N. Zhang, J. Inglis, J. Li, and J. R. Dahn, *J. Electrochem. Soc.*, **166**, A429–A439 (2019).
10. T. Reddy, *Linden's Handbook of Batteries, 4th Edition*, 4 edition., p. 1456, McGraw-Hill Education, New York, (2010).
11. R. Jung, M. Metzger, F. Maglia, C. Stinner, and H. A. Gasteiger, *J. Electrochem. Soc.*, **164**, A1361–A1377 (2017).
12. N. Zhang, J. Li, H. Li, A. Liu, Q. Huang, L. Ma, Y. Li, and J. R. Dahn, *Chem. Mater.*, **30**, 8852–8860 (2018).
13. H.-J. Noh, S. Youn, C. S. Yoon, and Y.-K. Sun, *J. Power Sources*, **233**, 121–130 (2013).
14. S.-T. Myung, H.-J. Noh, S.-J. Yoon, E.-J. Lee, and Y.-K. Sun, *J. Phys. Chem. Lett.*, **5**, 671–679 (2014).
15. J. Li, J. Camardese, R. Shunmugasundaram, S. Glazier, Z. Lu, and J. R. Dahn, *Chem. Mater.*, **27**, 3366–3377 (2015).
16. X. Zeng, C. Zhan, J. Lu, and K. Amine, *Chem*, **4**, 690–704 (2018).

17. F. Schipper, E. M. Erickson, C. Erk, J.-Y. Shin, F. F. Chesneau, and D. Aurbach, *J. Electrochem. Soc.*, **164**, A6220–A6228 (2017).
18. S.-T. Myung, F. Maglia, K.-J. Park, C. S. Yoon, P. Lamp, S.-J. Kim, and Y.-K. Sun, *ACS Energy Lett.*, **2**, 196–223 (2017).
19. M. N. Obrovac and V. L. Chevrier, *Chem. Rev.*, **114**, 11444–11502 (2014).
20. K. Xu, *Chem. Rev.*, **104**, 4303–4418 (2004).
21. J. O. Besenhard and G. Eichinger, *J. Electroanal. Chem. Interfacial Electrochem.*, **68**, 1–18 (1976).
22. R. Younesi, G. M. Veith, P. Johansson, K. Edström, and T. Vegge, *Energy Environ. Sci.*, **8**, 1905–1922 (2015).
23. J. T. Dudley, D. P. Wilkinson, G. Thomas, R. LeVae, S. Woo, H. Blom, C. Horvath, M. W. Juzkow, B. Denis, P. Juric, P. Aghakian, and J. R. Dahn, *J. Power Sources*, **35**, 59–82 (1991).
24. M. L. Lazar and B. L. Lucht, *J. Electrochem. Soc.*, **162**, A928–A934 (2015).
25. K. Xu, S. Zhang, T. R. Jow, W. Xu, and C. A. Angell, *Electrochem. Solid-State Lett.*, **5**, A26–A29 (2002).
26. H.-B. Han, S.-S. Zhou, D.-J. Zhang, S.-W. Feng, L.-F. Li, K. Liu, W.-F. Feng, J. Nie, H. Li, X.-J. Huang, M. Armand, and Z.-B. Zhou, *J. Power Sources*, **196**, 3623–3632 (2011).
27. K. Matsumoto, K. Inoue, K. Nakahara, R. Yuge, T. Noguchi, and K. Utsugi, *J. Power Sources*, **231**, 234–238 (2013).
28. C. L. Champion, W. Li, and B. L. Lucht, *J. Electrochem. Soc.*, **152**, A2327–A2334 (2005).
29. S. E. Sloop, J. K. Pugh, S. Wang, J. B. Kerr, and K. Kinoshita, *Electrochem. Solid-State Lett.*, **4**, A42–A44 (2001).
30. M. Stich, M. Göttliger, M. Kurniawan, U. Schmidt, and A. Bund, *J. Phys. Chem. C*, **122**, 8836–8842 (2018).
31. E. R. Logan, E. M. Tonita, K. L. Gering, J. Li, X. Ma, L. Y. Beaulieu, and J. R. Dahn, *J. Electrochem. Soc.*, **165**, A21–A30 (2018).
32. K. Xu, *Chem. Rev.*, **114**, 11503–11618 (2014).
33. E. Peled, *J. Electrochem. Soc.*, **126**, 2047–2051 (1979).

34. S. Jurng, Z. L. Brown, J. Kim, and B. L. Lucht, *Energy Environ. Sci.*, **11**, 2600–2608 (2018).
35. M. Nie, D. Chalasani, D. P. Abraham, Y. Chen, A. Bose, and B. L. Lucht, *J. Phys. Chem. C*, **117**, 1257–1267 (2013).
36. S. S. Zhang, *J. Power Sources*, **162**, 1379–1394 (2006).
37. K. Min, K. Kim, C. Jung, S.-W. Seo, Y. Y. Song, H. S. Lee, J. Shin, and E. Cho, *J. Power Sources*, **315**, 111–119 (2016).
38. J. Xia, S. L. Glazier, R. Petibon, and J. R. Dahn, *J. Electrochem. Soc.*, **164**, A1239–A1250 (2017).
39. L. Ma, J. Xia, and J. R. Dahn, *J. Electrochem. Soc.*, **161**, A2250–A2254 (2014).
40. J. Xia, L. Madec, L. Ma, L. D. Ellis, W. Qiu, K. J. Nelson, Z. Lu, and J. R. Dahn, *J. Power Sources*, **295**, 203–211 (2015).
41. G. Yan, X. Li, Z. Wang, H. Guo, and C. Wang, *J. Power Sources*, **248**, 1306–1311 (2014).
42. Z. Wang, L. Xing, J. Li, M. Xu, and W. Li, *J. Power Sources*, **307**, 587–592 (2016).
43. L. Ma, L. Ellis, S. L. Glazier, X. Ma, Q. Liu, J. Li, and J. R. Dahn, *J. Electrochem. Soc.*, **165**, A891–A899 (2018).
44. L. D. Ellis, J. Xia, A. J. Louli, and J. R. Dahn, *J. Electrochem. Soc.*, **163**, A1686–A1692 (2016).
45. M. Xu, L. Zhou, Y. Dong, Y. Chen, J. Demeaux, A. D. MacIntosh, A. Garsuch, and B. L. Lucht, *Energy Environ. Sci.*, **9**, 1308–1319 (2016).
46. L. Madec, J. Xia, R. Petibon, K. J. Nelson, J.-P. Sun, I. G. Hill, and J. R. Dahn, *J. Phys. Chem. C*, **118**, 29608–29622 (2014).
47. D. Y. Wang, J. Xia, L. Ma, K. J. Nelson, J. E. Harlow, D. Xiong, L. E. Downie, R. Petibon, J. C. Burns, A. Xiao, W. M. Lamanna, and J. R. Dahn, *J. Electrochem. Soc.*, **161**, A1818–A1827 (2014).
48. D. Y. Wang, N. N. Sinha, R. Petibon, J. C. Burns, and J. R. Dahn, *J. Power Sources*, **251**, 311–318 (2014).
49. R. Petibon, E. C. Henry, J. C. Burns, N. N. Sinha, and J. R. Dahn, *J. Electrochem. Soc.*, **161**, A66–A74 (2014).
50. J. Xia, N. N. Sinha, L. P. Chen, and J. R. Dahn, *J. Electrochem. Soc.*, **161**, A264–A274 (2014).

51. J. Xia, L. Ma, C. P. Aiken, K. J. Nelson, L. P. Chen, and J. R. Dahn, *J. Electrochem. Soc.*, **161**, A1634–A1641 (2014).
52. J. Xia, N. N. Sinha, L. P. Chen, G. Y. Kim, D. J. Xiong, and J. R. Dahn, *J. Electrochem. Soc.*, **161**, A84–A88 (2014).
53. J. Li, H. Liu, J. Xia, A. R. Cameron, M. Nie, G. A. Botton, and J. R. Dahn, *J. Electrochem. Soc.*, **164**, A655–A665 (2017).
54. L. Ma, J. Xia, and J. R. Dahn, *J. Electrochem. Soc.*, **162**, A1170–A1174 (2015).
55. B. S. Parimalam and B. L. Lucht, *J. Electrochem. Soc.*, **165**, A251–A255 (2018).
56. Y. Zhu, Y. Li, M. Bettge, and D. P. Abraham, *J. Electrochem. Soc.*, **159**, A2109–A2117 (2012).
57. M. Hu, J. Wei, L. Xing, and Z. Zhou, *J. Appl. Electrochem.*, **42**, 291–296 (2012).
58. M. Xu, N. Tsiouvaras, A. Garsuch, H. A. Gasteiger, and B. L. Lucht, *J. Phys. Chem. C*, **118**, 7363–7368 (2014).
59. J. E. Harlow, X. Ma, J. Li, E. Logan, Y. Liu, N. Zhang, L. Ma, S. L. Glazier, M. M. E. Cormier, M. Genovese, S. Buteau, A. Cameron, J. E. Stark, and J. R. Dahn, *J. Electrochem. Soc.*, **166**, A3031–A3044 (2019).
60. R. Petibon, J. Xia, L. Ma, M. K. G. Bauer, K. J. Nelson, and J. R. Dahn, *J. Electrochem. Soc.*, **163**, A2571–A2578 (2016).
61. J. Li, S. L. Glazier, K. Nelson, X. Ma, J. Harlow, J. Paulsen, and J. R. Dahn, *J. Electrochem. Soc.*, **165**, A3195–A3204 (2018).
62. B. Li, Y. Wang, W. Tu, Z. Wang, M. Xu, L. Xing, and W. Li, *Electrochimica Acta*, **147**, 636–642 (2014).
63. S. Mai, M. Xu, X. Liao, J. Hu, H. Lin, L. Xing, Y. Liao, X. Li, and W. Li, *Electrochimica Acta*, **147**, 565–571 (2014).
64. Y. Watanabe, S. Kinoshita, S. Wada, K. Hoshino, H. Morimoto, and S. Tobishima, *J. Power Sources*, **179**, 770–779 (2008).
65. Y. Zhu, M. D. Casselman, Y. Li, A. Wei, and D. P. Abraham, *J. Power Sources*, **246**, 184–191 (2014).
66. A. Abouimrane, I. Belharouak, and K. Amine, *Electrochem. Commun.*, **11**, 1073–1076 (2009).
67. J. Xia, J. Self, L. Ma, and J. R. Dahn, *J. Electrochem. Soc.*, **162**, A1424–A1431 (2015).

68. E. Markevich, G. Salitra, K. Fridman, R. Sharabi, G. Gershinsky, A. Garsuch, G. Semrau, M. A. Schmidt, and D. Aurbach, *Langmuir*, **30**, 7414–7424 (2014).
69. H. Duncan, N. Salem, and Y. Abu-Lebdeh, *J. Electrochem. Soc.*, **160**, A838–A848 (2013).
70. J. Xia, M. Nie, J. C. Burns, A. Xiao, W. M. Lamanna, and J. R. Dahn, *J. Power Sources*, **307**, 340–350 (2016).
71. J. Li, L. E. Downie, L. Ma, W. Qiu, and J. R. Dahn, *J. Electrochem. Soc.*, **162**, A1401–A1408 (2015).
72. N. Nitta, F. Wu, J. T. Lee, and G. Yushin, *Mater. Today*, **18**, 252–264 (2015).
73. C. Fang, J. Li, M. Zhang, Y. Zhang, F. Yang, J. Z. Lee, M.-H. Lee, J. Alvarado, M. A. Schroeder, Y. Yang, B. Lu, N. Williams, M. Ceja, L. Yang, M. Cai, J. Gu, K. Xu, X. Wang, and Y. S. Meng, *Nature*, **572**, 511–515 (2019).
74. M. S. Whittingham, *Chem. Rev.*, **104**, 4271–4302 (2004).
75. K. Brandt, *Solid State Ion.*, **69**, 173–183 (1994).
76. J.-J. Woo, V. A. Maroni, G. Liu, J. T. Vaughey, D. J. Gosztola, K. Amine, and Z. Zhang, *J. Electrochem. Soc.*, **161**, A827–A830 (2014).
77. D. Aurbach, *J. Power Sources*, **89**, 206–218 (2000).
78. Y. S. Cohen, Y. Cohen, and D. Aurbach, *J. Phys. Chem. B*, **104**, 12282–12291 (2000).
79. W. Xu, J. Wang, F. Ding, X. Chen, E. Nasybulin, Y. Zhang, and J.-G. Zhang, *Energy Environ. Sci.*, **7**, 513–537 (2014).
80. K. Kanamura, S. Shiraishi, and Z. Takehara, *J. Electrochem. Soc.*, **143**, 2187–2197 (1996).
81. K. Kanamura, S. Shiraishi, and Z. Takehara, *J. Fluor. Chem.*, **87**, 235–243 (1998).
82. S. Shiraishi, K. Kanamura, and Z. Takehara, *J. Electrochem. Soc.*, **146**, 1633–1639 (1999).
83. R. Mogi, M. Inaba, S.-K. Jeong, Y. Iriyama, T. Abe, and Z. Ogumi, *J. Electrochem. Soc.*, **149**, A1578–A1583 (2002).
84. Y. Lu, Z. Tu, and L. A. Archer, *Nat. Mater.*, **13**, 961–969 (2014).
85. X. Fan, L. Chen, X. Ji, T. Deng, S. Hou, J. Chen, J. Zheng, F. Wang, J. Jiang, K. Xu, and C. Wang, *Chem*, **4**, 174–185 (2018).

86. L. Suo, Y.-S. Hu, H. Li, M. Armand, and L. Chen, *Nat. Commun.*, **4**, 1–9 (2013).
87. J. Qian, W. A. Henderson, W. Xu, P. Bhattacharya, M. Engelhard, O. Borodin, and J.-G. Zhang, *Nat. Commun.*, **6**, 6362 (2015).
88. Y. Gofar, M. Ben-Zion, and D. Aurbach, *J. Power Sources*, **39**, 163–178 (1992).
89. Z. Takehara, *J. Power Sources*, **68**, 82–86 (1997).
90. Z. L. Brown and B. L. Lucht, *J. Electrochem. Soc.*, **166**, A5117–A5121 (2019).
91. N. Kamaya, K. Homma, Y. Yamakawa, M. Hirayama, R. Kanno, M. Yonemura, T. Kamiyama, Y. Kato, S. Hama, K. Kawamoto, and A. Mitsui, *Nat. Mater.*, **10**, 682–686 (2011).
92. Y. Kato, S. Hori, T. Saito, K. Suzuki, M. Hirayama, A. Mitsui, M. Yonemura, H. Iba, and R. Kanno, *Nat. Energy*, **1**, 1–7 (2016).
93. G. M. Stone, S. A. Mullin, A. A. Teran, D. T. Hallinan, A. M. Minor, A. Hexemer, and N. P. Balsara, *J. Electrochem. Soc.*, **159**, A222–A227 (2012).
94. Y. Zhu, X. He, and Y. Mo, *ACS Appl. Mater. Interfaces*, **7**, 23685–23693 (2015).
95. P. Barai, K. Higa, A. T. Ngo, L. A. Curtiss, and V. Srinivasan, *J. Electrochem. Soc.*, **166**, A1752–A1762 (2019).
96. Y. Ren, Y. Shen, Y. Lin, and C.-W. Nan, *Electrochem. Commun.*, **57**, 27–30 (2015).
97. C. Brissot, M. Rosso, J.-N. Chazalviel, and S. Lascaud, *J. Power Sources*, **81–82**, 925–929 (1999).
98. A. Manuel Stephan and K. S. Nahm, *Polymer*, **47**, 5952–5964 (2006).
99. D. Zhou, D. Shanmukaraj, A. Tkacheva, M. Armand, and G. Wang, *Chem*, **5**, 2326–2352 (2019).
100. H. Pfeiffer, F. Tancret, M.-P. Bichat, L. Monconduit, F. Favier, and T. Brousse, *Electrochem. Commun.*, **6**, 263–267 (2004).
101. K. Yan, Z. Lu, H.-W. Lee, F. Xiong, P.-C. Hsu, Y. Li, J. Zhao, S. Chu, and Y. Cui, *Nat. Energy*, **1**, 16010 (2016).
102. M. Genovese, A. J. Louli, R. Weber, R. J. Sanderson, M. B. Johnson, and J. R. Dahn, *J. Electrochem. Soc.*, **165**, A3000–A3013 (2018).
103. L.-L. Lu, J. Ge, J.-N. Yang, S.-M. Chen, H.-B. Yao, F. Zhou, and S.-H. Yu, *Nano Lett.*, **16**, 4431–4437 (2016).

104. Y. Shi, Z. Wang, H. Gao, J. Niu, W. Ma, J. Qin, Z. Peng, and Z. Zhang, *J. Mater. Chem. A*, **7**, 1092–1098 (2019).
105. N. Zhang, Y. Zheng, A. Trifonova, and W. Pfleging, *J. Appl. Electrochem.*, **47**, 829–837 (2017).
106. X. Ke, Y. Cheng, J. Liu, L. Liu, N. Wang, J. Liu, C. Zhi, Z. Shi, and Z. Guo, *ACS Appl. Mater. Interfaces*, **10**, 13552–13561 (2018).
107. J.-Y. So, C.-H. Lee, J.-E. Kim, H.-J. Kim, J. Jun, and W.-G. Bae, *Materials*, **11** (2018).
108. H. N. Umh, J. Park, J. Yeo, S. Jung, I. Nam, and J. Yi, *Electrochem. Commun.*, **99**, 27–31 (2019).
109. C. Xu, Z. Ahmad, A. Aryanfar, V. Viswanathan, and J. R. Greer, *Proc. Natl. Acad. Sci.*, **114**, 57–61 (2017).
110. W. S. LePage, Y. Chen, E. Kazyak, K.-H. Chen, A. J. Sanchez, A. Poli, E. M. Arruda, M. D. Thouless, and N. P. Dasgupta, *J. Electrochem. Soc.*, **166**, A89–A97 (2019).
111. J. Wang, W. Huang, A. Pei, Y. Li, F. Shi, X. Yu, and Y. Cui, *Nat. Energy*, **4**, 664–670 (2019).
112. A. J. Louli, M. Genovese, R. Weber, S. G. Hames, E. R. Logan, and J. R. Dahn, *J. Electrochem. Soc.*, **166**, A1291–A1299 (2019).
113. D. P. Wilkinson, H. Blom, K. Brandt, and D. Wainwright, *J. Power Sources*, **36**, 517–527 (1991).
114. T. Hirai, I. Yoshimatsu, and J. Yamaki, *J. Electrochem. Soc.*, **141**, 611–614 (1994).
115. D. P. Wilkinson and D. Wainwright, *J. Electroanal. Chem.*, **355**, 193–203 (1993).
116. A. Pei, G. Zheng, F. Shi, Y. Li, and Y. Cui, *Nano Lett.*, **17**, 1132–1139 (2017).
117. H. Sano, H. Sakaebe, H. Senoh, and H. Matsumoto, *J. Electrochem. Soc.*, **161**, A1236–A1240 (2014).
118. A. J. Bard and L. R. Faulkner, *Electrochemical Methods: Fundamentals and Applications*, p. 864, Wiley, (2000).
119. D. Pritzl, J. Landesfeind, S. Solchenbach, and H. A. Gasteiger, *J. Electrochem. Soc.*, **165**, A2145–A2153 (2018).
120. M.-T. F. Rodrigues, K. Kalaga, S. E. Trask, I. A. Shkrob, and D. P. Abraham, *J. Electrochem. Soc.*, **165**, A1697–A1705 (2018).

121. J. Landesfeind, D. Pritzl, and H. A. Gasteiger, *J. Electrochem. Soc.*, **164**, A1773–A1783 (2017).
122. D. Dees, E. Gunen, D. Abraham, A. Jansen, and J. Prakash, *J. Electrochem. Soc.*, **152**, A1409–A1417 (2005).
123. J. A. Gilbert, J. Bareño, T. Spila, S. E. Trask, D. J. Miller, B. J. Polzin, A. N. Jansen, and D. P. Abraham, *J. Electrochem. Soc.*, **164**, A6054–A6065 (2017).
124. K. J. Nelson, G. L. d'Eon, A. T. B. Wright, L. Ma, J. Xia, and J. R. Dahn, *J. Electrochem. Soc.*, **162**, A1046–A1054 (2015).
125. J. C. Burns, L. J. Krause, D.-B. Le, L. D. Jensen, A. J. Smith, D. Xiong, and J. R. Dahn, *J. Electrochem. Soc.*, **158**, A1417–A1422 (2011).
126. R. Petibon, C. P. Aiken, N. N. Sinha, J. C. Burns, H. Ye, C. M. VanElzen, G. Jain, S. Trussler, and J. R. Dahn, *J. Electrochem. Soc.*, **160**, A117–A124 (2013).
127. W. Zhou and Z. L. Wang, Eds., *Scanning Microscopy for Nanotechnology: Techniques and Applications*, Springer-Verlag, New York, (2007).
128. R. S. Mikhail and S. Brunauer, *J. Colloid Interface Sci.*, **52**, 572–577 (1975).
129. D. A. Payne, K. S. W. Sing, and D. H. Turk, *J. Colloid Interface Sci.*, **43**, 287–293 (1973).
130. S. Brunauer, P. H. Emmett, and E. Teller, *J. Am. Chem. Soc.*, **60**, 309–319 (1938).
131. S. Hofmann, *Auger- and X-Ray Photoelectron Spectroscopy in Materials Science: A User-Oriented Guide*, p. 544, Springer Science & Business Media, (2012).
132. B. D. Cullity and S. R. Stock, *Elements of X-Ray Diffraction*, 3 edition., p. 696, Pearson, Upper Saddle River, NJ, (2001).
133. H. M. Rietveld, *J. Appl. Crystallogr.*, **2**, 65–71 (1969).
134. V. Pecharsky and P. Zavalij, *Fundamentals of Powder Diffraction and Structural Characterization of Materials*, p. 732, Springer Science & Business Media, (2005).
135. A. C. Larson and R. B. Von Dreele, *General Structure Analysis System (GSAS)*, (2000).
136. B. H. Toby, *J. Appl. Cryst.*, **34**, 210–213 (2001).
137. C. Prescher and V. B. Prakapenka, *High Press. Res.*, **35**, 223–230 (2015).
138. R. Petibon, L. Rotermund, K. J. Nelson, A. S. Gozdz, J. Xia, and J. R. Dahn, *J. Electrochem. Soc.*, **161**, A1167–A1172 (2014).

139. M. Loudon, *By Marc Loudon - Organic Chemistry*, Fifth edition edition., Roberts and Company Publishers, (2008).
140. R. R. Ernst, G. Bodenhausen, and A. Wokaun, *Principles of Nuclear Magnetic Resonance in One and Two Dimensions*, Reprint edition., p. 634, Clarendon Press, Oxford, (1990).
141. T. Schedlbauer, S. Krüger, R. Schmitz, R. W. Schmitz, C. Schreiner, H. J. Gores, S. Passerini, and M. Winter, *Electrochimica Acta*, **92**, 102–107 (2013).
142. Z. L. Brown, S. Jurng, C. C. Nguyen, and B. L. Lucht, *ACS Appl. Energy Mater.*, **1**, 3057–3062 (2018).
143. S. Jiao, X. Ren, R. Cao, M. H. Engelhard, Y. Liu, D. Hu, D. Mei, J. Zheng, W. Zhao, Q. Li, N. Liu, B. D. Adams, C. Ma, J. Liu, J. G. Zhang, and W. Xu, *Nat. Energy*, **3**, 1–8 (2018).
144. G. Z. Tulibaeva, A. F. Shestakov, V. I. Volkov, and O. V. Yarmolenko, *Russ. J. Phys. Chem. A*, **92**, 749–755 (2018).
145. *NIST X-Ray Photoelectron Spectrosc. Database NIST Stand. Ref. Database Number 20 Natl. Inst. Stand. Technol. Gaithersburg MD 20899* (2000) <http://srdata.nist.gov/xps/>.
146. Z. L. Brown and B. L. Lucht, *J. Electrochem. Soc.*, **166**, A5117–A5121 (2019).
147. R. Crowe and J. P. S. Badyal, *J. Chem. Soc. Chem. Commun.*, **0**, 958–959 (1991).
148. Y. Zhu, Y. Li, M. Bettge, and D. P. Abraham, *J. Electrochem. Soc.*, **159**, A2109–A2117 (2012).
149. C. P. Aiken, J. Xia, D. Y. Wang, D. A. Stevens, S. Trussler, and J. R. Dahn, *J. Electrochem. Soc.*, **161**, A1548–A1554 (2014).
150. M. Genovese, A. J. Louli, R. Weber, C. Martin, T. Taskovic, and J. R. Dahn, *J. Electrochem. Soc.*, **166**, A3342–A3347 (2019).
151. I. A. Shkrob, Y. Zhu, T. W. Marin, and D. P. Abraham, *J. Phys. Chem. C*, **117**, 23750–23756 (2013).
152. A. Ahmadiparidari, R. E. Warburton, L. Majidi, M. Asadi, A. Chamaani, J. R. Jokisaari, S. Rastegar, Z. Hemmat, B. Sayahpour, R. S. Assary, B. Narayanan, P. Abbasi, P. C. Redfern, A. Ngo, M. Vörös, J. Greeley, R. Klie, L. A. Curtiss, and A. Salehi-Khojin, *Adv. Mater.*, **31**, 1902518 (2019).
153. J. Qian, B. D. Adams, J. Zheng, W. Xu, W. A. Henderson, J. Wang, M. E. Bowden, S. Xu, J. Hu, and J. G. Zhang, *Adv. Funct. Mater.*, **26**, 7094–7102 (2016).

154. A. A. Assegie, J.-H. Cheng, L.-M. Kuo, W.-N. Su, and B.-J. Hwang, *Nanoscale*, **10**, 6125–6138 (2018).
155. J. Alvarado, M. A. Schroeder, T. P. Pollard, X. Wang, J. Z. Lee, M. Zhang, T. Wynn, M. Ding, O. Borodin, Y. S. Meng, and K. Xu, *Energy Environ. Sci.*, **12**, 780–794 (2019).
156. T. T. Hagos, B. Thirumalraj, C.-J. Huang, L. H. Abrha, T. M. Hagos, G. B. Berhe, H. K. Bezabh, J. Cherng, S.-F. Chiu, W.-N. Su, and B.-J. Hwang, *ACS Appl. Mater. Interfaces*, **11**, 9955–9963 (2019).
157. P. Bai, J. Li, F. R. Brushett, and M. Z. Bazant, *Energy Environ. Sci.*, **9**, 3221–3229 (2016).
158. P. Patel, *ACS Cent. Sci.*, **1**, 161–162 (2015).
159. S. Liu, L. Xiong, and C. He, *J. Power Sources*, **261**, 285–291 (2014).
160. S. B. Majumder, S. Nieto, and R. S. Katiyar, *J. Power Sources*, **154**, 262–267 (2006).
161. R. Kostecki, J. Lei, F. McLarnon, J. Shim, and K. Striebel, *J. Electrochem. Soc.*, **153**, A669–A672 (2006).
162. S. Watanabe, M. Kinoshita, T. Hosokawa, K. Morigaki, and K. Nakura, *J. Power Sources*, **258**, 210–217 (2014).
163. S. Watanabe, M. Kinoshita, and K. Nakura, *J. Power Sources*, **247**, 412–422 (2014).
164. P. Keil, thesis, Technical University of Munich, Munich, Germany (2017).
165. J. Bareño, I. A. Shkrob, J. A. Gilbert, M. Klett, and D. P. Abraham, *J. Phys. Chem. C*, **121**, 20640–20649 (2017).
166. H. Nakai, T. Kubota, A. Kita, and A. Kawashima, *J. Electrochem. Soc.*, **158**, A798–A801 (2011).
167. Y. Li, M. Bettge, B. Polzin, Y. Zhu, M. Balasubramanian, and D. P. Abraham, *J. Electrochem. Soc.*, **160**, A3006–A3019 (2013).
168. K. Xu and A. von W. Cresce, *J. Mater. Res.*, **27**, 2327–2341 (2012).
169. J. Li, J. Harlow, N. Stakheiko, N. Zhang, J. Paulsen, and J. Dahn, *J. Electrochem. Soc.*, **165**, A2682–A2695 (2018).
170. T. Li, X.-Z. Yuan, L. Zhang, D. Song, K. Shi, and C. Bock, *Electrochem. Energy Rev.* (2019).

171. P.-C. Tsai, B. Wen, M. Wolfman, M.-J. Choe, M. S. Pan, L. Su, K. Thornton, J. Cabana, and Y.-M. Chiang, *Energy Environ. Sci.*, **11**, 860–871 (2018).
172. P. Yan, J. Zheng, M. Gu, J. Xiao, J.-G. Zhang, and C.-M. Wang, *Nat. Commun.*, **8**, 1–9 (2017).
173. J. Li, H. Liu, J. Xia, A. R. Cameron, M. Nie, G. A. Botton, and J. R. Dahn, *J. Electrochem. Soc.*, **164**, A655–A665 (2017).
174. F. Lin, I. M. Markus, D. Nordlund, T.-C. Weng, M. D. Asta, H. L. Xin, and M. M. Doeff, *Nat. Commun.*, **5**, 3529 (2014).
175. S. Muto, Y. Sasano, K. Tatsumi, T. Sasaki, K. Horibuchi, Y. Takeuchi, and Y. Ukyo, *J. Electrochem. Soc.*, **156**, A371–A377 (2009).
176. N. Y. Kim, T. Yim, J. H. Song, J.-S. Yu, and Z. Lee, *J. Power Sources*, **307**, 641–648 (2016).
177. T. Hayashi, J. Okada, E. Toda, R. Kuzuo, N. Oshimura, N. Kuwata, and J. Kawamura, *J. Electrochem. Soc.*, **161**, A1007–A1011 (2014).
178. L. Ma, S. Young, L. D. Ellis, Q. Huang, X. Ma, M. Chatzidakis, H. Li, L. Thompson, A. Eldesoky, C. R. M. McFarlane, G. A. Botton, I. G. Hill, and J. R. Dahn, *ACS Appl. Energy Mater.*, **1**, 7052–7064 (2018).
179. D. Streich, C. Erk, A. Guéguen, P. Müller, F.-F. Chesneau, and E. J. Berg, *J. Phys. Chem. C*, **121**, 13481–13486 (2017).
180. L. D. Ellis, J. P. Allen, L. M. Thompson, J. E. Harlow, W. J. Stone, I. G. Hill, and J. R. Dahn, *J. Electrochem. Soc.*, **164**, A3518–A3528 (2017).
181. N. P. W. Pieczonka, Z. Liu, P. Lu, K. L. Olson, J. Moote, B. R. Powell, and J.-H. Kim, *J. Phys. Chem. C*, **117**, 15947–15957 (2013).
182. D. Aurbach, B. Markovsky, G. Salitra, E. Markevich, Y. Talyossef, M. Koltypin, L. Nazar, B. Ellis, and D. Kovacheva, *J. Power Sources*, **165**, 491–499 (2007).
183. U. Kasavajjula, C. Wang, and A. J. Appleby, *J. Power Sources*, **163**, 1003–1039 (2007).
184. A. Van der Ven, J. C. Thomas, Q. Xu, B. Swoboda, and D. Morgan, *Phys. Rev. B*, **78** (2008).
185. K. J. Nelson, D. W. Abarbanel, J. Xia, Z. Lu, and J. R. Dahn, *J. Electrochem. Soc.*, **163**, A272–A280 (2016).
186. K. Nelson, thesis, Dalhousie University (2017).

187. L. Ma, L. Ellis, S. L. Glazier, X. Ma, Q. Liu, J. Li, and J. R. Dahn, *J. Electrochem. Soc.*, **165**, A891–A899 (2018).
188. J. Li, A. R. Cameron, H. Li, S. Glazier, D. Xiong, M. Chatzidakis, J. Allen, G. A. Botton, and J. R. Dahn, *J. Electrochem. Soc.*, **164**, A1534–A1544 (2017).
189. A. L. Patterson, *Phys. Rev.*, **56**, 978–982 (1939).
190. Y. Liu, J. Harlow, and J. Dahn, *J. Electrochem. Soc.*, **167**, 020512 (2020).
191. J. Zhu and G. Chen, *J. Mater. Chem. A*, **7**, 5463–5474 (2019).
192. L. Wang, B. Wu, D. Mu, X. Liu, Y. Peng, H. Xu, Q. Liu, L. Gai, and F. Wu, *J. Alloys Compd.*, **674**, 360–367 (2016).
193. H. Li, J. Li, X. Ma, and J. R. Dahn, *J. Electrochem. Soc.*, **165**, A1038–A1045 (2018).
194. H. Li, J. Li, N. Zaker, N. Zhang, G. A. Botton, and J. R. Dahn, *J. Electrochem. Soc.*, **166**, A1956–A1963 (2019).
195. A. Ueda and T. Ohzuku, *J. Electrochem. Soc.*, **141**, 2010 (1994).
196. C. Delmas, I. Saadoune, and A. Rougier, *J. Power Sources*, **44**, 595–602 (1993).
197. Y.-K. Sun, D.-J. Lee, Y. J. Lee, Z. Chen, and S.-T. Myung, *ACS Appl. Mater. Interfaces*, **5**, 11434–11440 (2013).
198. W. Li, J. N. Reimers, and J. R. Dahn, *Solid State Ion.*, **67**, 123–130 (1993).
199. H. Li, N. Zhang, J. Li, and J. R. Dahn, *J. Electrochem. Soc.*, **165**, A2985–A2993 (2018).
200. R. Weber, C. R. Fell, J. R. Dahn, and S. Hy, *J. Electrochem. Soc.*, **164**, A2992–A2999 (2017).
201. H. Li, A. Liu, N. Zhang, Y. Wang, S. Yin, H. Wu, and J. R. Dahn, *Chem. Mater.*, **31**, 7574–7583 (2019).
202. H. Beyer, S. Meini, N. Tsiouvaras, M. Piana, and H. A. Gasteiger, *Phys. Chem. Chem. Phys.*, **15**, 11025 (2013).
203. T. Mitsui and K. Hatakenaka, (2011)
<https://patents.google.com/patent/US20110183219A1/en>.
204. L. Qiao, Z. Cui, B. Chen, G. Xu, Z. Zhang, J. Ma, H. Du, X. Liu, S. Huang, K. Tang, S. Dong, X. Zhou, and G. Cui, *Chem. Sci.*, **9**, 3451–3458 (2018).
205. F. C. Laman and K. Brandt, *J. Power Sources*, **24**, 195–206 (1988).

206. S. Jiao, J. Zheng, Q. Li, X. Li, M. H. Engelhard, R. Cao, J.-G. Zhang, and W. Xu, *Joule*, **2**, 110–124 (2018).
207. F. Han, J. Yue, X. Zhu, and C. Wang, *Adv. Energy Mater.*, **8**, 1703644 (2018).
208. A. Liu, N. Zhang, H. Li, J. Inglis, Y. Wang, S. Yin, H. Wu, and J. R. Dahn, *J. Electrochem. Soc.*, **166**, A4025–A4033 (2019).

APPENDIX A



Home



Help



Email Support



Sign in



Create Account



Long cycle life and dendrite-free lithium morphology in anode-free lithium pouch cells enabled by a dual-salt liquid electrolyte

Author: Rochelle Weber et al

Publication: Nature Energy

Publisher: Springer Nature

Date: Jul 15, 2019

Copyright © 2019, Springer Nature

Author Request

If you are the author of this content (or his/her designated agent) please read the following. If you are not the author of this content, please click the Back button and select no to the question "Are you the Author of this Springer Nature content?".

Ownership of copyright in original research articles remains with the Author, and provided that, when reproducing the contribution or extracts from it or from the Supplementary Information, the Author acknowledges first and reference publication in the Journal, the Author retains the following non-exclusive rights:

To reproduce the contribution in whole or in part in any printed volume (book or thesis) of which they are the author(s).

The author and any academic institution, where they work, at the time may reproduce the contribution for the purpose of course teaching.

To reuse figures or tables created by the Author and contained in the Contribution in oral presentations and other works created by them.

To post a copy of the contribution as accepted for publication after peer review (in locked Word processing file, of a PDF version thereof) on the Author's own web site, or the Author's institutional repository, or the Author's funding body's archive, six months after publication of the printed or online edition of the Journal, provided that they also link to the contribution on the publisher's website.

Authors wishing to use the published version of their article for promotional use or on a web site must request in the normal way.

If you require further assistance please read Springer Nature's online [author reuse guidelines](#).

For full paper portion: Authors of original research papers published by Springer Nature are encouraged to submit the author's version of the accepted, peer-reviewed manuscript to their relevant funding body's archive, for release six months after publication. In addition, authors are encouraged to archive their version of the manuscript in their institution's repositories (as well as their personal Web sites), also six months after original publication.

v1.0

BACK

CLOSE WINDOW

Quantifying inactive lithium in lithium metal batteries



Author: Chengcheng Fang et al

Publication: Nature

Publisher: Springer Nature

Date: Aug 21, 2019

Copyright © 2019, Springer Nature

Order Completed

Thank you for your order.

This Agreement between Dalhousie University – Rochelle Weber ("You") and Springer Nature ("Springer Nature") consists of your license details and the terms and conditions provided by Springer Nature and Copyright Clearance Center.

Your confirmation email will contain your order number for future reference.

License Number 4760841055390

[Printable Details](#)

License date Feb 02, 2020

📄 Licensed Content

Licensed Content Publisher	Springer Nature
Licensed Content Publication	Nature
Licensed Content Title	Quantifying inactive lithium in lithium metal batteries
Licensed Content Author	Chengcheng Fang et al
Licensed Content Date	Aug 21, 2019

📄 Order Details

Type of Use	Thesis/Dissertation
Requestor type	non-commercial (non-profit)
Format	print and electronic
Portion	figures/tables/illustrations
Number of figures/tables/illustrations	1
High-res required	no
Will you be translating?	no
Circulation/distribution	1 - 29
Author of this Springer Nature content	no

📄 About Your Work

Title	PhD Thesis
Institution name	Dalhousie University
Expected presentation date	Apr 2020

📄 Additional Data

Portions	Figure 4
----------	----------

Requestor Location	Tax Details
Dalhousie University 6299 South Street	
Requestor Location	
Halifax, NS B3H 4R2 Canada Attn: Dalhousie University	
\$ Price	
Total	0.00 USD
	Total: 0.00 USD
CLOSE WINDOW	ORDER MORE

© 2020 Copyright - All Rights Reserved | [Copyright Clearance Center, Inc.](#) | [Privacy statement](#) | [Terms and Conditions](#)
 Comments? We would like to hear from you. E-mail us at customer care@copyright.com



RightsLink®

- [Home](#)
- [?](#)
- [Email Support](#)
- [Sign In](#)
- [Create Account](#)

SPRINGER NATURE Intragranular cracking as a critical barrier for high-voltage usage of layer-structured cathode for lithium-ion batteries

Author: Pengfei Yan et al
 Publication: Nature Communications
 Publisher: Springer Nature
 Date: Jan 16, 2017
 Copyright © 2017, Springer Nature

Creative Commons

This is an open access article distributed under the terms of the [Creative Commons CC BY](#) license, which permits unrestricted use, distribution, and reproduction in any medium, provided the original work is properly cited.

You are not required to obtain permission to reuse this article.
 To request permission for a type of use not listed, please contact [Springer Nature](#)

© 2020 Copyright - All Rights Reserved | [Copyright Clearance Center, Inc.](#) | [Privacy statement](#) | [Terms and Conditions](#)
 Comments? We would like to hear from you. E-mail us at customer care@copyright.com



Nanoscale Nucleation and Growth of Electrodeposited Lithium Metal



Author: Allen Pei, Guangyuan Zheng, Feifei Shi, et al

Publication: Nano Letters

Publisher: American Chemical Society

Date: Feb 1, 2017

Copyright © 2017, American Chemical Society

PERMISSION/LICENSE IS GRANTED FOR YOUR ORDER AT NO CHARGE

This type of permission/license, instead of the standard Terms & Conditions, is sent to you because no fee is being charged for your order. Please note the following:

- Permission is granted for your request in both print and electronic formats, and translations.
 - If figures and/or tables were requested, they may be adapted or used in part.
 - Please print this page for your records and send a copy of it to your publisher/graduate school.
 - Appropriate credit for the requested material should be given as follows: "Reprinted (adapted) with permission from (COMPLETE REFERENCE CITATION). Copyright (YEAR) American Chemical Society." Insert appropriate information in place of the capitalized words.
 - One-time permission is granted only for the use specified in your request. No additional uses are granted (such as derivative works or other editions). For any other uses, please submit a new request.
- If credit is given to another source for the material you requested, permission must be obtained from that source.

[BACK](#)

[CLOSE WINDOW](#)



Capacity fade of $\text{LiAl}_y\text{Ni}_{1-x-y}\text{Co}_x\text{O}_2$ cathode for lithium-ion batteries during accelerated calendar and cycle life tests (surface analysis of $\text{LiAl}_y\text{Ni}_{1-x-y}\text{Co}_x\text{O}_2$ cathode after cycle tests in restricted depth of discharge ranges)

Author:

Shoichiro Watanabe, Masahiro Kinoshita, Takashi Hosokawa, Kenichi Morigaki, Kensuke Nakura

Publication: Journal of Power Sources

Publisher: Elsevier

Date: 15 July 2014

Copyright © 2014 Elsevier B.V. All rights reserved.

Order Completed

Thank you for your order.

This Agreement between Dalhousie University – Rochelle Weber ("You") and Elsevier ("Elsevier") consists of your license details and the terms and conditions provided by Elsevier and Copyright Clearance Center.

Your confirmation email will contain your order number for future reference.

License Number 4760850739022

[Printable Details](#)

License date Feb 02, 2020

Licensed Content

Licensed Content Publisher	Elsevier
Licensed Content Publication	Journal of Power Sources Capacity fade of LiAl _y Ni _{1-x-y} Co _x O ₂ cathode for lithium-ion batteries during accelerated calendar and cycle life tests (surface analysis of LiAl _y Ni _{1-x-y} Co _x O ₂ cathode after cycle tests in restricted depth of discharge ranges)
Licensed Content Title	
Licensed Content Author	Shoichiro Watanabe, Masahiro Kinoshita, Takashi Hosokawa, Kenichi Morigaki, Kensuke Nakura
Licensed Content Date	Jul 15, 2014
Licensed Content Volume	258
Licensed Content Issue	n/a
Licensed Content Pages	8
Journal Type	S&T

About Your Work

Title	PhD Thesis
Institution name	Dalhousie University
Expected presentation date	Apr 2020

Requestor Location

	Dalhousie University 6299 South Street
Requestor Location	Halifax, NS B3H 4R2 Canada Attn: Dalhousie University

Price

Total	0.00 USD
-------	----------

Order Details

Type of Use	reuse in a thesis/dissertation
Portion	figures/tables/illustrations
Number of figures/tables/illustrations	1
Format	both print and electronic
Are you the author of this Elsevier article?	No
Will you be translating?	No

Additional Data

Portions	Figure 7
----------	----------

Tax Details

Publisher Tax ID	GB 494 6272 12
------------------	----------------

Total: 0.00 USD

[CLOSE WINDOW](#)

[ORDER MORE](#)